Pontifícia Universidade Católica
do Rio de Janeiro

Sergio Santiago Ribeiro

Cementing process in the presence of fluid loss.

Tese de Doutorado

Thesis presented to the Programa de Pós–graduação em Engenharia Mecânica of PUC-Rio in partial fulfillment of the requirements for the degree of Doutor em Engenharia Mecânica.

Advisor: Profa. Mônica Feijó Naccache

Rio de Janeiro
October 2020

PUC-Rio - Certificação Digital Nº 1612794/CA

Pontifícia Universidade Católica
do Rio de Janeiro

Sergio Santiago Ribeiro

Cementing process in the presence of fluid loss.

Thesis presented to the Programa de Pós–graduação em Engenharia Mecânica of PUC-Rio in partial fulfillment of the requirements for the degree of Doutor em Engenharia Mecânica. Approved by the Examination Committee.

Profa. Mônica Feijó Naccache
Advisor
Departamento de Engenharia Mecânica – PUC-Rio

Dra. Cristiane Richard de Miranda
Pesquisadora – Autônoma

Prof. Hans Joakim Skadsem
Departamento de Engenharia de Energia e Petróleo –
Universidade de Stavanger, Noruerga

Prof. Márcio da Silveira Carvalho
Departamento de Engenharia Mecânica – PUC-Rio

Prof. Paulo Roberto de Souza Mendes
Departamento de Engenharia Mecânica – PUC-Rio

Rio de Janeiro, October the 29th, 2020

PUC-Rio - Certificação Digital Nº 1612794/CA

All rights reserved.

Sergio Santiago Ribeiro

Sergio Ribeiro graduated in Control and Automation Engineering at Pontifical Catholic University of Rio de Janeiro (PUC-Rio) in 2006, and got his Masters degree on Signal Processing and Artificial Intelligence at Electrical Engineering Department also at PUC-Rio in 2008. During his masters, Sergio worked developing AI algorithms at Choice Technologies on several dedicated research and development projects.
In 2012, Sergio joined Halliburton Brazil Technology Center, where in 2016 was granted a Patent on the Well Physical Simulator Apparatus, and worked on a joint project with Petrobras to investigate cement hydration, gas migration, and fluid loss problems.
Currently, works in the Laboratory of Micro hydrodynamics and Porous Media Flow at PUC-Rio as a researcher, where is applying for a Doctorate Degree in Thermosciences at the Mechanical Engineeering Department.

PUC-Rio - Certificação Digital Nº 1612794/CA

Bibliographic data

Ribeiro, Sergio

Cementing process in the presence of fluid loss. / Sergio Santiago Ribeiro; advisor: Mônica Feijó Naccache. – Rio de janeiro: PUC-Rio, Departamento de Engenharia Mecânica, 2020.

v., 179 f: il. color. ; 30 cm

Tese (doutorado) - Pontifícia Universidade Católica do Rio de Janeiro, Departamento de Engenharia Mecânica.

Inclui bibliografia

1. Engenharia Mecânica – Teses. 2. Cimentação de Poços;. 3. Simuladores Físicos;. 4. Análise Numérica;. 5. Medições em Fluidos Complexos;. 6. Perda de Filtrado;. I. Naccache, Mônica. II. Pontifícia Universidade Católica do Rio de Janeiro. Departamento de Engenharia Mecânica. III. Título.

CDD: 621

PUC-Rio - Certificação Digital Nº 1612794/CA

To my wife and daughter for being my everything. "Love you 3000."

Acknowledgments

To my parents for the lifetime support and inspiration.
To my best friend and wife, Priscilla Varges, for the effusive technical discussions and compelling motivational arguments.
To my daughter Marina (Nina), which even not quite understanding why, she learned that dad had a work to finish.
To Ângela and Patrícia Varges, for being great listeners and for all their love and dedication to our family.
To my advisor, Prof. Mônica Feijó Naccache, for the trust and excellent technical discussions.
To Prof. Márcio Carvalho, for great lectures and technical partnership.
To Halliburton and Petrobras technical teams and to the laboratory colleagues at GReo and LMMP for the valuable discussions and all the help through these years.
To Halliburton, Petrobras, CNPq, CAPES and PUC-Rio, for finantial support.
This study was financed in part by the Coordenação de Aperfeiçoamento de Pessoal de Nível Superior - Brasil (CAPES) - Finance Code 001.

PUC-Rio - Certificação Digital Nº 1612794/CA

Abstract

Ribeiro, Sergio; Naccache, Mônica (Advisor). **Cementing process in the presence of fluid loss.**. Rio de Janeiro, 2020. 179p. Tese de doutorado – Departamento de Engenharia Mecânica, Pontifícia Universidade Católica do Rio de Janeiro.

This thesis aims to investigate the cementing process of an oil well in presence of a filtrate loss zone. An experimental setup was designed, built and operated to simulate an annular well field-like geometry where cement would cure under controlled conditions. This well simulator consisted of an $8\,m$ concentric annular column with a section of semi-permeable external wall, equipped with pressure and temperature sensors. It allows the investigation of the cementing cure mechanisms, as well as the impact of the fluid loss zone in the pressure drop behavior. In order to predict this behavior on real oil wells, a 2D transient numerical model is proposed. A finite element model was implemented in Python with the aid of an open source library named FEniCs. Mass and momentum conservation equations are solved to obtain the pressure and velocity fields, and the cement mixture is considered an incompressible single-phase mixture composed of two chemical species: the filtrate and the dissolved cement. Mass transport is modeled with an advection-diffusion equation and dissolved cement species is modeled as a viscoplastic fluid with shrinkage. Finally, the simulation results were confronted with the experimental data, and a good agreement was observed. Further investigation of numerical model parameters was performed, and a sensitivity analysis evaluated individual influence of those parameters in the pressure drop. The results indicate that pressure profile evolution has a strong dependency on thickening time, fluid loss flow rate magnitude and the Newtonian viscosity plateau for the evaluated shear rate regimen.

PUC-Rio - Certificação Digital Nº 1612794/CA

Keywords

Well Cementing; Physical Simulators; Numerical Analysis; Complex Fluids Measurements; Fluid Loss;

Resumo

Ribeiro, Sergio; Naccache, Mônica. **Análise do processo de cimentação na presença de perda de filtrado**. Rio de Janeiro, 2020. 179p. Tese de Doutorado – Departamento de Engenharia Mecânica, Pontifícia Universidade Católica do Rio de Janeiro.

O presente estudo tem como objetivo investigar o processo de cimentação de poços de petróleo, na presença de zonas de perda de filtrado. Um aparato experimental foi projetado, construido e operado com o objetivo de simular a cimentação de um poço de petróleo. Com diâmetros característicos dos poços reais, esse simulador permite que o processo de cura da coluna de cimento seja monitorado com condições controladas. O aparato consiste em uma coluna anular concêntrica com $8\,m$ de comprimento. A zona de perda de filtrado é modelada por uma parede semi-permeável, e todo poço é equipado com sensores de pressão e temperatura. Isso possibilita a investigação dos mecanismos de cura da pasta de cimento, bem como o impacto da perda de filtrado na evolução do perfil de pressão. Para tentar prever esse comportamento, um modelo numérico 2D de Elementos Finitos foi proposto e implementado em Python, utilizando bibliotecas pré-compiladas de código aberto denominadas FEniCs. As equações de conservação de massa e momento são resolvidas para obter os campos de velocidade e pressão. A mistura da pasta de cimento é considerada um fluido incompressível e composta de duas espécies químicas: a fase aquósa(ou filtrado) e o cimento dissolvido. O transporte de massa é modelado usando a equação de advecção-difusão, e a pasta é modelada como um fluido viscoplástico que sofre redução volumétrica com a cura. Finalmente, os resultados das simulações foram confrontados com os dados experimentais obtidos, e uma boa concordância foi observada. Uma investigação adicional foi realizada no modelo numérico, através de uma análise de sensibilidade individual dos parâmetros de entrada e seu respectivo impacto na queda de pressão. Para o regime de taxas de cisalhamento avaliados, os resultados indicaram uma forte dependência entre a evolução do perfil de pressão e o tempo de cura, a magnitude da vazão de filtrado e o patamar newtoniano da viscosidade.

Palavras-chave

Cimentação de Poços; Simuladores Físicos; Análise Numérica; Medições em Fluidos Complexos; Perda de Filtrado;

PUC-Rio - Certificação Digital Nº 1612794/CA

Table of contents

PUC-Rio - Certificação Digital Nº 1612794/CA

PUC-Rio - Certificação Digital Nº 1612794/CA

List of figures

PUC-Rio - Certificação Digital Nº 1612794/CA

PUC-Rio - Certificação Digital Nº 1612794/CA

PUC-Rio - Certificação Digital Nº 1612794/CA

PUC-Rio - Certificação Digital Nº 1612794/CA

List of tables

PUC-Rio - Certificação Digital Nº 1612794/CA

PUC-Rio - Certificação Digital Nº 1612794/CA

"Everything should be made as simple as possible, but no simpler."

Albert Einstein, *New York Times, January 8^{th}, 1950 - by Roger Sessions.*

1
Introduction

1.1
Overview

Well construction in one of the most complex operations performed on an oil well. It starts with drilling, which consists in digging through several layers of different rock formations, down to the reservoir where the oil can be found. The open hole is referred as wellbore, and it's drilled part by part by cutting and shredding each rock type with a specific rotating drill bit [1].

Regardless the rock type, a fluid needs to be pumped in to cool down the bit and carry out the cuttings to surface. It flows down inside the drill column, through some bit nozzles and back up by the annular section formed around the column, as illustrated in Fig. 1.1 [2].

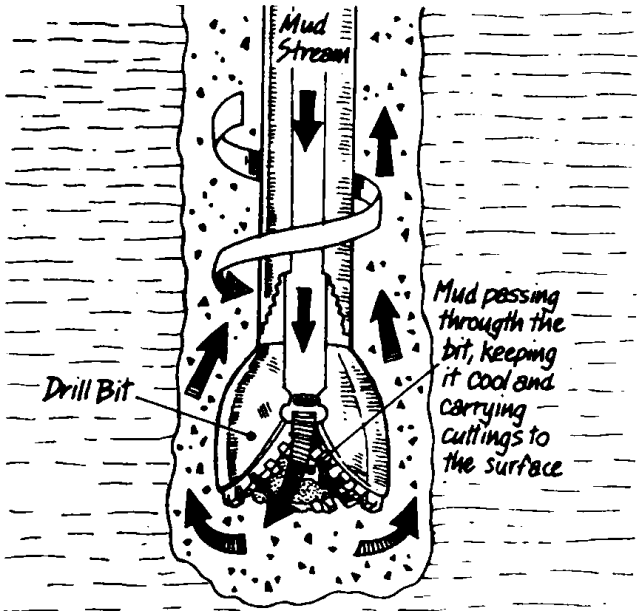

Figure 1.1: Drilling fluid circulation schematics.
From [2]

Among other functions, the drilling fluid prevents the well walls to collapse and also balances pressure of the rock pore fluids, named pore pressure. Fluid rheology and thermal aspects are important, but fluid density is the

PUC-Rio - Certificação Digital Nº 1612794/CA

major parameter to be tuned in this operation, since it determined the fluid static pressure.

At a certain moment during drilling, the formation pore pressure at the bottom will require a heavier drilling mud to keep pore pressure balanced. However, a denser fluid may exceed fracture gradient of top rock formations, inducing undesired fractures [3]. The fractured walls may enable contamination of rock formations, and also reduces the amount of drilling fluid circulating. Hence, this phenomena is usually named lost circulation.

From time to time drilling stops and steel pipe, called casing, is lowered and cemented in place. The deeper the section, the slender the casing installed, creating a telescopic configuration, as illustrated in Fig. 1.2 [4].

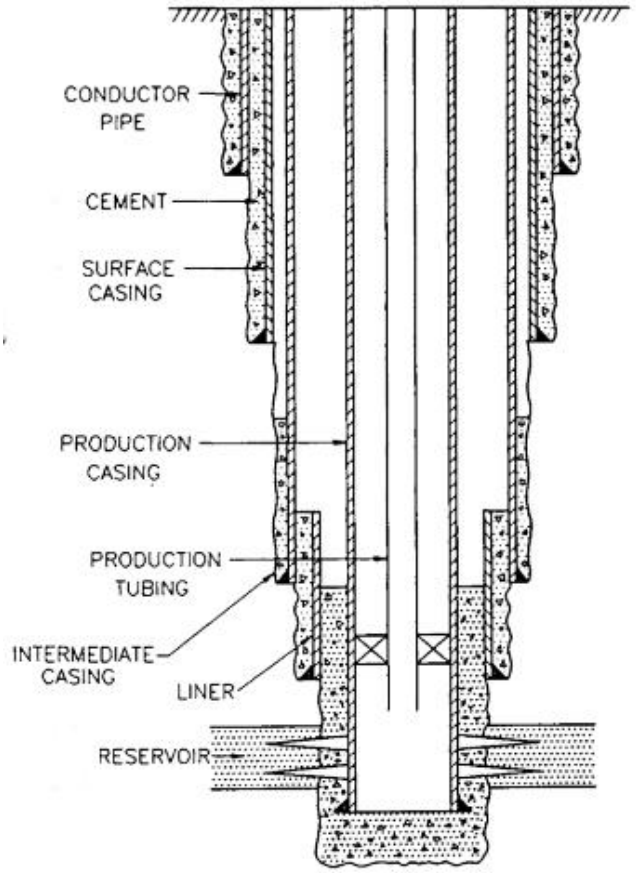

Figure 1.2: Telescopic well casing schematics.
From [4]

Cementing technology amalgams many interdependent scientific and engineering disciplines [5]. Besides binding the casings in place and providing well structure, cementing operation main goal is zonal isolation. Together with the casing, cement sheath must prevent leaks from inner oil production path to upper rock formation, and also insulate the different formations from

PUC-Rio - Certificação Digital Nº 1612794/CA

fluid exchange. This barrier must last throughout the whole well life, starting immediately after cement is displaced, while it is still a low viscous material.

Fluids are used as barriers on several natural and industrial processes for different applications. In lubrication, fluid films are used to avoid direct contact between two solids surfaces. Another fluid barrier is coating, which, for example, can be applied to protect solid from corrosion caused by the contact of another fluid, such as humid air. The liquid cement, also works as a fluid barrier, designed among other functions to protect well and reservoir fluids from contaminating or diffusing into each other.

Cementitious materials transition between liquid and solid states receives the name of curing. Despite registers of man-made cement-like materials date from before the Roman Empire [6], curing is still a vast object of study, specially on how mechanical properties change in this process. Several authors have experimentally studied curing cement pastes, and among the most analysed set of properties are differential pressure transmitted [7], density [8], elasticity and viscosity [9, 10].

Although the physical mechanisms of curing are yet being analysed nowadays, the operational processes of a cementing job have changed very little since the original patent was published in 1921 [11]. As it can be compared in Fig. 1.3, adapted from [11] and [12], almost all cementing components are yet present in a similar configuration and general procedures are mainly the same.

Primary cementing is performed by pumping down a cement paste through the casing filled with drilling fluid, and back up through the annular region formed between the casing and rock formation. First, using the cement head, bottom and top plugs are placed inside the casing. In the sequence, the slurry is pumped between two plugs, pushing bottom plug and displacing drilling fluid downwards. To clear the casing inside, top plug is displaced with a set of fluids, including spacers, cleaners and drilling fluid. Finally, bottom plug rupture disk bursts with pressure, and allows slurry to flow through the guide-shoe and up through the annulus.

Despite this procedure practically assures a perfect slurry displacement inside the casing, cement sheath contamination might still occur in the annular region. Common issues caused by problems with annular flow includes induced fracturing, channeling, microannuli and mudcake, as presented in Fig. 1.4, from Stokes [13]. Although this figure also shows the same problems happening in a cement plug, this work is focused in the annular space cementing.

PUC-Rio - Certificação Digital Nº 1612794/CA

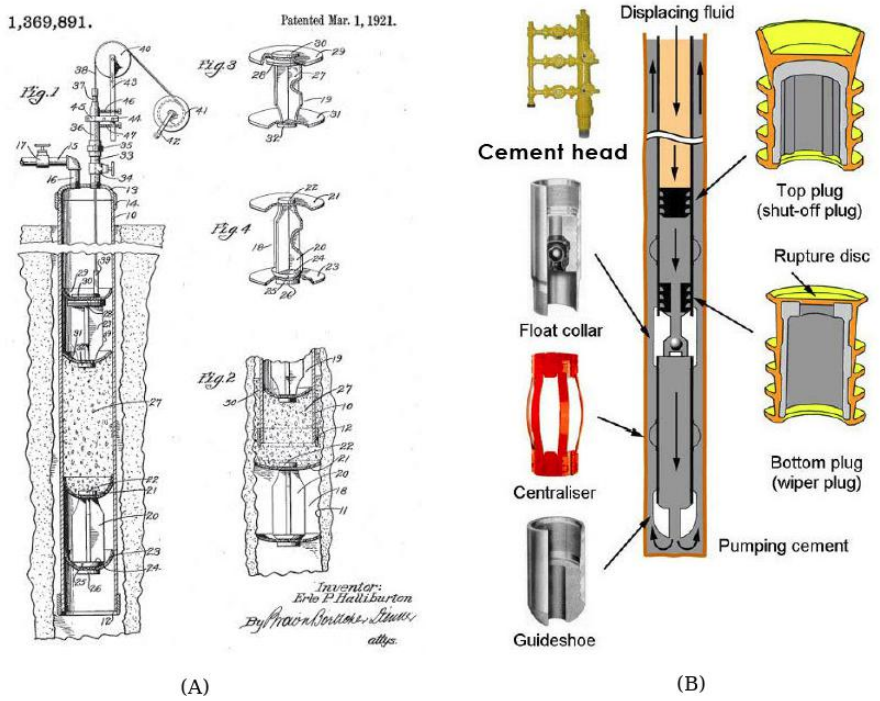

Figure 1.3: Primary Cementing Components Comparison: (A) Original Patent and (B) Recent Tutorial.
Adapted from [11] and [12]

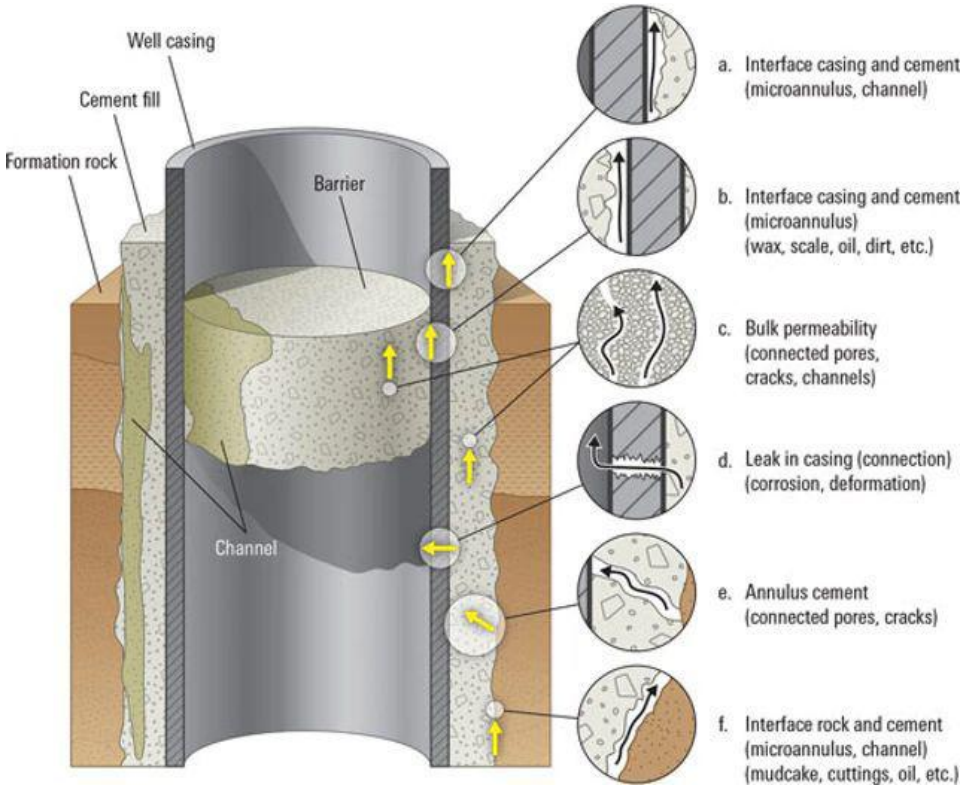

Figure 1.4: Potential Cement Issues.
From [13]

PUC-Rio - Certificação Digital Nº 1612794/CA

Nevertheless, a perfect cementing job does not depends simply on an annular region properly filled with slurry. As mentioned, cement cures with time, and during that process chemical reactions transforms water into the calcium carbonate responsible for the resistance of hardened cement. As presented by Banfill [9], a low water-to-cement ratio during cure, might impact the cement structural properties.

Lost circulation is defined as total of partial loss of drilling fluids or cement into highly permeable zones, cavernous formations and natural or induced fractures. In the particular case of permeable zones, where only part of the well fluids are filtered into the formation, are usually referred as fluid loss or spurt loss.

Although after placement cement could be considered static, the curing process is essentially dynamic, with time-dependent properties due to chemical reactions and fluid loss occurrence. Therefore, it is important to accurately predict the slurry properties throughout curing, such as viscosity, water concentration and pressure gradient among others.

PUC-Rio - Certificação Digital Nº 1612794/CA

1.2 Motivation

Specially due to growing environmental concern about leaks and spills on the last decades, well construction phase is seen as critical to well life safety. In addition to the ecological aspects, the previous decades faced three huge oil price crises. As expected, the decay of the market margins laid a big pressure on production efficiency and cost reduction.

In this scenario, the oil companies praise for: (i) reducing non-productive time, which means more assertive well construction techniques and less work-over events or environmental fees due to spills; (ii) increasing recovery rates, that translates to stimulating production from depleted wells; (iii) reducing break-even time, specially on ultra deep reserves, such as the pre-salt oil layer illustrated on Fig. 1.5 [14].

Brazilian's pre-salt reserves present several operational challenges that push production lead time, such as water huge depth and salt-layer variable thickness. But certainly pre-salt biggest challenge is the carbonates heterogeneous permeability. This karstified formation presents large porosity variations, from the microscopic porous matrix, up to fractures and vugs orders of magnitude bigger, as showed by Basso et al. [15].

Pre-salt carbonate reservoir present natural gas pockets, which introduces the risk of a gas invasion into a recently cemented well triggered by fluid loss, as illustrated in Figure 1.6. A simple fluid loss may result in several

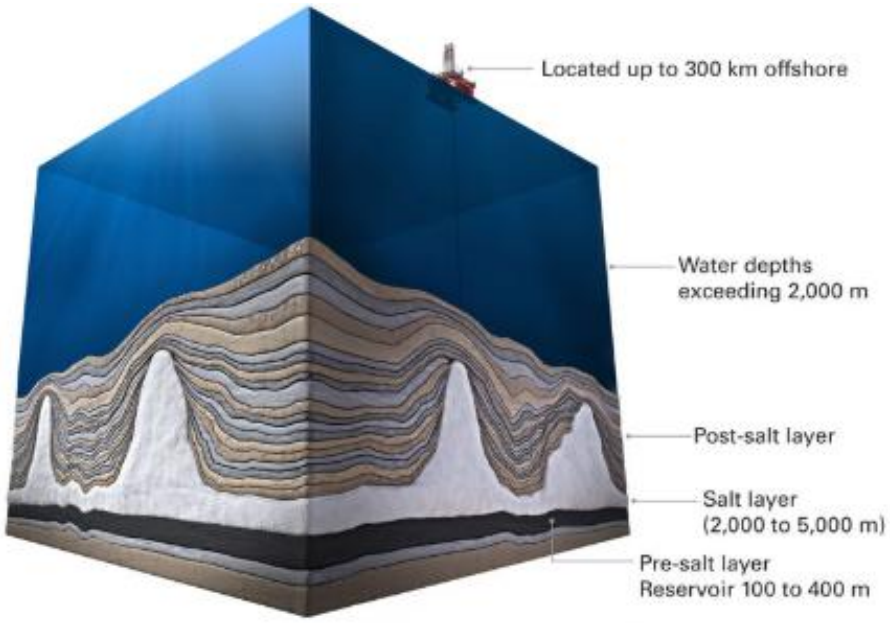

Figure 1.5: Pre-salt oil layer in Brazil.
From [14].

PUC-Rio - Certificação Digital Nº 1612794/CA

work-over operations and days of delayed production. Ultimately, gas influx bubbles may grow with pressure decay, increasing the risk of blowout.

Some historical blowouts had extreme consequences to the environment and to local economics. Consequently, operators and service companies worldwide have been working together on a deeper and more solid understanding of the zonal isolation problem. Thereupon, ISO 10.426 standards on Well Cementing [16] state that accurate prediction of well pressure profile evolution with time is critical for well integrity assurance.

Therefore, it's necessary to enrich pressure profile predictions in scenarios of fluid loss. Predicting local cement pressure transmission defects, caused by fluid loss, may save a considerable amount of money, and also anticipate production.

1.3 Objectives

As part of a wider research and development programs between Petrobras and Halliburton, the present Thesis is focused on improving comprehension of fluid loss impact in cement zonal isolation capabilities. To this end, an experimental analysis was performed to evaluate the physical mechanisms involved on the pressure profile depletion due to a fluid loss zone presence on a recently placed cement sheath. In addition theoretical and numerical studies are performed in order to identify a cost-effective prediction model for the pressure profile, that takes into account fluid loss, chemical shrinkage and

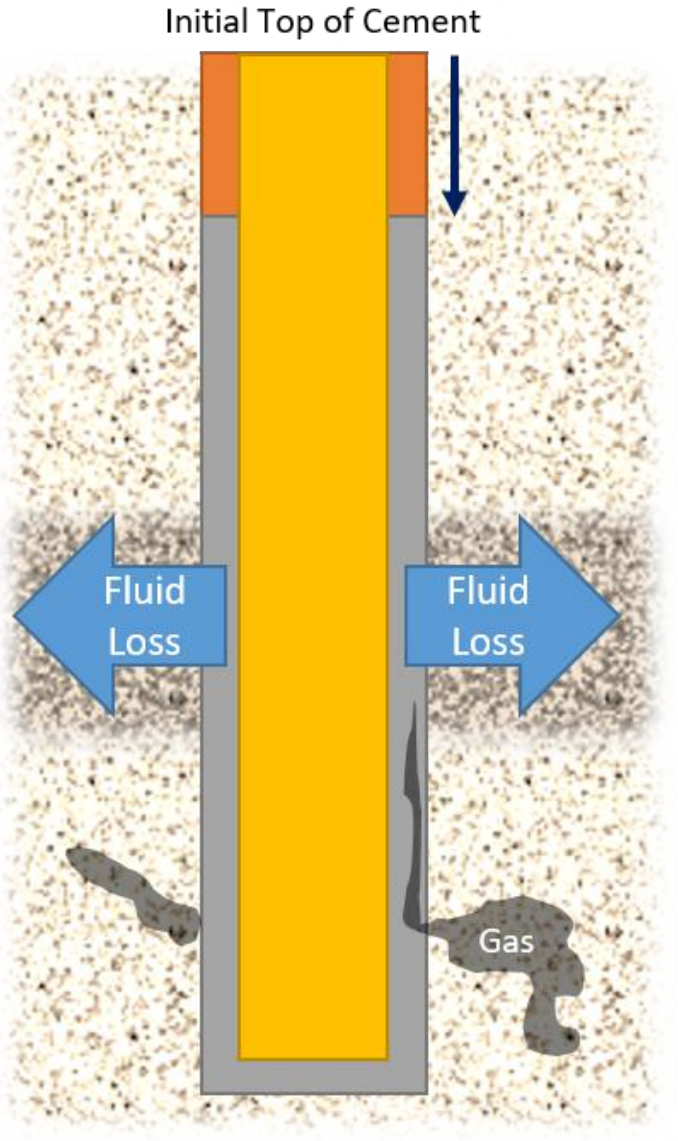

Figure 1.6: Gas invasion caused by fluid loss.

PUC-Rio - Certificação Digital Nº 1612794/CA

rheology.

1.4 Outline

This thesis topics are divided in the next six chapters:

In Chapter 2, a literature review is presented divided in three different sections. The first, presenting the review of well cementing methods used at fluid loss scenarios. The second, presenting the most relevant physical simulators developed and their applications. Finally the third, presenting the numerical simulations of cementing systems.

Chapter 3 details the of the Physical Well Simulator (PWS), an experimental setup developed to emulate a laboratory version of a well cementing

operation. This chapter also unveils the apparatus mechanical design, construction, instrumentation, and operation. In addition, the peripheral equipment developed to support the tests are also presented in this chapter.

On the folowing, the physical model proposed is elucidated in Chapter 4. This comprises all hypothesis assumed, the simplified conservative equations, models, and the considered boundary conditions.

Moreover, Chapter 5 outlines the numerical implementation of that model in Finite Elements. Time and spatial discretization is also detailed, and mesh tests results are presented.

In Chapter 6, the experimental and numerical results are presented and discussed. Finally, the conclusions and future steps proposition are presented in Chapter 7.

PUC-Rio - Certificação Digital Nº 1612794/CA

2
Literature review

Brazil pre-salt carbonate reservoirs have highly complex sedimentary lithology and were mostly formed during the early Cretaceous period. As studied by Tosca and Wright [17], the area experienced compression with reverse faulting and folding, combined with extensional faults in some regions. This results in the heterogeneous porosity and permeability observed. Together with the great sea depth, this karstic formation makes well drilling and cementing challenging operations in the oil industry, with high probability of induced fracturing.

As discussed in Chapter 1, the core objectives of well construction steps are to provide structural resistance and to avoid fluid exchanges between the well and the reservoir in any situation. During drilling and during cementing, the pressure operational window must be respected to avoid, or at least minimize, lost circulation or fluid influxes [1]. During cementing, fluid loss represents a problem not only due to contamination of the production reservoir, but also because it interferes with the cementing curing process, and consequently with the resultant sheath resistance and sealing capabilities [5].

For that matter, technical experts state that uncontrolled fluid loss might imply on a poor zonal isolation, and may allow fracture zones to communicate and ultimately flow up to the surface. Santra et al. [18] studied formation fluid influxes into cement slurries and observed short term problems, such as gas migration and pressure buildup behind the casing. They also point out some long term issues, like casing corrosion, presence of cement sheath cracks and microannulus formation.

Those failure modes might lead to minor oil spills during production phase, or even to a more severe blowout if in the presence of gas. Since Brazil carbonate reservoirs present a high content of CO_2 storage, there is a significant probability of gas influx occurrence under unbalanced conditions. Consequently, predicting and avoiding these conditions are an important safety concern. The consequences of ignoring or underestimating gas influxes can be catastrophic considering human safety, ecological and economical aspects, as witnessed recently in the Gulf of Mexico and reported by Chanton et al. in 2012 [19].

PUC-Rio - Certificação Digital Nº 1612794/CA

After a cement job, pressure checks must be performed to detect eventual flow channels in the sheath [3, 5]. In that case, remedial squeeze cementing jobs must be applied, implying on significant increase of rig-time costs, including waiting on cement and re-drilling operations. More than 12% of the non-productive time (NPT) in cementing and drilling phase in the Gulf of Mexico has been reported as due to lost circulation problems [20]. The worldwide impact of lost circulation is estimated between two and four billion dollars annually, between NPT, lost amounts of drilling fluids, and extra materials used to stem the losses [20]. In the worst case scenario, a severe fluid invasion could even force an indefinite well abandonment and complete loss of the investment. Therefore, it is crucial to better understand the mechanisms that potentially trigger well influxes, such as bad rheological slurry design or fluid loss, which can lead to bad predictions of the pressure profile.

In section 2.1, a historical overview of the field techniques used in cementing operations is performed. On the sequence, the literature work on cement rheology and rheometry is analyzed in section 2.2. More focused on the proposed scope of this thesis, section 2.3 presents an overview of the lost circulation and fluid loss studies. Also in this section, fluid loss mechanisms are presented and discussed. Moreover, section 2.4 describes previous physical simulators developed to specifically to evaluate pressure profile and analyse fluid loss or gas influx problems. Section 2.5 reviews the literature of numerical simulators developed, focusing on well pressure profile evolution prediction. And finally, section 2.6 outlines the contributions of this work.

PUC-Rio - Certificação Digital Nº 1612794/CA

2.1 Well cementing techniques and challenges

Back in 1911, Perking and Double [21] filed a patent on a method of cementing oil wells. It was mostly about the displacement process and describes how two packers or plugs could be used to physically keep the cement from mixing with the water or drilling fluid displaced. Ten years later, Halliburton [11] filed a very similar, though much more famous, patent presenting the top and bottom plug technique still used nowadays on cementing oil wells. Halliburton states in its patent that several studies have been performed, and by that time cement was identified as the only material that could close a well and avoid existing formation water to be produced together with the oil. Since then, several companies have simply applied the same techniques, with minor variations, as a service to oil production companies.

Sauer [22] reviewed that historical background and showed that other patents have been filed, but very little have changed up to the 1940s. Most

of the new patents within these two decades were focused on how cement proper hydration occur during mixing [23], on cement composition [24], and on mud displacement techniques [25]. Sauer [22] also shows that most of what have been published in the subsequent twenty years didn't make it to the field operations best practices for several decades. He emphasizes some important publications after the 1960s, such as Slagle [26], who for the first time brought rheological slurry design to oil industry attention.

Oil well cementing composition have evolved a lot along the 20^{th} century. Portland cement is the common base, mainly composed of alite or Tricalcium silicate $3(CaSiO_2)$, belite or Dicalcium silicate $2(CaSiO_2)$ and limestone or Calcium carbonate ($CaCO_3$), along with smaller additions of ferrite, aluminite and gypsum. Combined with water these compounds react, and the principal hydration product is the less-ordered Calcium silicate hydrate ($3CaO \cdot 2SiO_2 \cdot 4H_2O$, or simply C-S-H). It may be presented in a variety of concentrations in some free water solution of mineral salts. Calcium silicate hydrate is mostly the responsible for cement-base concrete strength. Although this work does not explore further chemical aspects, such as the detailed reaction stoichiometry or a deep sensitivity analysis on composite fractions, some interesting discussions on this topic were presented by Kunther et al. [27] and Barbosa [28].

Field and laboratory experimental evidence have been reported that the cemented well inner pressure decreases with time, a bit after placement, but still before complete cure. Wittmann et al. [29] have stated that this pressure drop is caused by absorption of water present among the gel particles. According to Wittmann, this absorption reduces the surface tension, and therefore lowers the hydrostatic pressure of the gel itself. After the initial set, cement reaction goes on for a long time, although on a much slower rate. He showed that cement properties continue to evolve for years into the life on hardened cement [30].

Appleby and Wilson [31] have performed a study on how cement permeability decreases five to six orders of magnitude in just a few hours. However, they also outline the physical mechanisms happening during cure, that directly contribute to pressure decay. The first is the gel viscosity build-up, which together with water absorption is responsible for the formation of a porous structure that adheres to the well walls and inhibits stress transmission downhole. The second is the shrinkage, or density change, which directly impacts hydrostatic pressure gradient. When this phenomenon happens before the viscosity buildup is complete, fluids from the reservoir might manage to flow into the well and ultimately to the surface. Actually, this is considered to be the initial cause of some historical blowouts, where gas was able to flow

PUC-Rio - Certificação Digital Nº 1612794/CA

through cement sheath. By this reason, many authors historically have studied in detail and tried to model the mechanisms responsible by pressure drop during the hydration period [32, 7, 33, 34, 35].

According to Chenevert and Shrestha [36], Le Chatelier reported in 1887 [37] that Portland cement showed around 4.6% shrinkage when it sets. This phenomena was briefly mentioned by Wittmann [29] in his work, but it was deeply studied by Mindess et al. [38]. Shrinkage consists in a combined reduction of volume and weight, as the curing chemical reaction gives cement its structure, while consumes the water within. In the oil industry, cement shrinkage is usually controlled with chemical additives which can promote an additional volume expansion. The additives quantities are adjusted to start the expansion moments before cement shrinkage occurs. Some empirical models have been developed to predict how and when cement shrinkage happens [7, 39, 40, 41].

In addition to gelation and shrinkage, another issue to cement column pressure drop prediction is when the well presents highly permeable zones along its length [42]. Fluid loss to well porous walls might also lead to an earlier and more dangerous pressure drop, simply by the decrease of the cement column height. This phenomena is usually referred as top of cement(ToC) misplace. If annular well pressure is high enough to induce a filtration of the cement into the formation, the designed ToC is not sustained.

Beyond that, with less water available cement cure is altered. Chemical proportions change and controlling cement hardening with designed additive amounts might be impossible. Therefore, many authors have proposed ways to stop or minimize cement fluid loss [43, 44, 45, 20, 46, 47], and most agree on the importance of better understanding the mechanisms that govern fluid loss in order to predict it [48, 49, 50, 51, 52].

PUC-Rio - Certificação Digital Nº 1612794/CA

2.2 Cement rheological analysis

Dellyes [53] presented rheological studies showing that fresh mixed cement slurries present shear-thickening behavior for high shear rates. Tattersall [54] was one of the first to deeply analyse the rheology of a cement slurry. Using a coaxial cylinder viscometer, he experimentally gathered data to plot flow curves of cement pastes. It was observed a pseudo plastic or shear-thinning behavior, for the values tested. Later on, Berg [55] reported that both phenomena might occur simultaneously, but only at high shear rates shear-thickening become dominant.

Although Tattersall tests did not cover lower shear-rate ranges [54], the

presented flow curves already indicated a point crossing the shear-stress axis different than zero. This is a characteristic shear stress beneath which the slurry behaved like a solid, named yield stress. Later on, Berg [55] and Min [56] showed the same Bingham [57] gel behavior on their respective studies. Tattersall rheometry results also presented hysteresis [54], indicating structural breakdown, which is a thixotropic effects. This behavior was also observed by Berg [55], who was also able to identify reversible structural buildup [55]. Therefore, the early placed cement pastes curing at lower shear-rates are frequently modeled as thixotropic yield-stress gels.

Jones and Taylor [58] reviewed the rheometry techniques used to obtain several flow curves with different water-to-cement ratios. They also reviewed some mathematical models to predict the cement paste behavior for a range of water-to-cement ratios. Hansen [8] has evaluated experimentally the effects of the absence of water during cure. Hansen shows that poor water-to-cement ratio increases shrinkage, accelerates viscosity buildup and ultimately result into poor structural properties. These observations are in agreement with Berg study on how solid concentration results in slurries with higher yield stress.

Rodrigues et al. [59] investigated the protocols usually employed to obtain flow curves of cement slurries. The importance of steady state and thixotropy were discussed.

More recently, Rodrigues and Souza Mendes [60] reviewed thixotropic cement slurries characterization techniques. A new phenomenological constitutive model, which correlates fluidity and microstructure structuring level, was proposed considering time dependence and irreversibility. A yield stress function that exponentially increases with time was employed to reproduce irreversible effects. In order to characterize cement slurries, they applied a modified Herschel-Buckley [61] to fit rheometry measurements of cement slurries and its time-dependent behavior. Finally, Marchesini et al. [62] proposed an irreversible time dependent constitutive model based on a single structure parameter. Viscosity bifurcation, shear banding, stress overshoots, effects of chemical reactions, and irreversible shear degradation were explored. Moreover, rheometric experiments were performed demonstrating good agreement with model predictions.

2.3 Lost circulation and fluid loss

Loss circulation was initially observed and analysed during drilling in the early forties [63]. The first extensive scientific study was performed in the early fifties by Howard et al. [64], followed by [65]. However, by that

PUC-Rio - Certificação Digital Nº 1612794/CA

time a loss zone in the well was almost always tackled by using fast time-setting cement clay applied directly as a plug [66, 67]. Recently, Therond et al. [52] presented field and laboratory study that confirms that opening a fracture with cement demands much more pressure than with synthetic oil-base drilling fluid. Although it might still be used nowadays in some severe cases [68, 69, 70, 52], this remedial treatment has several disadvantages. Howard et al. [64] already pointed out some of them, such as the increase of rig time due to plug placement, waiting on cement to set and re-drilling the plug.

The term Lost Circulation Materials (LCM) was first coined by some early fifties authors, as a possible way to preventing it from flowing into the well formation [64, 65, 71, 67]. However, before them some patents where filed on methods and means of preventing lost circulation through porous walls [72, 73]. Those articles mentioned mixing fibrous or flaky additives in drilling fluids.

Most LCM studies discuss how well these materials can mechanically obstruct the formation pores or fractures. LCM performance have been widely studied by the academic community [74, 75, 70]. Loeppke [76], for example, analyzed geothermal application LCM with specifically developed laboratory tools. Test results of commercial materials and mathematical models for evaluating their performance are presented, and physical attributes that govern the performance of LCM in geothermal wells are identified and correlated with test results.

In a balanced situation, the formation fluids are well contained by well fluid column weight pressure, without filtering severely into the formation. However, high pressure pockets of reservoir fluids (mostly gas) might have been crossed by the well. In those cases where lighter slurries just can't be used, LCM are also mixed to the cement. Therefore, majority of drilling and cementing operations are performed over balanced, which means the well inner pressure is higher than the pore pressure.

An adverse aspect described is the contamination effects of reminiscent drilling fluid layer on the placed cement, changing its setting time, viscosity or other mechanical properties vital to isolation capability. Despite that, LCM has been commonly used by the industry [77], but some studies showed that it might increase the risk of a blockage pipe [78] and of hole deviation [79] during re-drilling, mainly in depleted wells.

Partial or total influx of the well fluids into the formation can compromise the well pressure balance. Chaney [80] have presented experimental evidence of abnormal pressure decay triggered by lost circulation phenomena during drilling.

PUC-Rio - Certificação Digital Nº 1612794/CA

A particular case of lost circulation is when just a fraction of the drilling fluid or cement is filtered by the permeable zone. A high concentration of solids forms close to the well walls when drilling fluid or cement is filtered by the formation pores. It is referred as filter cake, and it reduces the formation permeability on the well surroundings [81].

By the early 90's, Daccord [49] performed a comprehensive literature review on how fluid loss scenarios impact primary cementing. Undesired flow can be caused by a high formation permeability with low pore pressure, but also induced by higher weight cement slurries used, which can even fracture the formation by the increase of bottom hole pressure.

The fluid loss in cementing is characterized by the lost of cement aqueous content, in which cement does not fracture the porous formation, but the slurry is filtered into the permeable zones. Cement column experiences a volumetric reduction [42], such as in the previously presented cases. In addition, the placed cement quality and designed properties are impacted due to the water-to-cement ratio reduction. With less water available for the chemical reaction, structural mechanical properties of the resultant sheath might also be compromised [8].

Most of the research performed on lost circulation or fluid loss during cementing phase focus on understanding which different additives can form a resistant cement filter cake and withhold the loss. A great variety of materials have been studied, including natural and synthetic fibers, hollow spheres, among others [82, 83, 45, 84].

A great evolution have been made in the development of chemical additives to prevent or minimize the fluid loss itself, as it can be seen on the review presented by Velayati et al. [85]. Nevertheless, API standard on Isolating Potential Flow Zones [86] states that conventional LCM, including pills, squeezes and other pre-treatment often reach their limit in effectiveness and become unsuccessful in the deeper hole conditions, where some formations are depleted, structurally weak, or naturally fractured and faulted.

Baret [43] calculated optimal cement filter cake thickness using Darcy's law [87], considering the presence of a drilling fluid filter cake beneath it. He presented his model sensitivity analysis, and stated the necessity of using fluid loss additives in cement in order to obtain a safe filter cake thickness, and achieve complete zonal isolation from gas influx.

However, independently of forming a good filter cake, slurry's water content is reduced due to fluid loss [48]. As outlined by Santra et al. [18], an ideal cement slurry design to resist formation influx must have a controlled fluid loss, allowing minimum volume reduction. To achieve that, it must present

PUC-Rio - Certificação Digital Nº 1612794/CA

a low viscosity during displacement, a short transient time and quick gelation after placement. In this sense, uncontrolled fluid loss in a recently placed cement slurry is considered one of the main responsible triggers for production problems related to gas migration in an oil well. Fomenkov et al. [88] recently suggested that highly thixotropic cement slurries can be applied in that sense.

There are few researches who applied fluid loss measurement techniques to develop prediction methods of pressure decay and subsequent gas migration. Christian et al. [89] exhibited field results indicating that a fluid loss rate of $50\,mL/30\,min$, measured with American Petroleum Institute (API) test, are related to no gas invasion in the real well. Since then, this value is used by industry as a standard for slurry design and testing.

In the last decade, apart from LCM, very few other proposed means of preventing, and mainly predicting the lost circulation during drilling and cementing have been widely used to improve field operations. Novel mechanical devices [90] and monitoring cement pressure gradients all the time [47], are some expensive initiatives, that are not worthy at low oil brent price scenarios. Lavrov [91] have developed engineering models aiming to predict those losses, based on empirical correlations and laboratory equipment slurry measurements, without proved accuracy and very limited similar-to-well configurations.

As an alternative, computational fluid dynamics is a considerably cheaper initial approach. It can be used to predict the pressure decay along the cementing process, or even indicate where losses might occur in a certain scenario. Therefore, the present work has the objective to present a simple yet cost-effective model that provides reasonably accurate predictions of fluid loss behavior and how it affects the well pressure profile.

PUC-Rio - Certificação Digital Nº 1612794/CA

2.4 Physical simulators

Cheung and Beirute [92] presented a review on gas migration and demonstrated experimentally that a combination of factors is necessary to control gas invasion, furthermore stated that fluid loss control helps to prevent the influx however it is not sufficient to interrupt it. Five years latter, Beirute and Cheung [93] developed a method to scale down the well environment to laboratory conditions. They employed a gas-flow cell to mimic well permeability, thickness, gas volume, pressure, and temperature conditions, however fluid loss was not considered.

Nguyen et al. [94] have performed some displacement efficiency analysis using a laboratory helical-flow device with adjustable inner-pipe eccentricity

and rotation. The apparatus is used for flow-visualization studies of annular-displacement flow of miscible fluids. The experiment aimed to analyze the behavior of a variety of viscoplastic fluids in various annular geometries and flow conditions. In addition, it was developed to run only with water-based fluids that mimic drilling fluids, spacers or cement, but not with those actual fluids. There are limitations of density (about $1200\,kg/m^3$ maximum), and of pressure because the device is made of clear plexi glass. The produced data was compared and used to validate some numerical simulations, detailed on the next section.

Also with the objective to analyze cement displacement, Miranda et al. [95] developed a large-scale test apparatus, where cement slurries displaced drilling fluid. It could run with operational fluids, and inclined and eccentric well configurations could be tested. More recently, Skadsem et al. [96] evaluated numerically and experimentally the flow of a non-Newtonian fluid in an inclined wellbore with concentric and eccentric configurations. Their experiment consisted in a $7\,in$ tubing placed inside a $9\,5/8\,in$ casing, and its main objective is to evaluate displacement efficiency. Those experimental setups investigated important eccentricity effects and presented dimensions much closer to the observed in real oil wells. Nevertheless, both apparatus were not focused on evaluating cement pressure drop or fluid loss effects.

In fact most of the physical simulators found in the literature were dedicated exclusively to evaluate displacement efficiency. However, Therond et al. [97] published in 2016 the results of a large-scale apparatus to evaluate cement zonal isolation, submitted to a high pressure water zone and different temperature conditions. Their work covers some important missing points on evaluating fluid loss and fluid invasion in cement annular columns. With their experiment, real slurries were tested at a larger scale than filter press equipment, and at higher pressure and temperature conditions ($200°C$ and $69\,bar$).

On Chapter 3, the physical well simulator proposed to evaluate cement curing with fluid loss is presented in details. The next section concludes the current chapter, presenting a review of the numerical models and algorithms focused on simulating pressure profile along the well.

2.5 Numerical simulators

The vast majority of numerical analysis of the cementing process of oil wells found in the literature, can be segmented in two main subjects: displacement efficiency and pressure profile prediction.

PUC-Rio - Certificação Digital Nº 1612794/CA

The first, focused in evaluating annular displacement of drilling fluids or spacers by cement slurries, is far more advanced. It is also the branch which concentrates most of the recent work coupled with experimental validation, specially due to increasing count of ultra-deep water and unconventional wells. Those scenarios demand for larger horizontal sections and drilling through harsh formations, generating all sorts of displacement issues.

Bittleston, Ferguson and Frigaard [98] have performed intensive 2D (axial-radial) numerical analysis on how rheological properties of the fluids displaced impacts displacement efficiency in eccentric annular spaces. Also using 2D simulations, but focused in column rotation effects, Escudier et al. [99] proposed a 2D (radial-azimuthal) model for a non-Newtonian fluid in eccentric annuli. Skadsem et al. [96, 96] recently also evaluated how irregular wells suffer from displacement issues. They investigated the displacement in eccentric and inclined wells, in addition to enlarged borehole sections, using 3D flow simulations with finite volumes method.

This problem is considered so important, that many oil companies have developed commercial simulators to address these concerns. iCEM, from Halliburton [100, 101] and Simentar, jointly developed by Petrobras and several companies and universities [102], are just two examples.

Pressure profile prediction numerical literature background comes most from the late nineties, since several blow-out incidents brought this problem to attention. In 1989, Chenevert and Jin [32] elaborated a mathematical unidimensional model to describe the time evolution of the downhole pressure through a force balance in an annular element excluding inertia. In the force balance, they considered that a volume reduction of the cement slurry causes a tendency of the slurry to move downward and consequently gives rise to a shear force in the opposite direction. The model takes into account chemical shrinkage, fluid loss to the formation, and gelation of the cement slurry by using transient experimental data. Besides that, compressibility was neglected and was neglected and elasticity of the cement slurry was considered by employing a simple rheological model to describe the low shear rate behavior of the material. Their mathematical model was solved numerically via finite element methods and the results were reported to agree quite well with field data presented by Cooke et al. in 1983 [103].

Two years after Chevernet and Jin [32] work, Daccord et al. [7] extended their model solving mass conservation and compressibility of the slurry. Prohaska et al. [33] discussed this model in more details, emphasizing the importance of considering depth-dependent gel strength. Two years later, Prohaska et al. [34] introduced the concept of critical distance and, using some simplifi-

PUC-Rio - Certificação Digital Nº 1612794/CA

cations, developed a model to predict the risk of gas invasion.

More recently, Nishikawa and Wojtanowicz [35] developed a mathematical expression for predicting the downhole pressure as a function of time based on a dynamic approach. They considered that (i) the annulus can be approximated by a rectangular slot, but only axial displacements are evaluated; (ii) inertia is negligible; (iii) the cement slurry compressibility is constant; (iv) chemical shrinkage does not contribute to volumetric change in early stages; (v) the volume increase due to downhole pressure loss and compressibility is equal to the volume of fluid loss; and (vi) the rheology of the cement slurry does not depend on time and can be described by the Bingham Equation [104]. According to them, the rheological model used by Chenevert and Jin [32] did not compare well with typical Static Gel Strength[1] (SGS) development patterns.

In addition, they argued that unlike the models based on a static approach and SGS development, the model based on a dynamic approach and fluid loss to the formation can predict well the exponential decay of the downhole pressure previously reported by Cooke et al. [103]. Moreover, they found that low compressibility and large annular gaps give rise to a more pronounced pressure drop. This result is very important, since it confirmed that experimental setups with very small diameters may mask the mechanisms observed in the field with real oil wells' dimensions.

This seems to be the case for Bybee et al. [105] analysis. One year after Nishikawa and Wojtanowicz [35] work, they proposed another 1D model, aiming to predict pressure drop considering fluid loss at the bottom, and a plug-flow downward movement through the annular gap. However, their experimental validation was performed with 36in(920mm) column, with less than $1\,in$ of annular gap. Their presented results completely disagree with Nishikawa and Wojtanowicz [35], although the authors claim to have verified pressure drop predictions against published field data. An interesting result that also go against almost all other articles on the subject is that chemical shrinkage does not control hydrostatic pressure loss after cement placement.

2.6 Contributions of this work

The objective of this work is to analyse the column pressure profile behavior immediately after placement. At the beginning of cure, shrinkage is not yet relevant, and cement slurry static pressure is supposed to balance formation pore pressure. In spite of that, mixture's viscosity is yet not high enough to prevent water from filtrating into the reservoir through a high

[1]Static Gel Strenght is the shear stress measured at low shear rate, after a resting time.

PUC-Rio - Certificação Digital Nº 1612794/CA

permeability zone. The water volume lost to the formation pulls the ToC down, and as presented in section 2.3, with less water, cement ideal curing behavior and local rheological properties are affected [8].

Regarding those aspects, the proposed experimental investigation consists in simulating a primary cementing operation in an annular section of the well, in the presence of a fluid loss scenario. These tests were conducted in a cutting edge experimental apparatus, specially designed to fill the gaps between literature laboratory cement analysis and real field well measurements. Sensing and automation of the novel apparatus developed, allow detailed comprehension of the physical mechanisms of fluid loss that impact regular curing pressure drop behavior.

In addition, the simulated fluid loss zone is geometrically a better proxy to real wells than common laboratory filtration measurements, but also from other simulators found in the literature. This apparatus modular layout enables full access to cured cement column, without the need of breaking or tearing the experiment apart. This is definitely an engineering innovation with respect to the literature simulators [92, 94, 106, 97].

Generally, due to the well huge difference between the characteristic lengths of each dimension, most literature models consider 1-D approximations to describe the flow. All presented pressure drop prediction models also solve the uni-dimensional problem, despite considering fluid loss scenarios. However, when analyzing the fluid loss problem the axial and radial velocities might be relevant, since both may vary considerably with well radius and length, i.e. $v_r = v_r(r, z)$ and $v_z = v_z(r, z)$. Therefore, this work numerically explores fluid loss scenarios with a 2-D (axial and radial) model, that aims to evaluate how shear and recirculation effects may impact pressure drop predictions.

Finally, fluid loss is modeled considering multi-component mass transport equations. This enabled a better understanding of cement filter cake formation by dehydrated slurry close to outer walls after filtrate is lost to formation. The resultant mathematical model is detailed in Chapter 4 and it was implemented to facilitate probing of different hypothesis along validation phase, and also facilitates the future development.

PUC-Rio - Certificação Digital Nº 1612794/CA

3
Physical Simulator

In the previous chapters, it has been showed that cementing job failures may cause inefficient zonal isolation and poor structural resistance. It was also pointed out that poor fluid loss control is frequently identified as the main cause of these failures, and not only reduces well safety, but also may compromise final oil production. Therefore, when modeling this phenomena, it is very important not to neglect relevant physical mechanisms involved.

Motivated by these challenges, the present work explores the fluid loss phenomenon during cement cure through theoretical, numerical, and experimental analyses. In current chapter an experimental apparatus developed [107] is briefly outlined. It was developed during a Technical Cooperation Term between Petrobras and Halliburton and was built at the Halliburton Brazil Technology Center at Fundão Island, in Rio de Janeiro.

Besides fluid loss analysis, this project objectives comprehend other simulation capabilities, and it was designed to be a physical well simulator (PWS) of most of the processes in a cementing job. Some of its capabilities are out of this thesis scope, such as simulating fluid displacement, gas migration and eccentric or tilted wells. Its also important to emphasize that, for the analysis presented in this work, the fluid used is solely a cement slurry, although the PWS supports all kind of fluids, such as drilling fluids, spacers and even crude oil[107].

To experimentally analyse the physical mechanisms involved in a phenomena, researchers have always made use of scaled models. As presented in section 2.4, most of the experimental setups built in the past address the problem of displacement efficiency, fluid or fluid loss and gas migration separately [95, 96]. However, as reported on several field data studies, these phenomenon are intrinsically connected with cement curing mechanisms highly dependent on the well geometry, such as shrinkage, dehydration and creep. Therefore, a modular and large-scale apparatus was needed to better reproduce the operational cementing processes within representative well dimensions, yet in a controlled lab environment.

With that in mind, PWS is the first patented modular lab apparatus device able to simulate several well cementing procedures [107]. Different

PUC-Rio - Certificação Digital Nº 1612794/CA

modules can be configured to simulate a different well section and attached together. Some modules are able to collect pressure measurements, and stacked they acquire a pressure profile along the column length evolution with time. Such analysis allows the investigation of how the mentioned mechanisms may trigger an early pressure drop. Figure 3.1[108] shows the PWS configured with 9 pressure modules stacked on the right, and some of the peripheral equipment necessary to run experiments on the left.

Figure 3.1: Physical Well Simulator (PWS).
From [108]

The following sections outline PWS experimental setup [108]. In section 3.1 the methodology is outlined, together with the physical quantities of interest and the experimental matrix. In section 3.2, PWS design steps are revisited, including the geometry definition and how the modular concept enables the simulation of impermeable formations and also fluid loss regions [108]. On the sequence, section 3.3 discusses the used slurries and their rheological characterization [62, 108]. Finally, all peripheral equipment necessary to run the analysis are mentioned [108] in section 3.4.

3.1 Materials and Methods

The individual experiment performed in the PWS consists mainly on placing a cement slurry in the annular space and analyzing the pressure

PUC-Rio - Certificação Digital Nº 1612794/CA

gradient, $\frac{\partial p}{\partial z}$, with time during the cement curing process [108]. Dynamic pressure measurements were taken with special pressure gauges placed around the external annular circumference and along the column height. In addition to pressure, other measurements are taken such as temperature and cement weight sensed at the well bottom.

A permeable low pressure formation zone is simulated at a certain point of the well to generate the fluid loss problem. In order to understand the effect of fluid loss on the pressure profile, knowing the amount of water leaving the system with time is very important [108]. Hence, the fluid passing by this permeable region is collected in an evaporation-proof container and its weight also needed to be registered periodically.

An acquisition software interface aggregates all this data, and also enables the real-time monitoring of measurements, for control and operation of the experiment. That software interface was implemented using LabVIEW [109] platform from National Instruments Corporation. Due to the long duration of each test, an automatic routine was also developed to synchronously save all the measurements collected every 10 seconds, and a safety backup hard copy of all acquired data every hour. All tests were performed at least twice, to assure data repeatability. The test results are presented in Chapter 6,

Besides the pressure transducer, PWS also has thermocouples associated with each pressure acquisition point along the apparatus length. The thermocouples are well known temperature sensors that consists on a joint of two different metal wires. When submitted to temperature changes, a small potential differential, or voltage, can be measured at the two wires. Therefore, within used thermo-couple range, this voltage is linearly correlated with the temperature variation experienced by the metal joint.

Measuring the temperature profile is important to evaluate the heat-of-hydration, which is associated with curing chemical reaction. To facilitate the sealing of the equipment, thermocouples were attached to its external surface. This is possible with the adoption of a lumped-capacitance of heat transfer model, which is based on the low value of the Biot (Bi) number, defined by equation 3-1. If Bi is lower than 0.1, its fair to say temperature gradient inside the solid negligible. Hence outer wall temperature is a good proxy of internal walls temperature.

$$Bi = \frac{L_C h_{Air}}{k_S} = \frac{0.254 \times 15}{80} = 4.7 \times 10^{-2} < 0.1 \tag{3-1}$$

where L_C is a characteristic length (in this case module thickness), h_{Air} is convection heat transfer coefficient of natural convection in air and k_s is the conduction thermal conductivity of the steel.

PUC-Rio - Certificação Digital Nº 1612794/CA

In addition to pressure and temperature, load cells also based on strain-stress correlations are installed at the bottom cap. They log cement column weight transmitted all the way down. Three cells were used in parallel, to sum the individual load capacity of each cell, and manage the full cement sheath weight, which, in a 5 meter column is around 1 *ton*. This measurements are important to evaluate the unloading phenomena, since the measured weight on the cells in a non-curing Newtonian fluid will remain the same if no mass escapes the annular space.

As mentioned, a scale is used to measure the accumulated filtrate mass coming out of the annular through the permeable zone. An evaporation-proof container outside of the Fluid Loss Module, collects the fluid which allows the filtrate density determination.

Finally, an in-house made optical distance sensor keeps track of the cement level. It is based on the same infrared technology used by most commercial digital rulers. This depth of the top cement interface in a well is better known as Top of Cement (ToC).

PUC-Rio - Certificação Digital Nº 1612794/CA

3.1.1 Experimental Matrix

The procedures performed before a PWS test are: assembling the apparatus; connecting the sensors and acquisition system; weighting and mixing around $550\,kg$ of cement, water and additives; and finally pumping the slurry into the annular space. Once in place, the cement curing process is monitored, and occurs under constant pressure and external temperature. Figure 3.2[108] shows some pictures illustrating some of those steps.

Despite these steps are seemingly simple, just the apparatus preparation usually takes around 8 hours. The test itself could last for a maximum of two days, and disassemble and clean-up times are around 8 to 12 hours. Due to the huge amount of cement mixed per test and long overall duration, the project budget and timeline only comprised a restricted number of tests.

The initial tests consist on simply placing cement inside the annulus and letting it cure with time, to isolate pressure gradient decay phenomena. With no fluid loss, the Top of Cement position, named ToC by oil industry, smoothly decays due to cement shrinkage and pressure diminishes mainly because the fluid stops transmitting stresses as effectively. This test explains a lot about the problem physics, especially confronting pressure measurements with rheological data of used slurries, presented by Marchesini et al. [62].

Finally, another scenario is set to investigate how the cement is filtered by formation porosity, loosing water to low pressure permeable zone in the

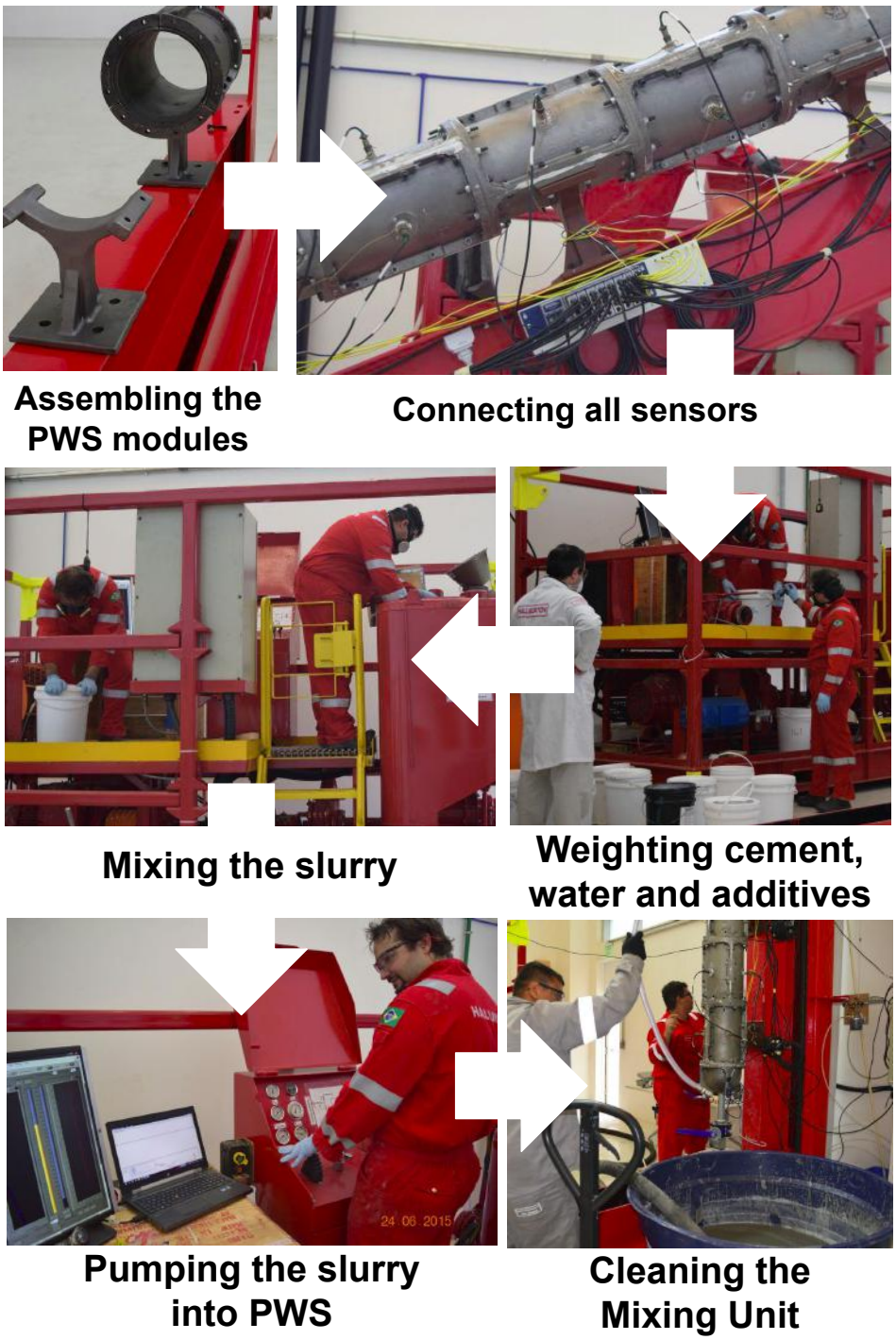

Figure 3.2: PWS pre-test procedures.
[108]

PUC-Rio - Certificação Digital Nº 1612794/CA

reservoir. Filtrate mass is collected with time, and $m_f(t)$ is logged by a digital scale. Consequently, filtrate mass flow rate $\dot{m}_f(t)$, can then be numerically calculated. These two scenarios are presented schematically on Fig. 3.3[108].

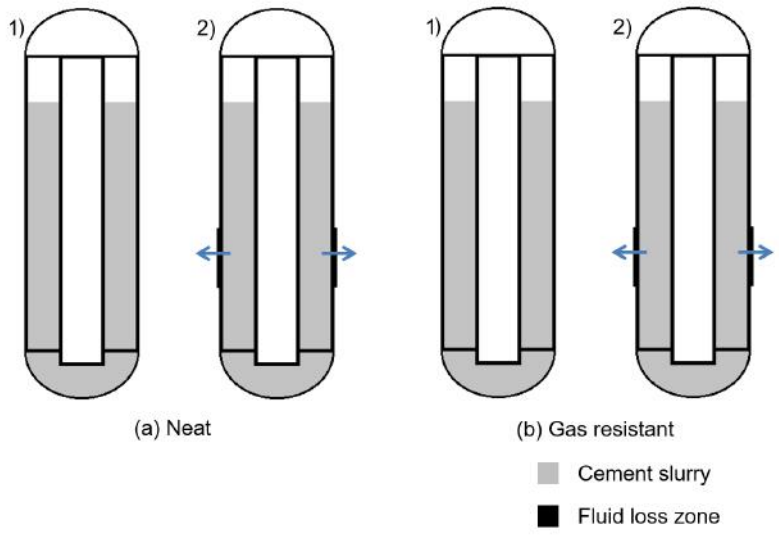

Figure 3.3: Experimental schematics for each test scenario.
From [108]

PUC-Rio - Certificação Digital Nº 1612794/CA

3.2 Apparatus Design

This complex mechanical system was designed from scratch and although some off-the-shelf parts were used, the major structural elements were specially cast and machined by contracted manufacturers and in the in-house machine shop. Without many prior prototyping phases during the project timeline, computer aided design (CAD) and computer-aided engineering (CAE) tools were intensively applied in the design of this modular structure.

The apparatus main functional requirements identified were:

- test representativeness;
- re-usability;
- modularity;
- reliability;
- field applicability.

Each of those functional requirements determined a set of engineering specifications that guided the design phase.

Test representativeness, for example, determined that the apparatus operational limits for pressure and temperature should target the oil-field

conditions. In this study, experiments were performed under atmospheric confining pressure, as detailed in 3.2.3.

Most of the literature cementing simulators that evaluate the curing process, demand cutting the cylinders forming the annular space for analyzing the experiment results. On the contrary, PWS was designed to be fully reusable. An unseen module geometry was engineered to enable such feature, and is described in detail in section 3.2.2.

Modularity is another very important functional requirement, since this apparatus should be reconfigured for different cementing simulation scenarios. The symmetrical individual structural arc module, illustrated in Fig. 3.4, present another benefit of modular design. CAD and CAE analysis were fairly reduced, since most common modules are composed of repetitions of that same pieces, and are submitted to very similar stress conditions.

The possibility of each module to be released independently after the cement is set, enables access to an intact annular sheath of cement of up to 8 meters long. This structure could be studied in medical CT scanners or X-ray machines to evaluate internal cracks or even to be digitized for additional simulations. This analysis is usually applied at smaller cement samples to better understand its structure matrix, and how much its porous network is actually interconnected.

Another crucial requirement considered nowadays for almost all hardware equipment in the oil-industry is reliability. Likewise, PWS should be robust enough to withstand corrosive fluids, resist several pressure and temperature cycles, as well as frequent assembly and dis-assembly routines. And since the apparatus pieces dimensions are just below the ergonomics limits of weight lifting, handling needs extra tools described at subsection 3.4. Structural components should still be reliable even after possible dents and scratches,

Finally, the last requirement is field applicability. It means that all slurries, additives or any other fluids used in the PWS testing should be able to be pumped in a actual well. This concern was specially due to several literature physical simulators,

3.2.1 Geometry definition

In order to downscale a field system down to a laboratory experimental setup, the usual approach is dimensional analysis of the flow regimen. Howbeit, as previously mentioned, only pumpable fluids must be employed in PWS tests [108], and thus a dimension reduction might just not be possible. The Reynolds number definition for the non-Newtonian viscosity η is showed in Equation 3-2.

PUC-Rio - Certificação Digital Nº 1612794/CA

$$Re = \frac{\rho \bar{v_z}(D_o - D_i)}{\eta} \tag{3-2}$$

where ρ and η are respectively the slurry density and viscosity, $\bar{v_z}$ is the downward average velocity, and D_o and D_i are the outer and inner diameters correspondingly.

The fluid density and viscosity values must be within the ranges observed in pumpable cement slurries. To reduce geometric parameters, flow velocity would have to be increased, demanding a pumped flow or higher permeability at the fluid loss region, which would distort fluid loss analysis. In addition, oil-wells cement slurries have an average density of $15\,ppg$ $(1800\,kg/m^3)$, which means that less than $2\,psi$ of pressure is observed for each additional meter of cement column height. For that matter, to collect accurate measurements of column pressure gradient, PWS needed to be as high as possible. Due to its modular design, the major height constraint was actually the laboratory ceiling height. Thus, the column can extend up to eight meters long, which is considerably high for a laboratory apparatus.

Moreover, the experiment must assure the slurry inside the model is submitted to shear rates equivalent to those observed in actual wells. Thereupon, inner and outer radii that form the annular space were chosen within usual production section ranges. The outer cylinder, that represents the well formation walls, have an internal diameter of 9 in (0.2286 m) and the inner pipe, which emulates the casing, and its external diameter can be set from 4 in (0.1016 m) to 7 in $(0,1778\ m)$.

The fluid loss region is emulated by a special module, detailed further in section 3.2. It works as a semi-permeable membrane, that filters cement, collects and measures the amount of fluid filtered. Despite more than one module could be used together to simulate this permeable zone, the fluid loss effective area is determined by the porous material inside each module, which for the used module is a cylindrical shell of $0.1m$ height and diameter of $9\,in\,(0.2286\ m)$.

3.2.2 Modular concept

Different modular concepts for the PWS have been sketched and extensively tested virtually, but one has stood out and led to a patent [107]. It is composed of three $\frac{2\pi}{3} rad\,(120^o)$ arc shells, that are assembled together to form the full circumference of the wellbore walls equivalent, as seen on Fig. 3.4 [107].

It allows easy removal of the hardened cement interior, without cutting any of the apparatus structure. Notches on the boundaries of each arc module

PUC-Rio - Certificação Digital Nº 1612794/CA

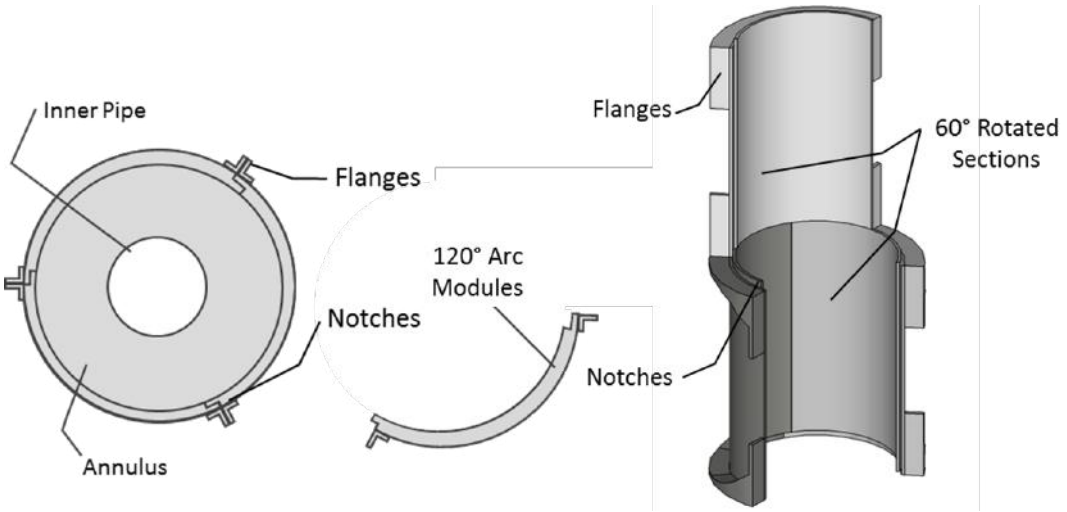

Figure 3.4: Re-usable and modular tripartite cylinder sections.
Adapted from [107]

penetrate the adjacent ones, interlacing the structure, reducing stress concentration and increasing the sealant contact area, zoomed in detail on the right corner of Figure 3.4. These tubular assemblies formed by the three arc modules are named sections, which are mounted on top of each other and fixed by bolted flanges.

To avoid module junctions to line up straight across the apparatus length, the sections are rotated by $\frac{\pi}{6} rad\,(60^o)$, as showed in Figure 3.4. The structurally weak arc tips are protected by the strong central part of the adjacent arc above and bellow. A cylinder is the strongest shapes to withhold internal pressure. However even a minor opening on its walls can propagate a vertical crack, and so, this design with twisted sections aims to recover part of the cylinder original strength.

Each section can represent a different formation of the wellbore, depending on the modules used to form it. Different modules can be designed fit for purpose, for simulation of the characteristics of a variety of actual well formations, as showed on Fig. 3.5.

Finally, bottom and top cap modules seal the cylindrical vessel formed. The bottom cap modules also respectively house the load cells, and the inlet for the cement to be injected. The top cap holds the inner pipe that represents the casing and forms the annular space, as seen on Figure 3.6 [108].

A pressurizing fluid can be injected through the top cap module, in order to change the column top pressure boundary condition. The casing inner tube weight is sustained by a holder, fixed to the top cap module, that adjusts its position from a centralized condition until the most extreme eccentric

PUC-Rio - Certificação Digital Nº 1612794/CA

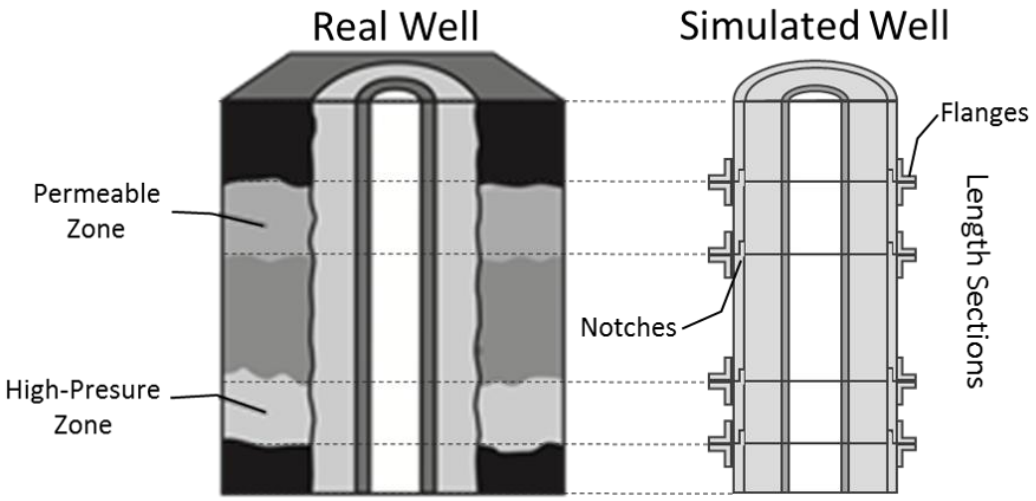

Figure 3.5: Experimental Schematics of sections simulating actual well different zones.

situation. At several points along its length, this tube has three radial bolts used to maintain the holder defined position it. For this particular cementing analysis, this inner pipe is not heavy as a real casing, and was closed at the bottom. Thus, an important check is if buoyancy forces would be enough to expel the inner tube from the cement column, or if some extra weight would be necessary. Nevertheless, for the tests performed, that countermeasure was not necessary.

In addition, disassembling and cleaning became much easier than to break apart the set cement with an hydraulic crusher, specially after the development of some special tools with that purpose. This is a direct example of continuous improvement methodology application. In Chapter 6 some preserved cement sheath are also presented.

Surely the modular design also presented some disadvantages. Assembling the test was not that simple. Sealing was performed with a industrial silicon-base paste, and, due to casting imprecision, some module joints demanded more work to avoid leaks. However, those issues were easily overcame by continuous improvement methodology, put in place at every test. For the sealing problem, for example, different ways of applying silicon between the pieces were experimented, and several brands of silicon adhesives were tested until an optimum set was discovered.

PUC-Rio - Certificação Digital Nº 1612794/CA

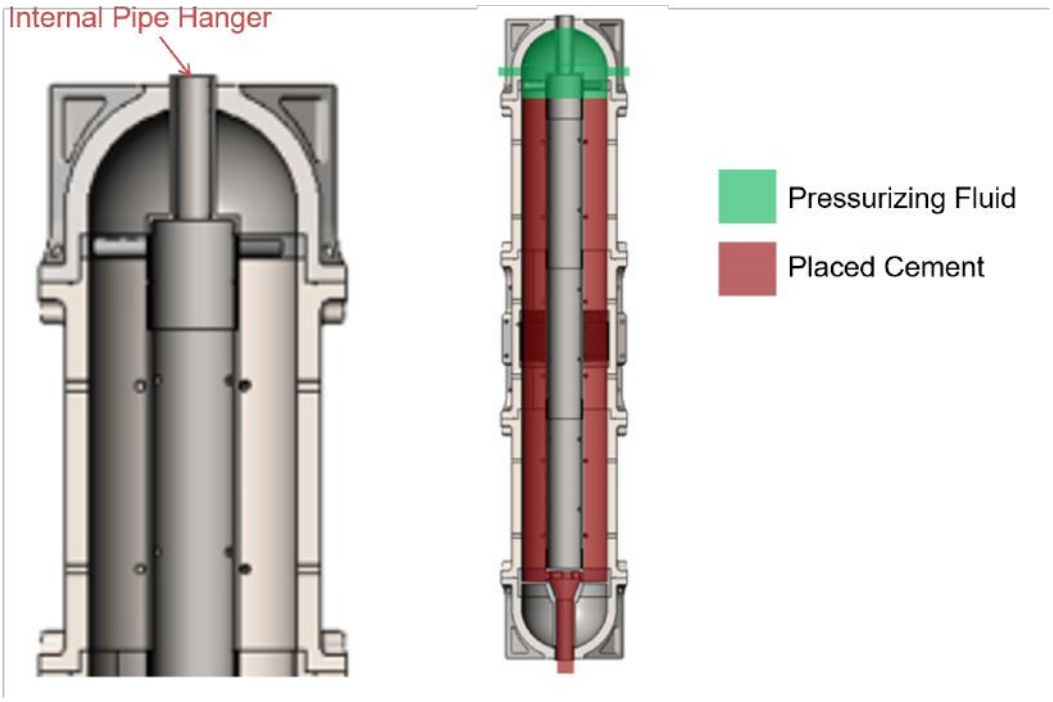

Figure 3.6: Annular space formed by the inner pipe, cement injection and pressurization schematics.

From [108]

PUC-Rio - Certificação Digital Nº 1612794/CA

3.2.2.1 Available Modules

The Regular Angular Module (RAM), which is merely a third of the well bore cross-section, that features pressure and temperature connections for the transducers and flanges that enabled connection with adjacent modules, and to the upper and bottom sections. The top and bottom cap modules are named Closure Spherical Modules (CSM), and are mirrored modules that hold the load cells, level sensor and the inlet main valve. Figure 3.7 [107] illustrates how these modules connect to each other.

The Filtrate Loss Module (FLM) consists of an internal fine mesh ($320\,per\,inch$), protected by thicker mesh($40\,per\,inch$), both placed in the outer annulus face. These values aimed to be as close as possible to the filtration tests detailed in API Recomended Prectice 10B [110] with the commercially available mesh sizes. As soon as initial pressure reading at each PWS sensors is stable, the fluid loss module can be opened through a valve. Figure 3.8 [108] shows FLM module and the internal mesh detail.

The inner column pressure pushes the cement through the porous media and the filtrate flow is collected by channels machined in the apparatus steel walls. This channels guide the filtrate to holes connected to the fluid loss

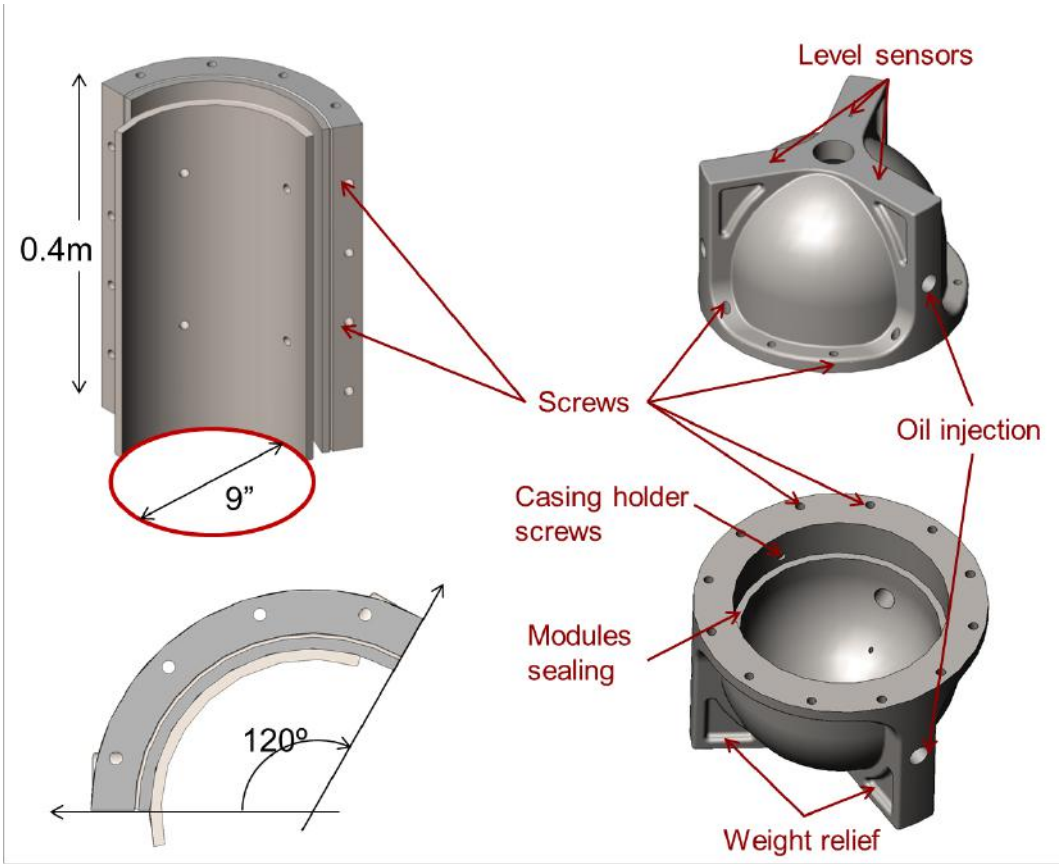

Figure 3.7: Modules connections and fittings.
From [107]

reservoir, which is placed over a scale. Its mass is recorded every 10 s and, despite the reservoir is open to the atmospheric pressure, a special lid avoids evaporation of the collected filtrate material.

3.2.3 Mechanical Design

As the mechanical design of the apparatus is not the focus of this doctorate thesis, the design steps are simply summarized in this section. The more complex analysis are referenced but not described in detail.

Initially simplified 2D free body diagrams of the arc module cross-sections were used to calculate good approximations of the loads applied, as seen on Fig. 3.9.

This analytical model assumes every module is equal and that connections between the modules are perfectly symmetric. F_1 is the force resultant of the inner pressure fluid pressure and the module area. The maximum bolt forces, ${F_P}^{12}$ and ${F_P}^{12}$, are easily calculated and used to specify off-the-shelf sets of bolts, washers and nuts.

PUC-Rio - Certificação Digital Nº 1612794/CA

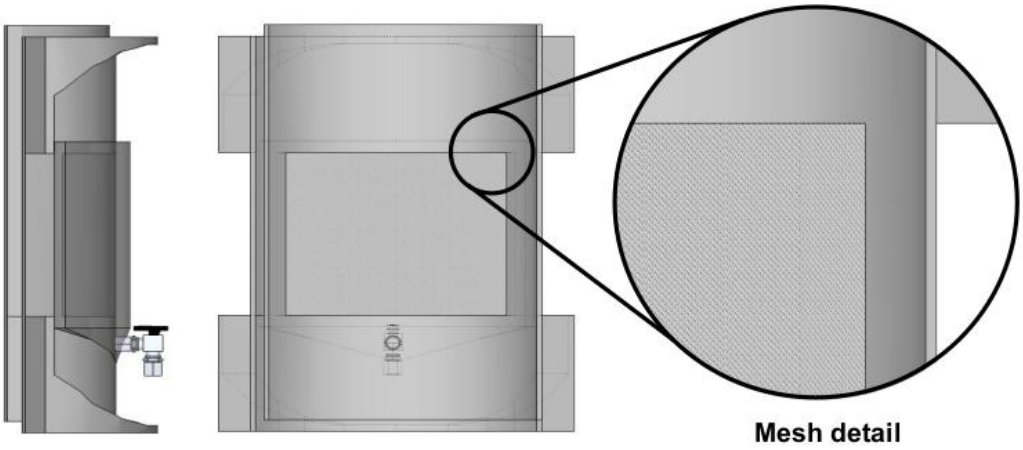

Figure 3.8: Filtrate Loss Module.
[108]

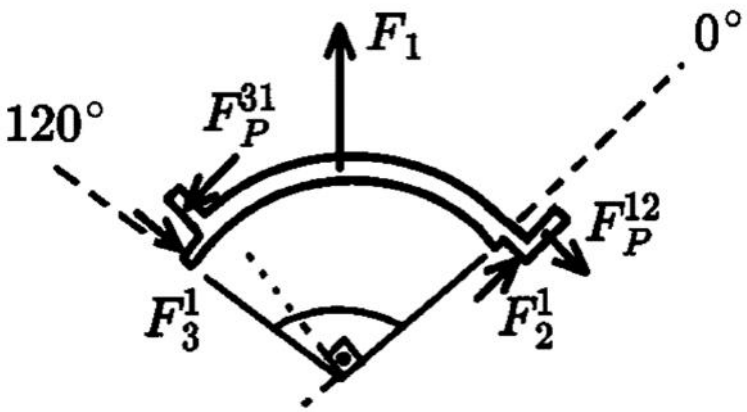

Figure 3.9: Free body diagram.

PUC-Rio - Certificação Digital Nº 1612794/CA

Notches and flanges of the modules are approximated by crimped beams, and knowing the concentrated and distributed loads applied, shear and tensile components are calculated. Thereafter, this extremely simplified model can be used to determine the minimum thickness for each of those those elements to hold the imposed internal pressure.

This first estimates are applied to a digital twin, based on finite element analysis (FEA) model of the arc module. All the loads and crimping are applied and static and dynamic load was simulated. It allowed a detailed stress evaluation of joints and lead to design adjustments that reduced stress concentration points. A static stress analysis on one arc module of the digital twin is exemplified in Figure 3.10.

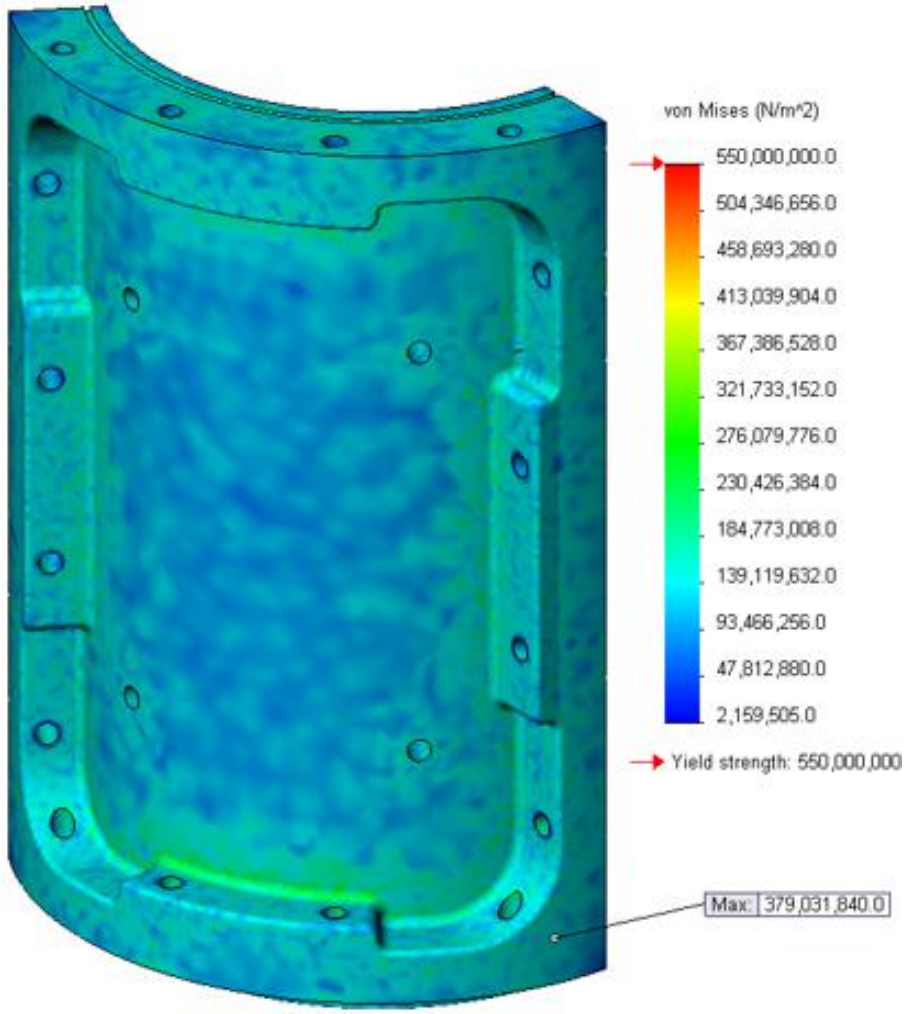

Figure 3.10: Digital twin.

3.2.4 Data acquisition system

Some sensors installed in the PWS enable the collection of physical measurements needed to monitor the simulated cementing job along the cure [108]. A complete Data acquisition system (DAQ) was assembled, and is comprised by the transducers, signal processing units and an user interface module. In the following subsections, these parts are described separably in order to outline the data acquisition concerns involved.

3.2.4.1 Sensors and transducers

The sensing devices are listed in this subsection, and the main reasons behind each sensors choice is outlined.

Regarding pressure measurements, static pressure in fluids varies linearly with the column length and fluid density, as given by the Pascal's principle

PUC-Rio - Certificação Digital Nº 1612794/CA

[111]. This simplification has been widely used in the oil-industry to calculate pressure gradient of fluid columns in motion. After placement, this could be the case due to low velocities observed. However, as seen on Chapter 2, many authors have showed that during cure the static column suffers a pressure drop [7, 32, 34, 70, 100, 103].

The changes in density suffered by the slurry, respond for part of this decay, and also thermal contraction after the initial heat of hydration have passed its peak. Nevertheless, another portion of this pressure unloading is influenced by rheological changes by the slurry during this process, and how stress is not equally transmitted along the column. The filtration changes the slurry to water ratio locally, increasing its yield stress component [8].

Regular internal diaphragm aneroid pressure transducers are well suited for dynamic pressure measurements in imcompressible Newtonian fluids. This type of transducer actually measures the elastic deformation of a mechanical element, such as an internal diaphragm, placed within a small channel. This deformation is due to the normal stress difference exerted at both sides of the diaphragm. The fluid pressure within that channel is then correlated with the measured deformation. However, cement viscoplastic behavior turns part of this normal stress into viscous stress on the transducer channel walls, thus leading to erroneous pressure measurements.

In addition, cement abrasive, corrosive and curing properties are too aggressive for the internal channel and could damage the transducer. Consequently, to accurately quantify the pressure profile evolution, flush transducers are used. As showed in Fig. 3.11, adapted from [112], in flush transducers a second diaphragm and a transmission fluid protects the internal sensor from abrasive, aggressive or corrosive media.

Honeywell model a-105 [113] was chosen due to its flush diaphragm, internal temperature correction and precision specs: 0.02% of full-scale stamp (FSS) and almost nonexistent hysteresis. To collect temperature readings, Figure 3.12 shows the mentioned pressure transducer, and the other sensing devices used in the PWS.

PUC-Rio - Certificação Digital Nº 1612794/CA

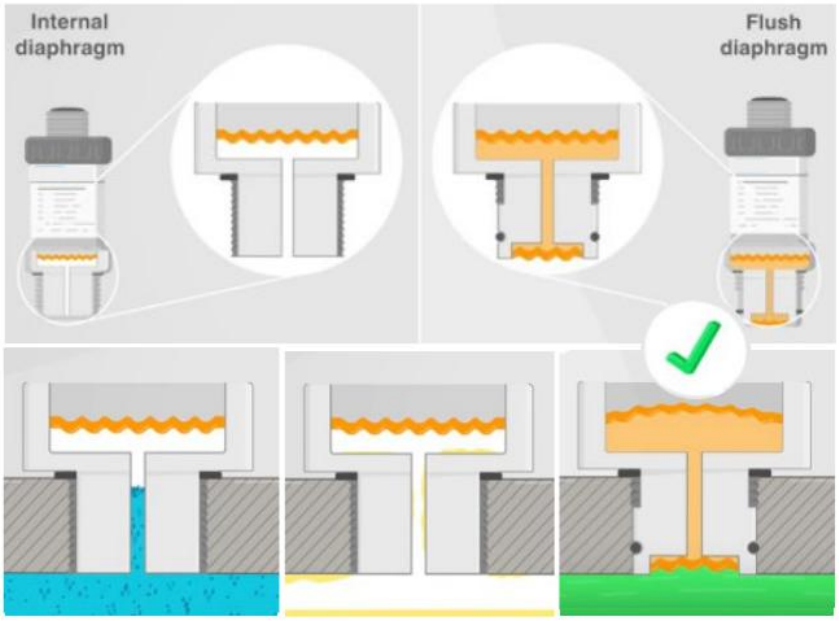

Figure 3.11: Internal diaphragm transducers comparison with flush diaphragm transducers.

PUC-Rio - Certificação Digital Nº 1612794/CA

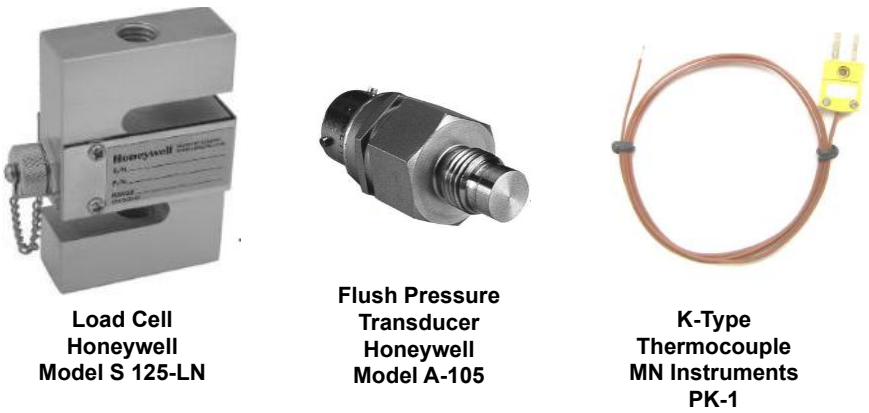

Figure 3.12: Sensing devices used

K-type thermocouples (TCs) were used, for the wide span of temperatures measured. This K-type TC can acquire within its linear range, temperatures from $32°F\,(0°C)$ to $200ºF(93.3ºC)$. Finaly, load cells were used to evaluate the cement column weight. The type S model 125-LN from Honeywell [114] applied can measures up to $500\,kg$ with 0.03% accuracy and also no hysteresis. Three of these cells were installed in parallel around the inner circumference of the bottom cap module.

3.2.4.2 Signal processing

A commercial signal processor from National Instruments Corporation (NI) was used. Model compactDAQ-9188XT (cDAQ) [115] performs sensors feeding, signal acquisition and serialization tasks. Different NI modules, that interfaces specifically with each type of sensor are coupled with the cDAQ chassis, which allows easier wiring and less interference between the readings. Figure 3.13, adapted from [116] shows the used NI acquisition modules used for each measurement and also the cDAQ chassis.

Figure 3.13: National Instruments compactDAQ chassis and acquisition modules.

The cDAQ controls the communication via Ethernet protocol between the sensor modules and the personal computer, where the user interface was installed. As seen on the schematic, the digital scale communicates directly with the same personal computer, sending a serial signal with the mass readings

PUC-Rio - Certificação Digital Nº 1612794/CA

through the RS-232 port. Both signals are then synchronized in the computer by the control software.

3.2.4.3 Control software and user interface

Software side of the DAQ System runs entirely on LabVIEW, a system-design platform and development environment for a visual programming language, also from NI. LabVIEW stands for Laboratory Virtual Instrument Engineering Workbench, and the graphical language is named G.

The full schematic data acquisition system connections between sensors, NI modules, cDAQ chassis and the personal computer for user interface is showed on Fig. 3.14 [108].

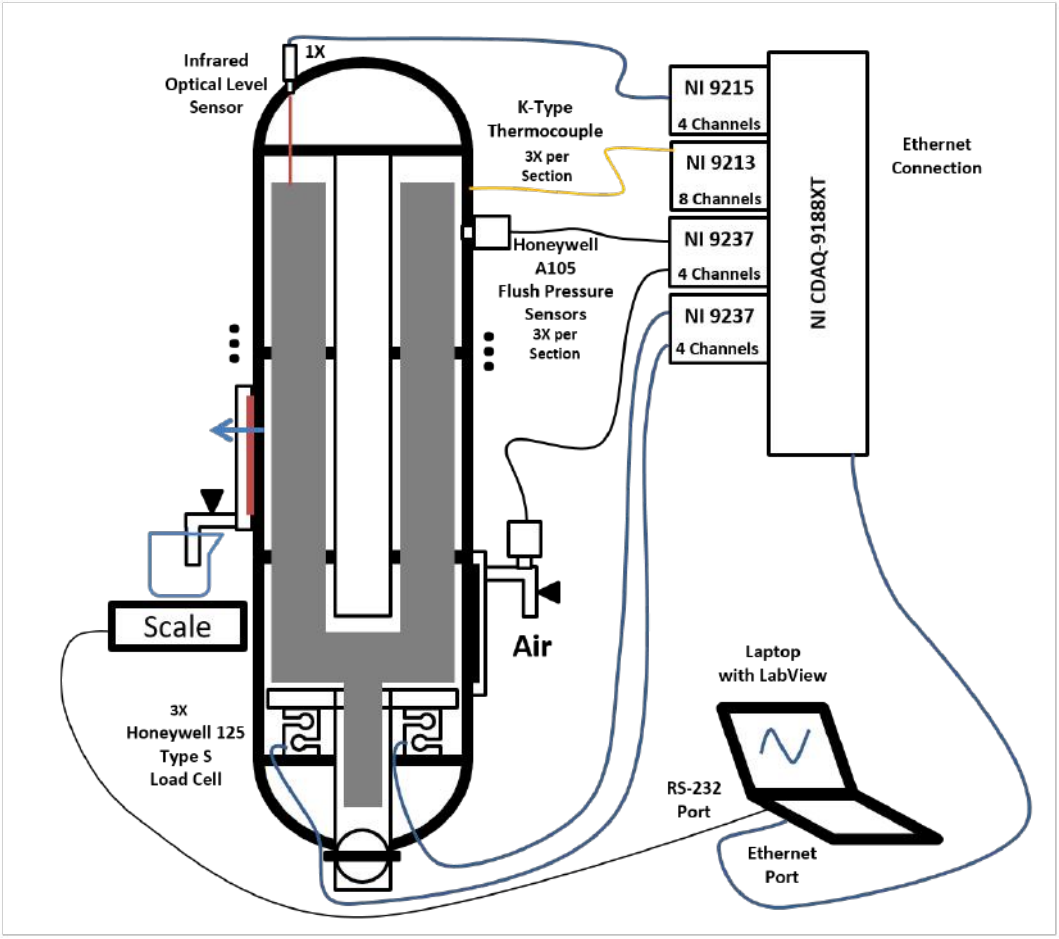

Figure 3.14: Pressure and Temperature Acquisition Schematic
From [108]

In addition to the sensors reading and data storage logic, an user interface was also developed to operate the apparatus in real-time and monitor the data acquired. This control screen can be seen on Fig. 3.15 [108].

PUC-Rio - Certificação Digital Nº 1612794/CA

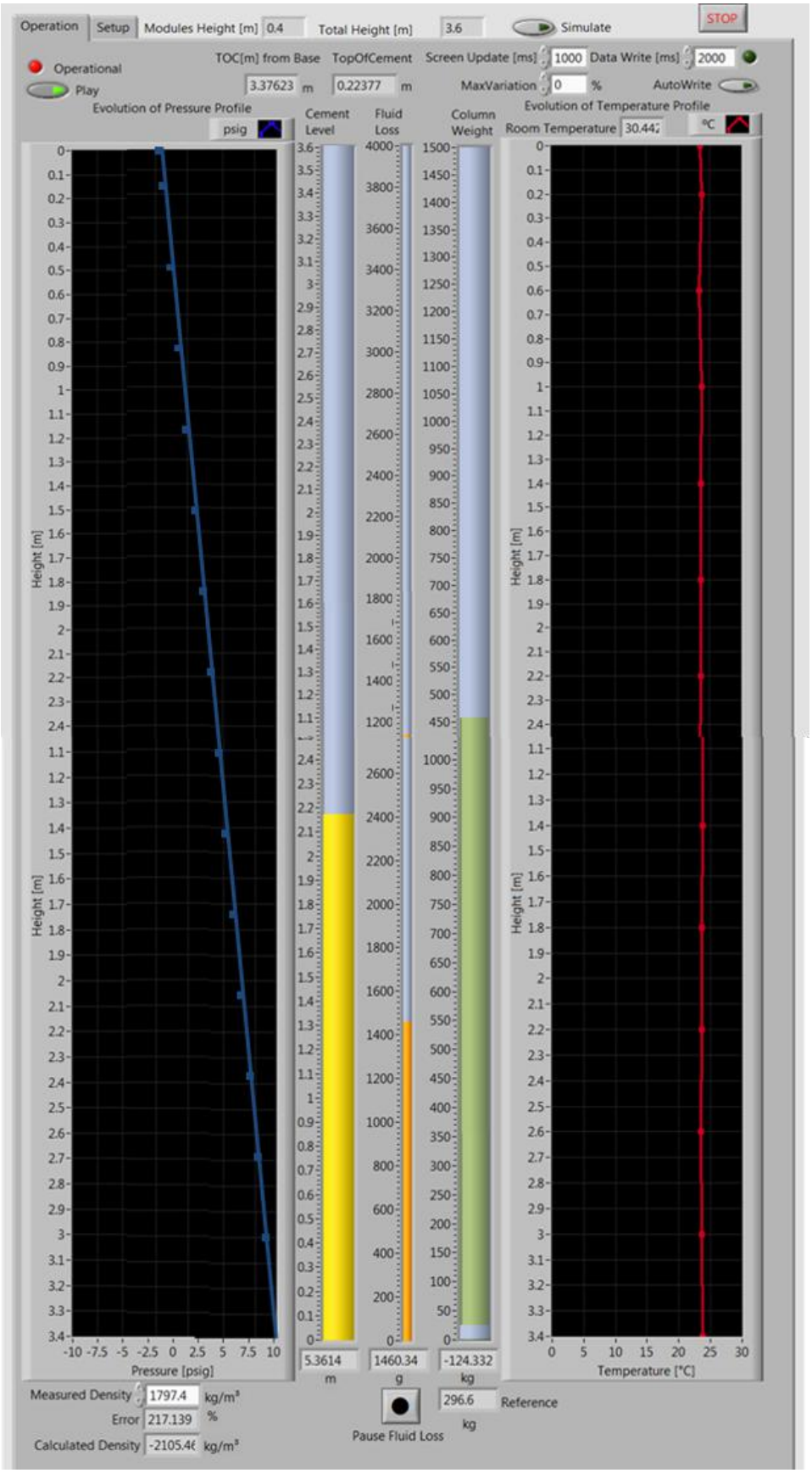

Figure 3.15: LabVIEW apparatus control interface.
From [108]

PUC-Rio - Certificação Digital Nº 1612794/CA

3.3 Cement slurries

The chemical part of this project was mainly developed between Halliburton Houston and Pune labs [108]. This team focused in performing several experiments concerning fluid loss, thickening time, transition time, compressive strength, shrinkage and fluid migration. Fig. 3.16, adapted from [117], shows some of the laboratory equipment used in the slurry design phase.

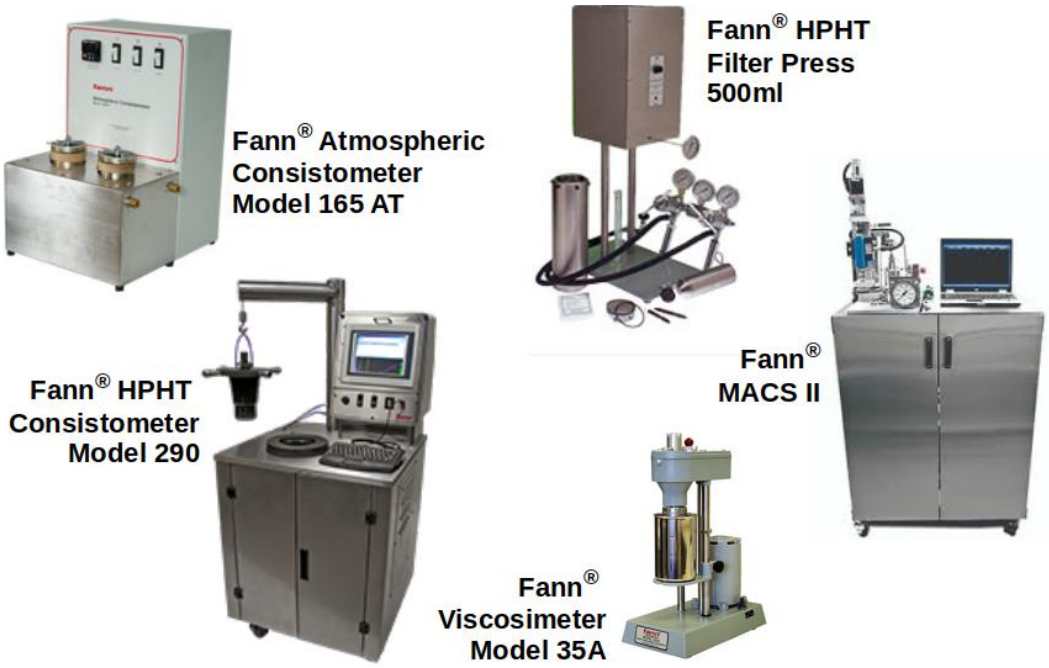

Figure 3.16: Oil-industry standard equipment used on slurry design phase. Adapted from [117]

Although, all PWS tests presented in this thesis were performed under constant room temperature and atmospheric pressure, all used slurries in this project should be able to be pumped in an real oil-wells[108]. In that sense, all slurry candidates were conditioned in an atmospheric consistometer for 20 minutes at $140°F$ $(60°C)$ prior to running a fluid loss test at $1000\,psi$ $(6.895 \cdot 10^6\,Pa)$ differential pressure, following the API Recommended Practice 10B [110].

The thickening time measurements were performed over a 30 minutes ramp at $140°F$ and $8000\,psi$ $(5.516 \cdot 10^7\,Pa)$. Moreover, fluid loss laboratory measurements were performed using Filter Cells with a $325\,per\,in$ mesh screen with $3.5\,in^2(22.6\,cm^2)$ filtration area, coupled with a $60\,per\,in$ mesh screen. The $60\,per\,in$ mesh screen provides a flow path for the cement filtrate as outlined in API Recommended Practice 10B [110].

PUC-Rio - Certificação Digital Nº 1612794/CA

Finally, the MACS II® analyzer were used in the design phase to measure the gel strength development. Rogers et al. [118] described the transition time T_t as the time required for a cement slurry to develop a SGS from 100 to $500\,lbf/100ft^2$. The authors stated that it has become an industry standard that when a cement slurry attains a SGS of $500\,lbf/100ft^2$, it has developed enough solid mass to prevent formation influx.

The slurries were conditioned for 2 hours and 30 minutes. The samples were brought to $140°F$ $(60°C)$ and $8000\,psi$ $(6.895 \cdot 10^6\,Pa)$ in a 30 minutes period, then the tests were performed at constant temperature and pressure.

Two different slurries were designed to perform the PWS tests, but their composition is a sensitive information for the companies and so, cannot be disclosed. The first, named Neat, is actually the minimum stable pumpable cement mixture, without any fluid loss controlling additives. The second slurry, named GasTight, was designed by Halliburton chemical engineers involved in the project, as the best indication for the fluid loss scenario simulated in PWS tests.

Besides all measurements performed during this design phase, rheological characterization was performed with these final slurries. Two models of scientific rheometers from TA Instruments were used in this characterization: ARES-G2 and DHR-2, showed in Figure 3.17 [119].

Figure 3.17: Scientific rheometers used on rheological characterization. Adapted from [119]

PUC-Rio - Certificação Digital Nº 1612794/CA

3.4 Support Equipment

Performing laboratory tests with an apparatus of this magnitude demands a huge background infrastructure [108]. First, simply to hold PWS in the upward position an elevation platform was designed and built inside the laboratory.

Commonly the mixing cement-to-water mass ratio is almost 2 and so, for each test, around $300\,kg$ of cement powder and $150\,kg$ of water needed to be mixed. Thus, to have this amount of cement in sacks available would be impossible. Therefore, a Silo was brought from operations, and filled with sufficient cement powder to run all the tests.

Finally, mixing and placing this volume of cement slurry requires some field-size equipment. However, in this case not only the size matters, and it is more important to control a variable known in the industry as the mixing energy. It is a conceptual estimate of how much mixing energy is necessary to get the cement mixture homogeneous and without larger aggregates. Hence, an adapted field Batch Mixer was used, and field mixing times were respected, in order to faithfully reproduce operational conditions.

The following subsections detail each of those support equipment used and present important aspects of their adaptation for the laboratory environment.

PUC-Rio - Certificação Digital Nº 1612794/CA

3.4.1 Elevator Platform

As mentioned before, this is a really heavy structure to hold in place. The maximum weight for the whole system is around $1400\,kg$. Since the apparatus pieces are so heavy, it would be impossible to assemble the apparatus vertically. Herein, the Elevator Platform works initially as a table where the modules assembled and sealed together. In addition, all the sensors are placed and tested, while leak and acquisitions tests with water are performed. Only after this the whole system is tilted vertically, as seen on the sequential images on Fig. 3.18 [108]. Moreover, this necessity attributed the PWS an additional and important feature: the capability to simulate directional well sections, since the designed controls have an inclination precision of 1°.

From [108]

Figure 3.18: Elevator Platform movement frames.

3.4.2 Cement batch mixer

As mentioned, the amount of cement to be mixed per experiment in the PWS is huge. However, to bring something straight from the operation site and place inside the lab is just not that simple. So, a used Recirculating Cement Mixer (RCM III), was adapted into a laboratory large-scale cement mixing unit.

Some old pieces were gathered from the junkyards of several Brazilian operational bases. In spite of that, some important pieces were just not available, such as the a smaller skid frame.

Besides the skid frame, an electrical motor was installed to drive the centrifugal pump, since the original diesel motor could not operate indoors. The original 50 *bbl* tank was replaced by an 8 *bbl* and the robot cement head, which in the field collects the powder cement straight from a silo, was removed. After preparing the slurry mixture, this adapted batch mixer also performed the cement placement, or pump-in.

3.4.3 Cement silo

As well as the mentioned parts of the batch mixer, an used cement silo was refurbished. Commonly in the operations, a cement silo is connected directly to the batch mixer by the robot cement head. Despite the amount of cement used in a test is a lot for a lab experiment, it is not enough to assure accuracy of this automatic valve. Therefore, the silo was used simply to store cement powder, where is was manually collected and weighted with more precision.

PUC-Rio - Certificação Digital Nº 1612794/CA

On the following Chapter, the physics involved in this problem is explored. Based on historical developments and in observed experimental behaviors, some simplification hypothesis are discussed and a mathematical model is proposed.

The results of the experiments performed with PWS setup are presented in a dedicated section of Chapter 6. Thereupon, this results are compared and contrasted with the model predictions.

PUC-Rio - Certificação Digital Nº 1612794/CA

4
Physical Model

This chapter presents the transient multi-component model developed to describe the problem physics. The proposed model is a composition of traditional and modern strategies. It is deeply supported by experimental evidence widely presented in the literature and observed during the experiments performed in this work.

First, in section 4.1, a theoretical oil well is defined, and used throughout the modeling process. Some geometric and operational simplifying assumptions were adopted with respect to real oil wells. They are outlined and justified in this section.

On the sequence, the flow model hypotheses are described in section 4.2. These assumptions aim to establish a comprehensive, yet simple and feasible model, suited for structured and scalable numerical implementation. All justifications for such hypotheses are discussed, specially regarding experimental evidence and practical applications.

In section 4.3, linear momentum and mass conservation equations are simplified by chosen hypotheses. In addition, a mass transport model is defined and the constitutive equations considered for the slurry properties, such as density and viscosity, are also presented. Yet in this section, the model final equations are disclosed.

For last, in section 4.4, the problem boundary conditions are presented. The model application as an engineering solution is the focal point of this section.

PUC-Rio - Certificação Digital Nº 1612794/CA

4.1
Theoretical Well

As detailed in Chapter 2, little has changed on how oil wells are cemented since the end of 19^{th} century. There are reports of metal casings being used in well construction in the late 1860's, to reduce the fraction of water produced with oil [120]. Hardison and Stewart are credited by the first application of cement to fix the casing in 1883 [120]. Perkings [21] and Halliburton [11] patents in the beginning of the 20^{th} century have improved the cement insertion techniques, and until today oil well structural sections follow the

same standard: inner telescopic metal casing, cemented inside a borehole in the ground section by section. Regarding the exploration goals or environmental conditions, different casing configurations may be used, with variations in section orientation, width or length.

Thereupon, to start building the physical model of curing and fluid loss, a theoretical and simplified well is considered as illustrated by the schematics showed in Figure 4.1. A global cylindrical coordinate system $R\Theta Z$ with origin at the top of the well is established, with the Z axis pointing downward and aligned with the well central axis. This configuration was chosen to reproduce the well construction industry standard, i. e., Z increasing with the well depth.

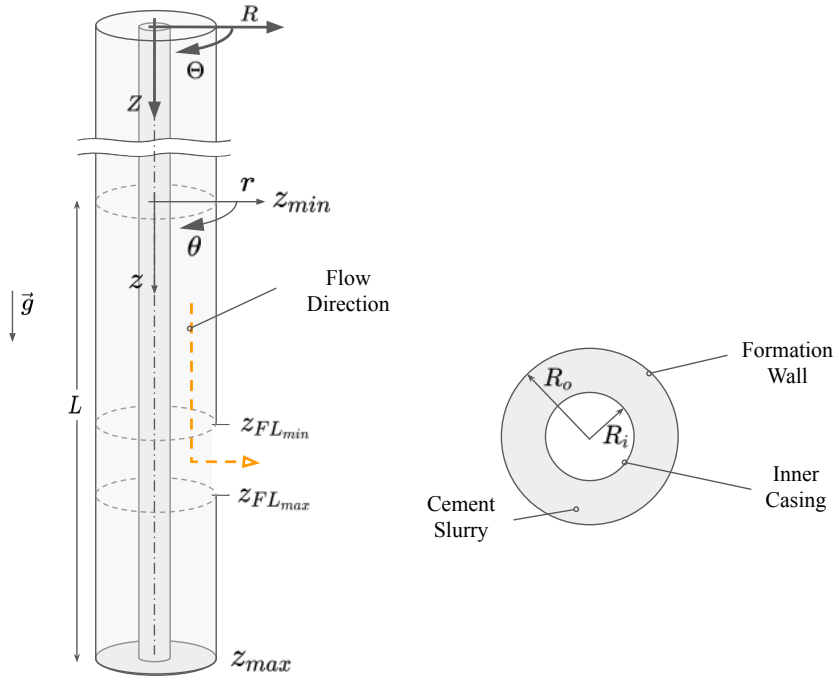

Figure 4.1: Theoretical well geometric definitions.

Only a section of the well length is modeled in this study. A local coordinate system $r\theta z$ is set with $r = R$, $\theta = \Theta$ and $z = Z - Z_{min}$. Therefore, $0 < z < L$, where L is the analyzed axial well section length, which can be defined in the global coordinate system by $Z_{max} - Z_{min}$. The section start depth is Z_{min} and analogously Z_{max} is the section maximum depth, which for the scope of this analysis is equal to the well bottom.

An annular space is formed between the borehole and the inner pipe. Therefore, inner and outer radii of this annular space are assumed constant along L, and are represented respectively by R_i and R_o. Finally, the fluid loss region limiting depths are defined in the local reference system by $z_{FL_{min}}$ and $z_{FL_{max}}$.

PUC-Rio - Certificação Digital Nº 1612794/CA

Those geometric assumptions describe a perfectly cylindrical borehole with a concentric metal casing inside; both straight and vertically aligned. Thus, gravity acceleration vector field acting on every fluid particle can be written using the cylindrical coordinates, as showed in Eq. 4-1

$$\vec{g} = g_r\hat{e_r} + g_\theta\hat{e_\theta} + g_z\hat{e_z} \tag{4-1}$$

where $\hat{e_r}$, $\hat{e_\theta}$ and $\hat{e_z}$ are the canonical unit vectors with respect to each cylindrical coordinate direction; and $g_r = g_\theta = 0$ can then be simplified as showed in Equation 4-2.

$$\vec{g} = g_z\hat{e_z} \tag{4-2}$$

Deviated well sections can be considered simply by discarding this assumption and defining the gravity field as a function of position. However, in this work only vertical well sections are evaluated.

4.2 Hypotheses and flow conditions

As showed in Chapter 2, cement pastes are characterized in the literature by a non-Newtonian behavior (usually viscoplastic [53, 54, 56], with irreversible effects [60, 62]). They also present some concentration of fine solids dispersed [55]. In this sense, an equivalent viscosity is usually defined as a function of shear rate regimen and curing time. Analogously, the density can be written as a function of solids concentration [121] and shrinkage time [7, 41, 122, 123].

The main objective of this model is to predict the evolution of pressure profile with time along the evaluated well section depth. Thus, this is intrinsically a transient problem. On the sequence, the considered simplification hypotheses regarding flow are outlined.

Cement slurries, as the majority of fluids, have negligible compressibility when compared to gases. However, inside an oil well, fluids suffer some compression due to the high depths and consequent pressures observed [103]. However, in present analysis, compressibility effects are assumed negligible, due to well-section depth evaluated. Nevertheless, since fluid loss region filters the slurry suspended fines, local density variation is expected due to this change in mixture mass fractions.

Regarding well temperature gradients, the theoretical well is assumed isothermal during cement set. Actually, the slurry indeed experiences some temperature variation in the well during set. In spite of that, during the early cure, thermal expansion effects due to external heat sources or due to

PUC-Rio - Certificação Digital Nº 1612794/CA

cement heat of hydration, are minimum with respect to flow velocities driven by fluid loss zone permeability. This is reported in the literature, and it was also clear from the experiments performed. Hypothesis (i) implies that temperature gradient or time variation is neglected, as presented in Eq. 4-3.

$$\frac{\partial T}{\partial z} \approx \frac{\partial T}{\partial r} \approx \frac{\partial T}{\partial \theta} \approx \frac{\partial T}{\partial t} \approx 0 \tag{4-3}$$

During the drilling phase of a well, the inner drill column rotates the bit and imposes an azimuthal flow around the well central axis. On the other hand, during cementing jobs this rotation movement is not usual. In some special cases, minor rotations coupled with vibrations, or even reciprocating (up and down) movements, may be applied to the inner casing to assure an uniform mud displacement ([22, 124]). But, during the slurry setting time, the objective is to fix the casing permanently in place, and so flow azimuthal velocities can be neglected. Specially with respect to axial and radial velocities, which in a fluid loss scenario are far more relevant. Equation 4-4 represents this dimensionality reduction of the physical problem described by hypothesis (ii).

$$u_\theta << u_z, u_r, \qquad \frac{\partial \vec{u}}{\partial \theta} \approx 0 \tag{4-4}$$

As presented in Chapter 2, the majority of authors choose to represent oil wells as uni-dimensional. Their choice is mainly supported by the fact the that the annular gap formed between the inner pipe and formation walls are much smaller than well length or any other axial characteristic dimension. This assumption is also the base for the lubrication theory, which is commonly used to neglect the cylinder curvature and assume inner and outer walls as parallel plates.

Azimuth velocities are neglected for the same reason, see Eq. 4-4, and velocities radial components, within rz plane, are usually also neglected. Indeed, in drilling or in cement displacement models, axial velocity components assume much higher magnitudes than radial. In this 1-D models, axial velocity is considered constant along the radius, calculated as the average of a fully developed flow velocity. Fig 4.2 shows some velocity profiles for the Poiseuille flow for a non-Newtonian fluid [125]. It is clear why for those scenarios this approximation is justified. Since in drilling flows may also be turbulent, this flat profile becomes even more accurate.

On the other hand, the analysis performed in this work is focused in understanding fluid loss, and thus radial velocities might not be neglected. In fact, radial velocity components plays a major role close to the permeable

PUC-Rio - Certificação Digital Nº 1612794/CA

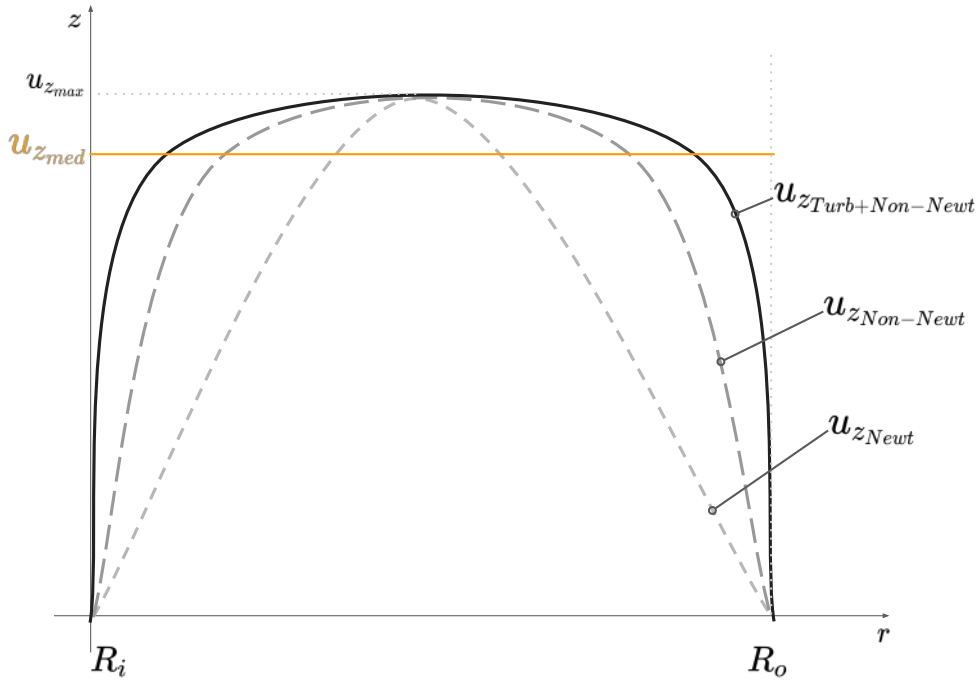

Figure 4.2: Constant axial velocity $u_{z_{med}}$, used specially in displacement models. The average of non-Newtonian turbulent velocity profile in a Poiseuille flow.

region, where fluid loss occurs. Hypothesis (ii) consists on keeping the radial direction terms, and so a 2-D model is considered within a spatial domain $\Omega \subset \mathbb{R}^2$, defined by Eq. 4-5.

$$\{\vec{x} = z\hat{e_z} + r\hat{e_r} \in \Omega \mid 0 \leq z \leq z_{max} \text{ and } R_i \leq r \leq R_o\} \tag{4-5}$$

After placement the cement slurry inside this domain is considered a single phase, and there is not a traceable interface between different fluids. In spite of that, the fluid loss region is reported to works as a filter, separating the slurry mixture components , henceforth referred as species. As discussed in detail in Chapter 2, several authors [75, 82, 83, 126, 127, 128, 44] have observed a higher concentration of solids close to the formation, named filter cake. In Chapter 3 and in agreement with the literature, the performed experiments also demonstrated that a yellowish water is collected across the permeable region, and a thicker and denser cement forms the filter cake inside the well.

To better predict those differences in water-to-cement ratio, the slurry is modeled as a single phase mixture of multiple species. The mass fractions of each species i is a function of spatial position $\vec{x}$ and time t, $C_i = C_i(\vec{x}, t)$. So, hypothesis (iii) states that the cement slurry mixture is modeled with two species: dissolved cement and aqueous component (or filtrate). Since the whole

PUC-Rio - Certificação Digital Nº 1612794/CA

mixture represents 100% of the mass, the sum of all species mass fractions must also be equal to 1, as showed in Eq. 4-6.

$$C_1 + C_2 = 1 \tag{4-6}$$

where C_1 and C_2 are respectively the dissolved cement and filtrate mass fractions.

Thinking back about the compressibility hypothesis, density-driven flows might indeed occur, caused by local variations of fluid species mass fractions. Some authors have studied cement slurries with sedimentation models, and observed that relative velocities between the mixture species have a small magnitude in comparison to bulk pressure-driven flows [129, 130, 131, 132, 133, 134, 121, 135, 136]. Since, the lower pressure formation of fluid loss region imposes a filtration flow rate, sedimentation models are not considered the proper modeling strategy for this problem. Hence, despite hypothesis (iii) considers two different species, the slurry mixture is assumed to move as a whole inside the domain, thus a single velocity field is solved, as stated in Eq. 4-7.

$$\vec{u}_{C_1} = \vec{u}_{C_2} = \vec{u} \tag{4-7}$$

In addition, the mixture is assumed an isotropic material, i.e., its physical properties are not dependent on the direction along which they are measured. Fluids are usually modeled as isotropic materials in the literature. In spite of behaving like a solid after set and presenting domain density variations caused by mass fractions, for this analysis time scope the cement slurry is a fluid. Hence, hypothesis (iv) assumes within an infinitesimal volume, the slurry properties are considered constant and independent on flow orientation.

This assumption represents a considerable reduction on the model complexity, that regards on how stress and rate-of-strain are related. This relation is described by the constitutive equation, which is derived step-by-step based on hypothesis (iv).

The stress tensor can be represented as a composition of an isotropic and a deviatoric terms, as showed in Eq. 4-8.

$$\overline{\overline{T}} = \overline{\overline{\pi}}\,\overline{\overline{I}} + \overline{\overline{\mathbb{S}}} \tag{4-8}$$

where, $\overline{\overline{T}}$ is the stress tensor, $\overline{\overline{I}}$ is the identity tensor and $\overline{\overline{\pi}}$ and $\overline{\overline{\mathbb{S}}}$ are respectively the isotropic and the deviatoric terms. In this case, the isotropic term is a third of the stress tensor trace and the deviatoric term is equivalent to the viscous stress, $\overline{\overline{\tau}}$. Eq. 4-9 shows both terms definitions.

$$\begin{cases} \overline{\overline{\pi}} = \frac{1}{3}\mathrm{tr}\left(\overline{\overline{T}}\right) \\ \overline{\overline{\mathbb{S}}} \equiv \overline{\overline{\tau}} \end{cases} \tag{4-9}$$

PUC-Rio - Certificação Digital Nº 1612794/CA

The mechanical pressure p is usually defined as pointing inwards the mass element, and thus, it is equal to minus π, as showed in Eq. 4-10.

$$p = -\frac{1}{3}\mathrm{tr}\left(\overline{\overline{T}}\right) = -\overline{\overline{\pi}} \tag{4-10}$$

Using the Index Notation, introduced by Einstein [137], the viscous stress tensor $\overline{\overline{\tau}}$ can be referred as τ_{ij}. Assuming the Generalized Newtonian Fluid model, τ_{ij} is proportional to the flow velocity gradient as showed in Eq.4-11.

$$\overline{\overline{\tau}} = \tau_{ij} = C_{ijkl}\frac{\partial u_k}{\partial x_l} \tag{4-11}$$

where C_{ijkl} is a rank-four coefficient tensor.

In a Cartesian space, a tensor of rank four is composed of 81 coefficients. As detailed by Mei [138], if the material is considered isotropic C_{ijkl} is simplified to only two scalar coefficients [139, 140]. Hence, hypothesis (iv) results in a major simplification, and the forth-rank tensor is of the form showed in Eq. 4-12.

$$C_{ijkl} = \lambda\delta_{ij}\delta_{kl} + \eta\left(\delta_{ik}\delta_{jl} + \delta_{il}\delta_{jk}\right) \tag{4-12}$$

where δ_{ij} is the Kronecker delta, η is the dynamic viscosity coefficient and λ is the second viscosity coefficient, both scalars.

As also reviewed in Chapter 2, many authors have experimentally observed the viscoplastic behavior of cement slurries [54, 141, 60, 62]. Hypothesis (v) states that the cement slurry is a non-Newtonian fluid, and so its viscosity depends on the magnitude of the local shear rate tensor, represented by $|\dot{\gamma}|$.

Moreover, cement chemical curing process is usually incorporated into the viscosity models, as an irreversible dependency with time t. The equations that model this function are fully presented in section 4.3.3, but for now hypothesis (v) is simply represented by Eq. 4-13.

$$\eta = \eta(|\dot{\gamma}|, t) \tag{4-13}$$

Finally, cement slurry is considered to present shrinkage during setting period, which is a density change with time observed by many authors in the literature [28, 142, 27]. Hypothesis (vi) implies that cement fraction density is a function of time, as showed in Eq. 4-14

$$\rho_1 = \rho_1(t) \tag{4-14}$$

Small volume reductions like shrinkage triggers a downward movement and hence a small decay of the cement level, thus slightly changing its hydrostatic pressure. However, during the setting process cement slurry develops a gel-like structure. This causes it to adhere to the well walls, which hinders

PUC-Rio - Certificação Digital Nº 1612794/CA

this liquid accommodation. Hypothesis (vi) depends on the use of a shrinkage model, which is also better detailed in section 4.3.4.

4.3 Problem Equations

In summary, the problem formulation considers the following hypothesis:

i. Isothermal well: $\frac{\partial T}{\partial t} \approx \frac{\partial T}{\partial z} \approx \frac{\partial T}{\partial r} \approx \frac{\partial T}{\partial \theta} \approx 0$;

ii. 2-D Flow: $u_\theta \ll u_r, u_z$ and $\frac{\partial \vec{u}}{\partial \theta} \approx 0$;

iii. Single phase with two species: $C_1 + C_2 = 1$;

iv. Isotropic fluid: $C_{ijkl} = \lambda \delta_{ij}\delta_{kl} + \eta\left(\delta_{ik}\delta_{jl} + \delta_{il}\delta_{jk}\right)$;

v. Viscoplastic Fluid + Irreversible Set: $\eta = \eta(|\dot{\gamma}|, t)$

vi. Chemical shrinkage: $\rho_1 = \rho_1(t)$

On the sequence, conservation and constitutive equations are simplified by these hypothesis, and the final model mathematical expressions are presented.

PUC-Rio - Certificação Digital Nº 1612794/CA

4.3.1 Mass Conservation

The net rate of mass flowing in and out the domain is zero. Taking the Eulerian [143] approach, and using using the Reynolds transport theorem [144], mass conservation statement can be written as showed in Eq. 4-15.

$$\frac{D}{Dt}\int_{\Omega} \rho dV = \int_{\Omega} \left[\frac{D\rho}{Dt} + \rho \nabla \cdot \vec{u}\right] dV = 0 \tag{4-15}$$

where dV is an infinitesimal volume inside the domain Ω. For this to be true in every possible sub-domain of Ω, the integrand must be zero.

In addition, the mixture density ρ only changes with time due to shrinkage, which only affects the final cure. An order of magnitude analysis was performed, and as this is not the focal point of this study, the partial time derivative of ρ can be neglected. Hence, using the the material derivative definition, the simplified mass conservation equation for the whole mixture can be written as in Eq. 4-16.

$$\frac{D\rho}{Dt} + \rho(\nabla \cdot \vec{u}) = 0$$

$$\cancel{\frac{\partial \rho}{\partial t}} + \vec{u} \cdot \nabla \rho + \rho(\nabla \cdot \vec{u}) = 0$$

$$\vec{u} \cdot \nabla\rho + \rho(\nabla \cdot \vec{u}) = 0 \tag{4-16}$$

Despite compressibility is also neglected in this model, as the mixture density may vary due to local species mass fractions, $\nabla\rho$ can't be neglected. Thus mass conservation equation does not simplify into conventional incompressible continuity equation ($\nabla \cdot \vec{u} = 0$).

Since the model comprises multiple species, the mass transport equation must be written for each species $i = [1, 2]$, as showed in Eq. 4-17.

$$\frac{D\left(\rho_i C_i\right)}{Dt} + \rho_i C_i \nabla \cdot \vec{u} = \nabla \cdot (j_i) + q_i \tag{4-17}$$

where C_i and ρ_i are respectively the mass fraction and constant bulk density of species i. In addition, j_i and q_i are the i species diffusion flux and creation rate, respectively.

Considering the aqueous component density ρ_2 is constant, and that dissolved cement density ρ_1 only varies with time due to shrinkage, the terms correspondent to density spatial variations of each species can be canceled. Since a species mass is never created inside the domain, the mass transport equation for the species i is simplified as showed in Eq. 4-18.

$$\begin{aligned}
\frac{\partial\left(\rho_i C_i\right)}{\partial t} + \vec{u} \cdot \nabla\left(\rho_i C_i\right) + \rho_i C_i \nabla \cdot \vec{u} + \nabla \cdot (j_i) &= q_i \\
\frac{\partial \rho_i C_i}{\partial t} + \nabla \cdot \left(\rho_i C_i \vec{u}\right) + \nabla \cdot (j_i) &= q_i \\
\frac{\partial \rho_i C_i}{\partial t} + \rho_i \nabla \cdot (C_i \vec{u}) + C_i \vec{u} \cancelto{0}{\nabla \rho_i} + \nabla \cdot (j_i) &= \cancelto{0}{q_i}
\end{aligned}$$

$$\frac{\partial \rho_i C_i}{\partial t} + \rho_i \vec{u} \cdot \nabla C_i + \rho_i C_i \nabla \cdot \vec{u} = -\nabla \cdot (j_i) \tag{4-18}$$

The diffusion flux j_i can be solved using Fick's Law [145], which states that flux goes from regions of high to low concentration. Mathematically, $j_i = -\mathbb{D}_{i,j} \nabla C_i$, where $\mathbb{D}_{i,j}$ is the diffusivity coefficient of species i in j, and which due to hypothesis (iv) is assumed constant. As only two species are considered, C_1 mass transport is solved with Eq.4-19, while C_2 can be obtained directly from hypothesis (iii).

$$\left[\frac{\partial \rho_1 C_1}{\partial t} + \rho_1 \nabla \cdot \left(C_1 \vec{u}\right)\right] = \mathbb{D}_{1,2} \nabla^2 C_1 \tag{4-19}$$

which is in accordance with Oatmans [126] static filtration hypothesis.

PUC-Rio - Certificação Digital Nº 1612794/CA

4.3.2
Linear Momentum Conservation

The free body forces diagram of an arbitrary control volume V inside the model domain Ω can be seen in Fig. 4.3. On the left, the zr plane is highlighted in the theoretical well. In the center the 2-D domain Ω is showed with its bounding box $\delta\Omega$ and the gravity acceleration vector oriented downward. Finally, on the right, the free body diagram for V is presented. The bounding box of this control volume is S and $\vec{F_w}$ is the weight force applied at the center of V. $\hat{n_i}$ are the normal vectors of each of boundary edges, and $\vec{t_{n_i}}$ are the stress vectors for each edge i of S. V can have any arbitrary shape, and it is represented as a square to simplify the understanding.

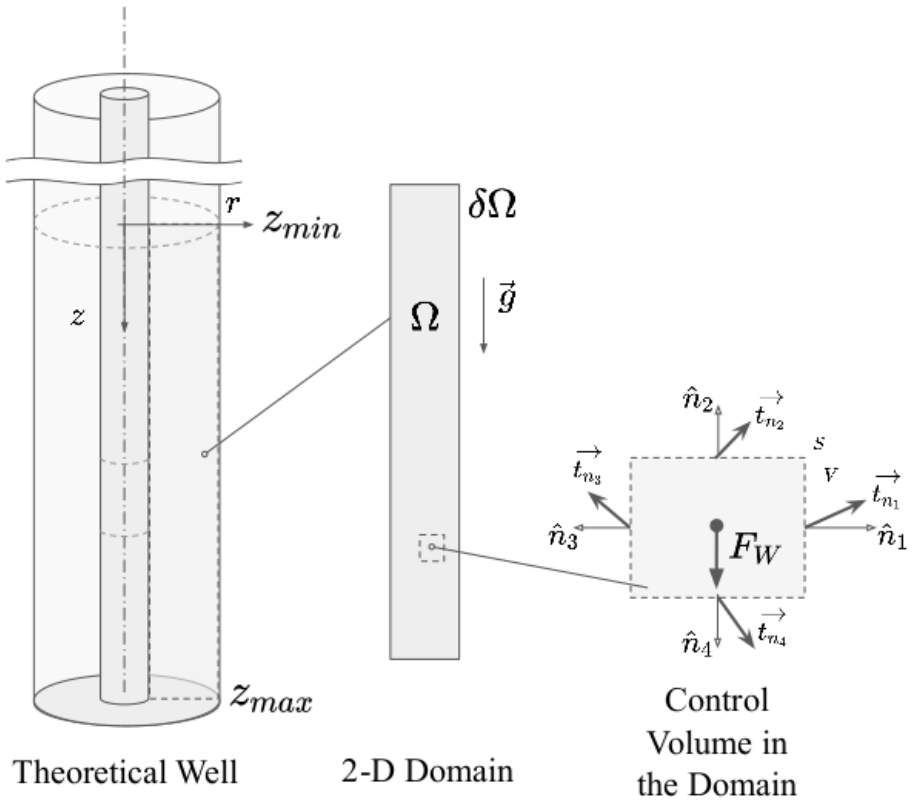

Figure 4.3: Fluid free-body diagram.

Using this free body diagram and Newton 2^{nd} Law of Motion [146], linear momentum balance equation is written as in Eq. 4-20. $\vec{f_w}$ represents weight force by mass unit, and $\vec{t_n}$ is the stress vector, resultant of surface forces acting on boundary S contour, which is represented by normal unit vectors $\hat{n}$. The fluid mixture, of density ρ is considered to move as a whole, and so, only one velocity field $\vec{u}$ must be solved for the domain Ω.

$$\frac{D}{Dt}\int_V \rho\vec{u}dV = \int_V \rho\vec{f_w}dV + \int_S \vec{t_n}dS \tag{4-20}$$

PUC-Rio - Certificação Digital Nº 1612794/CA

The Reynolds transport theorem [144] is used to rewrite the first term time derivative as an integral on V, and mass conservation equation can be used to simplify the same term. The stress principle of Cauchy [147] is also used on the last term, to express the stress vector $\vec{t_n}$ as the inner product of surface normal vector $\hat{n}$ and the stresses tensor $\overline{\overline{T}}$.

$$\int_V \left[\frac{D(\rho\vec{u})}{Dt} + \rho\vec{u}\nabla\cdot\vec{u}\right] dV = \int_V \rho\vec{f_w}dV + \int_S \hat{n}\cdot\overline{\overline{T}}dS$$

$$\int_V \left[\rho\frac{D(\vec{u})}{Dt} + \vec{u}\cancel{\left(\frac{D(\rho)}{Dt} + \rho\nabla\cdot\vec{u}\right)}\right] dV = \int_V \rho\vec{f_w}dV + \int_S \hat{n}\cdot\overline{\overline{T}}dS$$

The divergence theorem is then used to write S integral with respect to the control volume V, so all integrals can be merged.

$$\int_V \rho\frac{D(\vec{u})}{Dt}dV - \int_V \rho\vec{f_w}dV - \int_V \nabla\cdot\overline{\overline{T}}dV = 0$$

$$\int_V \left[\rho\frac{D(\vec{u})}{Dt} - \rho\vec{f_w} - \nabla\cdot\overline{\overline{T}}\right] dV = 0$$

For this equality to be true in any arbitrary V, the integrand must be equal to zero as well. Thus, Eq. 4-21 is the Cauchy Equation of Motion.

$$\rho\frac{D\vec{u}}{Dt} = \rho\vec{f_w} + \nabla\cdot\overline{\overline{T}} \tag{4-21}$$

Material derivative is written explicitly in the first term. Moreover, using Equations 4-8, 4-9 and 4-10 the stress tensor $\overline{\overline{T}}$ can be rewritten in the Cauchy Equation 4-22, representing in Eq. all surface forces acting in V.

$$\rho\left(\frac{\partial\vec{u}}{\partial t} + \vec{u}\cdot\nabla\vec{u}\right) = \rho\vec{f_w} + \nabla\cdot\left[-p\overline{\overline{I}} + \overline{\overline{\tau}}\right] \tag{4-22}$$

where $\overline{\overline{\tau}}$ is the extra stress tensor.

On the sequence, Equations 4-11 and 4-12 are combined and the viscous stress tensor is obtained. This manipulation is seen below and Eq. 4-25 expresses $\overline{\overline{\tau}}$ only with respect to the velocity gradients and material viscosity coefficients.

$$\overline{\overline{\tau}} = \tau_{ij} = C_{ijkl}\frac{\partial u_k}{\partial x_l}$$

$$\tau_{ij} = \left[\lambda\delta_{ij}\delta_{kl} + \eta\left(\delta_{ik}\delta_{jl} + \delta_{il}\delta_{jk}\right)\right]\frac{\partial u_k}{\partial x_l}$$

$$\tau_{ij} = \lambda\frac{\partial u_k}{\partial x_k}\delta_{ij} + \eta\left(\frac{\partial u_i}{\partial x_j} + \frac{\partial u_j}{\partial x_i}\right)$$

PUC-Rio - Certificação Digital Nº 1612794/CA

so, back on the vector notation:

$$\overline{\overline{\tau}} = \lambda \left(\nabla \cdot \vec{u}\right) \overline{\overline{I}} + \eta \left(\nabla \vec{u} + \nabla \vec{u}^T\right) \tag{4-23}$$

The velocity gradient is usually decomposed in a symmetric part plus an anti-symmetric. The first is the rate of deformation tensor, $\overline{\overline{D_u}}$, and the second is the spin tensor, $\overline{\overline{W_u}}$. Equation 4-24 shows rate of deformation tensor in terms of the velocity gradient.

$$\begin{aligned}
\nabla \vec{u} =& \overline{\overline{D_u}} + \overline{\overline{W_u}} \\
\nabla \vec{u} =& \frac{1}{2}\left(\nabla \vec{u} + \nabla \vec{u}^T\right) + \frac{1}{2}\left(\nabla \vec{u} - \nabla \vec{u}^T\right)
\end{aligned}$$

$$\overline{\overline{D_u}} = \frac{1}{2}\left(\nabla \vec{u} + \nabla \vec{u}^T\right) \tag{4-24}$$

In Eq. 4-25, the viscous stress tensor $\overline{\overline{\tau}}$ second term can now be rewritten as a function the deformation tensor, defined above.

$$\overline{\overline{\tau}} = \lambda \left(\nabla \cdot \vec{u}\right) \overline{\overline{I}} + 2\eta \overline{\overline{D_u}} \tag{4-25}$$

Replacing equation 4-25 in 4-22, both terms multiplying the Identity tensor $\overline{\overline{I}}$ can be merged. Hence, a modified pressure is defined including this term, as showed in Eq. 4-26.

$$\begin{aligned}
\frac{\partial \vec{u}}{\partial t} + \vec{u} \cdot \nabla \vec{u} =& \frac{1}{\rho} \nabla \cdot \left[-p\overline{\overline{I}} + \lambda \left(\nabla \cdot \vec{u}\right) \overline{I} + 2\eta \overline{\overline{D_u}}\right] + \vec{f_w} \\
\frac{\partial \vec{u}}{\partial t} + \vec{u} \cdot \nabla \vec{u} =& -\frac{1}{\rho} \nabla \left[\left(p - \lambda \nabla \cdot \vec{u}\right) \overline{\overline{I}}\right] + \frac{1}{\rho} \nabla \cdot \left(2\eta \overline{\overline{D_u}}\right) + \vec{f_w}
\end{aligned}$$

$$\frac{\partial \vec{u}}{\partial t} + \vec{u} \cdot \nabla \vec{u} = -\frac{1}{\rho} \nabla P + \frac{1}{\rho} \nabla \cdot \left(2\eta \overline{\overline{D_u}}\right) + \vec{f_w} \tag{4-26}$$

where, $P = p - \lambda \nabla \cdot \vec{u}$ is the modified pressure.

The following subsections describe respectively the considered rheological and shrinkage models. Hypotheses (v) and (vi) are detailed in those sections, and the equations used to determine the local mixture viscosity and density values are outlined.

4.3.3 Rheological Model

A rheological model is used to describe how the viscosity of complex fluids may vary. In accordance to hypothesis (v), the cement slurry is considered a viscoplastic fluid, and the yield stress is represented by τ_y.

PUC-Rio - Certificação Digital Nº 1612794/CA

As presented in Chapter 2, historically authors have chosen many different rheological models to describe cement slurry behavior. The oil industry most common choices are the Hershel-Bulkley model [61] and the Robertson-Stiff model [148], but both lack several aspects experimentally observed in the behavior of cement slurries [59, 62].

Souza Mendes and Dutra [149] developed SMD rheological model for fluids with yield stress. It fits well rheometry measurements of viscoplastic fluids' viscosity variation with shear rate. Some authors [59] recently have showed good results on using SMD model to describe the pre-set slurry behavior. In addition, SMD equation is continuous and do not need conditional sentences, as seen in Eq. 4-27, and therefore is the adopted rheological model.

$$\tau_{xy} = \left[1 - \exp\left(\frac{-\eta_0 \dot{\gamma}}{\tau_y}\right)\right](\tau_y + K\dot{\gamma}^n) \tag{4-27}$$

where τ_{xy} is the shear stress and the shear rate modulus $|\dot{\gamma}| \equiv \dot{\gamma}$ for simplicity. Similarly to the Herschel–Bulkley [61] model, K is the consistency index and n is the power-law or flow index. Finally, η_0 is Newtonian plateau of viscosity obtained when $\dot{\gamma}$ tends to 0.

According to hypothesis (v) and the Generalized Newtonian Fluid model, relation between the shear stress and shear rate is given by $\tau_{ij} = \eta(\dot{\gamma})\dot{\gamma}_{ij}$. Equation 4-28 is then divided by the shear rate modulus to obtain the non-Newtonian viscosity as a function $\eta(\dot{\gamma})$. Moreover, an extra parameter η_∞ was introduced by Souza Mendes [150] within the last term, as showed in Eq. 4-28.

$$\eta(\dot{\gamma}) = \left[1 - \exp\left(\frac{-\eta_0 \dot{\gamma}}{\tau_y}\right)\right]\left(\frac{\tau_y}{\dot{\gamma}} + K\dot{\gamma}^{n-1} + \eta_\infty\right) \tag{4-28}$$

where η_∞ is the constant viscosity plateau at high shear rates. Note that, as desired, $\lim(\eta(\dot{\gamma}, t))_{\dot{\gamma}\to 0} = \eta_0$ and $\lim(\eta(\dot{\gamma}, t))_{\dot{\gamma}\to\infty} = \eta_\infty$.

With regard to cement curing process, irreversible aspect is usually introduced in constitutive models. Cement hardening is modeled as a yield stress exponential increase as the hydration reactions evolve. This assumption is widely used in the oil industry to predict transient pressure profiles in cement columns [151, 152, 32, 7].

Marchesini et al. [62] has showed that this assumption may not represent the exact physics of this phenomenon. However, for the sake of simplicity, this approach is used in this work, with the yield stress and the Newtonian viscosity plateau modeled as an exponential functions of time, as showed in Eq. 4-29.

PUC-Rio - Certificação Digital Nº 1612794/CA

$$\begin{cases} \tau_y(t) = \tau_{y0} \exp\left(\frac{t}{T_t}\right) \\ \eta_0(t) = \eta_0 \exp\left(\frac{t}{T_t}\right) \end{cases} \tag{4-29}$$

where T_t is a characteristic curing time, and τ_{y0} and η_0 are respectively the initial yield stress and the initial Newtonian viscosity plateau, measured just after mixing the batch. The equations in 4-29 are replaced into Equation 4-28. The viscosity model used in this work is disclosed in Eq. 4-30.

$$\eta(\dot{\gamma}, t) = \left[1 - \exp\left(\frac{-\eta_0 \exp\left(t/T_t\right)\dot{\gamma}}{\tau_{y0} \exp\left(t/T_t\right)}\right)\right]\left(\frac{\tau_{y0} \exp\left(t/T_t\right)}{\dot{\gamma}} + K\dot{\gamma}^{n-1} + \eta_\infty\right) \tag{4-30}$$

4.3.4 Shrinkage Model

As hypothesis (i) assumes the theoretical well as isothermal, energy conservation equation is not solved. As well, all temperature effects on any of fluids properties are neglected in this analysis. However, hypothesis (vi) explicit that the slurry density may indeed vary locally. Part this variation can happen due to mass transport and fluid loss filtration, but mainly it is the result of the slurry chemical shrinkage [7, 40].

To account for that, one last set of equations must be proposed. First, hypothesis (iii) is used to calculate mixture density as a function of the species mass fractions. Since the mixture species add up to form the whole mass and volume of the fluid, Eq. 4-31 shows that for two species only one mass fraction is needed.

$$\rho \equiv \rho(C_i) = \sum_{i=1}^{N} \rho_i C_i$$

$$\rho = \rho_1 C_1 + \rho_2 C_2 \text{ (with two species)}$$

$$\rho(C_1) = \rho_1 C_1 + \rho_2(1 - C_1) \tag{4-31}$$

where, as mentioned before, C_1 and C_2 are respectively the dissolved cement and aqueous component mass fractions; and ρ_1 and ρ_2 are analogously density the dissolved cement and aqueous component bulk densities.

Finally, it is assumed that only the dissolved cement component suffers with shrinkage. As it has been showed in Chapter 2, Hansen [8] observed that slurries with poor water-to-cement ratio have higher shrinkage.

The dissolved cement density relates with shrinkage, as stated by Prohaska et al. [34], which is showed in Eq. 4-32. As in this analysis only small cement columns are studied, compressibility is neglected.

$$\rho_1(t) = \frac{\rho_{1_{0(t=0)}}}{(1 - S(t))}\left(1 + \cancel{c_p}^{0}\right) \tag{4-32}$$

PUC-Rio - Certificação Digital Nº 1612794/CA

As the shrinkage is not the focus of this analysis, a classical empirical model from Daccord et al. [7] is used for sake of simplicity, as showed in Eq. 4-33.

$$\frac{dS}{dt} = \frac{S_\infty}{\Delta T_c \sqrt{\pi}} \exp\left[\left(\frac{t - T_c}{\Delta T_c}\right)^2\right] \tag{4-33}$$

where S_∞ is the total shrinkage, and T_c and ΔT_c are the Gaussian constants. All these parameters are determined empirically for each slurry.

Ultimately, the conservation equations solved in this model are Eq. 4-15 and Eq. 4-26. Together with rheological and shrinkage models, respectively given by equations 4-30 and 4-33, they are the core of numerical implementations presented on Chapter 5. But before, the problem boundary conditions considered are outlined on the following.

4.4 Boundary conditions

The boundary conditions connect the domain, within which a problem is analyzed, to the physical world beyond that domain. They are defined as a set of mathematical statements that translate physical constrains imposed by domain surroundings upon the state variables. There are two basic types of boundary conditions [143].

The first is named Dirichlet conditions, and directly define the value of a state along the boundary. The no-slip and no-penetration conditions, are usually defined as Dirichlet condition. No-slip, means that velocity component tangent to the frontier segment is zero, and no-penetration defines the velocity component normal to the boundary is zero, as showed in Eq. 4-34.

$$\begin{cases} \text{no-slip:} & \vec{u} \cdot \hat{t} = 0 \\ \text{no-penetration:} & \vec{u} \cdot \hat{n} = 0 \end{cases} \quad \forall \vec{x} \in \delta\Omega_i \tag{4-34}$$

where $\vec{u}$ is the velocity vector field value at the domain points $\vec{x}$, $\hat{t}$ and $\hat{n}$ are respectively the unit vectors tangent and normal to the boundary $\delta\Omega_i$.

The second type are the Neumann conditions, which determines the value of the derivative of a state variable along the frontier. One example is the developed flow condition, where the differential velocity with respect to flow direction is zero, as showed in Eq. 4-35.

$$\text{for a flow along z: } \frac{\partial \vec{u}}{\partial z} = 0 \quad \forall \vec{x} \in \delta\Omega_i \tag{4-35}$$

Other types can arise from Dirichlet and Neumann basic conditions. Mixed condition, for example is configured when values and derivatives of

PUC-Rio - Certificação Digital Nº 1612794/CA

a state variables are both defined at the frontier. Another example are Robin conditions, which determines the value of a linear combination of state variables and the derivatives at the boundary. Therefore, before listing the constraints used in the model, it is important to review some aspects of the physical problem analyzed, such as the scope of state variables and the defined domain within its vicinity.

The object of study is the curing process of a recently placed cement slurry in an annular well in the presence of a fluid loss zone. Well pressure profile p along the depth and its evolution with time needs to be evaluated. Additionally, the flow velocity vector field $\vec{u}$, induced within the annular space by the formation permeable zone, must be analyzed. Lastly, the dissolved cement mass fraction (C_1) field closes the list of state variables in the scope for this analysis.

As showed in Fig. 4.3 the 2D-domain Ω is defined as a vertical slice of the annular space formed between the inner casing and well borehole. As mentioned in subsection 4.1, just a section of the well is evaluated and its final depth is assumed to be the well bottom. Regarding that, the domain bounding box, $\delta\Omega$, can be divided in five segments, each with different boundary conditions. Fig. 4.4 shows a detailed view of the domain with these segment $\delta\Omega_i$ represented.

PUC-Rio - Certificação Digital Nº 1612794/CA

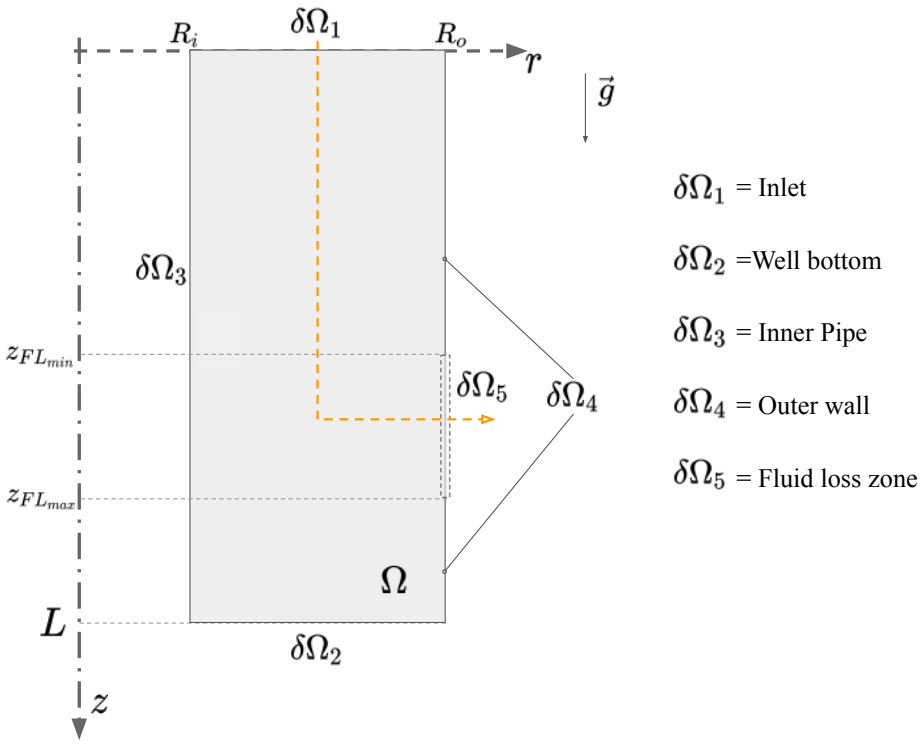

Figure 4.4: Detailed boundary sections $\delta\Omega_i$.

The first segment $\delta\Omega_1$ marks the analyzed section initial depth, or simply the inlet. The oil well extends above this domain frontier up to the surface, and so, the weight of the fluids above is responsible for a pressure Dirichlet condition. In addition, flow above the inlet is considered developed, which configures a Neumman condition of velocity $\vec{u}$ and mass fraction C_1. As a result, Eq. 4-36 shows the inlet mixed condition statements for inlet boundary.

$$\forall \vec{x} \in \delta\Omega_1 \begin{cases} \nabla \vec{u} \cdot \hat{n} = 0 \\ \nabla C_1 \cdot \hat{n} = 0 \end{cases} : \text{developed flow} \qquad p = P_{in} \quad : \text{imposed pressure} \tag{4-36}$$

The frontier $\delta\Omega_2$, $\delta\Omega_3$ and $\delta\Omega_4$ represents respectively the well bottom, the inner pipe and the outer formation. In a scenario without fluid loss, cement remains in the annular space throughout the curing time after placement. These three walls are considered impermeable and fluid adjacent to each wall does now move with respect to it. Moreover, at a fluid-solid interaction, pressure remains constant and mass fraction of the inner mixture is preserved for impermeable walls. This configures a Neumann conditions for both p and C_1, as showed with the combined no-slip and no-penetration Dirichlet condition in $\vec{u}$ Dirichlet in Eq. 4-37 for inner pipe, outer wall and well bottom.

$$\forall \vec{x} \in \{\delta\Omega_2, \delta\Omega_3, \delta\Omega_4\} \begin{cases} \vec{u} = 0 \quad : \text{no-slip/no-penetration} \end{cases} \tag{4-37}$$

In order to transcribe the permeability of a fluid loss zone, a new segment is added on the well external wall, with particular boundary conditions. In this low pressure permeable formation region, represented here by $\delta\Omega_5$, a flow is induced. In accordance to Oatmans [126] proposition, it is assumed that the slurry is filtered into the formation. One slurry species may flow into the formation, out of the model domain, while the other is trapped close to the wall, having its mass fraction locally augmented.

At the limit, permeable fluid loss zones can allow only water to flow through, and so the dissolved cement would be retained to form the filter cake. This assumption is vastly used in cement filtration literature [74, 128, 82, 83], and it was also observed in the experimental results performed in this work, presented in Chapter (6).

The flow velocity of this filtration and the mass fraction at the permeable wall are both defined as time-dependent Dirichlet conditions of $\vec{u}$ and C_1 respectively. At each time step, both values are updated based on the mass flow rate with time, determined as a problem input. Eq. 4-38 shows the Dirichlet conditions at the fluid loss zone.

PUC-Rio - Certificação Digital Nº 1612794/CA

$$\forall \vec{x} \in \delta\Omega_5 \begin{cases} C_1 = C_{1_{FL}} & : \text{imposed mass fraction} \\ \vec{u} = \vec{V}_{FL} & : \text{imposed fluid loss flow rate} \end{cases} \tag{4-38}$$

where $\vec{V}_{FL}$ is the average fluid loss velocity, calculated from the imposed mass flow rate.

In the next chapter, the numerical implementation of the model is detailed. The numerical method used is fully presented, together with the discretization strategies for time and space and the numerical solver.

PUC-Rio - Certificação Digital Nº 1612794/CA

5
Numerical model

Chapter 4 have outlined the governing equations for predicting the evolution with time of the recently placed cement sheath column pressure profile in a well annular section, in the presence of a fluid loss zone. A complete model can help field engineers to better design the cementing operation and to enable the prediction of its effects in the pressure balance. In addition, the implementation of this model as a numerical tool should aid operational teams not only during well design phase, but also during cement jobs, adjusting the model to the field dynamic scenarios.

Despite all simplification hypotheses assumed have reduced the physical problem complexity, this is still a transient, multi-variable and nonlinear boundary value problem. Therefore, no exact or analytical solution can be directly obtained. Assuming this solution exists and that it is represented by a continuous function, it is proposed that it can be approximated by a finite set of values, with a tolerable precision [153].

This is known as numerical approximation, and different methods have been developed to produce these practical results, regarding the way they approach the governing partial differential equations (PDEs). The PDEs derived in Chapter 4 are presented in their differential or strong formulation. The first classical numerical method developed, named Finite Differences Methods (FDM), arises straight from this differential formulation developed by Taylor [154], and its use to solve practical problems date back to the early 20^{th} century [155]. In FDM, the derivative terms are directly discretized, assuming the truncated approximation converges to the continuum derivative functions as spatial and time steps, respectively Δx and Δt, tends to zero.

An alternative approach has split into another branch of classical numerical methods, which analyze the PDEs in their integral or weak formulation [153]. If the PDE strong formulation is of the form $f(\vec{u}, p, ...) = \mathcal{A}(\mathbf{u}) = s$, the corresponding integral formulation can be obtained as showed in Eq. 5-1.

$$\mathcal{A}(\mathbf{u}) - s = 0$$
$$[\mathcal{A}(\mathbf{u}) - s] \cdot \mathbf{v} = 0$$

PUC-Rio - Certificação Digital Nº 1612794/CA

$$\int_{\Omega} \left[\mathcal{A}\left(\mathbf{u}\right) - s\right] \cdot \mathbf{v} \; d\vec{x} = 0 \tag{5-1}$$

where $\mathcal{A}\left(\mathbf{u}\right)$ aggregates all terms which are functions of any of the dependent variables within the array $\mathbf{u}$, and s is the compilation of remaining terms, or source terms. $\vec{x}$ is a vector in the independent variables space, and $\mathbf{v}$ is the array of test functions correspondent the trial functions in $\mathbf{v}$. With this formulation and assuming a solution exists, Eq. 5-2 indicates how to find it.

$$\text{Find } \mathbf{u} \in V : \; \mathcal{F}\left(\mathbf{u}; \mathbf{v}\right) = 0 \;\; \forall \mathbf{v} \in V \tag{5-2}$$

where the semicolon within the continuous variational formulation F indicates that it might present nonlinear dependence on $\mathbf{u}$, and depends linearly on $\mathbf{v}$.

The general idea of employing numerical methods in variational calculus was first developed in the late sixteenth century by Gottfried Wilheml Leibniz [156], As reviewed by Arroyo et al. [157], around 1742 Leonhard Euler [158] has solved the elastic beam deformation problem, using Bernoulli's formulation of the elastic as a variational problem in terms of the stored energy. But only after Strutt [159] and Ritz [160] it was used to obtain approximate solutions to an energy minimization problem. Known as Rayleigh-Ritz method, it was based in global interpolating functions with unknown coefficients. Later, Galerkin [161], in 1915, put forward a similar method where the coefficients are determined by convening the integral residual to zero, not requiring the minimization of an energy functional. Courant [162] paved the way to FEM, applying a Galerkin method, but with local basis interpolating functions. Due to computational power obvious limitations by the time of Ritz and Galerkin, FEM's birth is considered the work of Turner et al. of 1956 [163], who solved structural mechanics problems using the Ritz-Galerkin method. Although some has extended the Ritz-Galerkin methods [164, 165], it is until today the most prominent and representative FEM approach.

In this work the Galerkin method is used with local interpolating functions, also called weight functions. The fundamental idea is that the generalized continuous solution $\mathbf{u}$, showed in Eq. 5-2, can be approximated by polynomial weight functions piecewise across the domain. At each subset of Ω_h of the domain, the discrete variational formulation can be stated as in Eq. 5-3.

$$\text{Find } \mathbf{u}_h \in V_h : \; \mathcal{F}\left(\mathbf{u}_h; \mathbf{v}\right) \approx 0 \; \forall \mathbf{v} \in V_h \text{as } \mathbf{u}_h\left(\vec{x}\right) = \sum_{j=1}^{N} \left(U_j \psi_j\left(\vec{x}\right)\right), \text{ hence:}$$

$$\mathcal{F}\left(\sum_{j=1}^{N} \left(U_j \psi_j\left(\vec{x}\right)\right); \mathbf{v}\right) \approx 0 \tag{5-3}$$

PUC-Rio - Certificação Digital Nº 1612794/CA

where N is the number of weight functions, which might be different for each element type, V_h is a discrete finite element subspace of V, U_j is the coefficient that multiplies a specific local weight function $\psi_j(\vec{x})$.

To finally find the approximation of $\mathbf{u}$ by finite elements, the discrete nonlinear variational form of Eq. 5-3 must be rewritten as a system of nonlinear algebraic equations for the degrees of freedom (DoFs) in the domain. The Galerkin approach taken is to make the test functions $\mathbf{v} = \psi_i$, as showed in Eq. 5-4.

$$\underbrace{\mathcal{F}\left(\sum_{j=1}^{N}\left(U_j\psi_j\left(\vec{x}\right)\right);\psi_i\right)}_{\mathcal{R}_i(U)} = 0 \tag{5-4}$$

where $U \in \mathbf{R}^n$ and is the list of elements' DoFs. $\mathcal{R}_i$ is a scalar nonlinear algebraic function of U related to the weight functions ψ_i. Applying this to all N weight functions, the final system of equations to be solved is given by Eq. 5-5.

$$\mathcal{R}(U) = 0 \tag{5-5}$$

On the following sections, the steps generically described above are detailed for this particular case of study and objectives. In addition, other important steps of the numerical solution are also discussed.

PUC-Rio - Certificação Digital Nº 1612794/CA

5.1 Finite Elements Implementation

The Galerkin FEM algorithm briefly described previously was implemented in this work. It was developed in Python language, with the aid of an open source library named DOLFIN [166]. This library contains some basic FEM algorithms internally implemented in C++ and pre-compiled, allowing straightforward development of the main methods with enhanced performance, specially considering long simulations or large domains.

DOLFIN was originally developed by Logg and Wells [167], and it is currently maintained and updated as an open-source project in The FEniCs Project [168]. It counts with the collaboration of several developers and researchers, and with the institutional support and governance of several universities.

This implementation can be divided in four main steps:

i. variational formulation;

ii. time and space discretization;

iii. system solver definition;

iv. model validation.

Each of these steps are outlined along this chapter, together with the motivation for every FEM strategies adopted in this work.

5.1.1 Weak variational Form

To write the variational formulation of each of the problem conservative equations, the procedure detailed by Reddy and Gartling [169] is used.

Each of the steps of such procedure must be performed for the mixture momentum conservation equation (Eq. 4-26), mass conservation equation (Eq. 4-16) and for the species mass transport equation (Eq. 4-19). However, to avoid repetition, the procedure for getting the weak variational form is, from now on, outlined only for the momentum equation.

Initially, the time derivative must be written with respect to t and t_0, respectively the current and previous time steps. Central differences time discretization is used in this step and showed in Eq. 5-6.

$$\frac{\vec{u}-\vec{u_0}}{\Delta t}+\vec{u}\cdot\nabla\vec{u}=\frac{1}{\rho}\nabla\cdot\left(2\eta\overline{\overline{D_u}}\right)-\frac{1}{\rho}\nabla P+\vec{g} \tag{5-6}$$

On the sequence, both sides of the equation are multiplied by the respective test function and integrated over the domain Ω. This procedure is applied first to momentum equation, showed in the strong formulation in Eq. 5-6,

In order to simplify the notation, the inner product integration along the domain gamma is represented according to Eq. 5-7.

$$\int_{\Omega}(\mathbf{u}\cdot\mathbf{v})\,d\vec{x}=\langle\mathbf{u},\mathbf{v}\rangle \tag{5-7}$$

Hence, the left side of Eq. 5-6 can be writen in the integral formulation as showed in detail in Eq. 5-8.

$$\int_{\Omega}\left[\left(\frac{\vec{u}-\vec{u_0}}{\Delta t}+\vec{u}\cdot\nabla\vec{u}\right)\cdot\vec{v}\right]d\vec{x} \tag{5-8}$$

$$\int_{\Omega}\left(\frac{\vec{u}-\vec{u_0}}{\Delta t}\cdot\vec{v}\right)d\vec{x}+\int_{\Omega}(\vec{u}\cdot\nabla\vec{u}\cdot\vec{v})\,d\vec{x}$$

$$\int_{\Omega}\left(\frac{\vec{u}}{\Delta t}\cdot\vec{v}\right)d\vec{x}-\int_{\Omega}\left(\frac{\vec{u_0}}{\Delta t}\cdot\vec{v}\right)d\vec{x}+\int_{\Omega}(\vec{u}\cdot\nabla\vec{u}\cdot\vec{v})\,d\vec{x}$$

$$\left\langle\frac{\vec{u}}{\Delta t},\vec{v}\right\rangle-\left\langle\frac{\vec{u_0}}{\Delta t},\vec{v}\right\rangle+\langle\vec{u}\cdot\nabla\vec{u},\vec{v}\rangle \tag{5-9}$$

PUC-Rio - Certificação Digital Nº 1612794/CA

Before applying the same simplified notation to the right side of the equation, some manipulation is necessary. Equation 5-10 merges back in the same integral the modified pressure P term with the strain-rate $\overline{\overline{D_u}}$, but treating the gravitational body forces parcel separated.

$$\int_\Omega \left[\left(\frac{1}{\rho}\nabla\cdot\left(2\eta\overline{\overline{D_u}}\right)-\frac{1}{\rho}\nabla P+\vec{g}\right)\cdot\vec{v}\right]d\vec{x}$$

$$\int_\Omega \left[\left(\frac{1}{\rho}\nabla\cdot\left(2\eta\overline{\overline{D_u}}\right)-\frac{1}{\rho}\nabla P\right)\cdot\vec{v}\right]d\vec{x}+\langle\vec{g},\vec{v}\rangle \tag{5-10}$$

Integration by parts is applied to the first term, which eliminates the pressure gradient and leads to a natural statement of the pressure boundary conditions. Similarly to the velocity gradient in Eq. 4-24, the test function gradient $\nabla\vec{v}$ is decomposed as the sum of a symmetric tensor $\overline{\overline{D_v}}$ and an anti-symmetric tensor $\overline{\overline{W_v}}$. Finally, some of the resultant terms are inner products between symmetric and anti-symmetric tensors and consequently cancel out. This dense manipulation is detailed below in Eq. 5-11.

$$\begin{aligned}
&=\frac{1}{\rho}\left\{\int_\Omega\left[\nabla\cdot\left(2\eta\overline{\overline{D_u}}-P\overline{\overline{I}}\right)\cdot\vec{v}\right]d\vec{x}\right\}\\
&=\frac{1}{\rho}\left\{-\int_\Omega\left[\left(2\eta\overline{\overline{D_u}}-P\overline{\overline{I}}\right)\cdot\nabla\vec{v}\right]d\vec{x}+\oint_{\delta\Omega}\left[\left(2\eta\overline{\overline{D_u}}-P\overline{\overline{I}}\right)\cdot\vec{v}\right]\cdot\hat{n}dS\right\}\\
&=\frac{1}{\rho}\left\{-\int_\Omega\left[\left(2\eta\overline{\overline{D_u}}-P\overline{\overline{I}}\right)\cdot\left(\overline{\overline{D_v}}+\overline{\overline{W_v}}\right)\right]d\vec{x}+\oint_{\delta\Omega}\left[\left(2\eta\overline{\overline{D_u}}-P\overline{\overline{I}}\right)\cdot\vec{v}\right]\cdot\hat{n}ds\right\}\\
&=\frac{1}{\rho}\left\{-\int_\Omega\left[\left(2\eta\overline{\overline{D_u}}\cdot\overline{\overline{D_v}}+\cancelto{0}{2\eta\overline{\overline{D_u}}\cdot\overline{\overline{W_v}}}-P\overline{\overline{I}}\cdot\overline{\overline{D_v}}-\cancelto{0}{P\overline{\overline{I}}\cdot\overline{\overline{W_v}}}\right)\right]d\vec{x}\right.\\
&\qquad\left.+\oint_{\delta\Omega}\left[\left(2\eta\overline{\overline{D_u}}-P\overline{\overline{I}}\right)\cdot\vec{v}\right]\cdot\hat{n}ds\right\}\\
&=\frac{1}{\rho}\left\{-\int_\Omega\left[\left(2\eta\overline{\overline{D_u}}\cdot\overline{\overline{D_v}}-P\overline{\overline{I}}\cdot\overline{\overline{D_v}}\right)\right]d\vec{x}+\oint_{\delta\Omega}\left[\left(2\eta\overline{\overline{D_u}}-P\overline{\overline{I}}\right)\cdot\vec{v}\right]\cdot\hat{n}ds\right\}\\
&=\frac{1}{\rho}\left\{-\int_\Omega\left[\left(2\eta\overline{\overline{D_u}}-P\overline{\overline{I}}\right)\cdot\overline{\overline{D_v}}\right]d\vec{x}+\oint_{\delta\Omega}\left[\left(2\eta\overline{\overline{D_u}}-P\overline{\overline{I}}\right)\cdot\vec{v}\right]\cdot\hat{n}ds\right\}\\
&=\frac{1}{\rho}\left\{-\left\langle\overline{\overline{T_P}},\overline{\overline{D_v}}\right\rangle+\oint_{\delta\Omega}\overline{\overline{T_P}}\left(\vec{v}\cdot\hat{n}\right)ds\right\}
\end{aligned}\tag{5-11}$$

where $\overline{\overline{T_P}}$ is the modified stress tensor, equal to $2\eta\overline{\overline{D_u}}-P\overline{\overline{I}}$.

PUC-Rio - Certificação Digital Nº 1612794/CA

Analogously, the same procedure is applied both to the mass conservation equation and to the advection-diffusion equation of mass transport. In mass conservation, it starts from Eq.4-16, which after the first step becomes Eq. 5-12.

$$\int_{\delta\Omega} \left\{ \left[\vec{u} \cdot \nabla\rho + \rho(\nabla \cdot \vec{u}) \right] \cdot q \right\} d\vec{x} = 0 \tag{5-12}$$

where q is the respective test function.

The terms are then integrated individually and the same time discretization is applied to the mixture density ρ time derivative. Since there are no higher derivative terms of the velocity or pressure, the final variational form of the mixture mass conservation equation is showed in Eq. 5-13.

$$\langle \vec{u} \cdot \nabla\rho, q \rangle + \langle \rho \left(\nabla \cdot \vec{u} \right), q \rangle = 0$$

$$\langle q\vec{u}, \nabla\rho \rangle + \langle \rho \left(\nabla \cdot \vec{u} \right), q \rangle = 0 \tag{5-13}$$

The advection-diffusion of the dissolved cement mass fraction, showed in Eq. 4-19, is the model last equation to be written in the variational form. Again, the first step is to multiply by the respective test function l and integrate over the domain Ω. Finally, the integration by parts step unveils the natural declaration of mass fraction boundary conditions, as showed in Eq. 5-14.

$$\int_{\Omega} \left\{ \left[\frac{\partial \rho_1 C_1}{\partial t} + \rho_1 \vec{u} \cdot \nabla C_1 + \rho_1 C_1 \nabla \cdot \vec{u} \right] \cdot l \right\} d\vec{x} = \mathbb{D}_{1,2} \int_{\Omega} \left(\nabla^2 C_1 \cdot l \right) d\vec{x}$$

$$\left\langle \frac{\partial \rho_1 C_1}{\partial t}, l \right\rangle + \langle \rho_1 \vec{u}, \nabla C_1 l \rangle + \langle \rho_1 C_1 \nabla \cdot \vec{u}, l \rangle = \mathbb{D}_{1,2} \left\langle \nabla^2 C_1, l \right\rangle$$

$$\left\langle \frac{\rho_1 C_1}{\Delta t}, l \right\rangle - \left\langle \frac{\rho_{1_0} C_{1_0}}{\Delta t}, l \right\rangle + \langle \rho_1 \vec{u}, \nabla C_1 l \rangle + \langle \rho_1 C_1 \nabla \cdot \vec{u}, l \rangle = \mathbb{D}_{1,2} \left\langle \nabla^2 C_1, l \right\rangle$$

$$\begin{aligned} \left\langle \frac{\rho_1 C_1}{\Delta t}, l \right\rangle - \left\langle \frac{\rho_{1_0} C_{1_0}}{\Delta t}, l \right\rangle + \langle \rho_1 \vec{u}, \nabla C_1 l \rangle + \langle \rho_1 C_1 \nabla \cdot \vec{u}, l \rangle = \\ -\mathbb{D}_{1,2} \langle \nabla C_1, \nabla l \rangle + \mathbb{D}_{1,2} \oint_{\delta\Omega} (l \nabla C_1 \cdot \hat{n}) ds \end{aligned} \tag{5-14}$$

where ρ_{1_0} and C_{1_0} are respectively the species 1 density and mass fraction on the previous time step.

Some of the terms of Equations 5-11, 5-13 and 5-14 appear integrated over the domain boundaries $\delta\Omega_i$ and can be simplified. These simplification steps are individually justified in the next subsection.

PUC-Rio - Certificação Digital Nº 1612794/CA

5.1.2 Boundary Conditions Implementation

As detailed in Chapter 4, treating the cemented well as two-dimensional assumes axial symmetry and the annular gap is represented by a rectangular domain Ω. Figure 4.4 shows the domain boundaries $\delta\Omega$ divided in five different sections, with different boundary conditions each. Therefore, each boundary condition implementation is here outlined separately, according to the respective conservative equation.

Some boundary conditions need to be imposed while solving the problem. An example is the no-slip and no-penetration Dirichlet condition, where velocity is simply forced zero at boundary sections $\delta\Omega_2$, $\delta\Omega_3$ and $\delta\Omega_4$. On the other hand, some must be naturally defined within the problems equations. This is done splitting the boundary integral term that appears in variational formulation Equations 5-11, 5-13 and 5-14. Starting with the momentum equation, the boundary integral term is showed in Eq. 5-15.

$$\oint_{\delta\Omega} \overline{\overline{T_P}}\,(\vec{v}\cdot\hat{n})\,ds = \oint_{\delta\Omega_1} \overline{\overline{T_P}}\,(\vec{v}\cdot\hat{n})\,ds + \oint_{\delta\Omega_{2,3,4}} \overline{\overline{T_P}}\,(\vec{v}\cdot\hat{n})\,ds + \oint_{\delta\Omega_5} \overline{\overline{T_P}}\,(\vec{v}\cdot\hat{n})\,ds \quad (5\text{-}15)$$

where $\delta\Omega_1$ and $\delta\Omega_5$ are respectively the inlet and the outlet regions, and $\delta\Omega_{2,3,4}$ are the impermeable well inner and outer walls. Notice that this term aggregates all the sections where boundary conditions are the same.

Since conditions are imposed on the dependent variables P and $\vec{u}$, the modified stress tensor $\overline{\overline{T_P}}$ is written back in the $2\eta\overline{\overline{D_u}} - P\overline{\overline{I}}$ form. Equation 5-16 shows that for boundary sections $\delta\Omega_{2,3,4}$, when velocity vector $\vec{u}$ is known, the respective test function $\vec{v}$ becomes zero, simply canceling the whole term, as indicated in Eq. 5-16.

$$\delta\Omega_2, \delta\Omega_3, \delta\Omega_4 : \left\{ \vec{u} = 0 \quad \longrightarrow \oint_{\delta\Omega_{2,3,4}} \left(2\eta\overline{\overline{D_u}} - P\overline{\overline{I}}\right) \cancelto{0}{(\vec{v}\cdot\hat{n})}\,ds = 0 \right. \quad (5\text{-}16)$$

For the boundary section $\delta\Omega_5$, the mass flow rate is given as input. However, since filtrate density and fluid loss zone area are constants, the actual imposed condition for the flow is the known filtrate velocity $u_{r_{FL}}$. Analogously, as the velocity is known, Equation 5-17 shows how for $\delta\Omega_5$ the test function $\vec{v}$ also cancels out the boundary term.

$$\delta\Omega_5 : \left\{ \vec{u} = [0 \;\; u_{r_{FL}}]^T \quad \longrightarrow \oint_{\delta\Omega_5} \left(2\eta\overline{\overline{D_u}} - P\overline{\overline{I}}\right) \cancelto{0}{(\vec{v}\cdot\hat{n})}\,ds = 0 \right. \quad (5\text{-}17)$$

On the other hand, for the inlet section $\delta\Omega_1$, developed flow is assumed, implying that the tangent velocity and the normal velocity gradient are zero. An inlet pressure equal to P_{in} is also imposed. This pressure is actually not

PUC-Rio - Certificação Digital Nº 1612794/CA

constant with time, since the ToC(Top of Cement level) decays as some mass is lost to the formation. However, within a time step, this pressure is assumed constant, and this is treated in a quasi-static manner. The P_{in} value is updated for the next time step, according to the amount of mass filtrated through the outlet.

Concerning the boundary term, the closed integral inner pressure and strain terms are separated but only the strain term can be canceled out, as showed in Eq. 5-18.

$$\delta\Omega_1 : \left\{ \frac{\partial \vec{u}}{\partial \hat{t}} = \frac{\partial \vec{u}}{\partial r} = 0 \quad \longrightarrow \oint_{\delta\Omega_1} \left(\cancelto{0}{2\eta \overline{\overline{D_u}} \left(\vec{v} \cdot \hat{n}\right)} - P\overline{\overline{I}} \left(\vec{v} \cdot \hat{n}\right) \right) ds \right. \\ \left. \oint_{\delta\Omega_1} - P_{in} \left(\vec{v} \cdot \hat{n}\right) ds \right. \tag{5-18}$$

Hence, applying these simplification in Equation 5-11, the final momentum conservation equation in the variational form is represented in Eq. 5-19.

$$\left\langle \frac{\vec{u}}{\Delta t}, \vec{v} \right\rangle - \left\langle \frac{\vec{u_0}}{\Delta t}, \vec{v} \right\rangle + \left\langle \vec{u} \cdot \nabla \vec{u}, \vec{v} \right\rangle = \\ -\frac{1}{\rho} \left\langle \overline{\overline{T_P}}, \overline{\overline{D_v}} \right\rangle + \left\langle \vec{g}, \vec{v} \right\rangle + \frac{1}{\rho} \oint_{\delta\Omega_1} - P_{in} \left(\vec{v} \cdot \hat{n}\right) ds \tag{5-19}$$

Repeating this to Equation 5-14, the boundary integral term split between each section $\delta\Omega_i$ is showed in Eq. 5-20.

$$\mathbb{D}_{1,2} \oint_{\delta\Omega} \left(l \ \nabla C_1 \cdot \hat{n}\right) ds = \mathbb{D}_{1,2} \oint_{\delta\Omega_1} \left(l \nabla C_1 \cdot \hat{n}\right) ds \\ + \mathbb{D}_{1,2} \oint_{\delta\Omega_{2,3,4}} \left(l \ \nabla C_1 \cdot \hat{n}\right) ds + \mathbb{D}_{1,2} \oint_{\delta\Omega_5} \left(l \ \nabla C_1 \cdot \hat{n}\right) ds \tag{5-20}$$

At the impermeable well walls, identified as sections $\delta\Omega_{2,3,4}$, thw assumption is that gradient of mass fraction along the section normal direction is zero. Hence, Eq. 5-21 shows that this term is canceled out.

$$\delta\Omega_{2,3,4} : \left\{ \nabla C_1 \cdot \hat{n} = 0 \quad \longrightarrow \mathbb{D}_{1,2} \oint_{\delta\Omega_{2,3,4}} \left(l \cancelto{0}{\nabla C_1 \cdot \hat{n}} \right) ds = 0 \right. \tag{5-21}$$

Likewise, at the inlet is assumed a developed flow also concerning mass fraction, and thereby the $\delta\Omega_1$ is similarly canceled, as showed Eq. 5-22.

$$\delta\Omega_1 : \left\{ \nabla C_1 \cdot \hat{n} = 0 \quad \longrightarrow \mathbb{D}_{1,2} \oint_{\delta\Omega_1} \left(l \cancelto{0}{\nabla C_1 \cdot \hat{n}} \right) ds = 0 \right. \tag{5-22}$$

In contrast, at the outlet the mass fraction of dissolved cement is assumed

PUC-Rio - Certificação Digital Nº 1612794/CA

constant. Thereupon, Eq. 5-23 shows the test function l is zero when the correspondent trial function C_1 is known.

$$\delta\Omega_5 : \Big\{ C_1 = C_{FL} \quad \longrightarrow \mathbb{D}_{1,2} \oint_{\delta\Omega_5} \left(\cancelto{0}{l} \nabla C_1 \cdot \hat{n} \right) ds = 0 \tag{5-23}$$

Subsequently, the final variational form for the mass fraction advection-diffusion equation is showed Eq. 5-14.

$$\left\langle \frac{\rho_1 C_1}{\Delta t}, l \right\rangle - \left\langle \frac{\rho_{1_0} C_{1_0}}{\Delta t}, l \right\rangle + \langle \rho_1 \vec{u}, \nabla C_1 l \rangle + \langle \rho_1 C_1 \nabla \cdot \vec{u}, l \rangle = -\mathbb{D}_{1,2} \langle \nabla C_1, \nabla l \rangle \tag{5-24}$$

5.2 Discretization

5.2.1 Spatial discretization

The spatial domain Ω is then discretized with a mesh composed of finite individual elements. Several authors have researched the mathematical aspects of mesh generation [170, 171] and the effects of its shape on numerical simulations [172].

This work does not have the intention to deeply discuss mesh generation strategies, neither will focus in analyzing the numerous aspects that correlate meshing techniques to the model numerical precision and stability. Only the most basic and important aspects regarding the mesh choice and elements for this problem are analyzed. Those aspects are: regularity, structure, refinement, smoothness, and interpolation order. The following subsections present separately the choices of mesh type and element type.

5.2.1.1 Mesh Definition

Regular structured meshes are defined by a grid of congruent parallelotopes [173] disposed side-by-side, like the one showed in Figure 5.1. Notice that, since the problem domain is too elongated, from now on it is showed rotated counterclockwise to show elements in scale.

This mesh configuration certainly facilitates the element flux calculations, but also might imply in a greater general computational effort. If some refinement is required, as the mesh is uniform, the total number of mesh elements increases drastically.

PUC-Rio - Certificação Digital Nº 1612794/CA

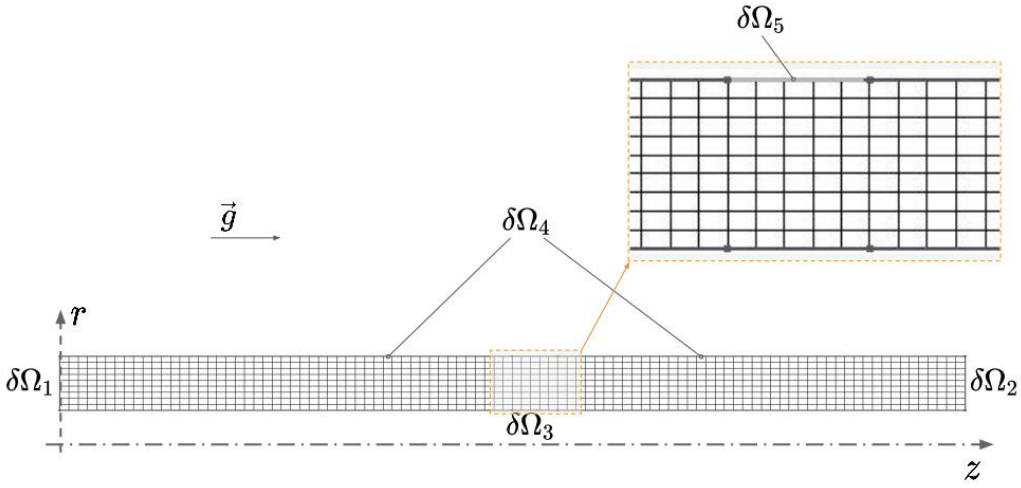

Figure 5.1: Regular structured mesh with 1104 elements.

For example, the fluid loss zone in this problem is expected to concentrate the major velocity variations, and a finer grid is needed close by. So an irregular structured mesh can be applied to enable detailed approximation where it is necessary, despite keeping the overall number of elements comparable, as showed in Fig. 5.2.

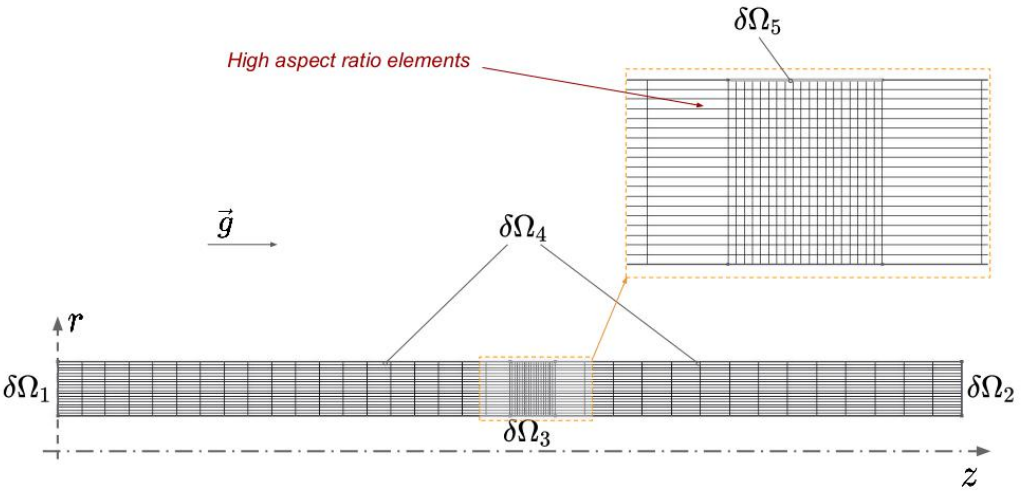

Figure 5.2: Locally refined irregular structured mesh with 1138 elements.

Oil wells have an intrinsically high aspect ratio, with inner and outer radius much smaller than the characteristic axial length, and this is usually a problem for this strategy. As it can be observed in Fig. 5.2, high aspect ratio elements are created, which has been proved to generate numerical errors.

Unstructured meshes present better control to element aspect ratio, but might still suffer from other problems. Abrupt size changes must be minimized to avoid associated numerical flux calculation errors. Figure 5.3 shows an

PUC-Rio - Certificação Digital Nº 1612794/CA

unstructured mesh with quadrilateral Cartesian elements, where this problem is commonly observed.

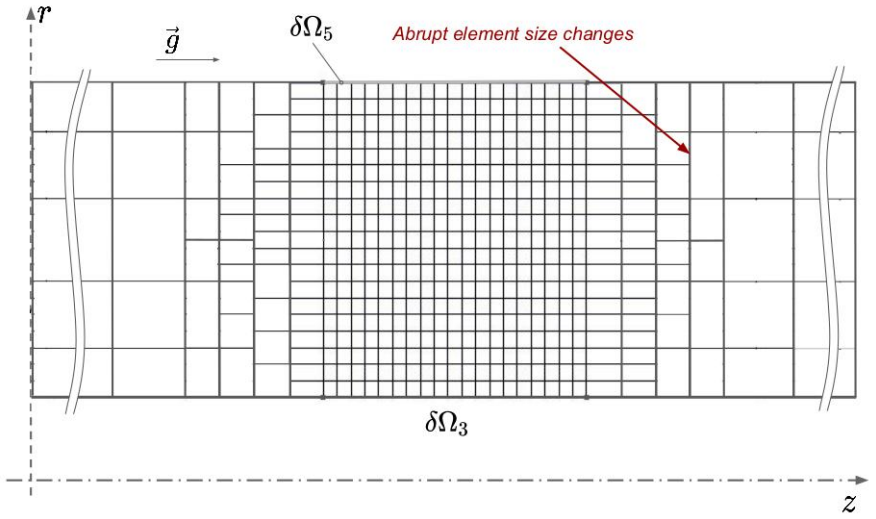

Figure 5.3: Zoom on local refinement of unstructured mesh with quadrilateral Cartesian elements.

PUC-Rio - Certificação Digital Nº 1612794/CA

Triangular unstructured meshes allow smoother transitions between different element size regions. As soon as obtuse triangles are avoided, this type of mesh suits well the problem domain. Consequently, a triangular unstructured mesh was chosen, as illustrated in Fig. 5.4.

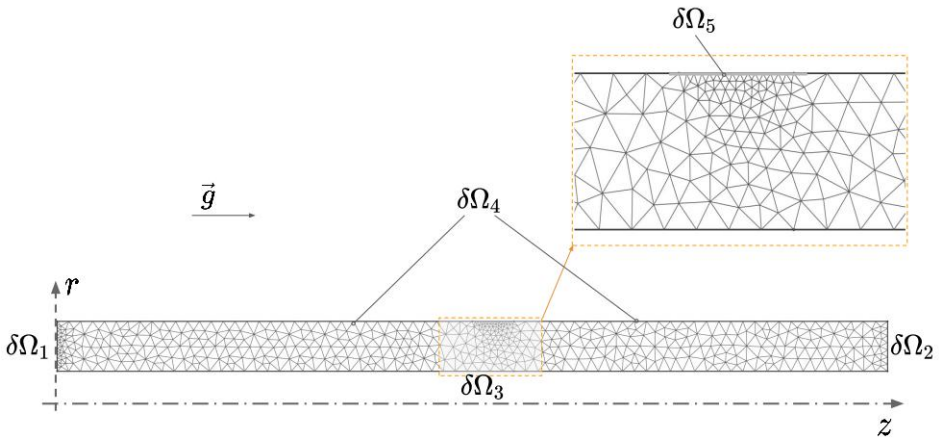

Figure 5.4: Locally refined unstructured triangular mesh with 1117 elements.

Regarding the element interpolation functions order, the choice was guided by two main factors: the nature of the physical problem itself and the reported stability of different element families used for similar applications. Unnecessary higher order elements increase considerably the computational efforts and sometimes, regarding the scope, with no relevant gain in interpolation accuracy. This choice is carefully detailed in Section 5.2.1.2.

5.2.1.2 Element definition

A finite element space is a function space in a certain domain, where piecewise polynomial functions are defined and approximate the problem's exact continuous solution [174]. This space is determined by three main entities. First, the mesh that splits the domain into polygonal cells called elements. Second, the shape functions, which is the finite dimensional space of polynomial functions on each element. And finally, the set of DoFs, associated with an element node or face. Each DoF specifies a quantity that takes a single value for all elements sharing that same node or face.

The nature of the physical problem and the reported stability of the different element families were used to define the used element. In recently cemented wells without fluid loss zones, pressure behavior is essentially like that observed in a quasi-static fluid column, which can be modeled as a Stokes problem. Stable mixed finite element methods for the Stokes equations must satisfy the Ladyzhenskaya–Babuška–Brezzi (LBB) (or inf–sup) compatibility condition, independently proposed by Babuška [175] and Brezzi [176], in the early seventies. According to them, the most straightforward scheme, which consists on equal-order continuous Lagrange finite element spaces for both pressure and velocity components, leads to an unstable problem. Considering that, it is used a higher order for the velocity in comparison with the pressure elements.

A classical set of elements that fill these requirements was proposed in 1973 by Taylor and Hood [177]. It consists of a mixed space of Lagrangian interpolation functions [162], where pressure is solved with a linear element and velocity field is solved with a quadratic element, as illustrated in Fig. 5.5.

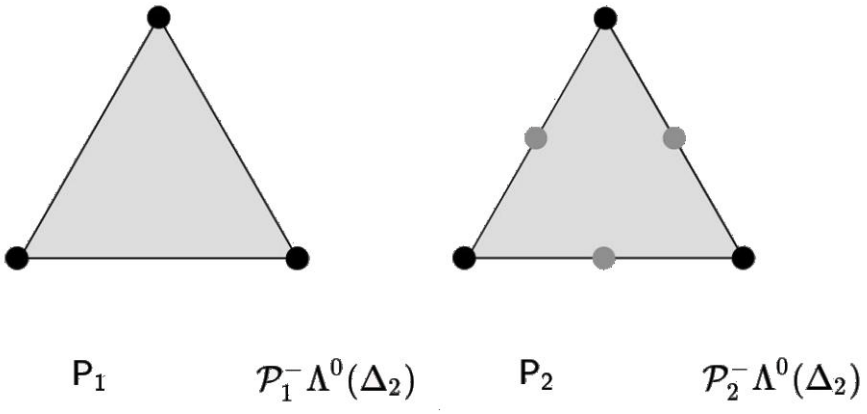

Figure 5.5: Taylor-Hood set of finite elements. Linear for pressure and quadratic for velocity.

The Taylor-Hood set of elements have also been proved stable according

PUC-Rio - Certificação Digital Nº 1612794/CA

to the patch test for mixed displacement-strain formulations, presented by Zienkiewicz [178], in 1986. It have also been widely used for simulating Stokes and Navier-Stokes flow Equations in the literature, and several authors have evaluated its stability and accuracy, such as Bercovier and Pironneau [179], and more recently Lee and Li [180] and Guzmán and Sánchez [181], just to name a few.

5.2.2 Time discretization

Time discretization is performed using a finite differences method, which dates back from 1717, with Taylor [154]. The Taylor series expansion is truncated, and the higher order terms are neglected. Only the first order term is used to obtain the numerical calculation for the time derivative term, as showed in Eq. 5-25.

$$f(t_0+h) = f(t_0) + \frac{f'(t_0)\,h}{1!} + \frac{f''(t_0)\,h^2}{2!} + ... + \frac{f^{(n\prime)}(t_0)\,h^n}{n!} + R_h$$

$$f(t_0+h) - f(t_0) = f'(t_0)\,h + \cancel{\frac{f''(t_0)\,h^2}{2!} + ... + \frac{f^{(n\prime)}(t_0)\,h^n}{n!}} + R_h$$

$$f'(t_0) \approx \frac{f(t_0+h) - f(t_0)}{h} \tag{5-25}$$

where f is any function of time t, f' is the time derivative of this function, h is the discrete time step and n and R_h are respectively the truncation order and residuum.

As the time step $h = \Delta t$ tends to zero, the truncation errors introduced by suppression of the higher order terms also decrease. As one of the calculated functions is the velocity, the maximum time step required for convergence is intrinsically connected to the spatial discretization.

To assure convergence and stability of the calculated flow velocity, time and spatial discretization must be conditioned. This because, adjacent elements flux must not be high enough to overcome more than one spatial element within a discrete time step. To determine the maximum time step to be used, the classical Courant–Friedrichs–Lewy [182](CFL) convergence condition is applied, as showed in Eq. 5-26.

$$\mathrm{CFL}_{max} = \frac{max(u_z)\,\Delta t_{max}}{min(\Delta z)} + \frac{max(u_r)\,\Delta t_{max}}{min(\Delta r)} <= 1 \tag{5-26}$$

Since the spatial discretization varies along the domain, the minimum element components in each direction, Δz and Δr, and also the maximum

PUC-Rio - Certificação Digital Nº 1612794/CA

velocity components, u_z and u_r are used to determine the maximum time step, as showed in equation, so the Courant number C_{max} does not exceed 1.

A variable time step is imposed through the evolution of the simulation. The number of iterations taken by the system solver to reach the tolerance residuum for each time iteration is analyzed. Based on how fast the convergence occurred for the time t_n determines the used numerical step size Δt for the next time t_{n+1}. The maximum time step, calculated with the CFL, is simply a hard limit imposed. It get less restraining as the flow velocity decreases.

This strategy considerably increases the simulation speed, specially for long simulation times and low-Reynolds-number flows, as this particular case of interest.

5.3 Solver definition

The advection-diffusion mass transport equation was solved with a variation of the Gaussian Elimination, named Multi-frontal Massively Parallel Sparse direct Solver (MUMPS) [183, 184]. MUMPS comes implemented within FEniCs library, and it is a linear solver suited for parallel solution of highly sparse matrices.

For the nonlinear coupled flow problem, the Newton-Raphson method was used. Once the discrete variational problem is written as a system of algebraic equations, FEniCs already has implemented a function that calculates the inverse Jacobian matrix. Hence, at each convergence iteration, the matrix operations described in Eq. 5-27 are solved.

$$\mathbf{U}^{n+1} = \mathbf{U}^n + J\left(\mathbf{U}^n\right)^{-1} \cdot \mathcal{R}\left(\mathbf{U}^n\right) \tag{5-27}$$

where $J\left(\mathbf{U}^n\right)^{-1}$ is the inverse of the numerical Jacobian matrix and $R\left(\mathbf{U}^n\right)$ is the multi-variable nonlinear algebraic system of equations to be solved (Eq. 5-5). $\mathbf{U}^n$ and $\mathbf{U}^{n+1}$ are respectively the array of DoFs for the iteration n and $n+1$ respectively

The Newton-Raphson method is quite robust as showed in the literature [185, 186, 187], and in this work convergence is considered achieved when two simple conditions are simultaneously satisfied:

- - absolute residual: $Res_{abs} \leq 10^{-10}$
- - relative variation between iteration steps: $Tol_{rel} \leq 10^{-15}$

Convergence usually occurs in less than five iterations, and apart from some tests with courser meshes, instabilities due to solver convergence was observed in very few of the tested cases. Those are related specifically to certain parameter ranges, as presented in Chapter 6.

PUC-Rio - Certificação Digital Nº 1612794/CA

5.3.1 Simulation workflow

The goal is to numerically obtain the column pressure and velocity profiles, given the fluid loss zone position, flowrate and slurry properties. The overall algorithm used is described below:

Algorithm 1 Simulation Algorithm

Initial pressure and velocity fields = 0;
P_{in} = top initial pressure;
C_{1_0} = Initial mass fraction of dissolved cement.
while $t <= t_{end}$ **do** Time loop
    Calculate viscosity η and density ρ fields from:
        mass fraction field C_1, time t and shear rate $\dot{\gamma}(\vec{u})$
    while Change $<= 1e^{-10}$ and Residue $<= 1e^{-15}$ **do** Convergence Loop
        numerically solve Equations 5-13 and 5-19
        update pressure and velocity fields
    Mass transport: numerically solve Equation 5-24
    update mass fraction field

PUC-Rio - Certificação Digital Nº 1612794/CA

5.4 Mesh Analysis

An important step for validating any numerical model implementation is the mesh analysis, also commonly named mesh testing. The numerical approximation becomes closer to the exact analytical problem solution as the spatial discrete steps tend to zero. Hence, an asymptotic behavior is expected from a characteristic problem response, as the mesh is refined.

At a certain discrete spatial step size, despite any further refinement no relevant change is produced in this characteristic response. This method is commonly used to define the minimum mesh required for a specific simulation domain. Figure 5.6 shows the tested meshes with the correspondent element count.

As described in 5.2.1.1, the triangular unstructured mesh was chosen to enable local refinement where higher gradients are expected to occur. So in the presented mesh test, the total number of elements used to describe the domain is increased, but the local refinement factors are proportionally the same for all mesh sizes.

At the upper part of the well, the velocity profile along the radius is expected to be similar to the one between two parallel plates. Therefore, the characteristic model response utilized to evaluate the mesh is the axial velocity values at the cross-section plane, indicated at Fig. 5.6 by the red dashed line. Figure 5.7 shows the velocity profiles obtained for each mesh size. This flow

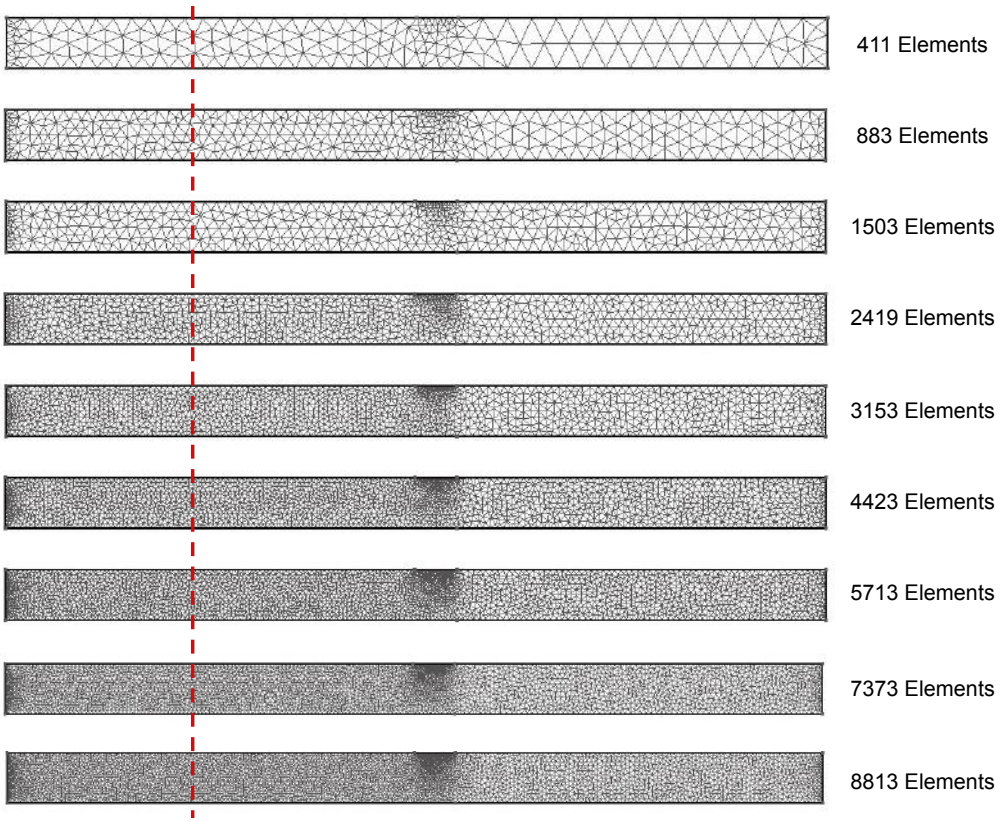

Figure 5.6: Meshes used in mesh test.

static picture is taken for all mesh sizes, arbitrarily at time $t = 200$ seconds of simulation. Table 5.4 shows, for each tested mesh, the number of elements, maximum velocity and difference with respect to the finest mesh.

For comparison, a simulation of 200 s of flow with the coarsest mesh takes 10 s, and with the finest mesh it takes 44 s. Notice that over 7000 elements, the results are almost completely overlapping, with less than half percent of error, as it can be seen in Table 5.4. However, as the Execution to simulation time ratio increment was not relevant (0.18 s/s to 0.23 s/s), the minimum mesh chosen to perform the simulations is the finest presented in this test, with 8813 elements.

PUC-Rio - Certificação Digital Nº 1612794/CA

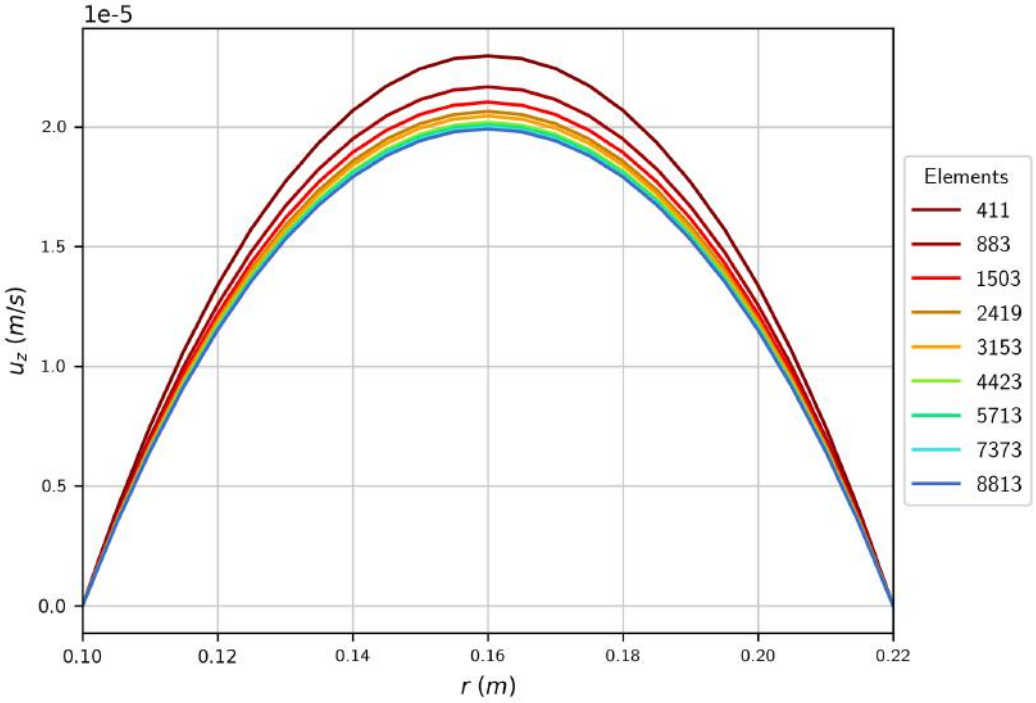

Figure 5.7: Velocity profile for each mesh tested.

Elements	Velocity (m/s)	Difference (%)
411	$2.30 \cdot 10^{-05}$	15.34
883	$2.17 \cdot 10^{-05}$	8.80
1503	$2.10 \cdot 10^{-05}$	5.63
2419	$2.06 \cdot 10^{-05}$	3.66
3153	$2.04 \cdot 10^{-05}$	2.70
4423	$2.02 \cdot 10^{-05}$	1.40
5713	$2.01 \cdot 10^{-05}$	0.87
7373	$2.00 \cdot 10^{-05}$	0.40
8813	$1.99 \cdot 10^{-05}$	0.00

Table 5.1: Mesh test results.

PUC-Rio - Certificação Digital Nº 1612794/CA

6
Results

In the current chapter, the results obtained are presented. Experimental and numerical results are separately disclosed in the following sections. Some of the analysis that compose the overall project results were conducted by third party collaborators, and those are acknowledged as mentioned.

6.1
Experimental results

The performed experiments mainly consisted on reproducing a cement job in a smaller scale.

6.1.1
Slurry design and characterization

Prior to the experiments the slurry design and characterization were performed. As mentioned in section 3.3, Halliburton cementing chemists jointly applied standard oil-industry methodology and equipment to design the cement slurries used in the PWS experiments.

As mentioned in Chapter 3, two final slurries were defined to be tested in the PWS apparatus, the Neat slurry used for control, and the GasTight slurry as the low fluid loss cement. Almost 300g of each slurry was prepared in the laboratory using a cement blender and named Lab Test Samples. Moreover, every slurry batch tested in the PWS apparatus was also characterized simultaneously with the on going test. However, the amount of cement needed to perform the paste displacement and to fill the apparatus was around $550\,kg$. Therefore, despite the same composition, this sample was mixed with the adapted field mixing unit, and so are named PWS Samples. Table 6.1 shows how much mass of cement mixed for each sample of each slurry type.

Besides all measurements performed in the design phase, a rheological characterization was performed with these two different versions the GasTight slurry. It was performed by other project members, and is presented in detail at Marchesini et al. [62]. Since the Neat slurry presented a great amount of free water after some time, its rheological characterization was not possible.

PUC-Rio - Certificação Digital Nº 1612794/CA

Table 6.1: Mixed amount by slurry type and test sample.

Slurry	GasTight	Neat
Lab Test Sample	230,84g	269,60g
PWS Sample	550 kg	550 kg

Some of the results of the GasTight slurry Lab Sample are briefly summarized in Figures 6.1 and 6.2, both adapted from [62].

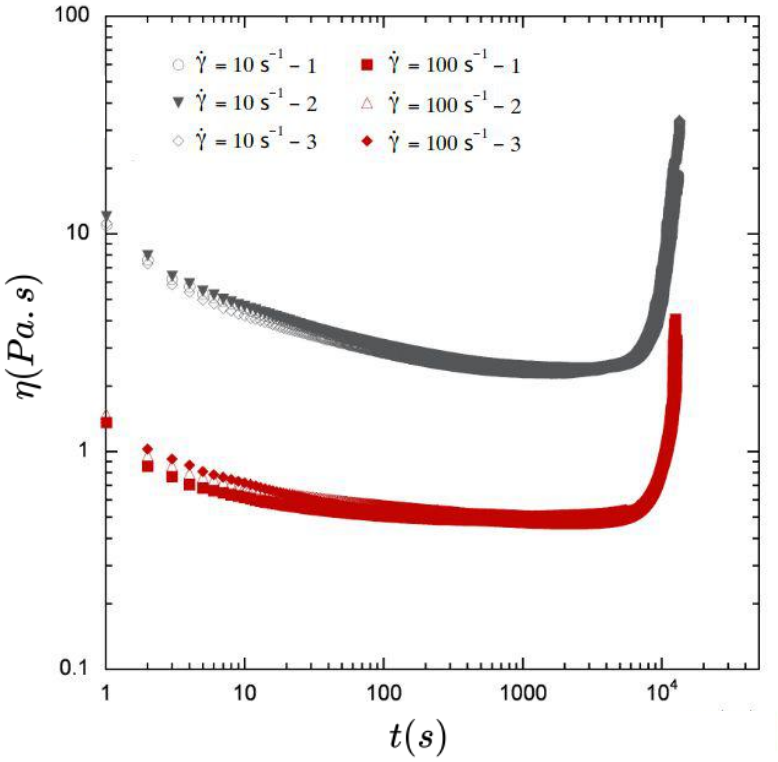

Figure 6.1: Test repeatability for the Lab Sample of GasTight slurry. Adapted from [62]

Figure 6.1, adapted from [62], shows viscosity as a function of time for two different shear rates. It's possible to notice that the three tests performed with Lab Samples prepared at different moments present good agreement. Figure 6.2 shows the shear stress τ and viscosity η as a functions of shear rate $\dot{\gamma}$.

The slurries rheological behavior is fitted by the model described by Equations 4-28 and **??**, at section 4.3.3. The fitted model parameters for the GasTight slurry are: $K = 1.463\,Pa.s^n$, $n = 0.54$, $\tau_{y0} = 19.79\,Pa$, $T_t = 8000\,s$, $\eta_0 = 4500\,Pa.s$ and $\eta_\infty = 0.292\,Pa.s$. Ultimately, these parameters are applied as inputs of the physical model presented in Chapter 4.

PUC-Rio - Certificação Digital Nº 1612794/CA

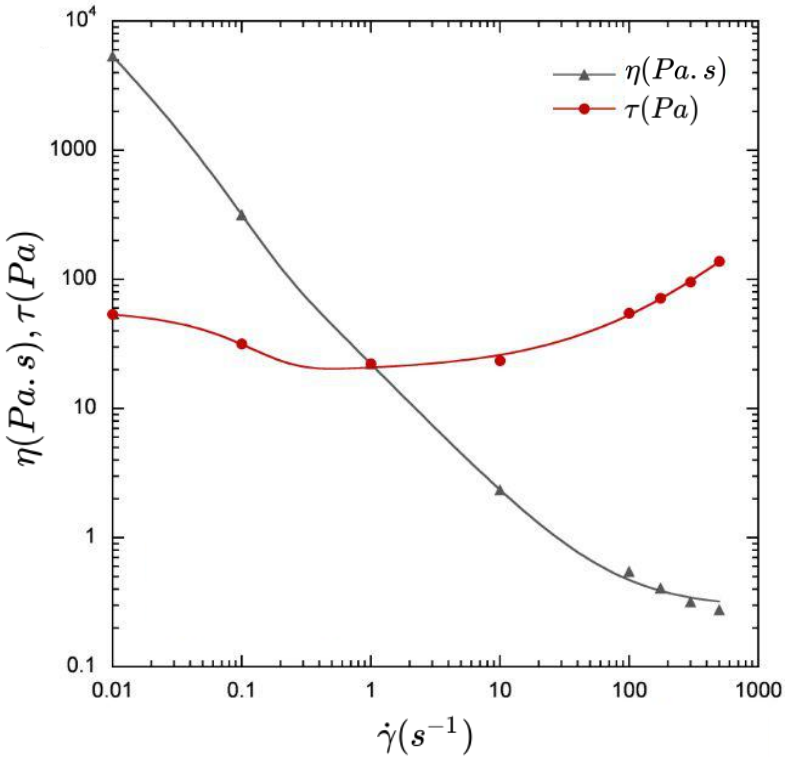

Figure 6.2: Flow curve for the Lab Sample of GasTight slurry.
Adapted from [62]

The last model parameter is the diffusion coefficient $\mathbb{D}_{1,2}$. Since this physical quantity was not measured for the chosen slurries, literature characteristic values were used. Garbalińska [188] have performed long term measurements of water diffusivity in cement mortars, and showed the diffusion coefficient decays with cure. In the early cure stages, the average diffusion coefficient observed is 10^{-9}. Although Zhang and Ye [189] have observed diffusion coefficient time-dependency in cement pastes, given the focus of this work, the average early value observed by Garbalińska was used as a constant. Some tests have been performed with $\mathbb{D}_{1,2}$ values one order of magnitude higher and lower this characteristic value, and no significant changes were observed.

6.1.2 PWS Experiments

In this section, the PWS experimental results performed with these slurries regarding fluid loss analysis are presented. Initially, tests were performed without the fluid loss region. Cement was positioned inside the annulus, as presented in Section 3.1.1, to obtain the pressure profile over time and position. Figures 6.3 and 6.4 presents the results for GasTight slurry and Neat slurry, respectively. In all presented experimental results, P_{e1} and P_{e2} correspond to

PUC-Rio - Certificação Digital Nº 1612794/CA

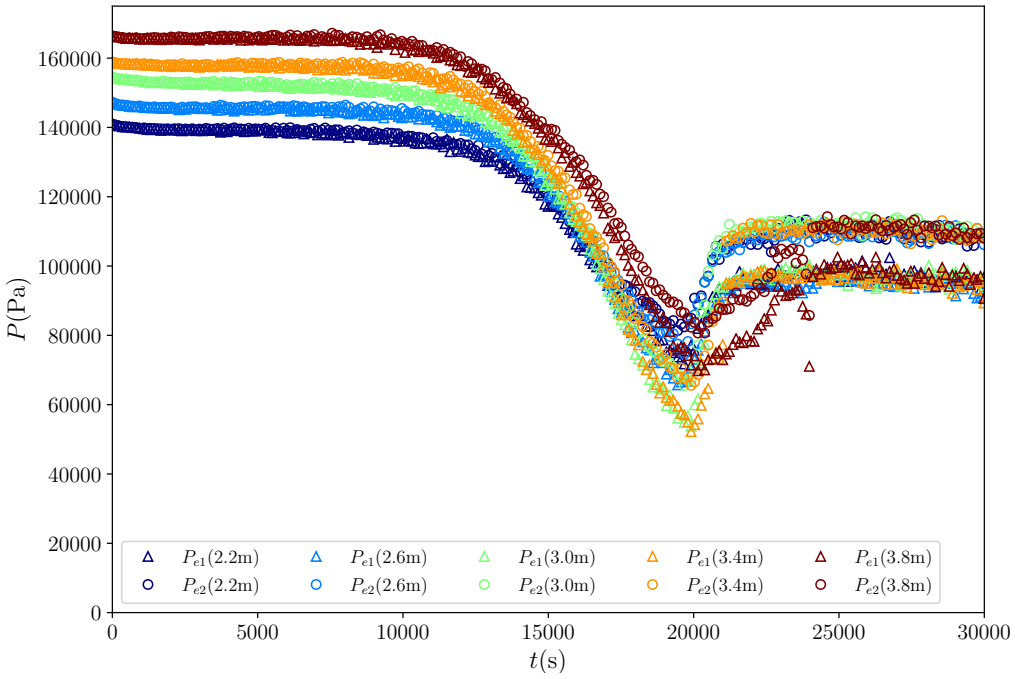

Figure 6.3: GasTight slurry PWS pressure tests without fluid loss region.

the two experiment repetitions.

These results are used as a control, against which the fluid loss tests are compared and contrasted. Figure 6.3 presents two different tests performed with GasTight slurry. Pressure values show repeatability before 18000 s. The data oscillations within collected curves from 0 to 18000 s of both experiments are small and within the pressure transducers precision [113].

However, after setting time (15000 $s \approx 4\,h$) cement becomes more like a solid material, and the transducers' diaphragms normal deformation can no longer be correlated with cement sample pore pressure the same way. In addition, rheological data could only be measured until around 11000 s, when the viscosity spikes up. Therefore, as the focus is to observe pressure decay before viscosity buildup, all further analysis is performed only until 11000 s.

In each of these repetition tests, the Cement Mixing Unit procedure managed to mix slurries with approximately the same density. Initial pressure values acquired at each column height correspond to the static pressure generated by a fluid column with a density of 14.7 ppg, which is quite close to the nominal 15 ppg aimed for.

Curves for the same height of both tests also present similar qualitative behavior, although at greater elapsed time measurements divergence increases. Some possible causes for the overall experimental differences between these two test repetitions are:

PUC-Rio - Certificação Digital Nº 1612794/CA

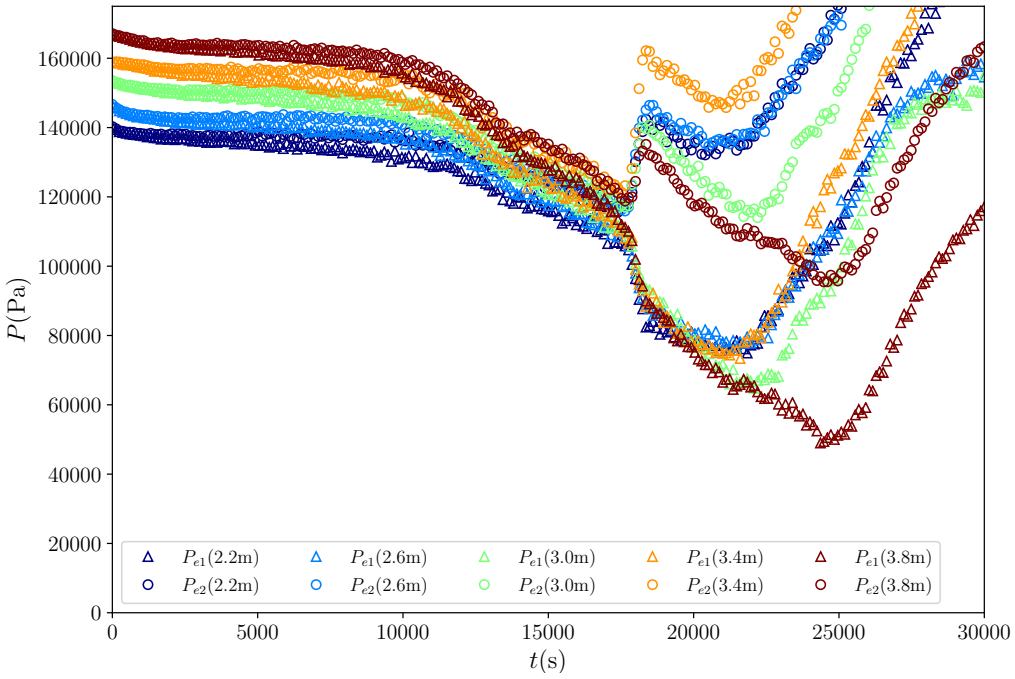

Figure 6.4: Neat slurry PWS pressure tests without fluid loss region.

– the temperature control, which has an uncertainty of $\pm 2°C$;
– the dispersion observed in rheological measurements for the PWS tests.

This second cause can be observed analysing the rheological measurements made with the slurries mixed in the CMU. Figure 6.5, adapted from Marchesini et. al [62], shows average flow curve with error bars.

Although this flow curve had to be built with very few test points, the data dispersion is mostly due to differences in mixing procedures. The lab blenders rotate up to $15000\,rpm$, but have small blades with respect to the cup. Contrarily, the CMU centrifuge pump vanes drive the slurry through a very narrow channels. As the impeller rotates at up to $1800\,rpm$ and the paste recirculates into the tank sprayed directly against a metal sheat for around $10min$. Therefore, this recirculating mix is able to impose a much higher, although more variable shear rate to the slurry.

These issues are all familiar to a field cementing job, and further analysis of Figures 6.3 and 6.4 indicate for both slurries a classic behavior commonly described in the literature [32, 123, 190]. It comprises two different decay rates at the pressure drop. The first is attributed to gelation and the second to shrinkage process triggered by the chemical reaction peak. This behavior is graphically explained in an schematic curve in Fig. 6.6,

PUC-Rio - Certificação Digital Nº 1612794/CA

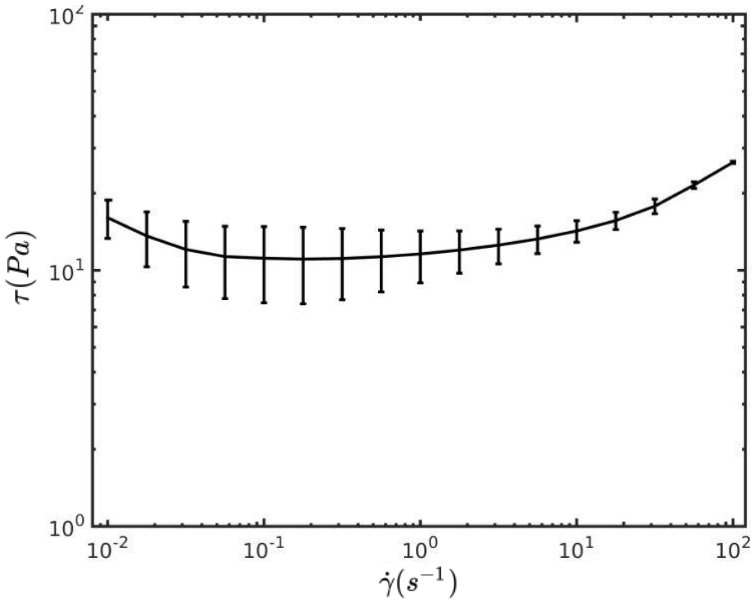

Figure 6.5: GasTight Slurry PWS sample flow curve, with error bars. Adapted from [62]

For the Neat slurry, showed in Fig. 6.4. these two different slopes are more pronounced. Despite the Neat cement presents higher discrepancy between the two tests after the transition time. However, qualitatively these experiments present good agreement, specially within the zone of interest.

In the next set of tests a fluid loss region of $20\,cm$ height is centered at the column depth of $3.6\,m$. Figures 6.7 and 6.8 [108] respectively shows the GasTight slurry pressure and filtrate mass with time.

The differences between the pressure measurements of both tests are higher in the presence of the fluid loss region, which was expected since more uncertainties were added to the system. Some of the identified uncertainties are the filtration module mesh pre-saturation process and the exact start of filtrate flow, due to differences in pressure stabilization times.

Comparing Figures 6.3 and 6.7, it's possible to observe a slightly more negative initial slope. As mentioned in the literature [48, 50, 52], fluid loss effects impacts the pressure drop in early stages of cure. In the presence of gas regions, an early incapacity of the slurry transmitting pressure while viscosity in not high enough can lead to a kick [191, 151, 92, 34, 106].

Analogously, the same tests with the fluid loss region is also performed with the Neat slurry. Figures 6.9 and 6.10 show respectively the pressure measurements and filtrate mass collected.

Due to the lack of fluid loss additives, the amount of mass lost is significantly higher. This impacts directly in an even more negative initial slope of pressure decay. Although a subtle change for a 4 meter column length,

PUC-Rio - Certificação Digital Nº 1612794/CA

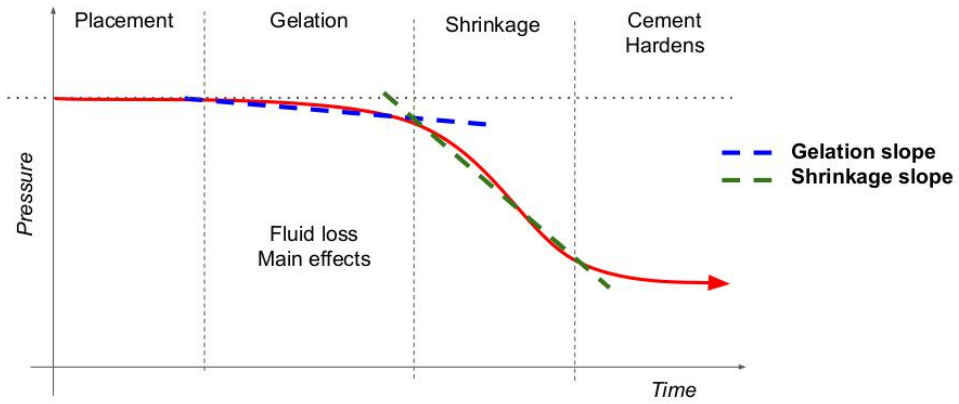

Figure 6.6: Characteristic behavior of pressure drop by curing phase. Adapted from [190]

at real well scale a correspondent pressure decay would surely jeopardize the capacity of this slurry withhold gas influxes at the early curing stages. For the sake of a better comparison both graphs are placed side-by-side, and some horizontal guidelines are traced, as showed in Fig 6.11.

PUC-Rio - Certificação Digital Nº 1612794/CA

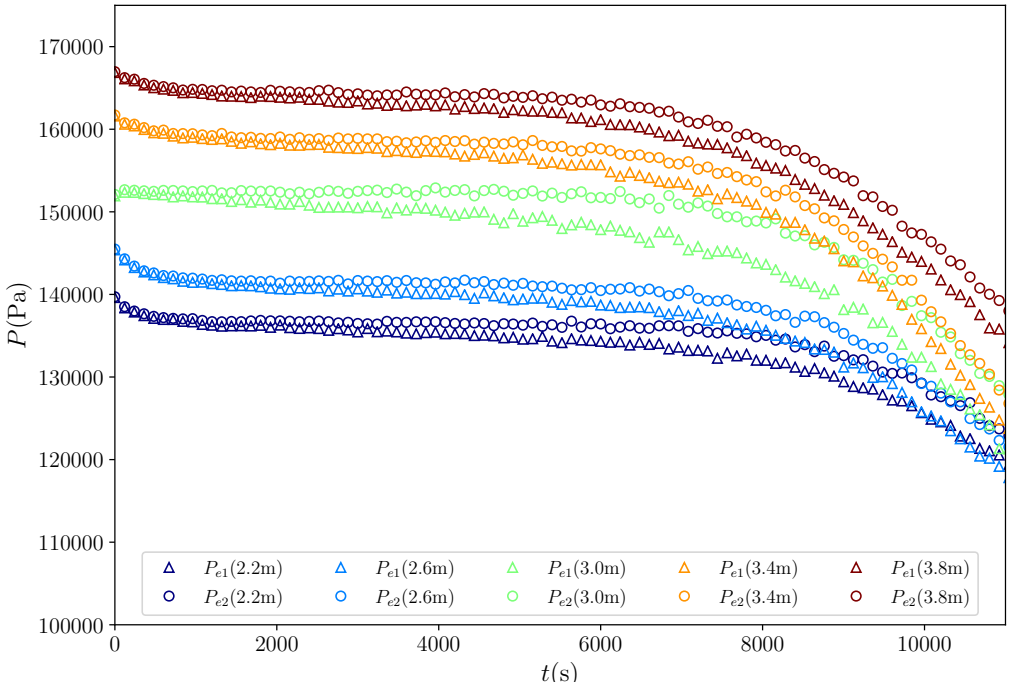

Figure 6.7: GasTight slurry PWS pressure tests with fluid loss region. From [108]

PUC-Rio - Certificação Digital Nº 1612794/CA

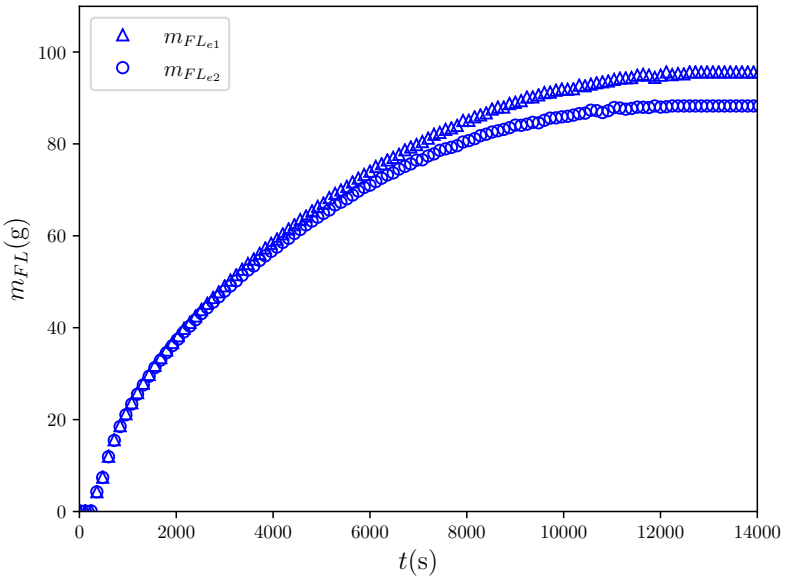

Figure 6.8: GasTight slurry PWS filtrate mass tests. From [108]

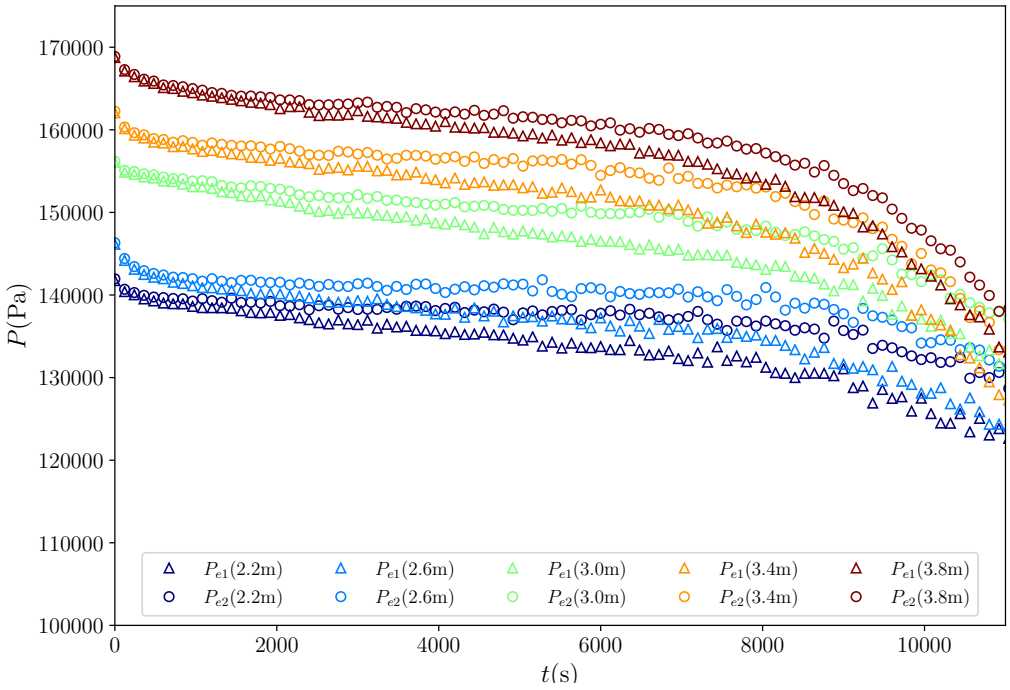

Figure 6.9: Neat slurry PWS pressure tests with fluid loss region.

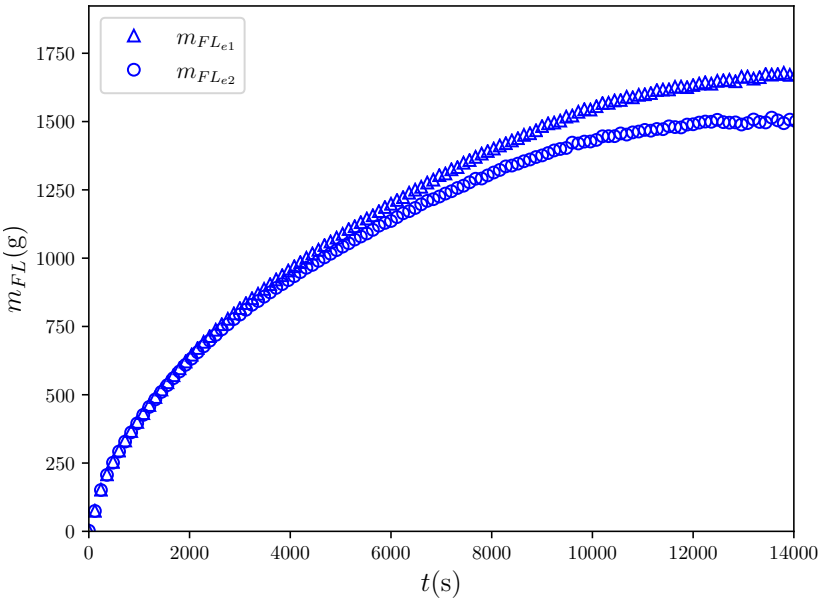

Figure 6.10: Neat slurry PWS filtrate mass tests.

PUC-Rio - Certificação Digital Nº 1612794/CA

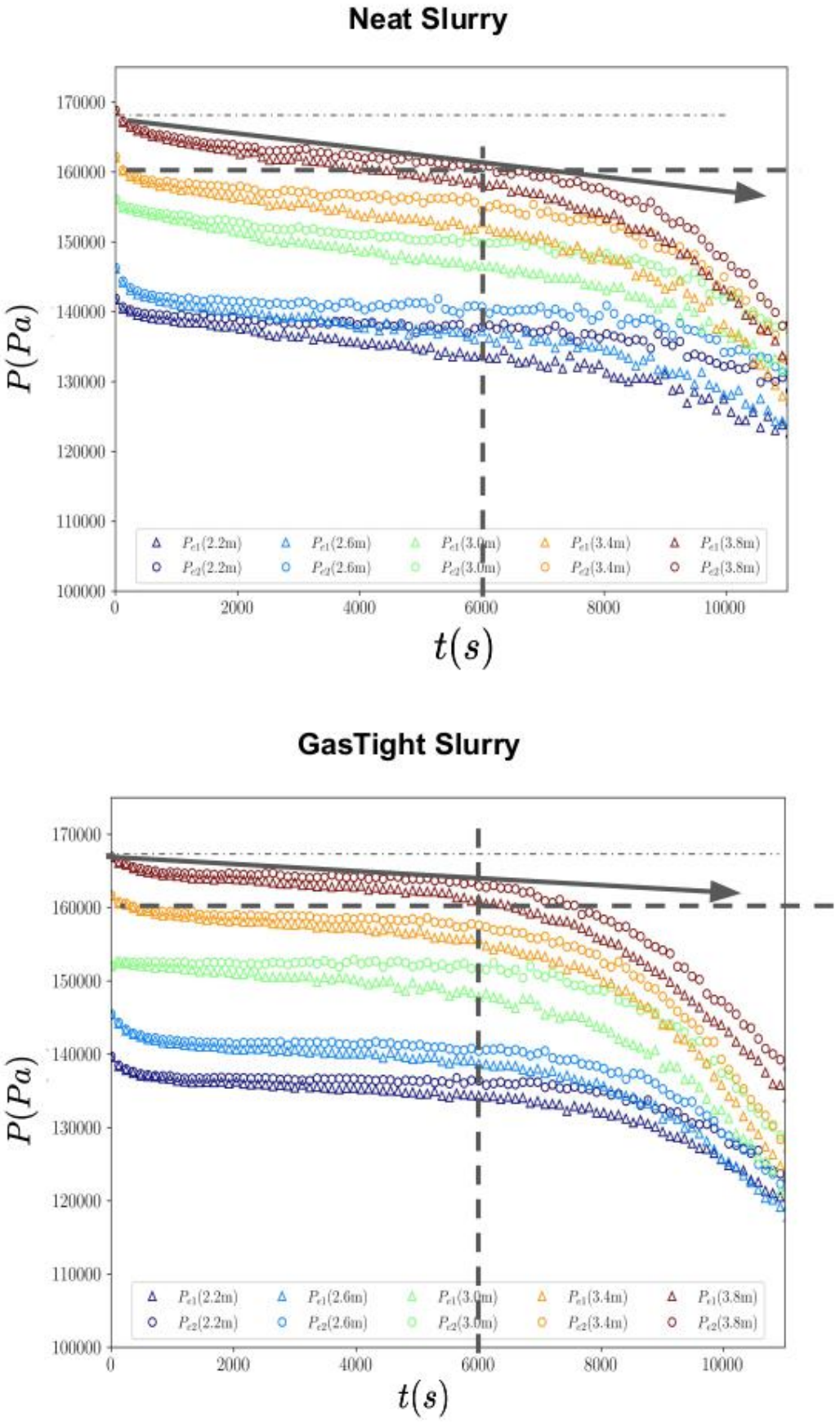

Figure 6.11: GasTight and Neat Slurries pressure test: Gelation slope comparison.

PUC-Rio - Certificação Digital Nº 1612794/CA

One interesting aspect of this apparatus is the possibility to retrieve the cement annular column after each test, without damaging any parts of the PWS. Its modular structure, composed by independent and interchangeable modules, can be opened with the aid of an hydraulic jack, and the depth sections of cement are exposed. Although this is not the objective of this work, this preserved cured sheath could be used to generate compression tests specimens, or even analyzed using micro-tomography. Figure 6.12 shows some pictures that illustrate this process.

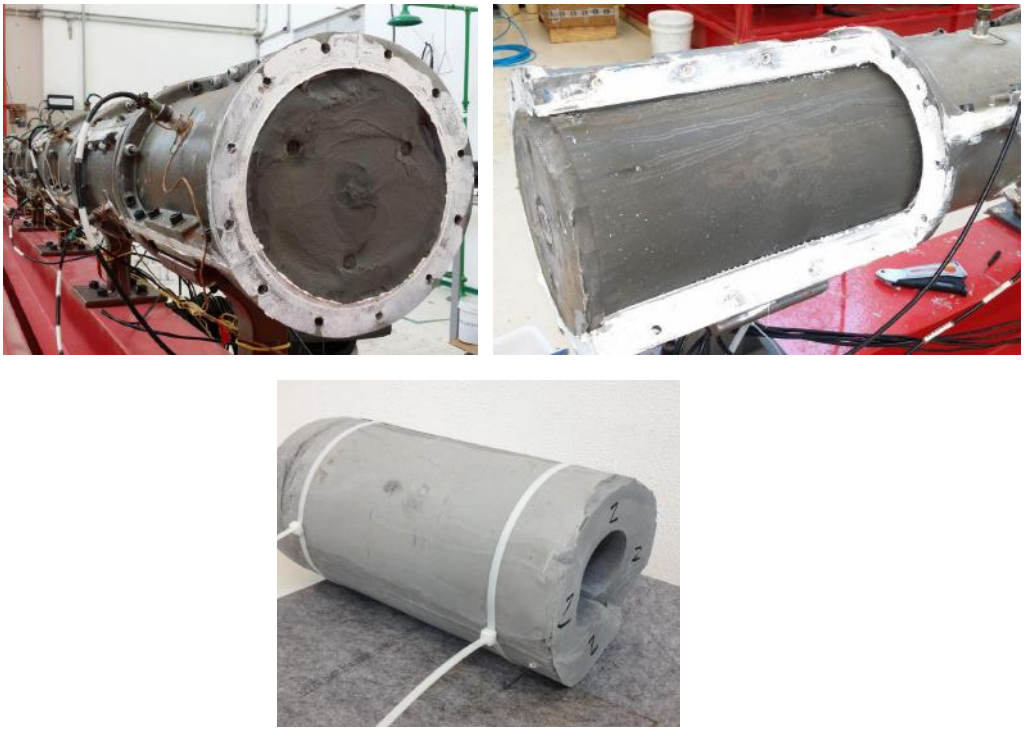

Figure 6.12: Preserved cement sheath.

6.2 Numerical Results

In the current section, the developed numerical model results are compared and contrasted against the GasTight slurry PWS tests. Good rheological data was obtained for this slurry. Therefore, this data is used for fitting the rheology model presented in Eq. 4-30 and collect the parameters, as showed in section 6.1.1.

On the following, some sensitivity tests are performed to evaluate the numerical model response to differences in its parameters.

PUC-Rio - Certificação Digital Nº 1612794/CA

6.2.1 Model Predictability

In this section, the finite element numerical model developed is used to predict the experimental pressure values measured in the PWS for the GasTight slurry in the presence of a fluid loss region, presented in Fig.6.7. It is worth mentioning that the Neat slurry was not evaluated due to the lack of rheological characterization.

As showed in Chapter 5, the boundary conditions passed as inputs are the inlet top pressure and the filtrate velocity at the fluid loss region wall. The top pressure is set correspondingly to an initial ToC of $4m$, plus atmospheric pressure. This input value varies with time, and it is automatic calculated based on the previous value and the mass of filtrate flowing out the permeable zone at each iteration. This calculation assumes two hypotheses: a developed flow above the highest simulated depth; and that, before the chemical reaction peak, ToC decays are mostly caused by the fluid loss.

To obtain the filtrate outlet velocity, first the fluid loss mass flow rate $\dot{m}_{FL}$ is calculated from experimental mass m_{FL} data acquired, by performing a numerical differentiation with respect to time. A linear ramp and an exponential decay functions are used to fit $\dot{m}_{FL}$ data points, and interpolate them. Finally, fitted filtrate flow rate as a function of time is used to calculate the outlet velocity input. Figure 6.13 shows the GasTight slurry tests filtrate mass average $m_{FL_{Avg}}$ and the experimental standard deviation $m_{FL_{Er}}$ shaded area. In the secondary axis, the filtrate mass flow rate $\dot{m}_{FL}$ is showed with the curve fitting values.

The rheological parameters obtained for the Lab Sample of the GasTight slurry, showed in section 6.1.1, are initially applied to the model. Figure 6.14 [108], shows the pressure simulated values for measured column heights, in comparison with pressure tests average and standard deviation values.

These qualitative results show the model capability on predicting the column height pressure value, as well as a pressure decay trend. However, predictions indicate a higher pressure value than experienced, specially along the early cure. As flow rate is imposed, high pressure values may indicate that simulated fluid viscosity is too high. Thus, the used rheological parameters are explored.

Figure 6.15 [108] shows the viscosity values measured with time for the two version of the GasTight slurry. Some guiding dashed lines and arrows are plotted to aid the visualization of the viscosity differences. It is interesting to compare the results from these graphs together with the flow curves showed in Figures 6.2 and 6.5.

PUC-Rio - Certificação Digital Nº 1612794/CA

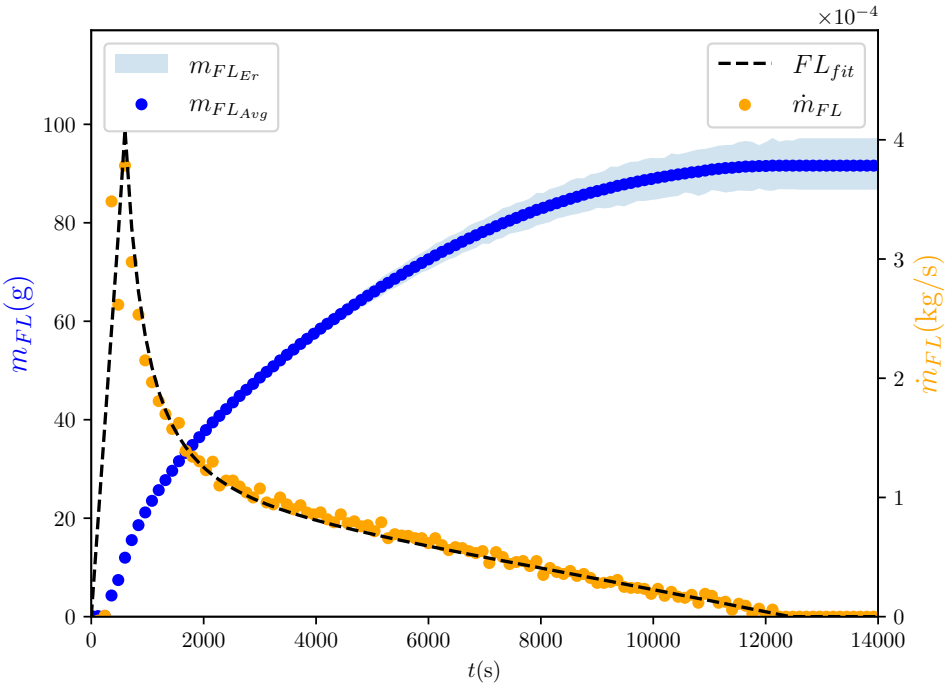

Figure 6.13: GasTight slurry test mass and mass flow rate with fit.

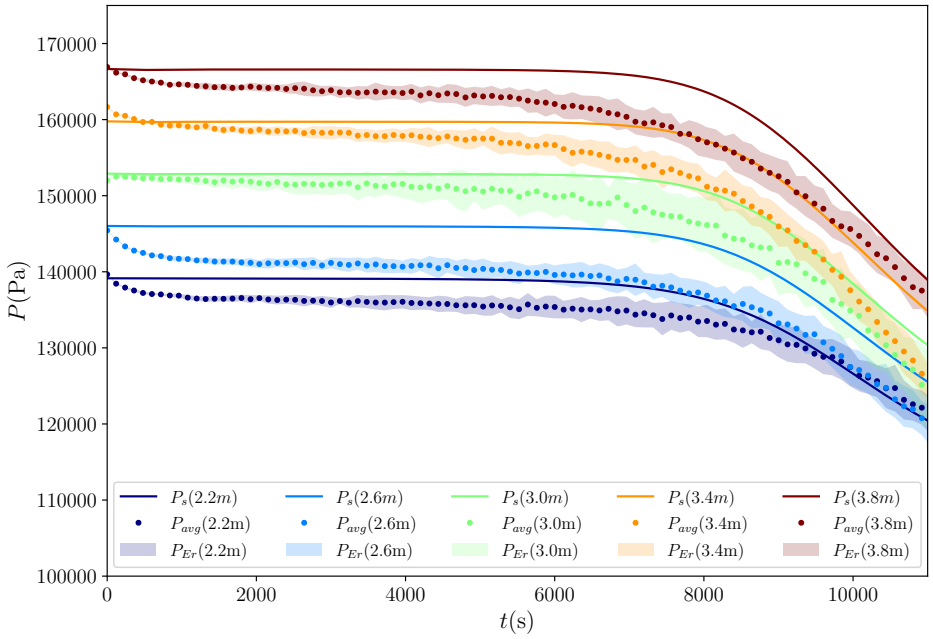

Figure 6.14: GasTight slurry tests compared with the model prediction. From [108]

PUC-Rio - Certificação Digital Nº 1612794/CA

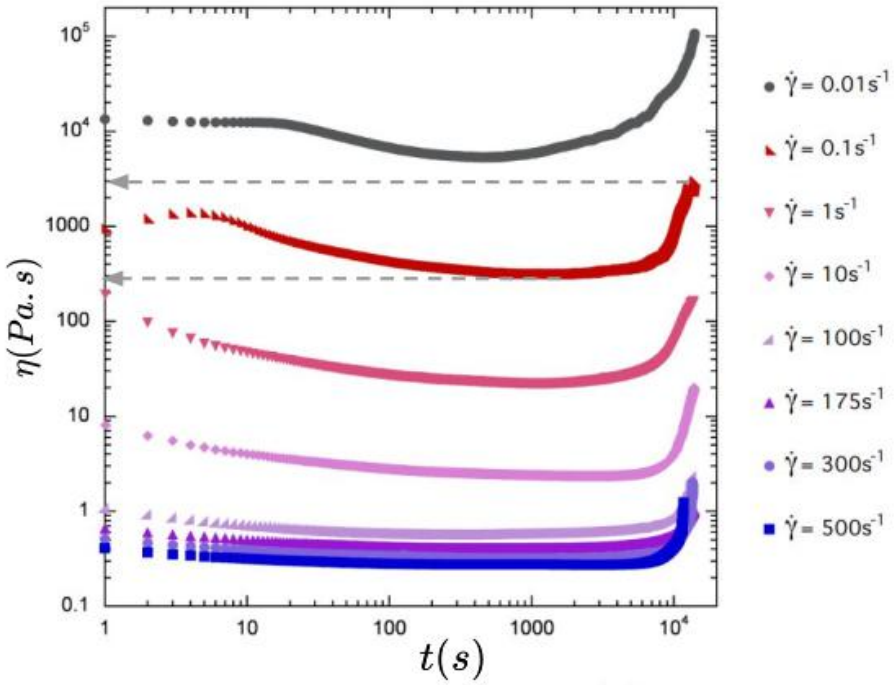

(a) GasTight Lab Sample

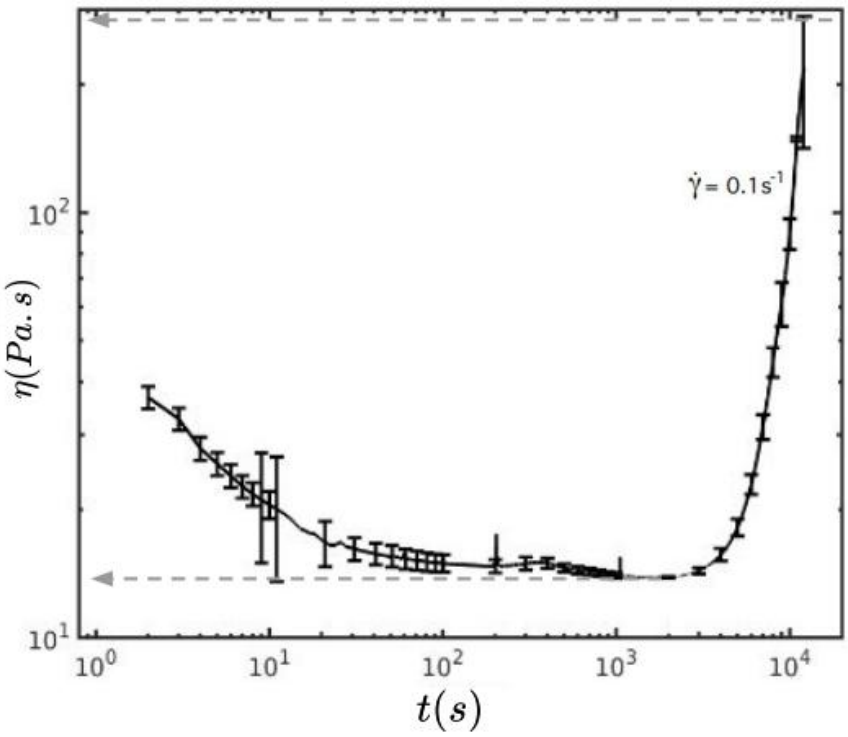

(b) GasTight PWS Sample

Figure 6.15: Gas Tight slurry viscosity η with time: (a) Lab Sample for all measured shear rates; (b) PWS Sample for the experiment characteristic shear rate.

From [108]

PUC-Rio - Certificação Digital Nº 1612794/CA

The overall viscosity values observed for the slurry prepared at the cement mixing unit are much smaller than the slurry mixed in the laboratory blender. Based on those curves, rheological parameters of the GasTight slurry PWS Samples should be: $K = 0.76\,Pa.s^n$, $n = 0.98$, $\tau_{y0} = 11\,Pa$, $T_t = 6000\,s$, $\eta_\infty = 0.292\,Pa$ and $\eta_0 = 700\,Pa.s$. Figure 6.16 shows both Lab and PWS Samples shear stress as a function of shear rate data, with their respective fit of the modified SMD rheological model, showed in Eq. 4-28.

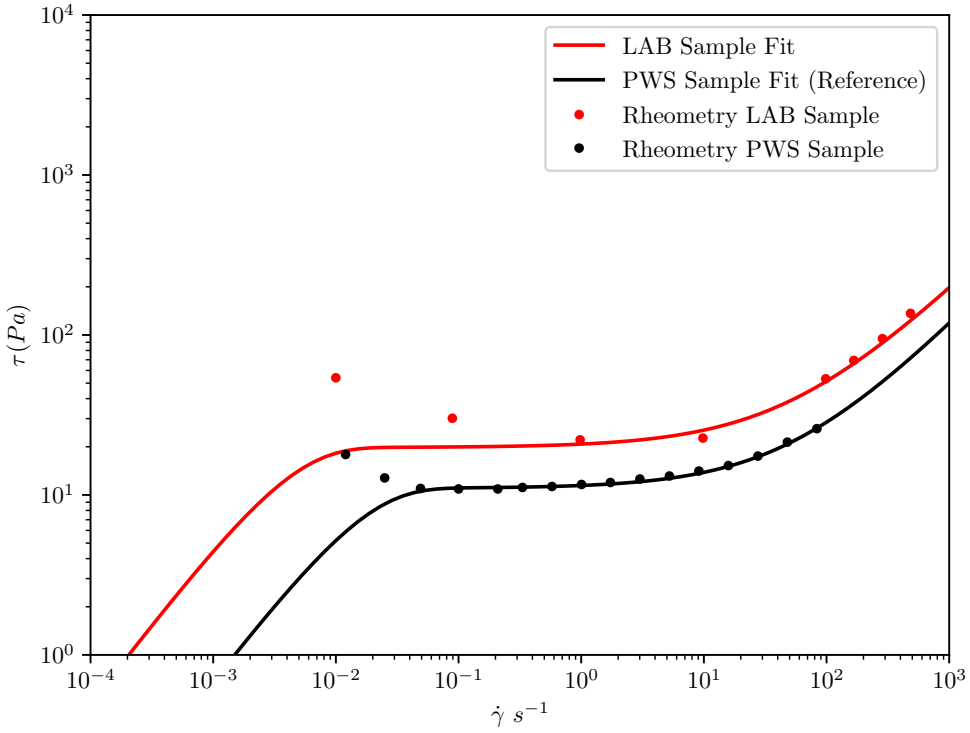

Figure 6.16: Flow curves and rheological model fitting for both samples.

Errors observed in collecting and weighting the large additives amounts used in the PWS Sample are estimated around 0.2%, and thus both samples can be considered equivalent regarding their composition. Therefore, flow curves differences can be attributed mainly to mixing regimen each sample was submitted to. This aspect is well known by the industry and some authors have deeply reviewed the influence of in the cement slurry rheology [192, 193], such that field samples are usually checked before displacement, and sometimes adjusted with any needed additives.

The pressure estimates are than performed for the same test, but with the PWS Sample rheological parameters. As showed in Figure 6.17 [108], the results present an earlier prediction of the decay with respect to the Lab Sample rheology.

PUC-Rio - Certificação Digital Nº 1612794/CA

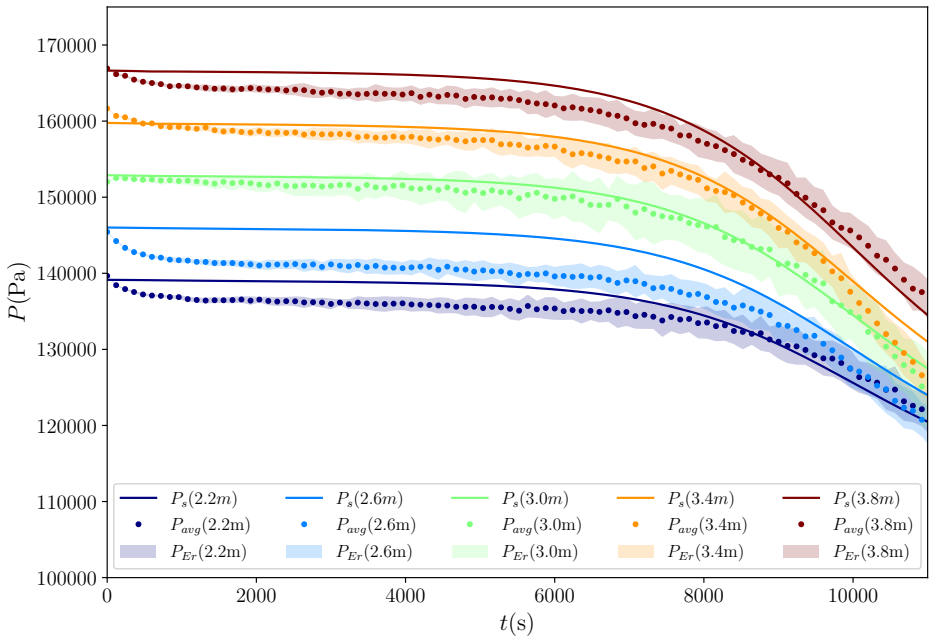

Figure 6.17: GasTight slurry tests compared with the corrected model prediction.

From [108]

The comparison between Figures 6.14 and 6.17 illustrate how using design slurry characterization values, without any field correction factors, can lead to prediction errors. The model also calculates the velocity 2D vector field and cement mass fraction fields along the simulated annular column. Although these variables were not measured in the performed experiments, this is a possibility for future studies, which may allow a richer understanding of the filter cake problem. Figures 6.18 and 6.19 show respectively the time evolution of the axial velocity v_z and of the cement mass fraction C_1. The simulated cement mass fraction could also be used to calculate local water-to-cement ratio values, which in the literature [38, 8] is showed to be correlated with the mechanical properties of cured cement.

PUC-Rio - Certificação Digital Nº 1612794/CA

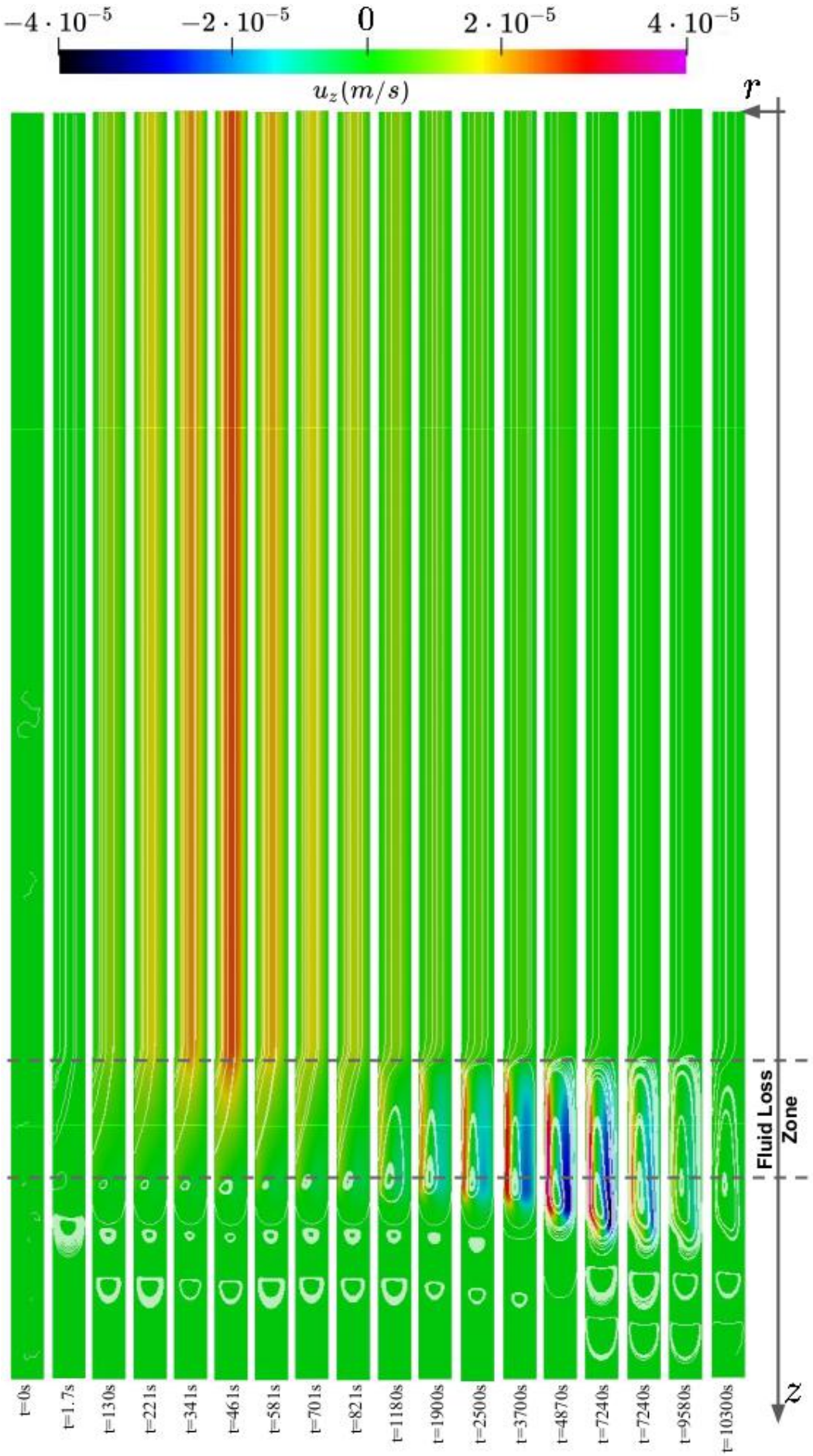

Figure 6.18: Velocity in axial direction field evolution with time.

PUC-Rio - Certificação Digital Nº 1612794/CA

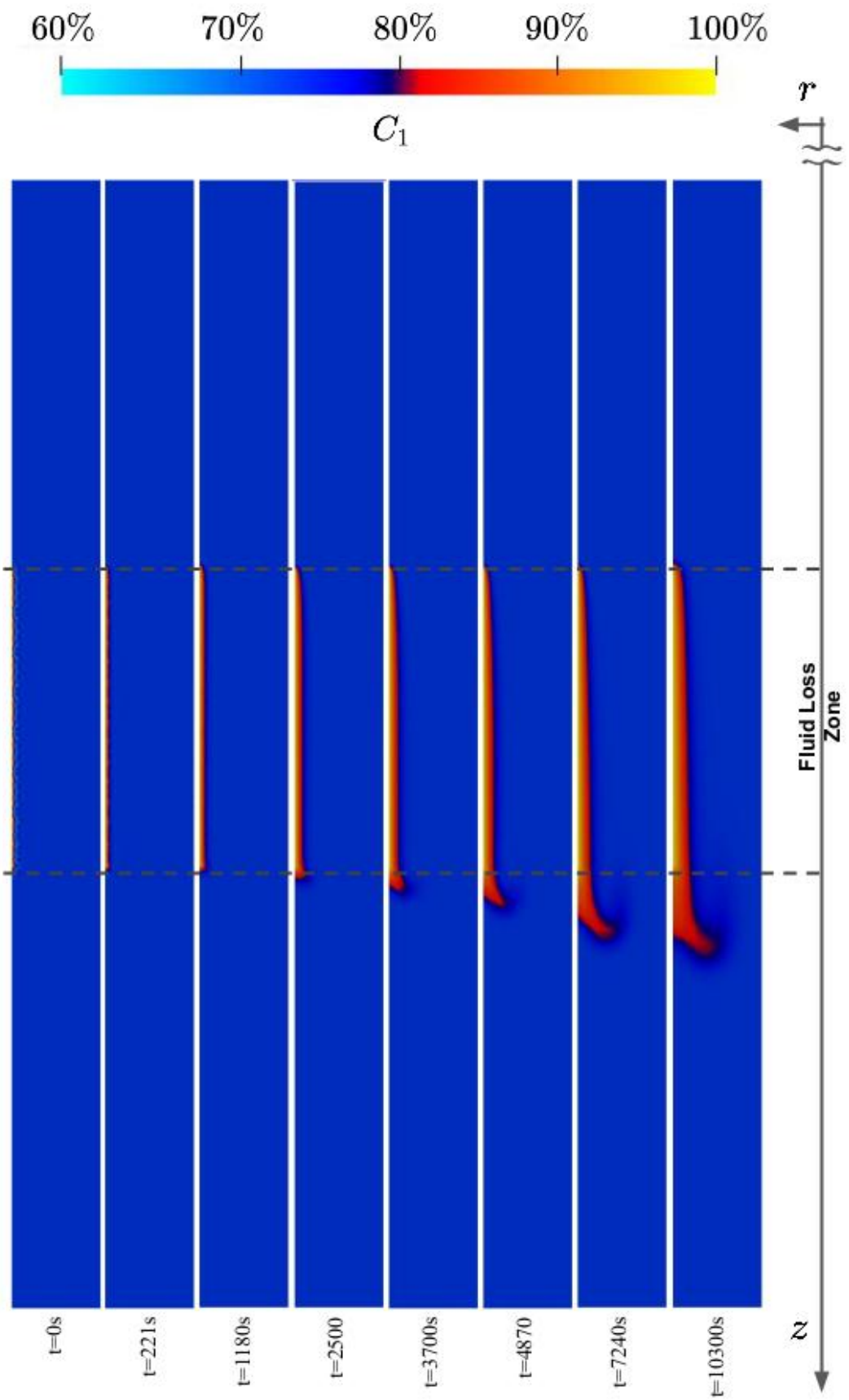

Figure 6.19: Cement mass fraction field evolution with time.

PUC-Rio - Certificação Digital Nº 1612794/CA

In Fig. 6.18, the velocity fields are obtained with the GasTight Sample rheology and inputting the same well geometry and same fluid loss flow rate with time. It's possible to observe that the maximum axial velocity v_z is around $2.5{\cdot}10^{-5}\,m/s$. Given that velocity and annular gap, the simulated characteristic flow shear stress is always below the fluid yield stress. Thus, in the experimental case, the slurry viscosity is always within the Newtonian plateau η_0. This can be confirmed by the axial velocity profile shapes, plotted for the depth of $2.2m$ in Fig. 6.20.

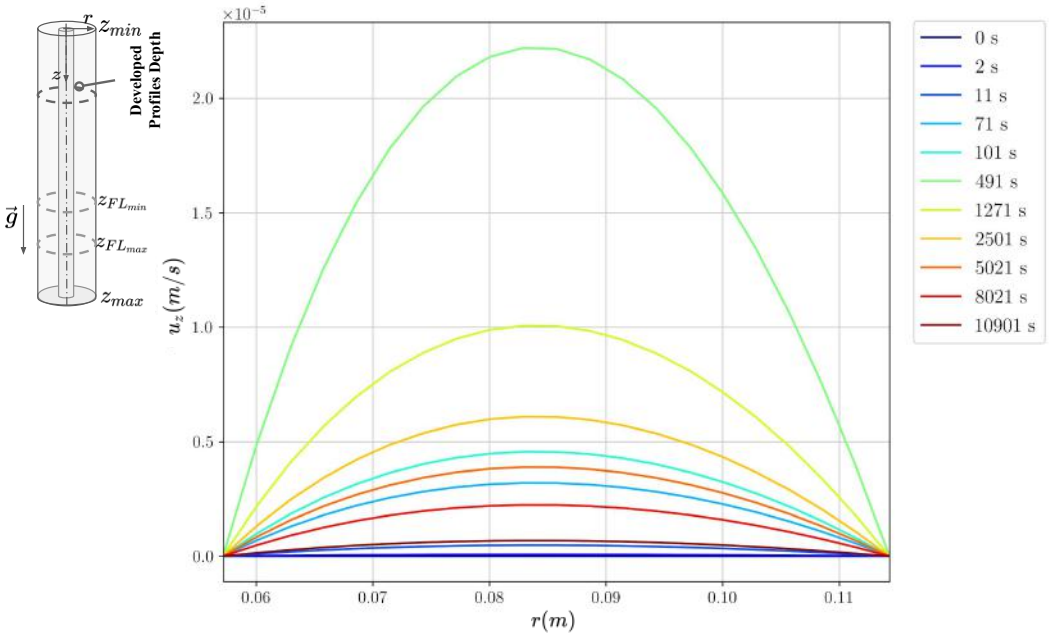

Figure 6.20: Velocity in axial direction evolution with time at depth $2.2m$.

It's also possible to observe, a recirculation close to the fluid loss region. This is caused by the change in the flow direction entering from the well top and exiting through the fluid loss region. Figures 6.21 and 6.22 show respectively the axial and radial velocity radial profiles in the middle of the fluid loss region, at column depth of $3.6m$.

Another interesting behavior, present in the experiments but yet not reproduced by the model, is the asymptotic decay from the initial pressure towards an apparent plateau, from which the gelation slope actually starts. Two different aspects might explain why the model did not capture this behavior.

The first is related to the fluid loss flow rate fitting function, which was fitted linearly. As very few points are experimentally measured within that period, maybe the linear fit is not the best to represent the real flow rate elevation curve.

PUC-Rio - Certificação Digital Nº 1612794/CA

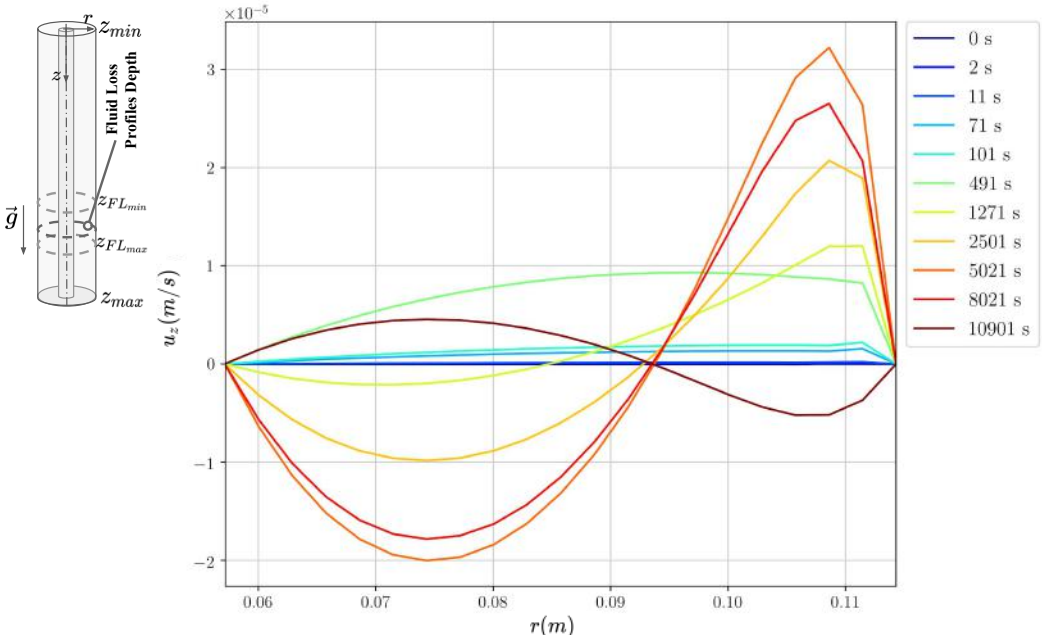

Figure 6.21: Velocity in axial direction evolution with time at depth $3.6m$.

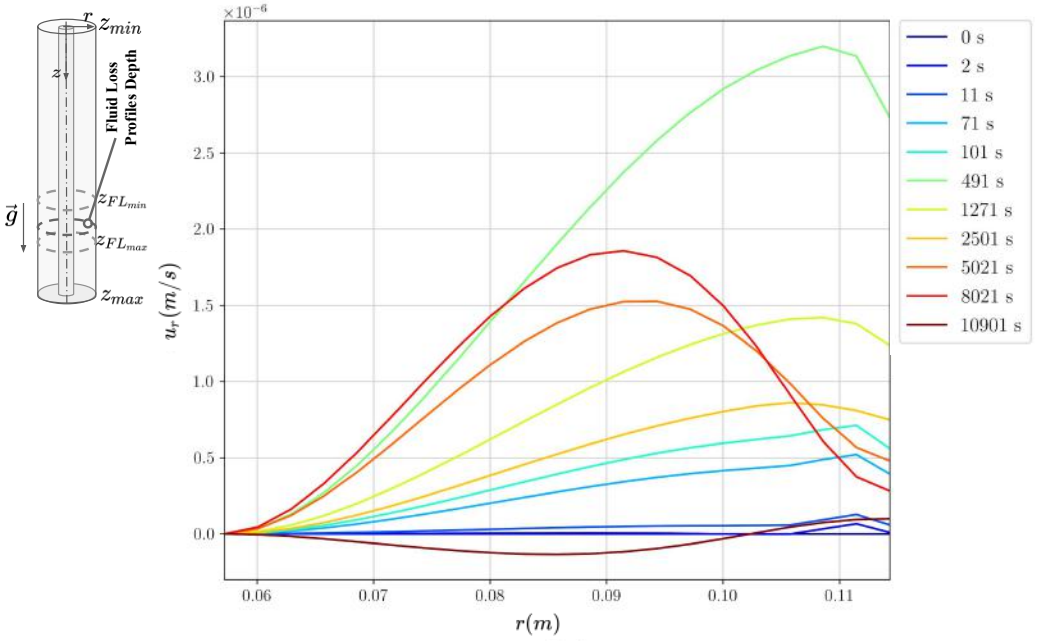

Figure 6.22: Velocity in radial direction evolution with time at depth $3.6m$.

PUC-Rio - Certificação Digital Nº 1612794/CA

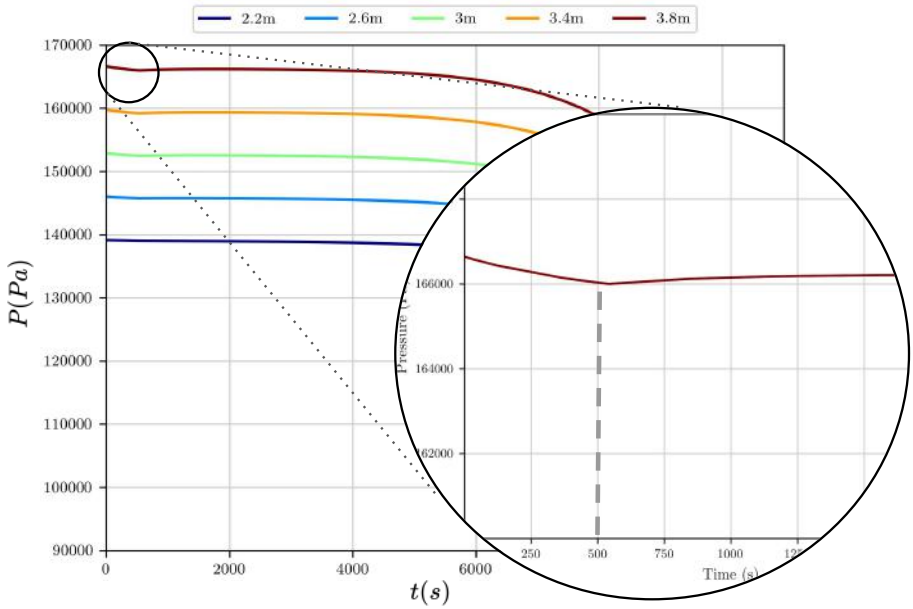

Figure 6.23: Pressure simulation for considering $\eta_0 *$ 10 times higher than the fitted value of η_0. Detail shows similar early pressure drop due to increasing flow rate.

With a linear increase of flow rate, and the viscosity around the Newtonian Plateau, the increase in the differential pressure needed to drive that flow is also linear, which translates in an subtle early drop in the absolute pressure showed in the graphs. Although faded by the experimental case particular properties, this correlation can be better observed increasing parameter η_0^* 10 times and zooming in the initial moments of the pressure curve at depth $3.8\,m$, as showed in Fig. 6.23.

Comparing with Fig. 6.13, the absolute pressure drop coincides with imposed flow rate ramp, and slightly decreases at the same moment, just after $500s$. If $\tau < \tau_y$ during this period of increasing velocity, viscosity is constant in the Newtonian plateau, η_0. Thus, if pressure variation ΔP was simply due to velocity, it should not increase asymptotically. However, as it can be observed in Fig. 6.3, in the case without fluid loss, this initial asymptotic pressure drop is present, although much more subtle. Therefore, a combined effect between velocity increase and thixotropic transient viscosity, might be the cause of this smooth early drop not being fully captured by the model.

During the experiments, the fluid loss flow rate did not start to ramp up immediately after cement placement, as in the simulation. The placed slurry stayed in the annulus for a couple minutes, until all pressure sensors presented a stable measurement. Only then, the fluid loss module valve was opened and this is the time $t = 0$ showed in all graphs.

PUC-Rio - Certificação Digital Nº 1612794/CA

A thixotropic slurry that has been stopped for a while, is in a micro-structure build-up process, assuming different rheological properties than the ones simulated. As time goes by, the micro-structure breaks down and steady state viscosity values can be achieved. That dynamic process would change the pressure drop shape.

6.3 Model Sensitivity Analysis

In this final results section, a sensitivity analysis is performed with the model's main parameters. Three different categories of parameters are treated separately: fluid loss flow rate, transition time and rheological parameters.

The pressure prediction for each parameter changed is plotted with respect to the GasTight PWS Sample slurry, which is used as the reference. For all further analyses P_S (plotted with a solid line) is the pressure prediction of the evaluated parameter sensitivity, and P_R (plotted with a dashed line) is the pressure prediction of the reference case. Also in order to facilitate understanding, the parameters changed for that particular analysis are represented with a superscript $*$.

6.3.1 Fluid loss flow rate

The first parameter tested is the fluid loss amount itself. A multiplying factor, f_{FL}, is applied to scale the flow rate fitted curve. The reference case, where $f_{FL} = 1$, already presents reduced fluid loss, and thus, only higher factors were tested. Figures 6.24 and 6.25 show the pressure prediction for flow rate factors $f^*_{FL} = 10$ and $f^*_{FL} = 20$, respectively.

One interesting point is to analyze the velocity profiles change with the increase of flow rate. Figure 6.26 shows the reference case, $f^*_{FL} = 10$ and $f^*_{FL} = 20$ velocity profiles for comparison. As observed, at higher fluid loss flow rates, the velocity profiles far from the fluid loss region become less like the Poiseuille profile, and more like a plug-flow, characteristic of viscoplastic fluids [194]. This happen because at these higher flow rates, the characteristic shear rate range is not also a bit higher, and shear stress is around the yield stress. Therefore, the viscosity η assume different values along the radius. Lower than η_0 close to the walls, and around η_0 far from the walls.

PUC-Rio - Certificação Digital Nº 1612794/CA

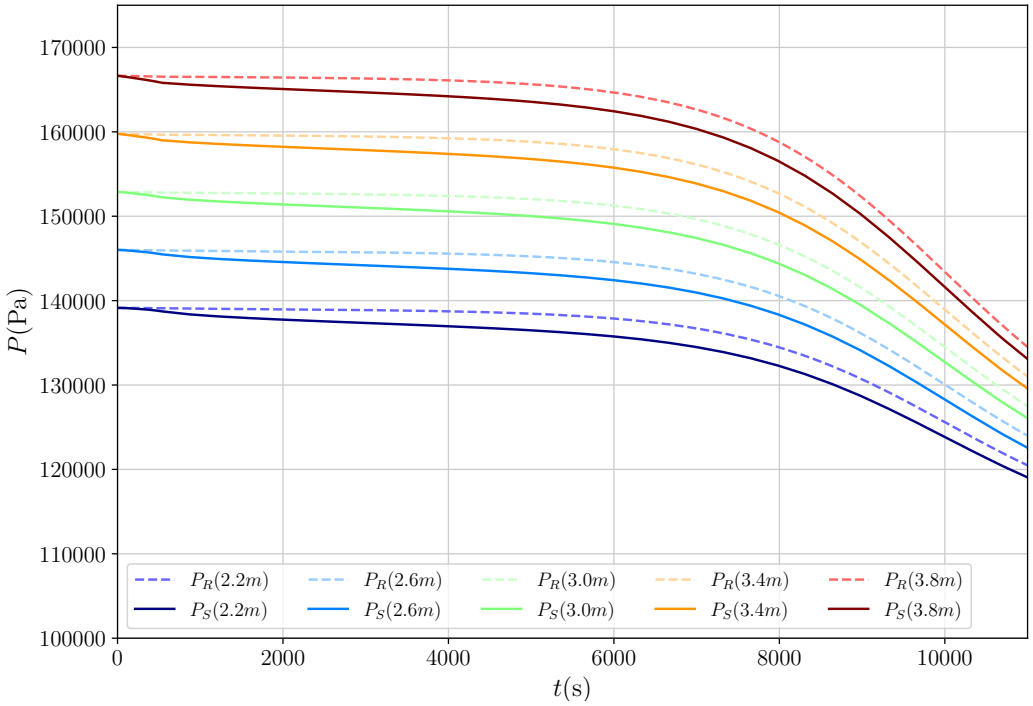

Figure 6.24: Pressure prediction comparison: solid line for $f^*_{FL} = 10$ and dashed line for the reference case.

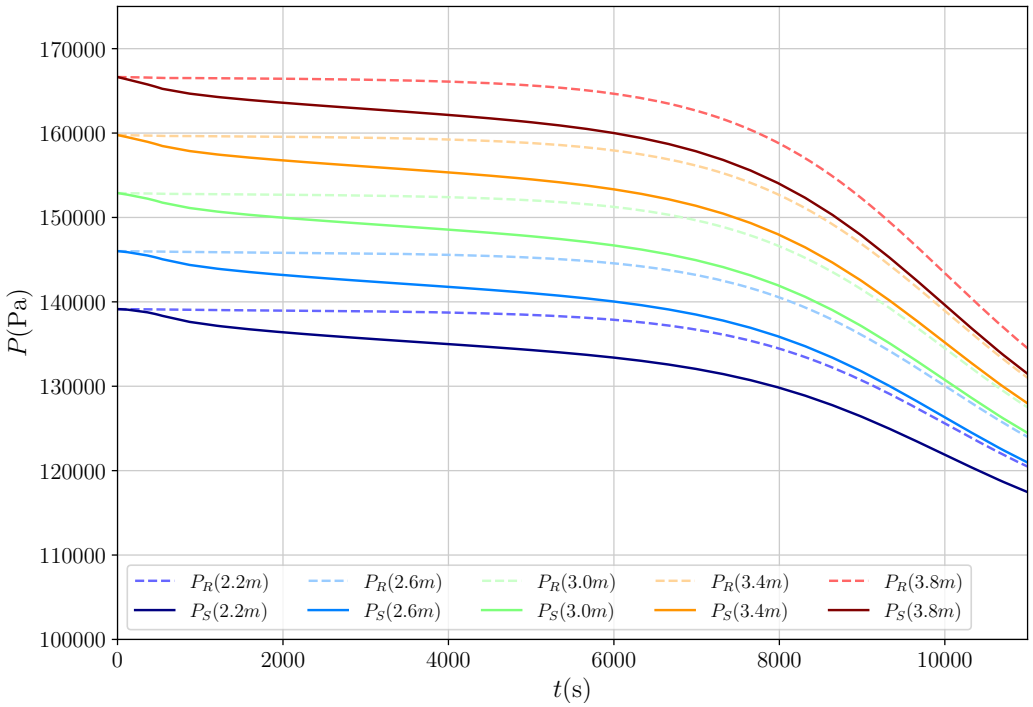

Figure 6.25: ressure prediction comparison: solid line for $f^*_{FL} = 20$ and dashed line for the reference case.

PUC-Rio - Certificação Digital Nº 1612794/CA

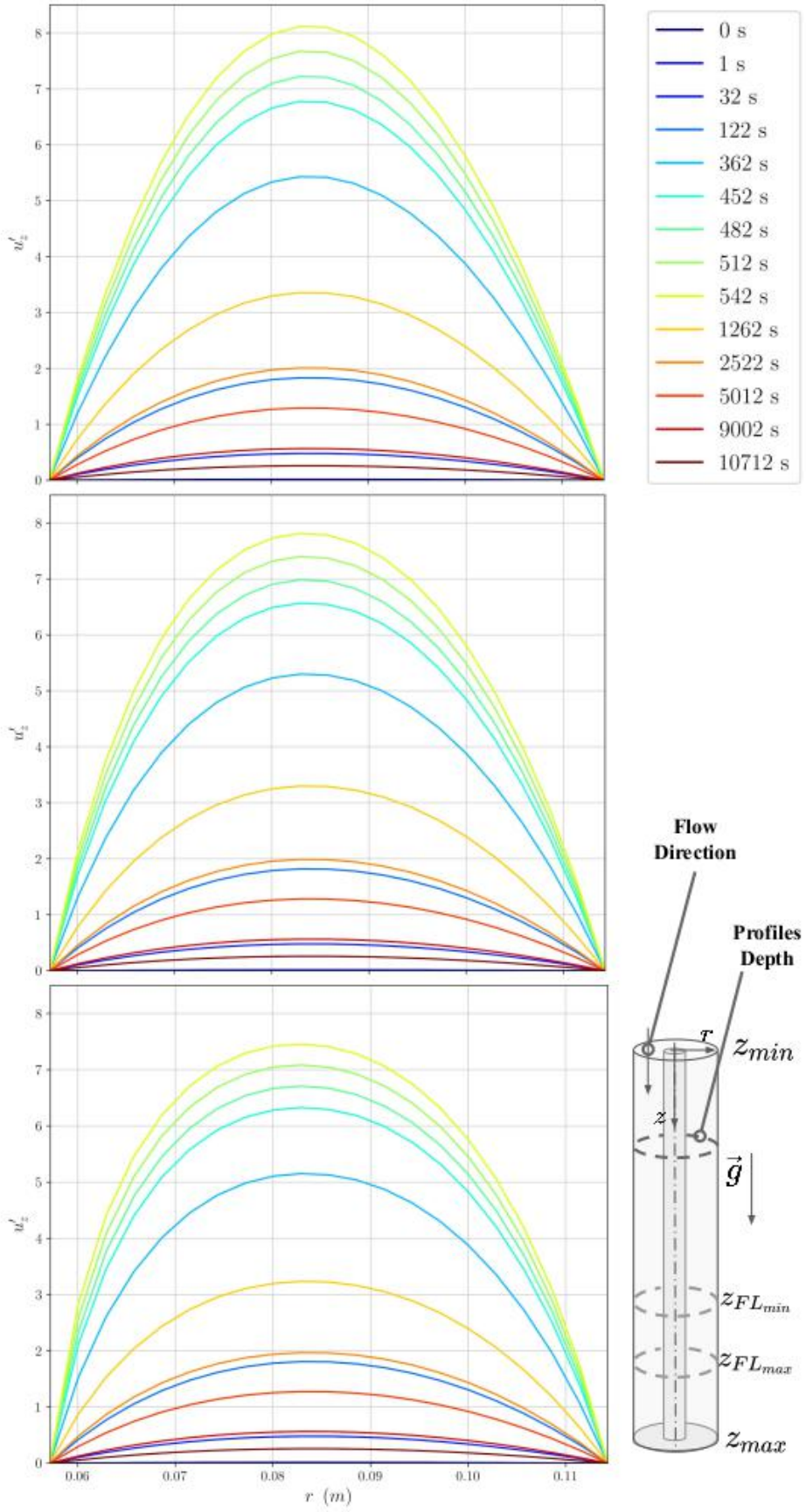

Figure 6.26: Velocity profiles at 2.2m depth. From top to bottom: $f_{FL} = 1$, $f^*_{FL} = 10$ and $f^*_{FL} = 20$

PUC-Rio - Certificação Digital Nº 1612794/CA

6.3.2 Thickening Time

The slurry transition time and the shrinkage characteristic time are also parameters of the model. The transition time T_t triggers an irreversible increase in τ_y and η_0, that is used to model the cement cure. This moment is also named viscosity build-up. The measured values for the GasTight PWS slurry of the transition time measured is $6000\,s$. Figure 6.27 shows viscosity as a function of time, at a characteristic shear rate of $\dot{\gamma} = 0.001 s^{-1}$, for each evaluated value of T_t^*.

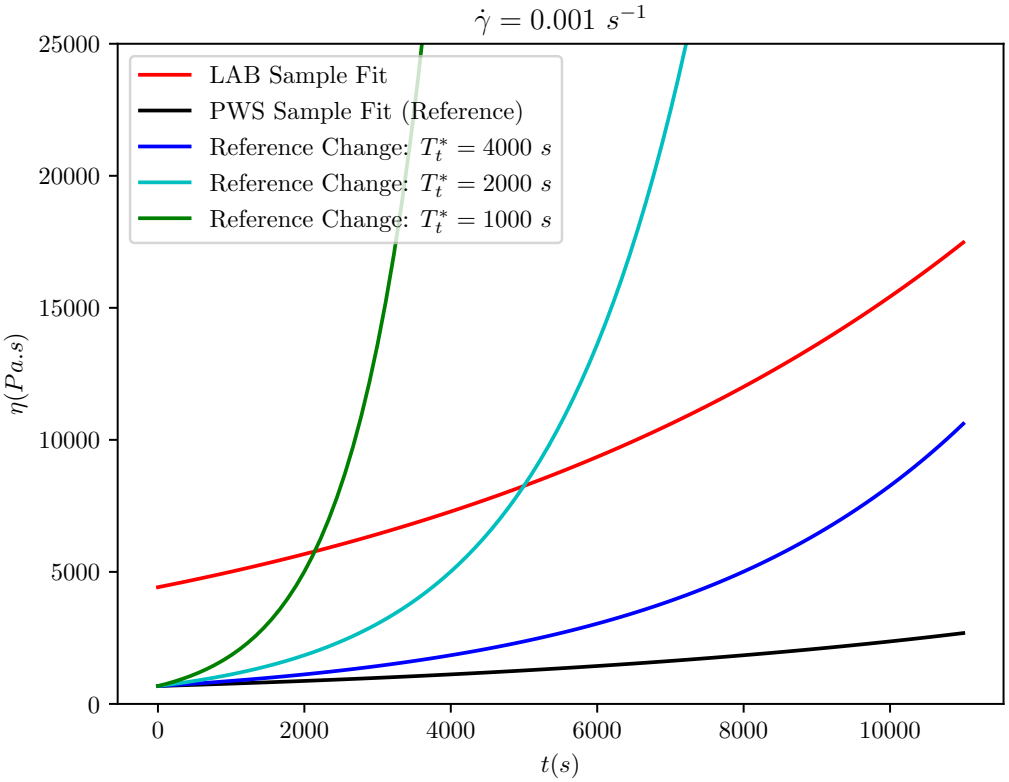

Figure 6.27: Viscosity as a function of time for $\dot{\gamma} = 0.001\,s^-1$: comparison between PWS and Lab Samples with $T_t^* = 4000\,s$, $T_t^* = 2000\,s$ and $T_t^* = 1000\,s$

It is possible to observe the viscosity effects triggered by the different T_t. For comparison, the viscosity curves $\eta(t)$ for PWS and Lab Samples are calculated with the SMD model fit showed in Eq. 4-27, and plotted together.

Figures 6.31 and 6.32 presents the evaluated transition times. As the filtrate flow rate decreases very fast in the experimental case, the pressure prediction for $T_t^* = 4000\,s$ and $T_t^* = 1500\,s$ did not diverge much from the reference. On the other hand, the cases with and $T_t^* = 1000\,s$ imposed a significant change in the predicted pressure profiles. Impact in pressure of $T_t^* = 1500\,s$ and $T_t^* = 1000\,s$ can be seen respectively in Figures 6.28 and 6.29

PUC-Rio - Certificação Digital Nº 1612794/CA

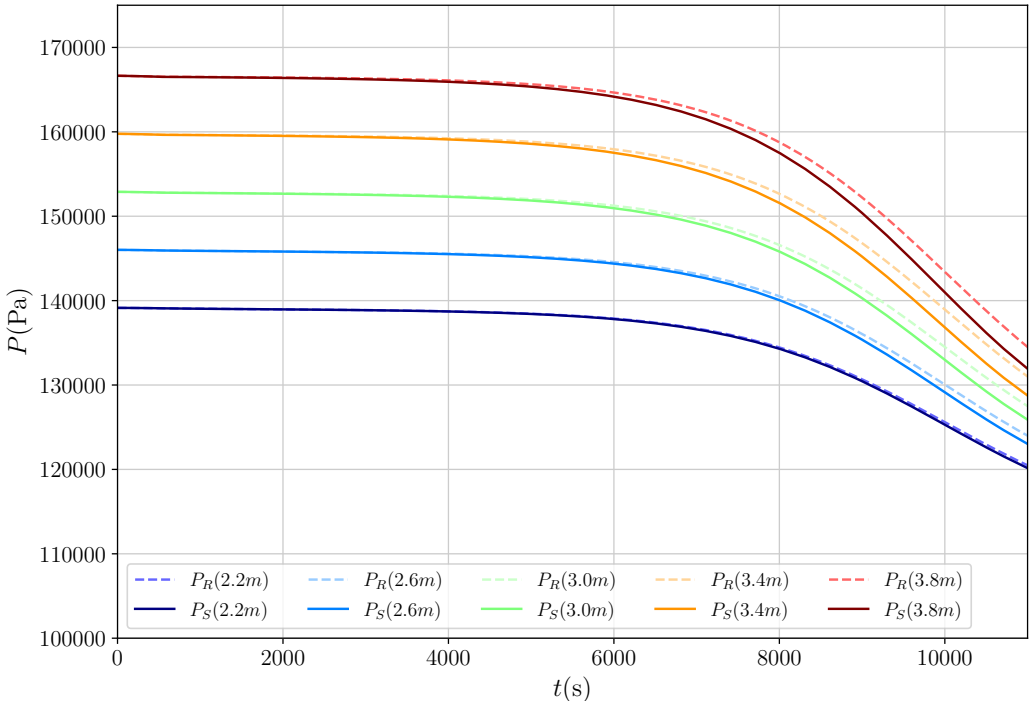

Figure 6.28: Pressure prediction comparison: solid line for $T_t^* = 2000\,s$ and dashed line for the reference case.

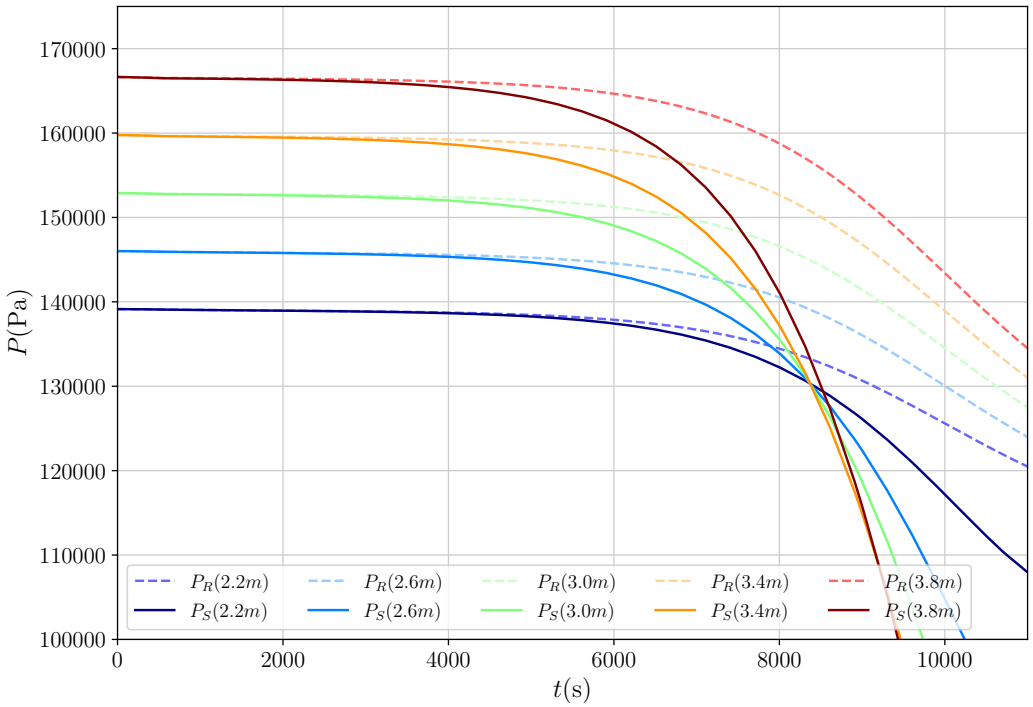

Figure 6.29: Pressure prediction comparison: solid line for $T_t^* = 1000\,s$ and dashed line for the reference case.

PUC-Rio - Certificação Digital Nº 1612794/CA

Evaluating these curves, the tested curing times might seem unrelated to field values, specially thinking about all slurry displacement necessary in a real well cementing job. For the experimental case flow rate velocity, higher viscosity increases are needed to impact the pressure drop. This is why the transition time happening away from the period of fluid loss peak velocities ($T_t* > 3000\,s$ for this case) seems to make no difference in the pressure.

This way, advancing the transition time may not be the best alternative to handle fluid loss problems. Despite the fast viscosity buildup might be able to reduce or stop the flow, the risk of poor displacement is too high. Nevertheless, a slow viscosity build-up triggered early, as the one showed in Fig. 6.28, would increase the pressure drop, before fluid viscosity is high enough to withhold possible formation influxes.

The shrinkage characteristic time T_c was measured during the slurry design phase, and occurs after the viscosity build-up, at around $10000\,s$. As this thesis is focused in the early cure mechanisms, T_c was not vastly explored.

6.3.3 Rheological parameters

Continuing an analysis briefly mentioned in Section 6.2.1, the first rheological parameter to be evaluated is the Newtonian viscosity plateau η_0, achieved at lower shear-rates. Before executing the pressure prediction, the rheological effects of the tested values are analyzed.

Within the range of possible values, the tested values of $\eta_0^* \in 70, 7000, 14000\,Pa.s$. The values of η_0^* which can affect the reference case are evaluated according to the experiment range of $\dot{\gamma}$.

Figures 6.30 and 6.31 show respectively the shear stress and the viscosity curve as a function of $\dot{\gamma}$. The shear rate experiment range appears shaded, and for comparison, PWS and Lab Samples fits are plotted together as reference.

It's possible to observe that for $\eta_0^* = 70\,Pa.s$, within that range of $\dot{\gamma}$, viscosity η is practically constant at that Newtonian plateau. Evaluating the pressure predictions for those values of η_0^*, that hypothesis was confirmed. $\eta_0^* = 70\,Pa.s$ showed no significant change in pressure profiles, and therefore it is not relevant to present it. Pressure prediction values for $\eta_0^* = 7000\,Pa.s$ and $\eta_0^* = 14000\,Pa.s$ are showed respectively in Figures 6.32 and 6.33.

Again, for this experimental case, the small velocities imply in low shear rate values. Despite the large viscosity change, at low shear stress regimen, the small pressure drop observed is close to the expected. To demonstrate that, a force balance is performed for the annular control volume, and it results in

PUC-Rio - Certificação Digital Nº 1612794/CA

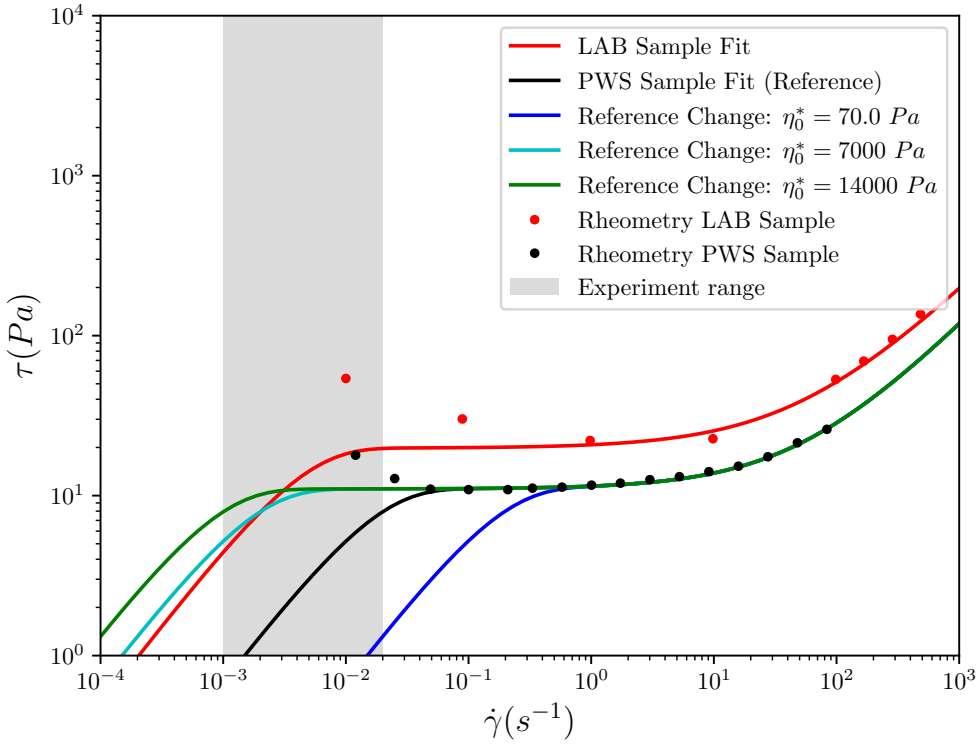

Figure 6.30: Shear stress comparison: LAB and PWS Samples *vs* η_0^* of 70, 7000 and 14000 $Pa.s$

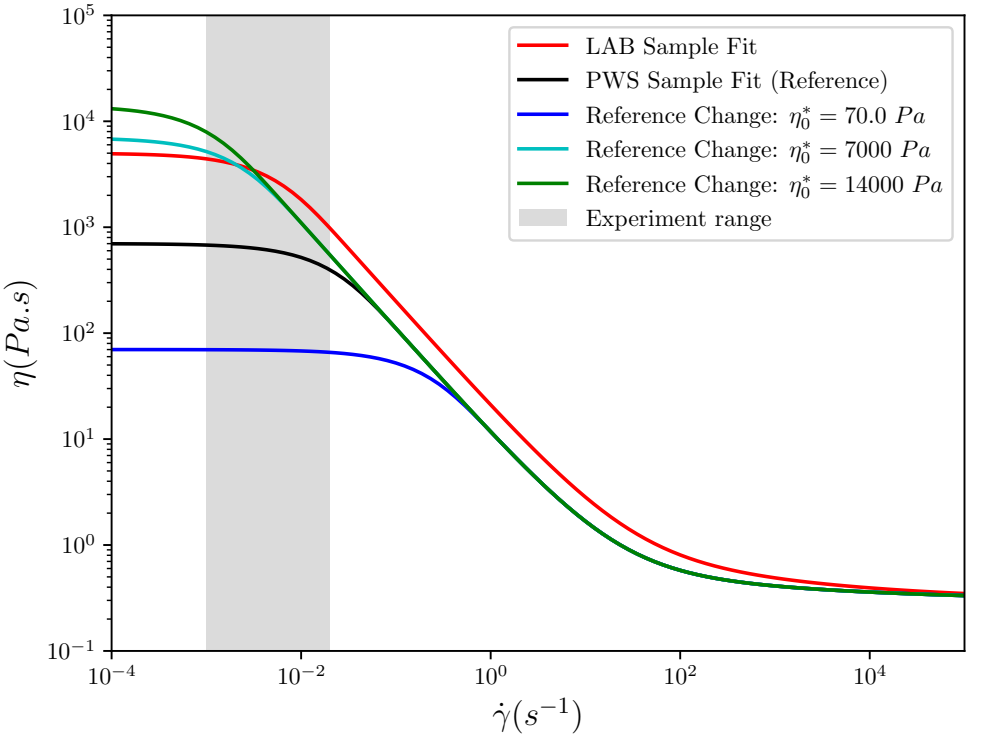

Figure 6.31: Viscosity comparison: LAB and PWS Samples *vs* η_0^* of 70, 7000 and 14000 $Pa.s$

PUC-Rio - Certificação Digital Nº 1612794/CA

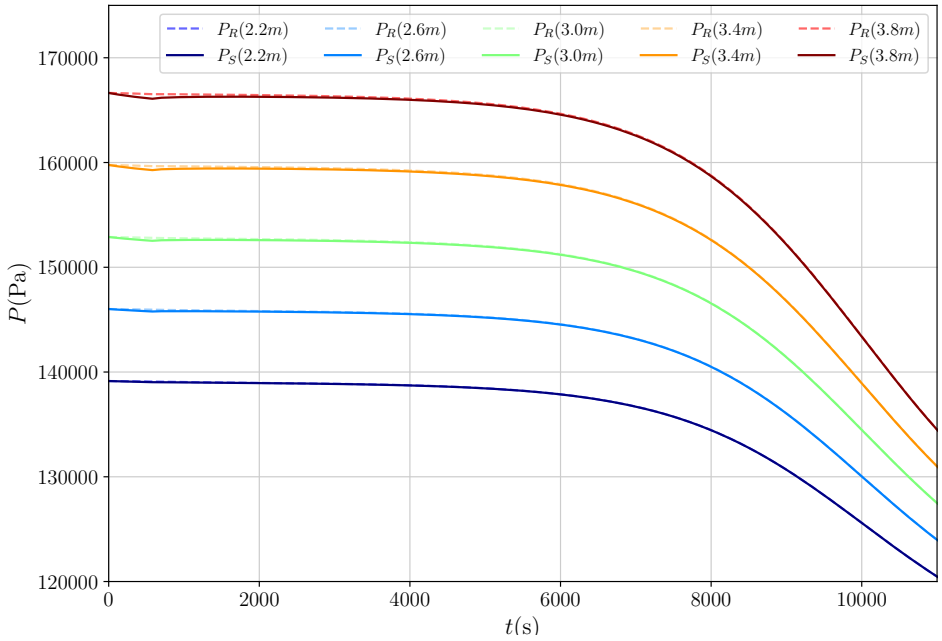

Figure 6.32: Pressure prediction comparison: solid line for $\eta_0^* = 7000\,Pa.s$ and dashed line for the reference case.

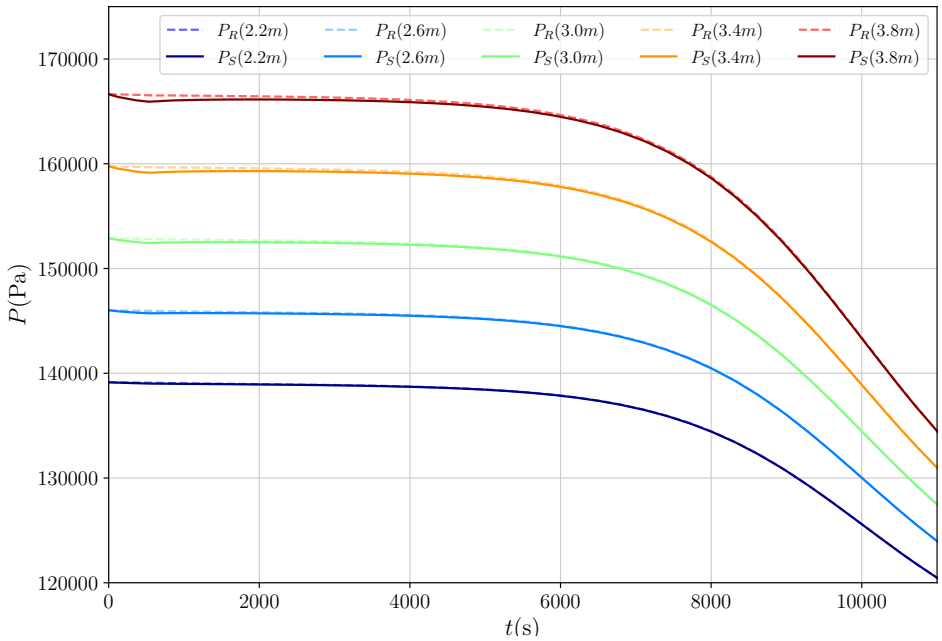

Figure 6.33: Pressure prediction comparison: solid line for $\eta_0^* = 14000\,Pa.s$ and dashed line for the reference case.

PUC-Rio - Certificação Digital Nº 1612794/CA

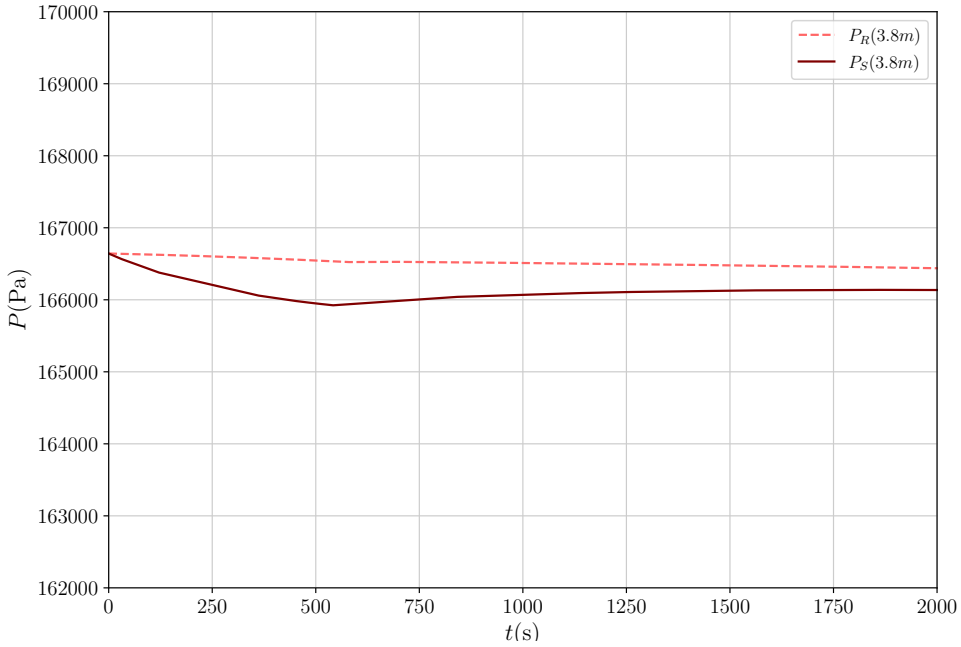

Figure 6.34: Pressure prediction comparison detail: solid line for $\eta_0^* = 14000\,Pa.s$ and dashed line for the reference case.

PUC-Rio - Certificação Digital Nº 1612794/CA

Eq. 6-1. It correlates the pressure loss for a Newtonian, developed and laminar flow with the shear stress at the walls.

$$h_f = \frac{4\tau_w L_c}{\rho g D_h} \tag{6-1}$$

where g is the gravity acceleration; ρ is the fluid density; h_f is equal to the pressure loss $\frac{\Delta P}{\rho g}$; D_h is the hydraulic diameter; L_c is annulus length, from the fluid loss region to the depth evaluated; and τ_w is the shear stress at the walls. τ_w can be approximated, within this Newtonian plateau, as $\eta_0 \frac{\partial u_z}{\partial r}$.

Replacing the values for a slurry with $\eta_0 = 700\,Pa.s$ and another with $\eta_0 = \eta_0^* = 14000\,Pa.s$, the calculated pressure drop difference is of $439\,Pa$. This estimate is close to what can be observed analysing the zoomed pressure predictions difference, showed in Fig. 6.34. Lower η_0 values were also tested, but no significant changes in pressure were observed, for the same reasons mentioned above.

The next rheological parameters analyzed are the consistency index K and the power law index n. Again, before running the pressure predictions, the rheological model fits are analyzed for the evaluated parameters. Initially, the consistency index K is evaluated, and Figures 6.35 and 6.36 show respectively the shear stress and viscosity as a function of shear rate, for K^* values tested.

As it can be observed, the changes happen outside the shear rate experimental range. Accordingly, even for the highest values evaluated, no significant change is observed in the pressure prediction, as it can be seen in

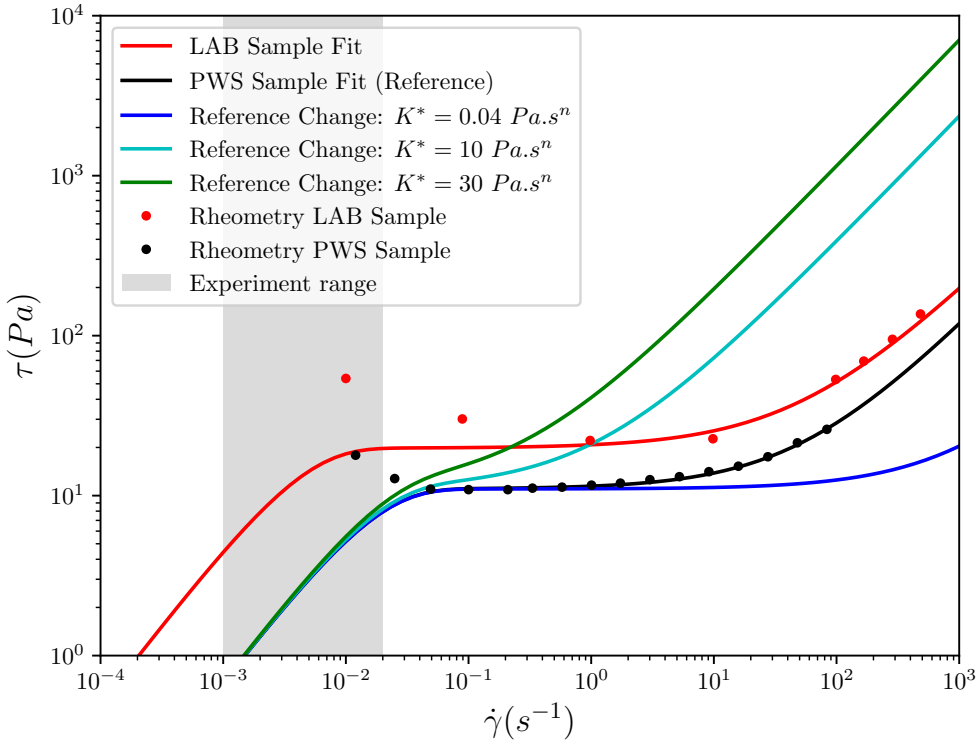

Figure 6.35: shear stresss comparison: LAB and PWS Samples *vs* K^* of 0.04, 10 and 30 $Pa.s^n$

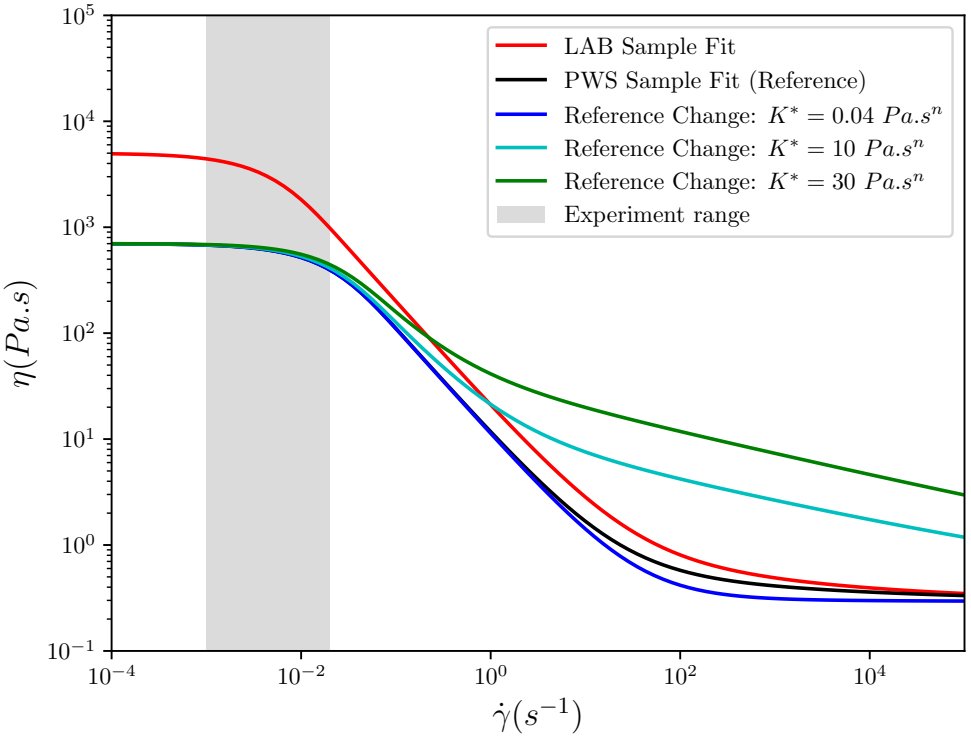

Figure 6.36: Viscosity comparison: LAB and PWS Samples *vs* K^* of 0.04, 10 and 30 $Pa.s^n$.

PUC-Rio - Certificação Digital Nº 1612794/CA

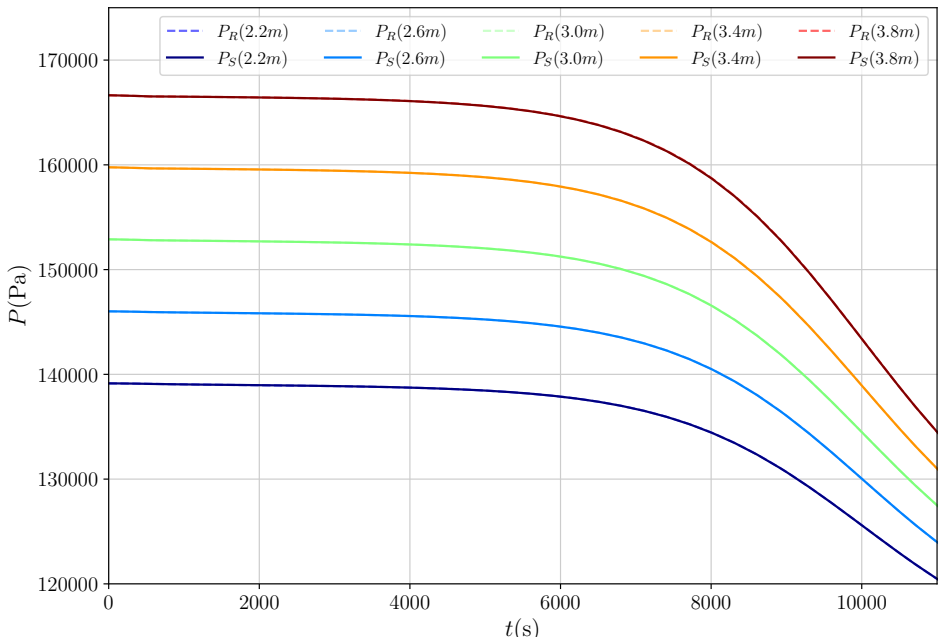

Figure 6.37: Pressure prediction comparison: solid line for $K^* = 30\,Pa.s^n$ and dashed line for the reference case.

Fig. 6.37.

The same behavior is observed evaluating changes with the power law index n. Figures 6.38 and 6.39 show respectively the shear stress and viscosity as a function of shear rate, for $n^* = 0.29$, $n^* = 0.55$ and $n^* = 0.9$.

Again, for this test range of shear rate, the individual change at the power law index n has no apparent effect on pressure predictions, as showed in Fig. 6.40

The final sensitivity analysis is performed with the initial yield stress of the slurry, τ_{y0}. This is one of the parameters that increases exponentially with time in this curing model. At early stages, lower values of τ_{y0} might force a regimen change. However, to be able to analyze the effects in the pressure predictions for the reference case, $\tau_{y0}*$ values needed are smaller than usually observed for cement slurries. This can be observed in Figures 6.41 and 6.42, respectively the shear stress and viscosity as a function of shear rate.

For higher values τ^*_{y0} tested, no relevant changes in pressure predictions were observed. And even for the lowest value that could be tested, $\tau^*_{y0} = 5.5$, yet no relevant change could be observed, as showed in Fig. 6.43.

In fact, when τ^*_{y0} smaller than 5 were tested, the simulation did not manage to pass $3500\,s$, and convergence was not reached. This was the only numerical instability observed with this model for all parameter values tested. Smaller CFL condition limiting values were also tested, but apparently decreasing the time step didn't aid convergence. Velocity and viscosity profiles

PUC-Rio - Certificação Digital Nº 1612794/CA

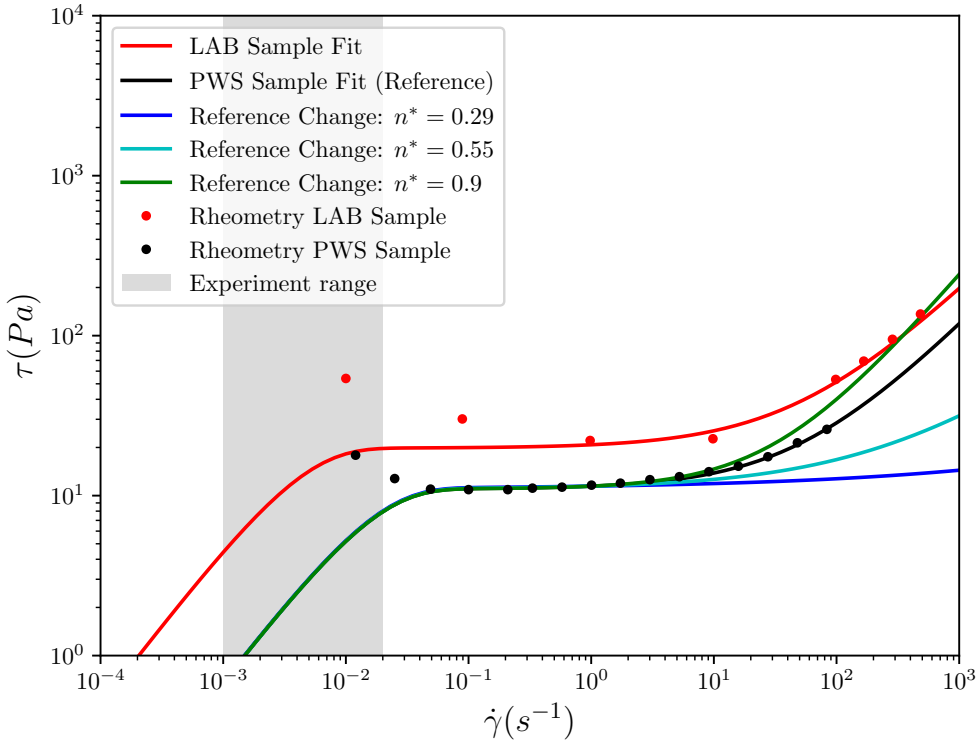

Figure 6.38: Shear stress comparison: LAB and PWS Samples *vs* n^* of 0.29, 0.55 and 0.9.

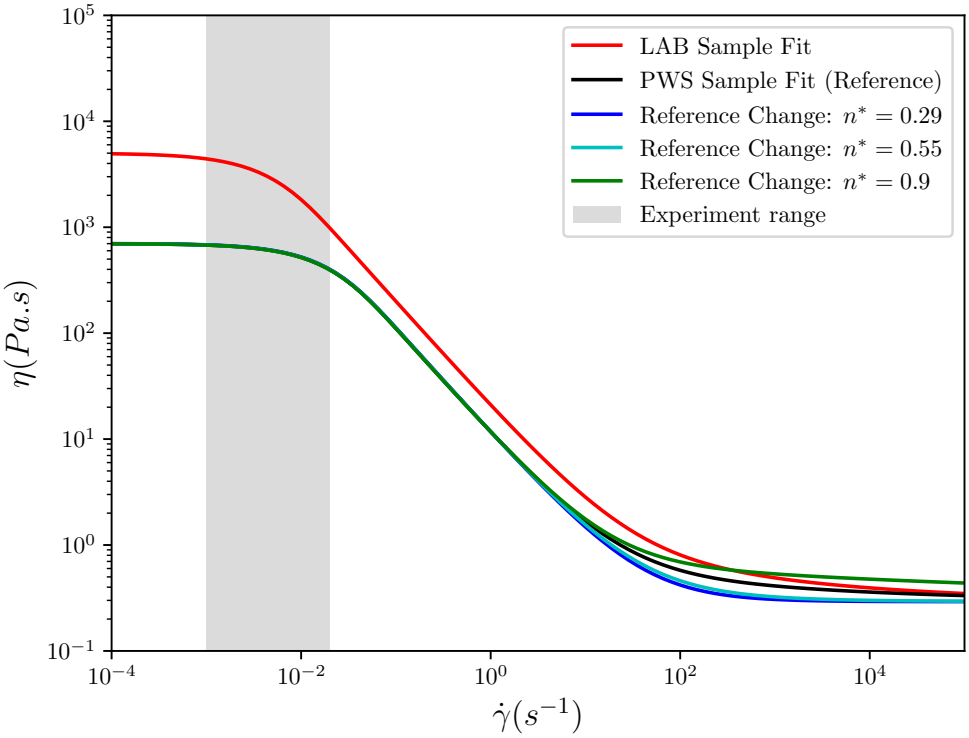

Figure 6.39: Viscosity comparison: LAB and PWS Samples *vs* n^* of 0.29, 0.55 and 0.9.

PUC-Rio - Certificação Digital Nº 1612794/CA

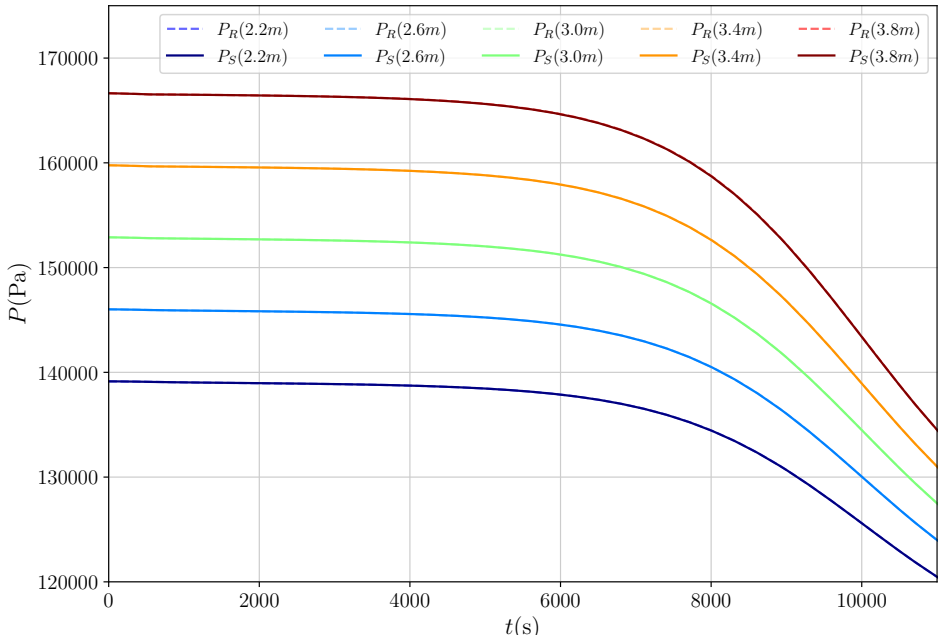

Figure 6.40: Pressure prediction comparison: solid line for $n^* = 0.29\,Pa.s^n$ and dashed line for the reference case.

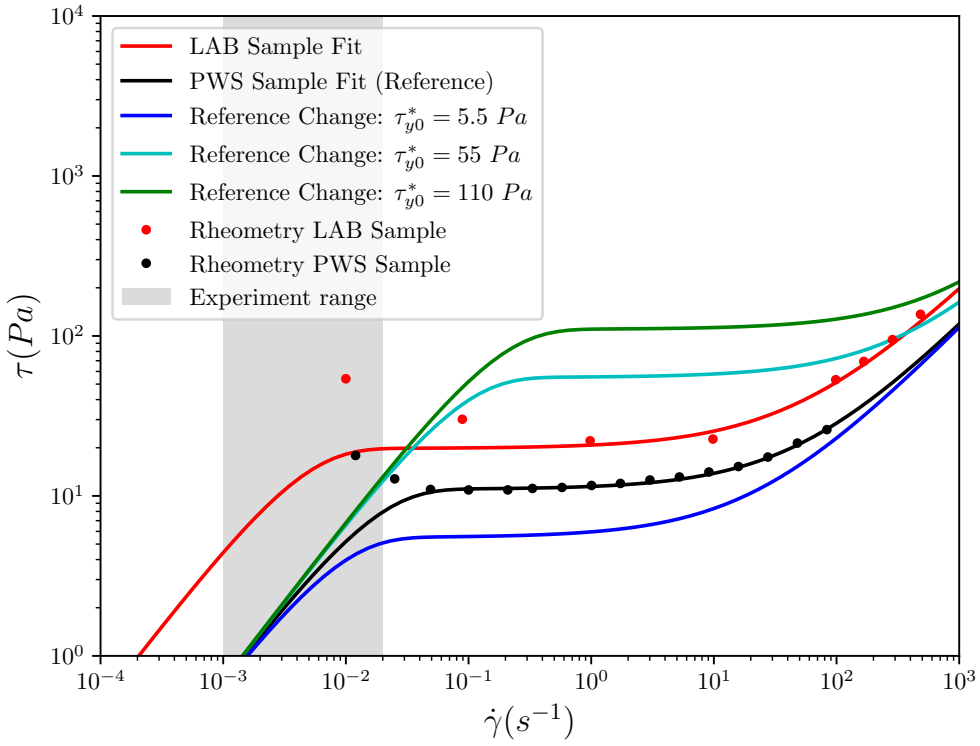

Figure 6.41: Shear stress comparison: LAB and PWS Samples *vs* τ^*_{yo} of 5.5, 55 and 110 Pa.

PUC-Rio - Certificação Digital Nº 1612794/CA

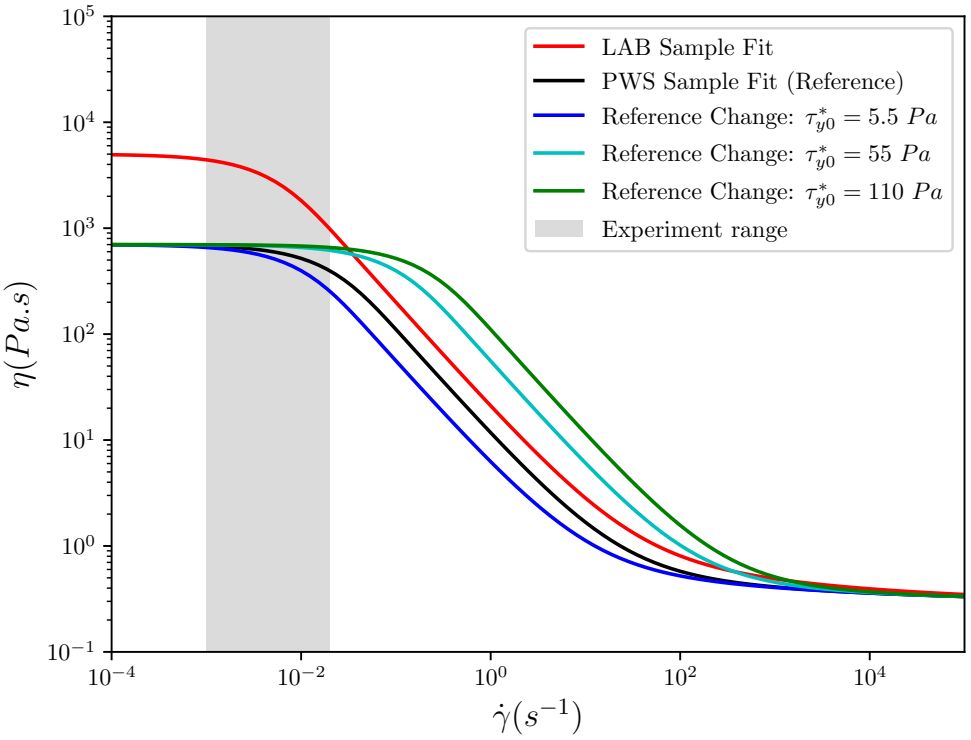

Figure 6.42: Viscosity comparison: LAB and PWS Samples *vs* $\tau_{y0}*$ of 5.5 Pa, 55 Pa and 110 Pa.

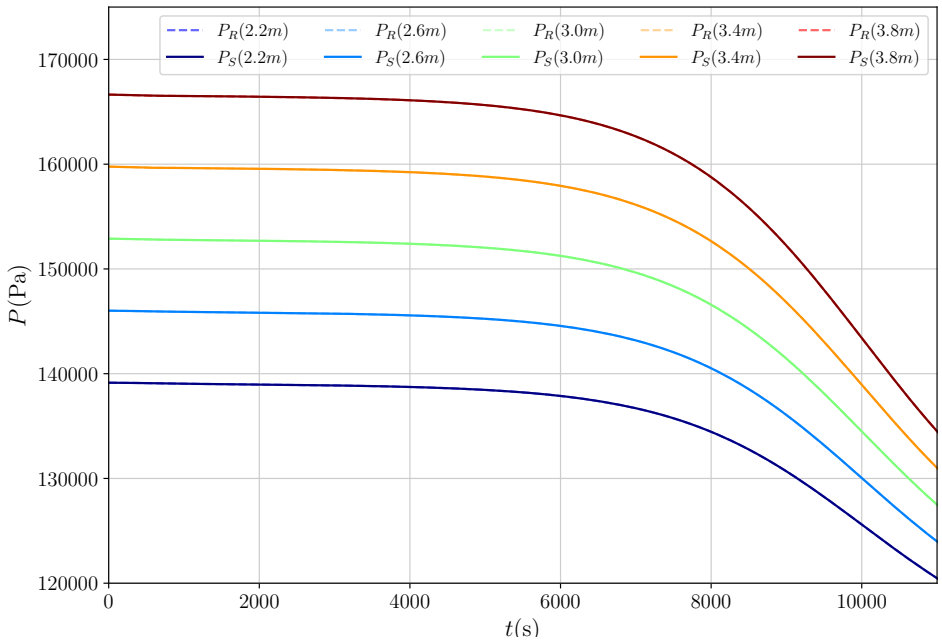

Figure 6.43: Pressure prediction comparison: solid line for $\tau_{y0}^* = 5.5\,Pa$ and dashed line for the reference case.

PUC-Rio - Certificação Digital Nº 1612794/CA

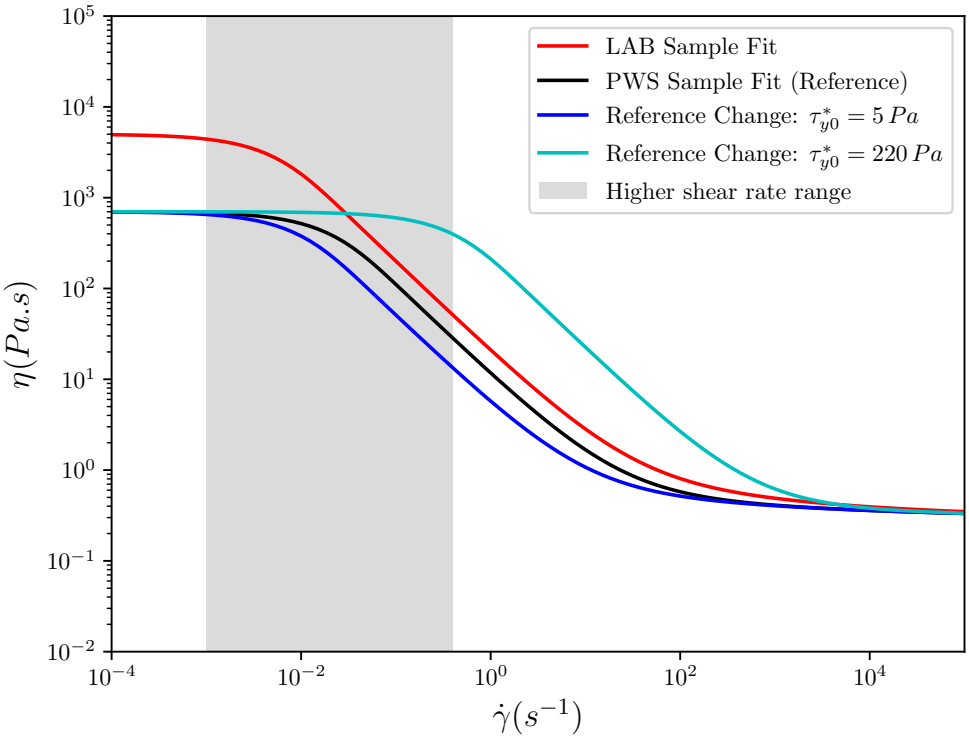

Figure 6.44: Viscosity comparison: LAB and PWS Samples *vs* $\tau_{y0}*$ of 5 Pa and 220 Pa, with 20 times higher fluid loss flow rate magnitude.

were analyzed right before divergence, but no abnormal behavior could be observed. Although the this code proved to be robust, further investigation needs to be performed in order to fully map its numerical limits.

To test if a higher fluid loss flow rate could increase the model sensitivity to any of the tested parameters, those tests were repeated with an hypothetical fluid loss flow rate 20 times higher than the experimental case. The shape of the flow rate curve was maintained the same, and only the magnitude was changed, but yet most parameters showed no significant change when changed individually. One exception was the yield stress, which for the new shear rate range simulated, showed some early effects similar to those caused by the η_0. Figure shows the comparison of the tested viscosity curves as a function of shear rate, for the new shear rate range. Figures 6.45 and 6.46 shows the early effects mentioned, respectively for $\tau^*_{y0} = 5\,Pa$ and $\tau^*_{y0} = 220\,Pa$.

The parameter responsible for most relevant changes in the pressure, for the same amount of fluid loss, is the transition time. However, changes in the rheological parameters in a slurry probably impose some correlated variations of transition time. This should be inputted in the model in order to actually analyze its impact in pressure predictions.

PUC-Rio - Certificação Digital Nº 1612794/CA

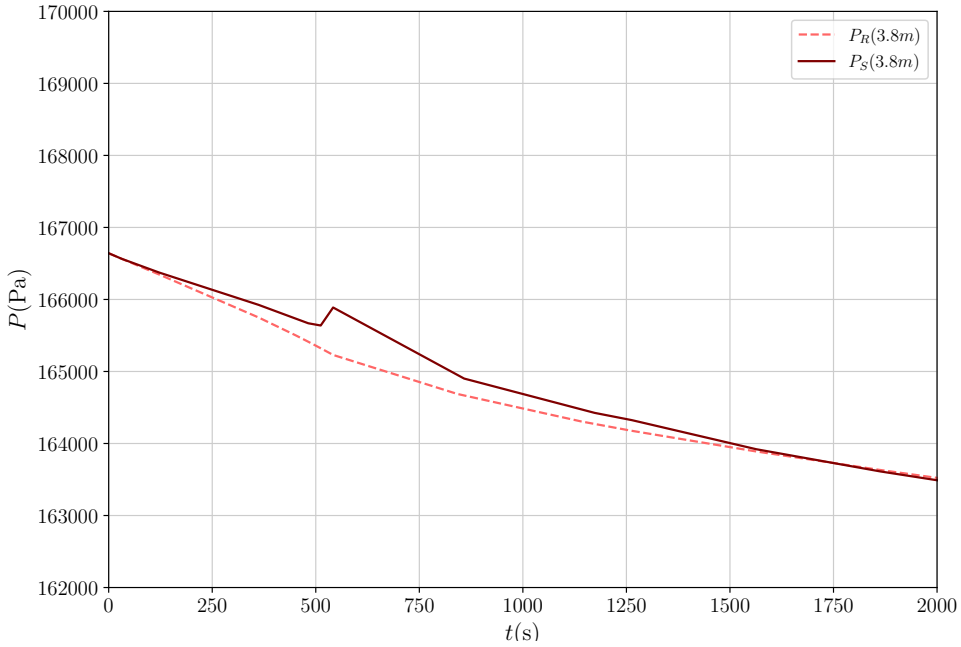

Figure 6.45: Pressure prediction detail comparison: solid line for $\tau_{y0}^{*} = 5\,Pa$ and dashed line for the reference case.

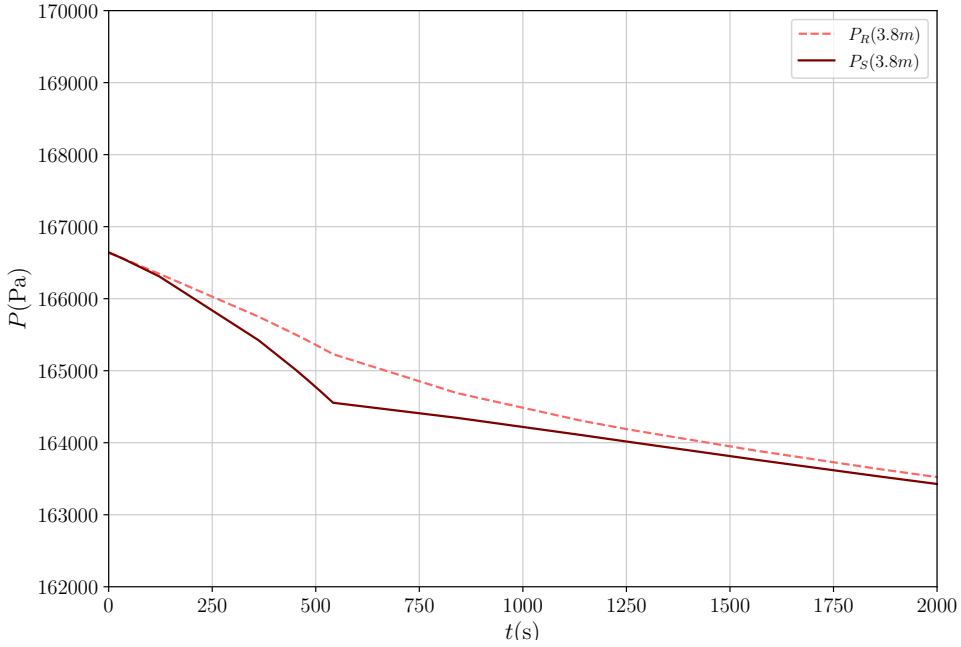

Figure 6.46: Pressure prediction detail comparison: solid line for $\tau_{y0}^{*} = 220\,Pa$ and dashed line for the reference case.

PUC-Rio - Certificação Digital Nº 1612794/CA

Effectively, changing individually any rheological parameter showed limited effects in the pressure predictions. Two other set of parameters were defined, driven simply by a shear stress shift up and down respectively. In order to show how these virtual slurries, with shifted shear stress, impact the pressure predictions, Figures 6.47 and 6.48 show respectively the shear stress and viscosity as a function of shear rate comparisons.

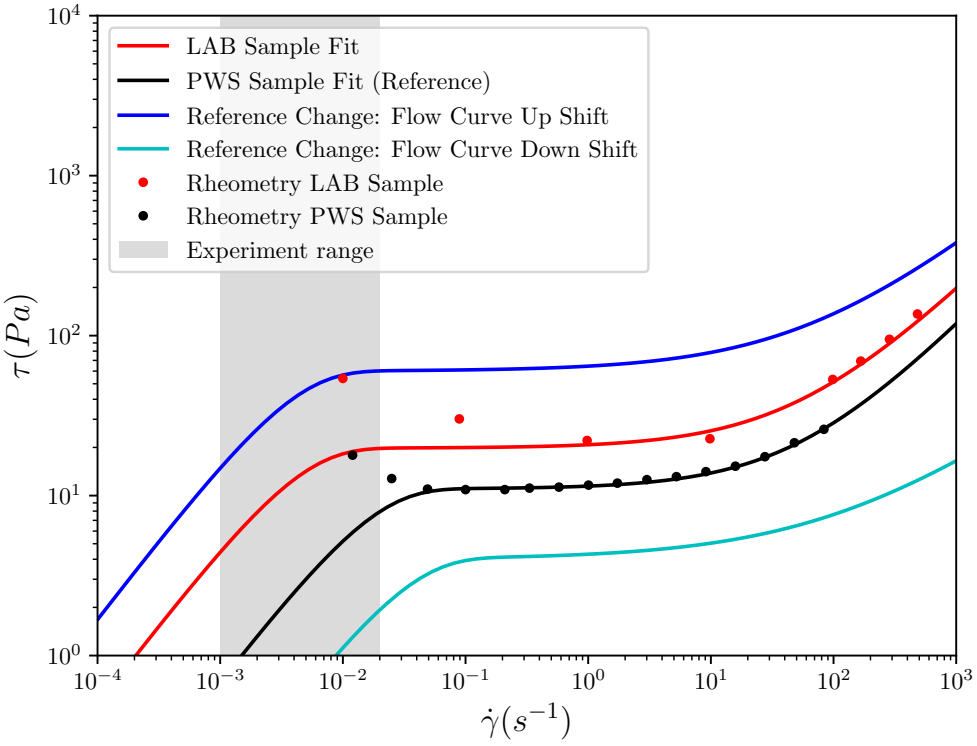

Figure 6.47: Shear stress comparison: LAB and PWS Samples *vs* test virtual slurries.

Figures 6.49 and 6.50 show the pressure predictions, correspondent to the same fluid loss flow rate, although for virtual slurries with shear stress shifted up and down, respectively.

PUC-Rio - Certificação Digital Nº 1612794/CA

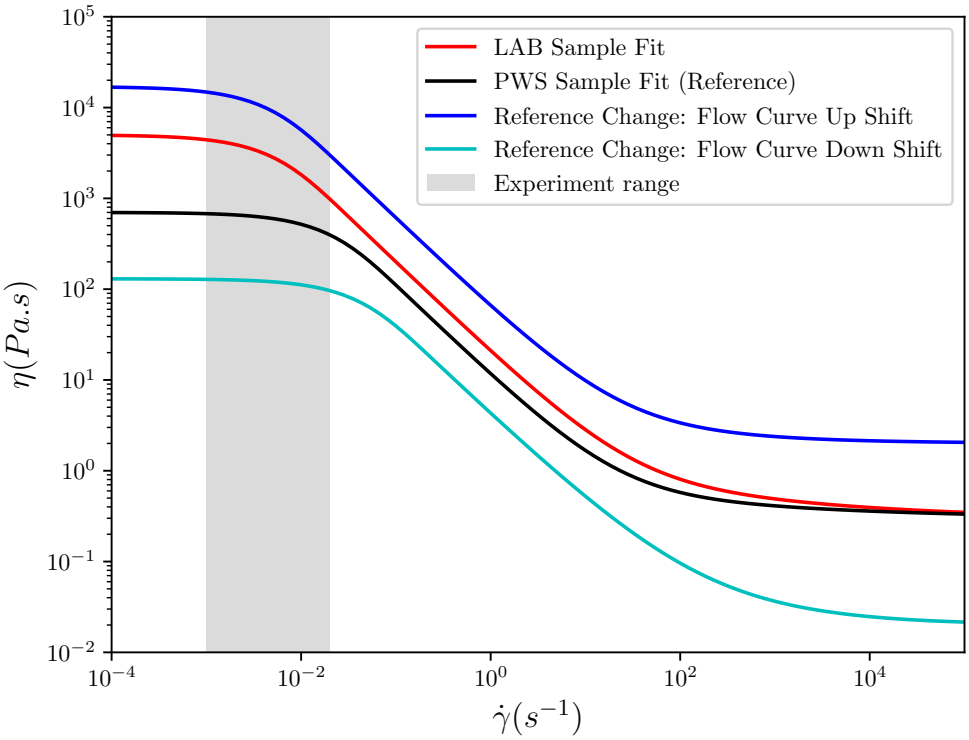

Figure 6.48: Viscosity comparison: LAB and PWS Samples *vs* test virtual slurries.

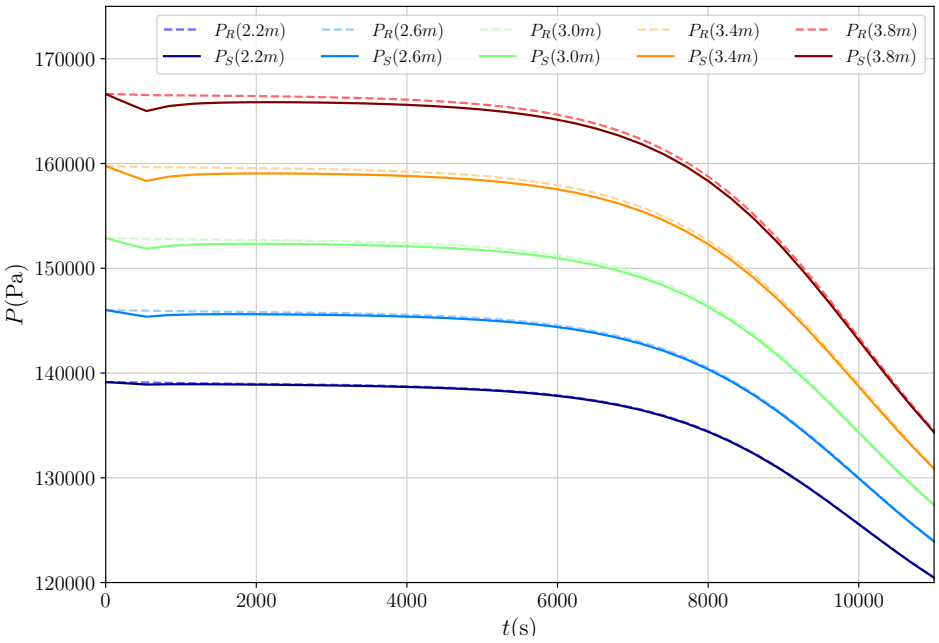

Figure 6.49: Pressure prediction comparison: solid line a virtual slurry with shear stress curve shifted up and dashed line for the reference case.

PUC-Rio - Certificação Digital Nº 1612794/CA

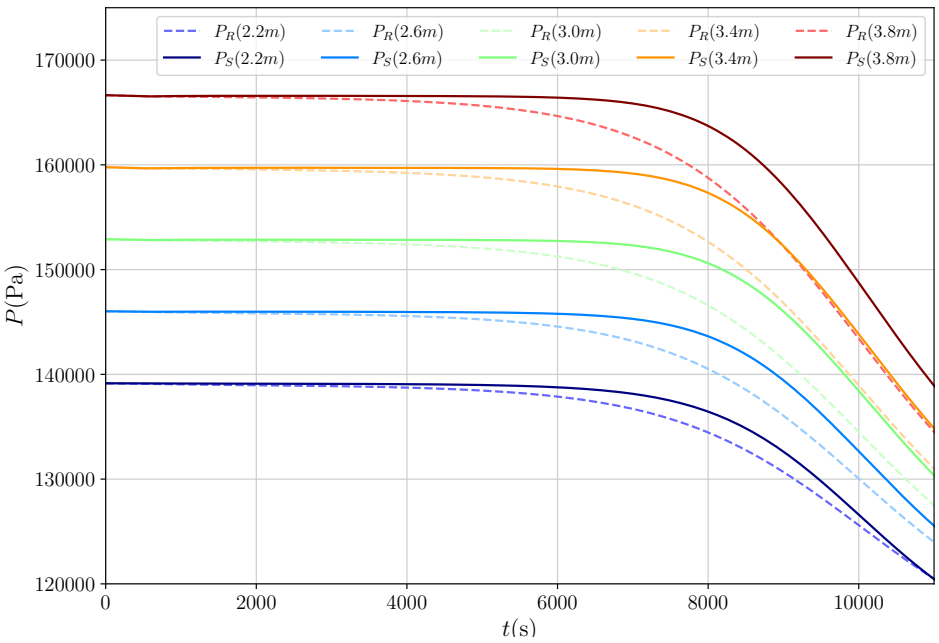

Figure 6.50: Pressure prediction comparison: solid line a virtual slurry with shear stress curve shifted down and dashed line for the reference case.

Apparently, these results may seem not intuitive, that a shifted down flow curve results in a higher pressure prediction along the curing time. However, the mechanism observed is related to the high value of η_0 more than everything else. This high viscosity fluid, submitted to an increasing flow rate, creates an initial pressure drop that is never recovered along the cure. Closer to the transition time, the increasing viscosity make the problem even worse.

On the other hand, a very low viscosity fluid, accelerates without generating such pressure loss. In addition, it takes longer to reach critical viscosity values, when the curing build-up starts. The major drop actually only occurs when shrinkage becomes more important.

These results, must take into account that in this tests the fluid viscosity does not stop or decrease fluid loss flow rate. In real wells, this are usually not true, since a more viscous fluid would impose a greater flow resistance inside a porous media. Therefore, future analysis could be performed taking that into account.

6.4 Simulation performance

One important field requirement for a numerical simulation is the execution time. The calculations performed are not trivial and the meshes involved present thousands of degrees of freedoms unknown variables, or degrees of freedoms to be calculated, per time step.

PUC-Rio - Certificação Digital Nº 1612794/CA

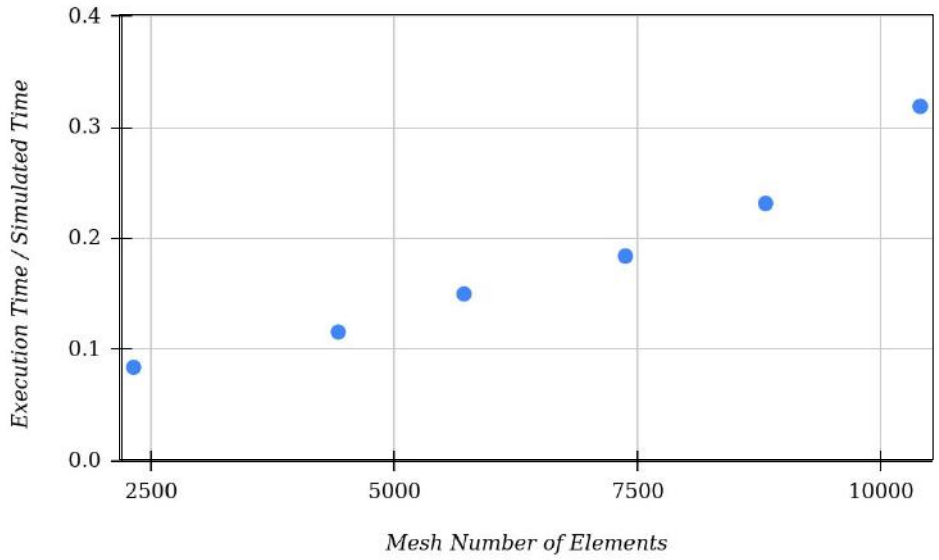

Figure 6.51: Execution to simulation time ratio with mesh elements increase obtained in Mesh Test

PUC-Rio - Certificação Digital Nº 1612794/CA

This requirement also guided the development of the presented numerical model. The architecture of the platform addresses this requirement by using pre-compiled libraries [166], modular coding and a sparse and parallel solver [195, 196].

As showed in Chapter 5, during the mesh testing phase, short simulations of 200 s were performed for different mesh sizes. This tests could be used as an evaluation of how the ratio of execution times by simulated time respond to different mesh sizes, as seen in Figure 6.51.

It's possible to notice that, as expected, the time ratio increases with the number of elements. The execution time is plotted dividing the simulated time, so a comparison can be established between these mesh tests times and the actual case simulations results, which simulated longer periods of flow.

Actual cases focused in simulating 15000 s, but the mesh sizes evaluated did not vary as much as in the mesh tests. Using a the regular mesh of 8000 elements, the execution take an average 21 min. With a mesh of around 18.800 elements, which represents an increase of 113 %, the numerical model takes an average 24 min to run the same case. The execution time increase is only around 14 % and the execution to simulated time ratio is around 0.09, indicating that the parallel solver is able reduce the impact of bigger meshes.

All presented comparison were performed with the regular Courant-Friedrichs-Lewy[182] condition of $\text{CFL}_{max} \leq 1$. Reducing the maximum CFL

to 0.5, execution time reached $48\,min$, which represents an execution to simulated time ratio of 0.18. As expected, this result shows a great dependency of the execution to simulated time ratio with the maximum time step.

A more detailed performance analysis is necessary, specially to actually evaluate the application of this architecture to simulate longer cement column sections. However, the preliminary results indicate a low execution to simulation time ratio, specially when compared with other software. An initial version of this model implemented using finite volumes methods in Matlab presented much higher execution to simulation time ratio, on the order of 10. Very few benchmarks were found on the literature between FEniCs and other solutions, like OpenFOAM. Although those were not performed with MUMPS solver, nor with a specific CFL condition, they already show FEniCs present comparable accuracy and much lower simulation times.

PUC-Rio - Certificação Digital Nº 1612794/CA

7
Conclusions

Cement curing pressure predictions under fluid loss scenarios are one of the biggest challenges in well construction operations. In an ideal case, the viscosity build-up happens immediately after placement, and fluid loss is minimized. However, this short thickening time is hard to design, and cement slurries can loose a huge amount of water to well permeable zones before complete cure occurs. Consequently, this over dehydration may unbalance the paste rheological properties, increasing the risk of loosing well control.

Fluid loss scenarios may considerably increase well construction time and costs, including extra additives, wait-on-cement non productive time, and squeeze and secondary cement jobs. Moreover, the probability of reservoir fluids influx is also higher in such cases. Large gas influxes, for example, may cause immediate blowout accidents, risking human lives and the environment. Nevertheless, undetected influxes may also compromise cement long term integrity, reducing well safety during production or abandonment phases.

In this sense, the present work aimed to improve physical comprehension regarding cementing fluid loss impacts on pressure profile prediction. The performed analyses were focused in fluid loss during early cure, in the recently placed cement column. The physical mechanisms involved on the pressure profile depletion were evaluated, by the means of combined theoretical, experimental and numerical study.

An experimental evaluation was performed in a novel physical well simulator (PWS), aiming to cover some pending points in the fluid loss pressure prediction literature. Examples are the annular geometry with field diameter range, the large-scale column height and the distributed pressure acquisition. Another important gain of those addressed points was to reduce the gap between laboratory slurry design and the oil field operations reality. Therefore, the Physical Well Simulator was granted a patent [107].

PWS modular design, allows it to be used not only in the slurry design phase, but also to be reconfigured to mimic an specific operational situation, such as multiple fluid loss zones, or gas high pressure zone. Furthermore, it can be used as a controlled test environment of possible engineering solutions for those problems.

PUC-Rio - Certificação Digital Nº 1612794/CA

A Finite Elements numerical model for cement pressure prediction in fluid loss scenarios was also developed. Implemented with a scalable and modular architecture, this simulator uses open-source pre-compiled libraries, that grants it high speed and robust performance.

Adopted hypotheses resulted in a simple yet comprehensive 2-D model, that was able to predict pressure drop in the presence of fluid loss zone. A good agreement was observed between experimental and numerical results. Simulations with PWS Sample slurry rheological parameters showed better adherence to experimental data than Lab Sample slurry. This result corroborates with literature, in the sense that mixing regimen and shear rate history are determinant for the obtained slurry rheology.

A sensitivity analysis was performed to evaluate the influence of fluid loss flow rate magnitude, thickening time and the rheological parameters in the pressure profile predictions.

The fluid loss flow rate magnitude, as expected, showed a direct correlation with the pressure drop and with the gelation negative slope. It was observed that transition time changes presented the greatest impacts on pressure drop, specially when coincident with a period of yet significant fluid loss flow rate. If thickening time happens after the flow rate values decay, pressure profiles seem to be less affected.

Both transition time and fluid loss flow rate impacts on pressure profile can be observed throughout the curing time. Nevertheless, some rheological parameters, only seem to affect the early cure, when the flow rate increases before it drops. It should be taken into account that fluid loss flow rate curve shape is an input of this model. In fact, within a porous media, high viscous fluids might experience lower flow rates earlier than low viscous fluids.

Lower τ_{y0} and higher η_0 promote greater pressure drops within the period where fluid loss flow rate is increasing. This behavior is emphasized in tests with higher flow rate magnitudes. For the experiment shear rate range tested, no significant change in pressure profile was observed for individual changes in n, K and η_∞, since they affect the flow curve majorly at higher shear rate ranges.

It is worth mentioning that no implementation of a classical 1D model for pressure prediction was confronted with the experimental results presented in this thesis. Indeed, the observed experimental pressure decay resembles the characteristic pressure profiles found in the literature for the lubrication framework method.

Ultimately, the developed program was designed to be a strong foundation for future developments in fluid loss applications. For example, it can

PUC-Rio - Certificação Digital Nº 1612794/CA

be used to evaluate more complex rheological or shrinkage models, and also incorporate other important features, such as temperature gradients and compressibility.

7.1 Future work

Fluid loss impacts in the early cure pressure drop is a vast problem. Although some of its aspects have been covered in this Thesis, further investigation would certainly deeper the understanding of the overall problem physics. In this section, some guidelines for future studies are proposed and discussed.

Building upon the findings of this work, the rheological model studied presented some limitations in modeling the initial asymptotic shape of pressure drop, observed in the experiments. More complex rheological models, considering thixotropic aspects, could be able to capture such behavior.

In addition, in some of the literature reviewed, the authors observed dependence of viscosity model parameters with the cement-to-water ratio [58, 8], which was not considered in this work. Simulated velocity profiles presented some recirculation close to the permeable zone, which would be affected by this hypothesis.

For some extreme parameters tested, model convergence was not achieved. Therefore, an extensive evaluation of the model limitations should be performed. Fully defining the model operational envelope could also extend its applicability to different scenarios, such as drilling fluids circulation loss, foamed cement and even synthetic resin-based materials.

Moreover, multiple fluid loss zones and longer columns could also be investigated. Such tests would not only approximate the model to real well scenarios, but also enable a richer performance evaluation.

Furthermore, for axisymmetric wells, the 2D compositional model proposed certainly enlightens the fluid loss impacts on the filter cake formation and on how cement-to-water ratio may vary locally. It also allows a better understanding of the evolution of creep flow velocity profiles for different fluid loss flow rates and slurry rheological properties. Nevertheless, to evaluate its real gain with respect to the classical 1D lubrication framework for the pressure prediction accuracy, further experiments must be performed with a wider range of the annular diameters ratio.

Other natural continuations of this research passes by introducing temperature variation as well as the neglected azimuthal dimension θ. External temperature gradients could be directly introduced as boundary conditions,

PUC-Rio - Certificação Digital Nº 1612794/CA

and its effects evaluated with respect to common thermal dependent parameters, such as diffusion coefficient and overall viscosity.

Computing the temperature field would also enable the evaluation of the heat of hydration on well pressure. Regarding a 3D numerical model, it would enable the evaluation of pipe eccentricity and eroded wells influence in the fluid loss main flow, and consequently in the pressure drop. Both temperature and 3D implementations, certainly benefit from the modular and scalable architecture built.

Finally, the proposed model addresses the direct problem, where fluid loss is known or measured and pressure drop is predicted based on the knowledge. A different approach could also be investigated, working with the inverse problem. This could be achieved changing the boundary conditions at the outlet from velocity to pressure, and could be used to estimate the amount of filtrate lost to a specific formation.

PUC-Rio - Certificação Digital Nº 1612794/CA

Bibliography

[1] BAKER, R.. **A Primer of Oil-well Drilling**. Petroleum Extension Service, 1979.

[2] **Environmentally friendly drilling systems**. `http://stochasticgeomechanics.civil.tamu.edu/efd/Definitions.html`. [Online; accessed November-2019].

[3] LAVROV, A.; TORSÆTER, M.. **Physics and Mechanics of Primary Well Cementing**. SpringerBriefs in Petroleum Geoscience & Engineering. Springer International Publishing, 1 edition, 2016.

[4] RAHMAN, S.; CHILINGARIAN, G.. **Casing Design Theory and Practice**. Developments in Petroleum Science 42. Elsevier, Academic Press, 1995.

[5] NELSON, E. B.; GUILLOT, D.. **Well Cementing**, volumen 2. Schlumberger, 2006.

[6] COWAN, H. J.. **An historical note on concrete**. Architectural Science Review, 18:10–13, 1975.

[7] DACCORD, G.; DE ROZIERES, L. ; BOUSSOUIRA, B.. **Cement slurry behavior during hydration and consequences for oil-well cementing**. First International Workshop on Hydration and Setting, 07 1991.

[8] HANSEN, W.. **Drying shrinkage mechanisms in portland cement paste**. Journal of the American Ceramic Society, 70(5):323–328, 1987.

[9] BANFILL, P.. **Rheology of fresh cement and concrete**. Rheol Rev, 01 1991.

[10] DE SOUZA MENDES, P. R.; THOMPSON, R. L.. **A unified approach to model elasto-viscoplastic thixotropic yield-stress materials and apparent yield-stress fluids**. Rheologica Acta, 52(7):673–694, apr 2013.

[11] HALLIBURTON, E. P.. **Method and means for cementing oil-wells**, 03 1921. US Patent 1,369,891-A.

PUC-Rio - Certificação Digital Nº 1612794/CA

[12] **Main components of oil well cement**. https://oilfieldteam.com/en/a/learning/well-cement-14102017. [Online; accessed November-2019].

[13] STOKES, D.. **Offshore magazine - integrated milling, underreaming approach streamlines p&a operations in the north sea**. https://www.offshore-mag.com/drilling-completion/article/16756041/integrated-milling-underreaming-approach-streamlines-pa-operations-in-the-nort [Online; accessed October-2020].

[14] **Deep water brazil**. https://www.halliburton.com/en-US/ps/solutions/deepwater/deepwater-assets/brazil/deepwater-brazil.html. [Online; accessed November-2019].

[15] BASSO, M.; KURODA, M. C.; AFONSO, L. C. S. ; VIDAL, A. C.. **Three-dimensional seismic geomorphology of paleokarst in the cretaceous macaé group carbonates, campos basin, brazil**. Journal of Petroleum Geology, 41:513–526, 2018.

[16] ISO-10426. **Petroleum and natural gas industries - cements and materials for well cementing**, 2009.

[17] TOSCA, N. J.; WRIGHT, V. P.. **Diagenetic pathways linked to labile mg-clays in lacustrine carbonate reservoirs: a model for the origin of secondary porosity in the cretaceous pre-salt barra velha formation, offshore brazil**. Geological Society London Special Publications, 11 2015.

[18] SANTRA, A. K.; REDDY, B. R. ; ANTIA, M.. **Designing cement slurries for preventing formation fluid influx after placement**. Society of Petroleum Engineers - International Symposium on Oilfield Chemistry - Houston, Texas, U.S.A. (2007-02-28).

[19] CHANTON, J. P.; CHERRIER, J.; WILSON, R. M.; SARKODEE-ADOO, JAND BOSMAN, S.; MICKLE, A. ; GRAHAM, W. M.. **Radiocarbon evidence that carbon from the deepwater horizon spill entered the planktonic food web of the gulf of mexico**. Environmental Research Letters, 7, 12 2012.

[20] COOK, J.; GROWCOCK, F.; GUO, Q.; HODDER, M. ; OORT, E. V.. **Stabilizing the wellbore to prevent lost circulation**.

PUC-Rio - Certificação Digital Nº 1612794/CA

[21] PERKINS, A. A.; DOUBLE, E.. **Method of cementing oil-wells.**, 12 1911. US Patent 1,011,484.

[22] SAUER, C. W.. **Mud displacement during cementing state of the art**. Journal of Petroleum Technology, 39, 9 1987.

[23] HALLIBURTON, E. P.. **Method of hydrating cement and the like**, 04 1924. US Patent 1,486,883.

[24] HUBER, F. W.. **Method and composition for cementing oil wells**, 04 1923. US Patent 1,452,463.

[25] BOTKIN, J. W.. **Apparatus for cementing wells**, 04 1941. US Patent 2,327,092.

[26] SLAGLE, K. A.. **Rheological design of cementing operations**. Journal of Petroleum Technology, 14, 3 1962.

[27] KUNTHER, W.; FERREIRO, S. ; SKIBSTED, J.. **Influence of the ca/si ratio on the compressive strength of cementitious calcium–silicate–hydrate binders**. J. Mater. Chem. A, 5:17401–17412, 2017.

[28] BARBOSA, W.; PORTELLA, K. F.. **Síntese e caracterização das fases minerais c3s, c2s, c3a e c4af para utilização em cimento tipo portland**. Cerâmica, 65:54–62, 2019.

[29] WITTMANN, F.. **Surface tension skrinkage and strength of hardened cement paste**. Matériaux et Constructions, 1:547–552, 11 1968.

[30] BARNES, P.. **Structure and Performance of Cements, 1st Edition**, volumen 1. Applied Science, 1 edition, 1983.

[31] APPLEBY, S.; WILSON, A.. **Permeability and suction in setting cement**. Chemical Engineering Science, 51:251–267, 1996.

[32] CHENEVERT, M.; JIN, L.. **Model for predicting wellbore pressures in cement columns**. 1989. SPE Annual Technical Conference and Exhibition - San Antonio, Texas.

[33] PROHASKA, M.; OGBE, D. ; ECONOMIDES, M.. **Determining wellbore pressures in cement slurry columns**. 1993. SPE Western Regional Meeting - Anchorage, Alaska Meeting.

PUC-Rio - Certificação Digital Nº 1612794/CA

[34] PROHASKA, M.; FRUHWIRTH, R. ; ECONOMIDES, M. J.. **Modeling early-time gas migration through cement slurries (includes associated papers 36370 and 36766 and 37387 and 37684)**. SPE Drilling & Completion, 10, 09 1995.

[35] NISHIKAWA, S.; WOJTANOWICZ, A.. **Transient pressure unloading - a model of hydrostatic pressure loss in wells after cement placement**. 2002. SPE Annual Technical Conference and Exhibition.

[36] CHENEVERT, M. E.; SHRESTHA, B. K.. **Chemical shrinkage properties of oilfield cements**. SPE Annual Technical Conference and Exhibition, 1991.

[37] LE CHATELIER, H.. **Experimental Researches on the Constitution of Hydraulic Mortars**. PhD thesis, School of Civil Eng. Purdue Univ., 1887. Translated and published in the United States by J L Mack, McGraw Publishing Co, New York 1905.

[38] MINDESS, S.; YOUNG, J. ; LAWRENCE, F.. **Creep and drying shrinkage of calcium silicate pastes i. specimen preparation and mechanical properties**. Cement and Concrete Research, 8:591–600, 1978.

[39] BAŽANT, Z. P.; PANULA, L.. **Practical prediction of time-dependent deformations of concrete**. Materials and Structures, 11:307–316, 1978.

[40] BAŽANT, Z. P.; KIM, J.-K. ; PANULA, L.. **Improved prediction model for time-dependent deformations of concrete: Part 1-shrinkage**. Materials and Structures, 24:327–345, 1991.

[41] BAŽANT, Z. P.; MURPHY, W. P.. **Creep and shrinkage prediction model for analysis and design of concrete structures— model b3**. Materials and Structures, 28:357–365, 1995.

[42] TURKI, W.; MACKAY, A.. **Primary cementing across massive lost circulation zones**. In: MIDDLE EAST OIL TECHNICAL CONFERENCE AND EXHIBITION. Society of Petroleum Engineers, 1983.

[43] BARET, J. F.. **Why cement fluid loss additives are necessary.** Society of Petroleum Engineer, 1988. Int. J. Min. & Geo-Eng.

[44] DESBRIERES, J.. **Cement cake properties in static filtration. on the role of fluid loss control additives on the cake porosity**. Cement and Concrete Research, 23:1431–1442, 1993.

PUC-Rio - Certificação Digital Nº 1612794/CA

[45] LOW, N.; DACCORD, G. ; BEDEL, J.-P.. **Designing fibered cement slurries for lost circulation applications: Case histories**. Society of Petroleum Engineers, 2003.

[46] VEISI, M. S.; TAOUTAOU, S.; STEVEN, A.; PASTERIS, M.; WEDHASWARI, V. R.; AWALT, M.; KADRIE, M. ; PERMATA, E.. **Engineered highly crush-resistant cement slurry to prevent lost circulation**. In: SPE/IATMI ASIA PACIFIC OIL & GAS CONFERENCE AND EXHIBITION. Society of Petroleum Engineers, 2015.

[47] XU, B.; YUAN, B.; GUO, J.; XIE, Y. ; LEI, B.. **Novel technology to reduce risk lost circulation and improve cementing quality using managed pressure cementing for narrow safety pressure window wells in sichuan basin**. Journal of Petroleum Science and Engineering, 180:707–715, 2019.

[48] BANNISTER, C. E.; LAWSON, V. M.. **Role of cement fluid loss in wellbore completion**. Society of Petroleum Engineers SPE Annual Technical Conference and Exhibition - Las Vegas, Nevada.

[49] DACCORD, G.; BARET, J.. **How fluid loss influences primary cementing:literature review and methodology**. In: OFFSHORE TECHNOLOGY CONFERENCE. Offshore Technology Conference, 1992.

[50] CLARK, P. E.. **Analysis of fluid loss data ii: Models for dynamic fluid loss**. Journal of Petroleum Science and Engineering, 70:191–197, 2010.

[51] RAHEEM, A. M.; VIPULANANDAN, C.. **Testing and modeling of filter cake formation using new seepage-consolidation concept**. Engineering Science and Technology, an International Journal, p. 979–989, 2018.

[52] THEROND, E.; TAOUTAOU, S.; JAMES, S. G.; WAY, P. W.; GOMES, P. ; DONDALE, A.. **Understanding lost circulation while cementing: Field study and laboratory research**. SPE Drilling & Completion, 2018.

[53] DELLYES, R.. **La rhéologie des pâtes a ciment dans la voie humide**. Rev. matériaux construct., p. 193–213, 1954.

[54] TATTERSALL, G. H.. **The rheology of portland cement pastes**. British Journal of Applied Physics, 6:165–167, 1955.

PUC-Rio - Certificação Digital Nº 1612794/CA

[55] VOM BERG, W.. **Influence of specific surface and concentration of solids upon the flow behaviour of cement pastes**. Magazine of Concrete Research, 31:211–216, 1979.

[56] MIN, B. H.; ERWIN, L. ; JENNINGS, H. M.. **Rheological behaviour of fresh cement paste as measured by squeeze flow**. Journal of Materials Science, 29:1374–1381, 1994.

[57] BINGHAM, E. C.. **Plasticity**. Journal of Physical Chemistry, 29:1201–1204, 1925.

[58] JONES, T. E. R.; TAYLOR, S.. **A mathematical model relating the flow curve of a cement paste to its water/cement ratio**. Magazine of Concrete Research, 29:207–212, 1977.

[59] RODRIGUES, E. C.; DE ANDRADE SILVA, F.; DE MIRANDA, C. R.; DE SÁ CAVALCANTE, G. M. ; DE SOUZA MENDES, P. R.. **An appraisal of procedures to determine the flow curve of cement slurries**. Journal of Petroleum Science and Engineering, p. 617–623, 2017.

[60] RODRIGUES, E. C.; DE SOUZA MENDES, P. R.. **Predicting the time-dependent irreversible rheological behavior of oil well cement slurries**. Journal of Petroleum Science and Engineering, p. 805–813, 2019.

[61] HERSCHEL, W. H.; BULKLEY, R.. **Konsistenzmessungen von gummi-benzollösungen "measurement of consistency as applied to rubber-benzene solutions"**. Colloid & Polymer Science, 39:291–300, 1926.

[62] MARCHESINI, F. H.; OLIVEIRA, R. M.; ALTHOFF, H. ; DE SOUZA MENDES, P. R.. **Irreversible time-dependent rheological behavior of cement slurries: Constitutive model and experiments**. Journal of Rheology, 63:247–262, 2019.

[63] WILLIAMS, M.. **Radial filtration of drilling muds**. Transactions of the AIME, 136:57–70, 1940.

[64] HOWARD, G. C.; SCOTT, P.. **An analysis and the control of lost circulation**. Journal of Petroleum Technology, 3:171–182, 1951.

[65] SHUMATE, H. J.. **Lost circulation: Causes and remedies**. Petroleum Egineering, 23:84–86, 1951.

[66] MESSENGER, J.; MCNIEL, J.. **Lost circulation corrective: Time-setting clay cement**. Journal of Petroleum Technology, 4:59–64, 1952.

PUC-Rio - Certificação Digital Nº 1612794/CA

[67] BUGBEE, J. M.. **Procedures to be used fighting lost circulation**. World Oil, 136:132–140, 1953.

[68] FIDAN, E.; BABADAGLI, T. ; KURU, E.. **Use of cement as lost-circulation material: Best practices**. Petroleum Society of Canada, 2004.

[69] ALGU, D. R.; GALEY, R. L.; BARRETT, M. ; HUMPHRIES, M.. **Large-volume cement squeezes as cost-effective solutions for severe-loss zones**. In: IADC/SPE DRILLING CONFERENCE AND EXHIBITION. Society of Petroleum Engineers, 2010.

[70] COOK, J.; GUO, Q.; D PAUL WAY; BAILEY, L. ; FRIEDHEIM, J.. **The role of filtercake in wellbore strengthening**. In: IADC/SPE DRILLING CONFERENCE AND EXHIBITION. Society of Petroleum Engineers, 2016.

[71] GLENN, E. E.; JENKINS, R.. **Lost circulation: A new fibrous material for its correction**. Petroleum Egineering, p. B7–10, B12, 1951.

[72] WAN DYKE, O. W.. **Method and means of preventing fluid loss through porous walls**, 03 1947. US Patent 1,011,484.

[73] CAMPBELL, J. G.; CORPUS, C. ; TWINING, H. L.. **Method and means of preventing fluid loss through porous walls**, 06 1949. US Patent 1,011,484.

[74] SHIRATO, M.. **Porosity variation in filter cake under constant-pressure filtration**. J. Chem. Eng. Japan, 4:172–174, 1971.

[75] HE, D. X.. **An overview of investigations on filter cake characteristics**. Adv. Filtr. Separ. Tech., 11:404–417, 1997.

[76] LOEPPKE, G. E.; GLOWKA, D. A. ; WRIGHT, E. K.. **Design and evaluation of lost-circulation materials for severe environments**. Journal of Petroleum Technology, 42:328–337, 1990.

[77] WANG, G.; CAO, C.; PU, X. ; ZHAO, Z.. **Experimental investigation on plugging behavior of granular lost circulation materials in fractured thief zone**. Particulate Science And Technology, p. 1–5, 2015.

[78] OKETCH, B. A.. **Analysis of stuck pipe incidents in menengai**. 2015.

PUC-Rio - Certificação Digital Nº 1612794/CA

[79] LUZARDO, J.; OLIVEIRA, E. P.; DERKS, P. W. J.; NASCIMENTO, R. V.; GRAMATGES, A. P.; VALLE, R.; PANTANO, I. G.; SBAGLIA, F. ; INDERBERG, K.. **Alternative lost circulation material for depleted reservoirs**. In: OTC BRASIL. Offshore Technology Conference, 2015.

[80] CHANEY, P.. **Abnormal pressures and lost circulation**. SPE Drilling and Production Practice, New York, New York, 136:57–70, 1949.

[81] NUGROHO, W. A.; HERMAWAN, S.; LAZUARDI, B. H. ; MIRZA, R.. **Drilling problems mitigation in geothermal environment, case studies of stuck pipe and lost circulation**. SPE/IATMI Asia Pacific Oil & Gas Conference and Exhibition, 2017.

[82] GRIFFITH, J. E.; OSISANYA, S.. **Thickness optimization of drilling fluid filter cakes for cement slurry filtrate control and long-term zonal isolation**. In: SPE PRODUCTION OPERATIONS SYMPOSIUM. Society of Petroleum Engineers, 1995.

[83] OSISANYA, S.; GRIFFITH, J.. **Evaluation of cement slurry quality using filter cake permeability and thickness**. In: ANNUAL TECHNICAL MEETING. Petroleum Society of Canada, 1997.

[84] RITA, N.; MURSYIDAH ; SYAHINDRA, M.. **The use of additive ceramic hollow spheres on cement slurry to prevent lost circulation in formation 'x' having low pressure fracture**. 2018.

[85] VELAYATI, A.; KAZEMZADEH, E.; SOLTANIAN, H. ; TOKHMECHI, B.. **Gas migration through cement slurries analysis: A comparative laboratory study**. International Journal of Mining and Geo-Engineering, 49, 2015.

[86] STANDARD-API65-2-2010. **Isolating potential flow zones during well construction**, 12 2010.

[87] DARCY, H.. **Les fontaines publiques de la ville de Dijon**. Victor Dalmont, 1856.

[88] FOMENKOV, A.; PINIGIN, I.; MIKLIAYEV, M. ; FEDYANIN, A.. **Using thixotropic cement slurry for lost circulation control: Case history, volga-urals region**. In: SPE RUSSIAN PETROLEUM TECHNOLOGY CONFERENCE. Society of Petroleum Engineers, 2019.

PUC-Rio - Certificação Digital Nº 1612794/CA

[89] CHRISTIAN, W. W.; CHATTERJI, J. ; OSTROOT, G. W.. **Gas leakage in primary cementing - a field study and laboratory investigation**. Journal of Petroleum Technology, 28, 11 1976.

[90] CARPENTER, C.. **Liner-drilling technology mitigates lost circulation offshore mexico**. Journal of Petroleum Technology, 66:104–107, 2014.

[91] LAVROV, A.. **Lost circulation in primary well cementing**. Energy Procedia, 114:5182–5192, 2017.

[92] CHEUNG, P. R.; BEIRUTE, R. M.. **Gas flow in cements**. Journal of Petroleum Technology, 37, 06 1985.

[93] BEIRUTE, R. M.; CHEUNG, P. R.. **Method for selection of cement recipes to control fluid invasion after cementing**. SPE Production Engineering, 5, 11 1990.

[94] NGUYEN, Q. D.; DEAWWANICH, T.; TONMUKAYAKUL, N.; SAVERY, M. R.; CHIN, W.; CO, A.; LEAL, G. L.; COLBY, R. H.; GIACOMIN ; JEFFREY, A.. **Flow visualization and numerical simulation of viscoplastic fluid displacements in eccentric annuli**. volumen 1027, 2008. AIP THE XV INTERNATIONAL CONGRESS ON RHEOLOGY: The Society of Rheology 80th Annual Meeting - Monterey.

[95] MIRANDA, C.; CARVALHO, K.; VARGAS, A.; RODRIGUES, L. ; MARCHESINI, F.. **Minimizing fluid contamination during oilwell cementing operations**. 2007. Offshore Mediterranean Conference and Exhibition.

[96] SKADSEM, H. J.; KRAGSET, S.; LUND, B.; YTREHUS, J. D. ; TAGHIPOUR, A.. **Annular displacement in a highly inclined irregular wellbore: Experimental and three-dimensional numerical simulations**. Journal of Petroleum Science and Engineering, p. 998–1013, 2018.

[97] THEROND, E.; BOIS, A.-P.; WHALEY, K. ; MURILLO, R.. **Large scale testing & modelling for cement zonal isolation of water injection wells**. SPE Annual Technical Conference and Exhibition - Dubai, UAE.

[98] BITTLESTON, S. H.; FERGUSON, J. ; FRIGAARD, I. A.. **Mud removal and cement placement during primary cementing of an oil well – laminar non-newtonian displacements in an eccentric annular hele-shaw cell**. Journal of Engineering Mathematics, 43, 08 2002.

PUC-Rio - Certificação Digital Nº 1612794/CA

[99] ESCUDIER, M.; OLIVEIRA, P. ; PINHO, F.. **Fully developed laminar flow of purely viscous non-newtonian liquids through annuli, including the effects of eccentricity and inner-cylinder rotation**. International Journal of Heat and Fluid Flow, 23:52–73, 2002.

[100] SAVERY, M.; DARBE, R. ; CHIN, W.. **Modeling fluid interfaces during cementing using a 3-d mud displacement simulator**. In: OFFSHORE TECHNOLOGY CONFERENCE. Offshore Technology Conference, 2007.

[101] **The most robust cementing design tool in the industry dramatically increases the probability of wellbore integrity**. https://www.halliburton.com/content/dam/ps/public/cem/contents/Posters/iCem-Service_panel_C-76.pdf?nav=en-US_cementing_public. [Online; accessed July-2020].

[102] **Simulador da circulação de fluidos envolvidos em uma operação de cimentação de poços de petróleo.** http://e3s.me/servicos_desenvolvimento_projetos_simentar.php. [Online; accessed July-2020].

[103] COOKE, C. E.; KLUCK, M. P. ; MEDRANO, R.. **Field measurements of annular pressure and temperature during primary cementing**. Journal of Petroleum Technology, 35, 8 1983.

[104] BINGHAM, E. C.. **Plasticity and elasticity**. Journal of the Franklin Institute, 197:99–115, 1924.

[105] BYBEE, K.. **A model of hydrostatic pressure loss in wells after cement placement**. Journal of Petroleum Technology, 55:51–52, 2003.

[106] VEBA, J.; STAVANGER, H.; N.E.N., T. ; STAVANGER, P.. **Testing system to evaluate the resistance of cement slurries to gas migration**. CADE/CAODC Spring Drilling Conference, 10, 1995.

[107] RIBEIRO, S.; MARCHESINI, F. H.. **Modular sensed annular well apparatus for cement testing**, 04 2018. US Patent 9,939,419-B2.

[108] RIBEIRO, S.; OLIVEIRA, R. M.; ROCHA, J. M.; SILVA, E. C.; DEMIRANDA, C. R. ; MARCHESINI, F. H.. **Paper in preparation**, - 2020.

[109] **Labview is systems engineering software for applications that require test, measurement, and control with rapid access to**

PUC-Rio - Certificação Digital Nº 1612794/CA

hardware and data insights. https://www.ni.com/pt-br/shop/labview.html. [Online; accessed July-2020].

[110] STANDARD-API-RP-10B-2016. **Recommended practice for testing well cements**, 1 2016.

[111] PASCAL, B.; DESPREZ, G.. **Traitez de l'equilibre des liqueurs, et de la pesanteur de la masse de l'air**. Collection Léo Pariseau. chez Guillaume Desprez, 1698.

[112] **Flush sensor: 4 reasons why.** https://www.youtube.com/watch?v=lmbLwlnqI3g. [Online; accessed August-2020].

[113] **Honeywell a-105: Datasheet**. https://measurementsensors.honeywell.com/ProductDocuments/Pressure/Model_A-105_Datasheet.pdf. [Online; accessed August-2020].

[114] **Honeywell 125-types: Datasheet**. https://sensing.honeywell.com/honeywell-test-and-measurement-model-125-load-cell-produt-sheet-008665-2-
pdf. [Online; accessed August-2020].

[115] **National instruments cdaq 9188xt**. http://sine.ni.com/nips/cds/view/p/lang/pt/nid/211734/&pn=782824-01&qty=1&pn=151733-02&qty=1&pn=781093-01&qty=1&pn=779473-01&qty=1.

[116] **National instruments products**. https://www.ni.com/pt-br/shop.html. [Online; accessed October-2020].

[117] **Oil well cementing testing**. https://www.fann.com/fann/default.html. [Online; accessed November-2020].

[118] ROGERS, M. J.; DILLENBECK, R. L. ; EID, R. N.. **Definitions and misconceptions, related to annular fluid migration**. Society of Petroleum Engineers, 2004.

[119] **Rheometers**. https://www.tainstruments.com/products/rheology. [Online; accessed November-2020].

[120] INSTITUTE, A. P.. **Oil-well Cementing Practices in the United States**. American Petroleum Institute, Division of Production, 1958.

[121] YANG, M.; NEUBAUER, C. ; JENNINGS, H.. **Interparticle potential and sedimentation behavior of cement suspensions: Review and results from paste**. Advanced Cement Based Materials, 5:1–7, 1997.

PUC-Rio - Certificação Digital Nº 1612794/CA

[122] LILE, O. B.; ELVEBAKK, H.; BACKE, K. R.; SKALLE, P. ; LYOMOV, S.. **A new technique for measuring permeability and tensile strength of a curing oil well cement**. Advances in Cement Research, 9, 04 1997.

[123] COUSSY, O.; DANGLA, P.; LASSABATÈRE, T. ; BAROGHEL-BOUNY, V.. **The equivalent pore pressure and the swelling and shrinkage of cement-based materials**. Materials and Structures, 37:15–20, 2004.

[124] SISSENOV, O.; RUZHNIKOV, A.. **Modelling of casing reciprocation during cement displacement in ERD wells**. In: ABU DHABI INTERNATIONAL PETROLEUM EXHIBITION & CONFERENCE. Society of Petroleum Engineers, 2017.

[125] PRASANTH, N.; SHENOY, U. V.. **Poiseuille flow of a power–law fluid between coaxial cylinders**. Journal of Applied Polymer Science, 46:1189–1194, 1992.

[126] OUTMANS, H.. **Mechanics of static and dynamic filtration in the borehole**. Society of Petroleum Engineers Journal, 3:236–244, 1963.

[127] GRACE, H. P.. **Resistance and compressibility of filter cake**. Chem. Eng. Progr., 49:303–367, 1953.

[128] DESBRIERES, J.. **Cement cake properties in static filtration. influence of polymeric additives on cement filter cake permeability**. Cement and Concrete Research, 23:347–358, 1993.

[129] BATCHELOR, G. K.. **Sedimentation in a dilute dispersion of spheres**. Journal of Fluid Mechanics, 52:245, 1972.

[130] BATCHELOR, G. K.. **Sedimentation in a dilute polydisperse system of interacting spheres. part 1. general theory**. Journal of Fluid Mechanics, 119:379, 1982.

[131] BATCHELOR, G. K.; WEN, C.-S.. **Sedimentation in a dilute polydisperse system of interacting spheres. part 2. numerical results**. Journal of Fluid Mechanics, 124:495, 1982.

[132] VALIOULIS, I. A.; LIST, E. J.. **Numerical simulation of a sedimentation basin. 1. model development**. Environmental Science & Technology, 18:242–247, 1984.

[133] VALIOULIS, I. A.; LIST, E. J.. **Numerical simulation of a sedimentation basin. 2. design application**. Environmental Science & Technology, 18:248–253, 1984.

PUC-Rio - Certificação Digital Nº 1612794/CA

[134] KRISHNAPPAN, B. G.. **Modelling of settling and flocculation of fine sediments in still water**. Canadian Journal of Civil Engineering, 17:763–770, 1990.

[135] KARL, J. R.; WELLS, S. A.. **Numerical model of sedimentation/thickening with inertial effects**. Journal of Environmental Engineering, 125:792–806, 1999.

[136] XIAO, Y.; YANG, F. S.; ZHOU, Y. J. ; CHEN, W. S.. **1-d numerical modeling of the mechanics of gravity-driven transport of fine sediments in the three gorges reservoir**. Lake and Reservoir Management, 31:83–91, 2015.

[137] EINSTEIN, A.. **Die grundlage der allgemeinen relativitätstheorie**. Annalen der Physik, 354:769–822, 1916.

[138] MEI, C. C.. **Relations between stress and rate-of-strain tensors**. Lecture Notes on Fluid Dynamics. 2007.

[139] LONG, R.. **Mechanics of Solids and Fuels**. Prentice-Hall international series in engineering of the physical sciences. Prentice-Hall, 1961.

[140] ARIS, R.. **Vectors, tensors, and the basic equations of fluid mechanics**. Dover books on engineering. Dover Publications, dover ed edition, 1989.

[141] TATTERSALL, G.; BANFILL, P.. **The rheology of fresh concrete**. Pitman Advanced Publishing Program, 1983.

[142] BACKE, K. R.; SKALLE, P.; LILE, O. B.; LYOMOV, S. K.; JUSTNES, H. ; SVEEN, J.. **Shrinkage of oil well cement slurries**. Journal of Canadian Petroleum Technology, 37, 9 1998.

[143] CHENG, A. H.-D.; CHENG, D. T.. **Heritage and early history of the boundary element method**. Engineering Analysis with Boundary Elements, 29:268–302, 2005.

[144] REYNOLDS, O.. **Papers on mechanical and physical subjects**. Reprinted from Various Transactions and Journals, 11:740, 1881-1900.

[145] FICK, D. A.. **Ueber diffusion**. Annalen der Physik, 170:59–86, 1855.

[146] NEWTON, I.. **Philosophiae Naturalis Principia Mathematica**. 1687.

PUC-Rio - Certificação Digital Nº 1612794/CA

[147] CAUCHY, A.-L.. **Cours D'analyse de L'École Royale Polytechnique**. Cambridge Library Collection - Mathematics. Cambridge University Press, 1 edition, 1855.

[148] ROBERTSON, R.; STIFF, H.. **An improved mathematical model for relating shear stress to shear rate in drilling fluids and cement slurries**. Society of Petroleum Engineers Journal, 16:31–36, 1976.

[149] DE SOUZA MENDES, P. R.; DUTRA, E. S. S.. **Viscosity function for yield-stress liquids**. Applied Rheology, 14:296–302, 2004.

[150] DE SOUZA MENDES, P. R.. **Dimensionless non-newtonian fluid mechanics**. Journal of Non-Newtonian Fluid Mechanics, 147:109–116, 2007.

[151] TINSLEY, J. M.; MILLER, E. C.; SABINS, F. L. ; SUTTON, D. L.. **Study of factors causing annular gas flow following primary cementing**. Journal of Petroleum Technology, 32, 08 1980.

[152] SABINS, F. L.; TINSLEY, J. M. ; SUTTON, D. L.. **Transition time of cement slurries between the fluid and set states**. Society of Petroleum Engineers Journal, 22:875–882, 1982.

[153] PEIRÓ, J.; SHERWIN, S.. **Handbook of Materials Modeling**. Springer Netherlands, 2005.

[154] TAYLOR, B.. **Methodus incrementorum directa & inversa**. Inny, 1717.

[155] RICHARDSON, L. F.. **The approximate arithmetical solution by finite differences of physical problems involving differential equations, with an application to the stresses in a masonry dam**. Philosophical Transactions Mathematical Physical & Engineering Sciences, 210:307–357, 1911.

[156] LEIBNIZ, G.; KNOBLOCH, E.. **Mathematische Schriften: Infinitesimalmathematik**.

[157] ARROYO, J. J.; GARAY, O. J. ; PAMPANO, A.. **Boundary value problems for euler-bernoulli planar elastica. a solution construction procedure**. Journal of Elasticity, 2019.

[158] EULER, L.. **Methodus inveniendi lineas curvas maximi minimive proprietate gaudentes sive solutio problematis isoperimetrici**

PUC-Rio - Certificação Digital Nº 1612794/CA

latissimo sensu accepti, volumen 1. Springer Science & Business Media, 1952.

[159] STRUTT, J. W.. **The theory of sound**, volumen 1. Macmillan and Company, 1877.

[160] RITZ, V. H. W.. **Über eine neue methode zur lösung gewisser variationsprobleme der mathematischen physik.** Journal für die reine und angewandte Mathematik (Crelles Journal), 1909:1–61, 1909.

[161] GALERKIN, B.. **Rods and plates. series occurring in various questions concerning the elastic equilibrium of rods and plates. eng**. Bull.(Vestnik Inzhenerov), 19:897–908, 1915.

[162] COURANT, R.. **Variational methods for the solution of problems of equilibrium and vibrations**. Bulletin of the American Mathematical Society, 49:1–24, 1943.

[163] TURNER, M. J.; CLOUGH, R. W.; MARTIN, H. C. ; TOPP, L.. **Stiffness and deflection analysis of complex structures**. journal of the Aeronautical Sciences, 23(9):805–823, 1956.

[164] MOËS, N.; DOLBOW, J. ; BELYTSCHKO, T.. **A finite element method for crack growth without remeshing**. International Journal for Numerical Methods in Engineering, 46:131–150, 1999.

[165] BELYTSCHKO, T.; BLACK, T.. **Elastic crack growth in finite elements with minimal remeshing**. International journal for numerical methods in engineering, 45(5):601–620, 1999.

[166] **Dolfin: Automated finite elements**. `https://fenicsproject.org/docs/dolfin/dev/python/installation.html`. [Online; accessed June-2020].

[167] LOGG, A.; WELLS, G. N.. **Dolfin: Automated finite element computing**. ACM Trans. Math. Softw., 37(2), Apr. 2010.

[168] **The fenics computing platform**. `http://femtable.org`. [Online; accessed October-2020].

[169] GARTLING, D.KAND REDDY, J. N.. **The Finite Element Method in Heat Transfer and Fluid Dynamics, Third Edition**. CRC series in computational mechanics and applied analysis. CRC Press, 3rd ed edition, 2010.

PUC-Rio - Certificação Digital Nº 1612794/CA

[170] CASTILLO, J. E.; STEINBERG, S. ; ROACHE, P. J.. **Mathematical aspects of variational grid generation ii**. Journal of Computational and Applied Mathematics, 20:127–135, 1987.

[171] BERN, M.; PLASSMANN, P.. **Mesh Generation - Handbook of Computational Geometry**. Elsevier, 2000.

[172] MITTAL, S.. **On the performance of high aspect ratio elements for incompressible flows**. Computer Methods in Applied Mechanics and Engineering, 188:269–287, 2000.

[173] COXETER, H. S. M.. **The polytopes with regular-prismatic vertex figures**. Philosophical Transactions Mathematical Physical & Engineering Sciences, 229:329–425, 1930.

[174] XIAO, Y.; YANG, F. S.; ZHOU, Y. J. ; CHEN, W. S.. **Periodic table of the finite elements**. SIAM News, 47, 2014.

[175] BABUŠKA, I.. **The finite element method with lagrangian multipliers**. Numerische Mathematik, 20:179–192, 1973.

[176] BREZZI, F.. **On the existence, uniqueness and approximation of saddle-point problems arising from lagrangian multipliers**. ESAIM: Mathematical Modelling and Numerical Analysis - Modélisation Mathématique et Analyse Numérique, 8(R2):129–151, 1974.

[177] TAYLOR, C.; HOOD, P.. **A numerical solution of the navier-stokes equations using the finite element technique**. Computers & Fluids, 1:73–100, 1973.

[178] ZIENKIEWICZ, O. C.; QU, S.; TAYLOR, R. L. ; NAKAZAWA, S.. **The patch test for mixed formulations**. International Journal for Numerical Methods in Engineering, 23:1873–1883, 1986.

[179] BERCOVIER, M., P. O.. **Error estimates for finite element method solution of the stokes problem in the primitive variables.** Numerische Mathematik, 33:211–224, 1979.

[180] LEE, Y.-J.; LI, H.. **On stability, accuracy, and fast solvers for finite element approximations of the axisymmetric stokes problem by hood–taylor elements**. SIAM Journal on Numerical Analysis, 49:668–691, 2011.

PUC-Rio - Certificação Digital Nº 1612794/CA

[181] GUZMÁN, J.; SÁNCHEZ, M. A.. **Max-norm stability of low order taylor–hood elements in three dimensions**. Journal of Scientific Computing, 65:598–621, 2015.

[182] COURANT, R.; FRIEDRICHS, K. ; LEWY, H.. **Über die partiellen differenzengleichungen der mathematischen physik**. Mathematische Annalen, 100:32–74, 1928.

[183] AMESTOY, P.; DUFF, I. S.; KOSTER, J. ; L'EXCELLENT, J.-Y.. **A fully asynchronous multifrontal solver using distributed dynamic scheduling**. SIAM Journal on Matrix Analysis and Applications, 23(1):15–41, 2001.

[184] AMESTOY, P.; BUTTARI, A.; L'EXCELLENT, J.-Y. ; MARY, T.. **Performance and Scalability of the Block Low-Rank Multifrontal Factorization on Multicore Architectures**. ACM Transactions on Mathematical Software, 45:2:1–2:26, 2019.

[185] PAPADOPOULOS, P.; TAYLOR, R. L.. **A generalized newton method for higher-order finite element approximations in non-linear elasticity**. International Journal for Numerical Methods in Engineering, 39:2635–2646, 1996.

[186] SHADID, J. N.. **A fully-coupled newton-krylov solution method for parallel unstructured finite element fluid flow, heat and mass transfer simulations**. International Journal of Computational Fluid Dynamics, 12:199–211, 1999.

[187] KIM, S. D.; LEE, Y. H. ; SHIN, B. C.. **Newton's method for the navier-stokes equations with finite-element initial guess of stokes equations**. Computers & Mathematics with Applications, 51:805–816, 2006.

[188] GARBALIŃSKA, H.. **Measurement of the mass diffusivity in cement mortar: use of initial rates of water absorption**. International Journal of Heat and Mass Transfer, 45:1353–1357, 2002.

[189] YE, M. Z. G.. **Modelling of time dependency of chloride diffusion coefficient in cement paste**. Journal of Wuhan University of Technology-Mater. Sci. Ed., 25:687–691, 2010.

[190] KHODADADI, A.. **Investigation of gas migration in khangiran wells**. Gospodarka Surowcami Mineralnymi, 2008.

PUC-Rio - Certificação Digital Nº 1612794/CA

[191] GOODE, J. M.. **Gas and water permeability data for some common oilwell cements**. Journal of Petroleum Technology, 14:851–854, 1962.

[192] ORBAN, J.; PARCEVAUX, P. ; GUILLOT, D.. **Influence of shear history on the rheological properties of oil well cement slurries**. In: 8TH INTERNATIONAL CONGRESS ON THE CHEMISTRY OF CEMENT, volumen 6, p. 243–247, 1986.

[193] WILLIAMS, D. A.; SAAK, A. W. ; JENNINGS, H. M.. **The influence of mixing on the rheology of fresh cement paste**. Cement and Concrete Research, 29:1491–1496, 1999.

[194] FREDRICKSON, ARNOLD; BIRD, R. B.. **Non-newtonian flow in annuli**. Industrial & Engineering Chemistry, 50:347–352, 1958.

[195] AMESTOY, P.; DUFF, I. S.; KOSTER, J. ; L'EXCELLENT, J.-Y.. **A fully asynchronous multifrontal solver using distributed dynamic scheduling**. SIAM Journal on Matrix Analysis and Applications, 23(1):15–41, 2001.

[196] AMESTOY, P.; BUTTARI, A.; L'EXCELLENT, J.-Y. ; MARY, T.. **Performance and Scalability of the Block Low-Rank Multifrontal Factorization on Multicore Architectures**. ACM Transactions on Mathematical Software, 45:2:1–2:26, 2019.

PUC-Rio - Certificação Digital Nº 1612794/CA

A
Published patent

US 20160274078A1

(19) **United States**

(12) **Patent Application Publication**

Ribeiro et al.

(10) **Pub. No.: US 2016/0274078 A1**

(43) **Pub. Date: Sep. 22, 2016**

(54) **MODULAR SENSED ANNULAR WELL APPARATUS FOR CEMENT TESTING**

(71) Applicant: **HALLIBURTON ENERGY SERVICES, INC.**, Houston, TX (US)

(72) Inventors: **Sergio S. Ribeiro**, Rio de Janeiro (BR); **Flávio H. Marchesini**, Rio de Janeiro (BR)

(73) Assignee: **HALLIBURTON ENERGY SERVICES, INC.**, Houston, TX (US)

(21) Appl. No.: **14/411,994**

(22) PCT Filed: **Oct. 30, 2013**

(86) PCT No.: **PCT/US2013/067601**

§ 371 (c)(1),
(2) Date: **Dec. 30, 2014**

Publication Classification

(51) **Int. Cl.**
G01N 33/38 (2006.01)

(52) **U.S. Cl.**
CPC ***G01N 33/383*** (2013.01); *E21B 33/14* (2013.01)

(57) **ABSTRACT**

In some implementations, a cement testing system includes an upper end module and a lower end module. Casing-emulating tubing couples to the upper end module and to the lower end module and emulates a wellbore casing. A plurality of intermediate well-wall-emulating modules is configured to couple end-to-end and to couple to the upper end module and the lower end module to form an annulus around the casing emulating tubing. Each of the plurality of intermediate well-wall emulating modules is configured to emulate one or more characteristics of a well wall.

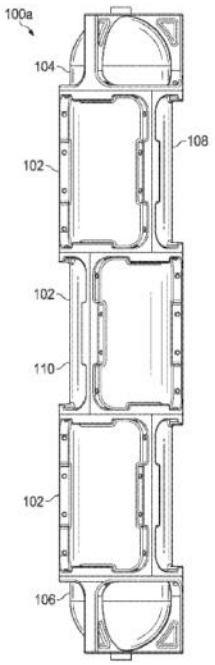

PUC-Rio - Certificação Digital Nº 1612794/CA

Patent Application Publication Sep. 22, 2016 Sheet 1 of 14 US 2016/0274078 A1

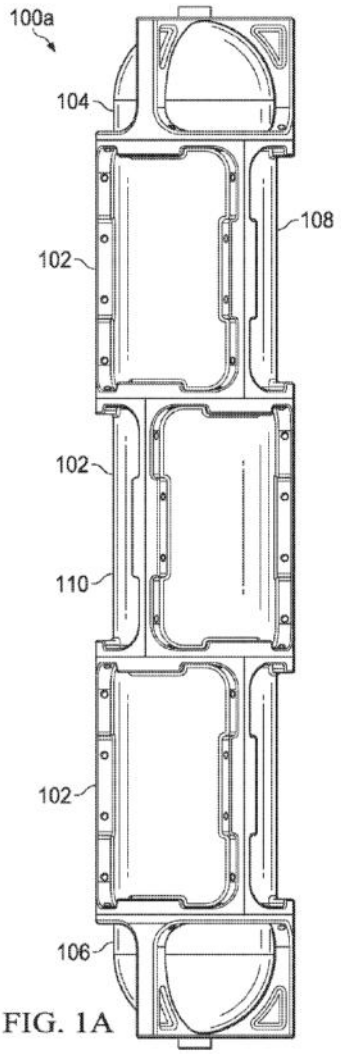

FIG. 1A

PUC-Rio - Certificação Digital Nº 1612794/CA

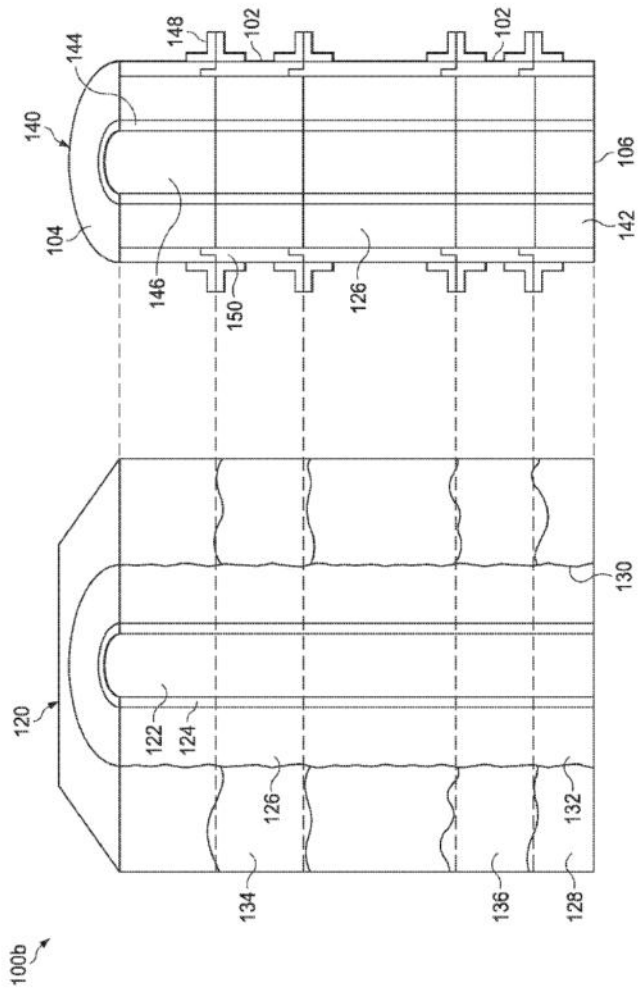

FIG. 1B

PUC-Rio - Certificação Digital Nº 1612794/CA

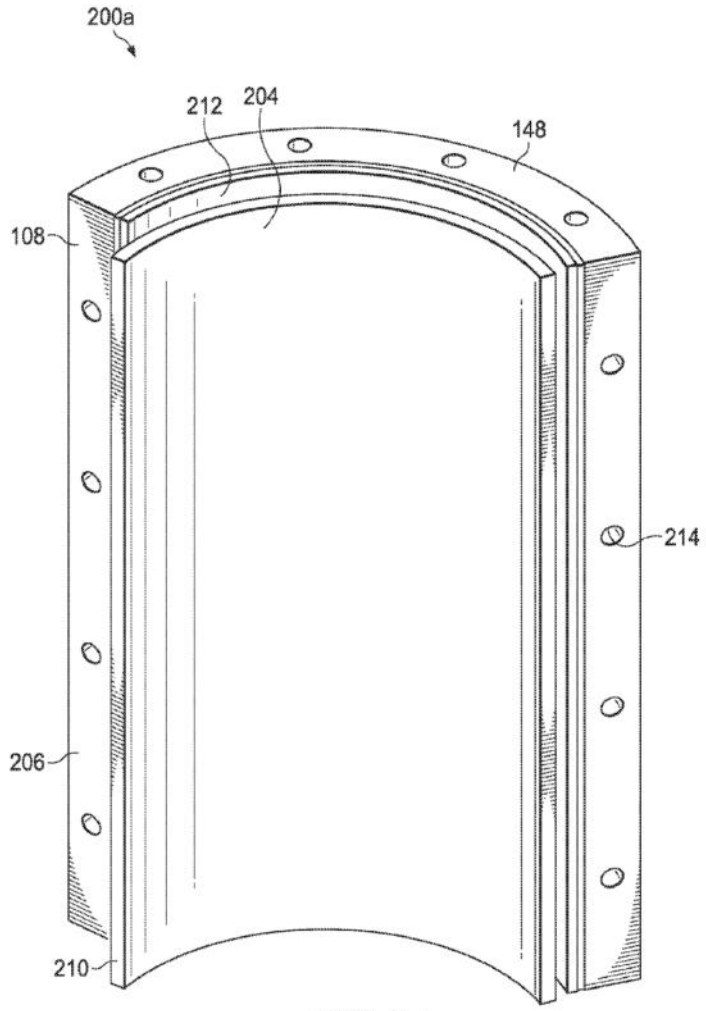

FIG. 2A

PUC-Rio - Certificação Digital Nº 1612794/CA

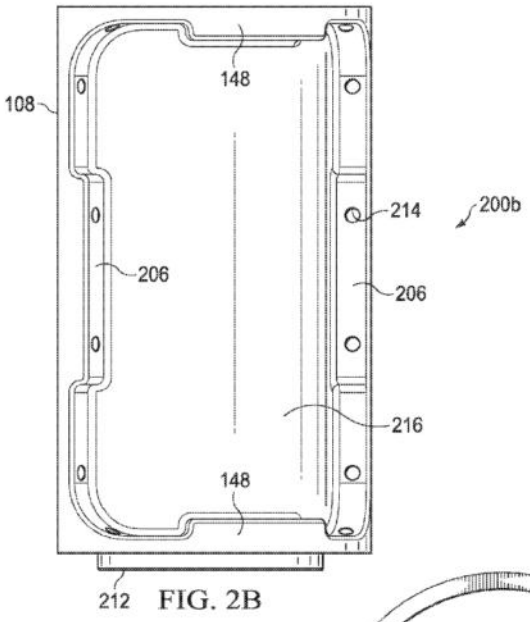

FIG. 2B

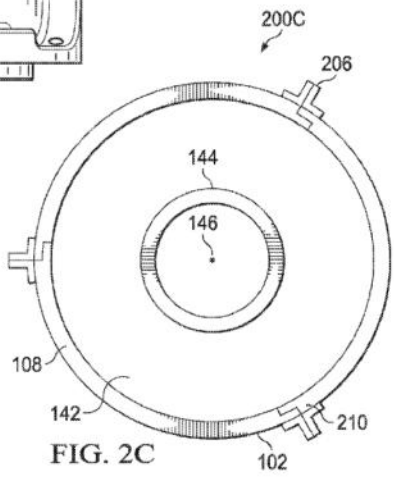

FIG. 2C

PUC-Rio - Certificação Digital Nº 1612794/CA

Patent Application Publication Sep. 22, 2016 Sheet 5 of 14 US 2016/0274078 A1

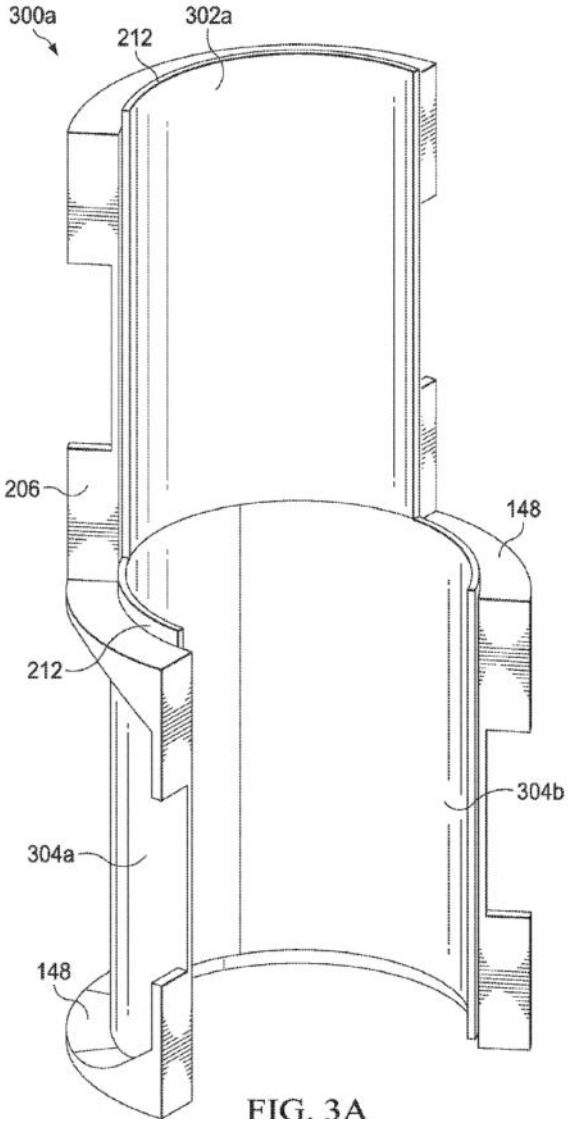

FIG. 3A

PUC-Rio - Certificação Digital Nº 1612794/CA

Patent Application Publication Sep. 22, 2016 Sheet 6 of 14 US 2016/0274078 A1

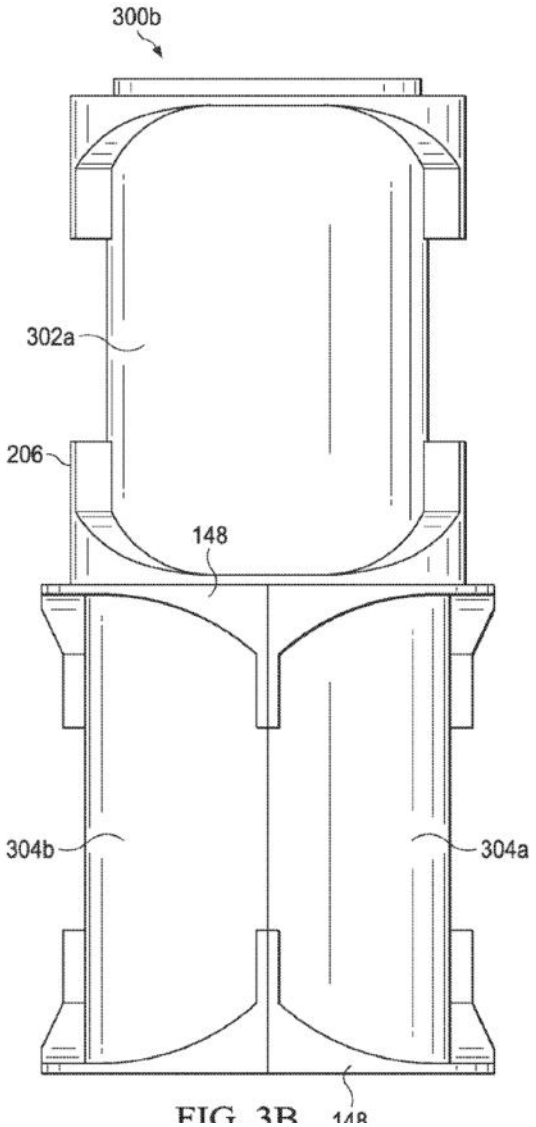

FIG. 3B

PUC-Rio - Certificação Digital Nº 1612794/CA

PUC-Rio - Certificação Digital Nº 1612794/CA

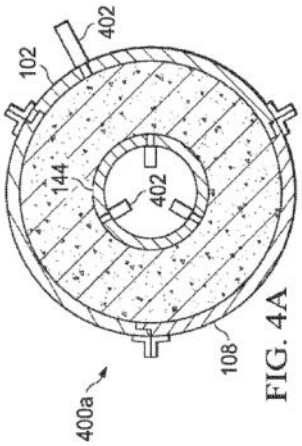

FIG. 4A

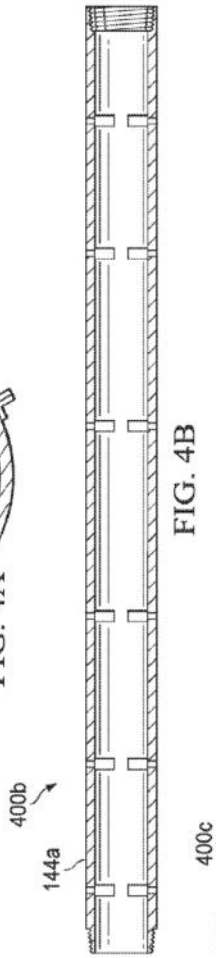

FIG. 4B

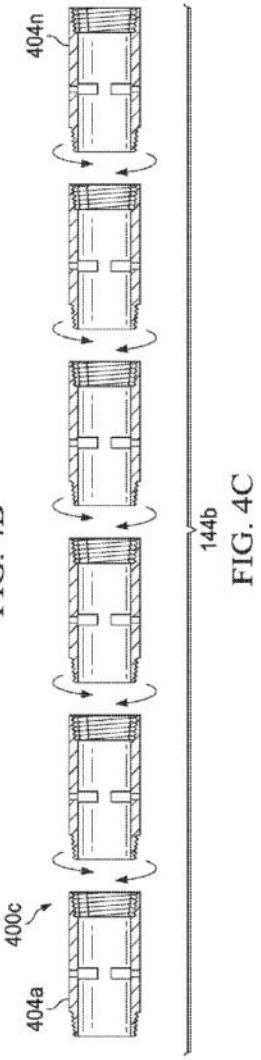

FIG. 4C

Patent Application Publication Sep. 22, 2016 Sheet 8 of 14 US 2016/0274078 A1

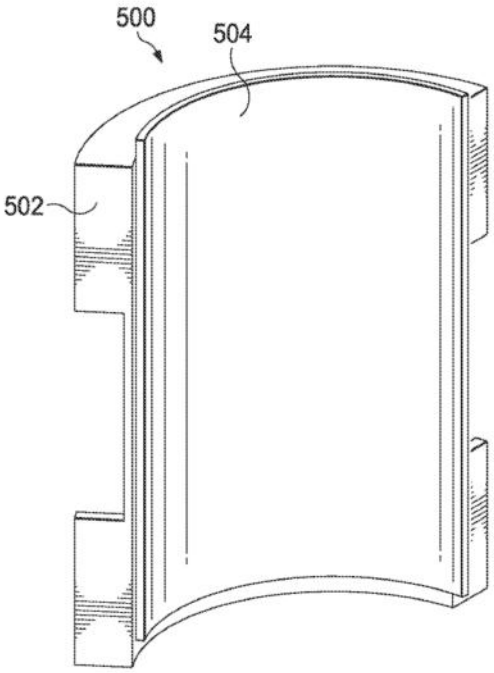

FIG. 5

PUC-Rio - Certificação Digital Nº 1612794/CA

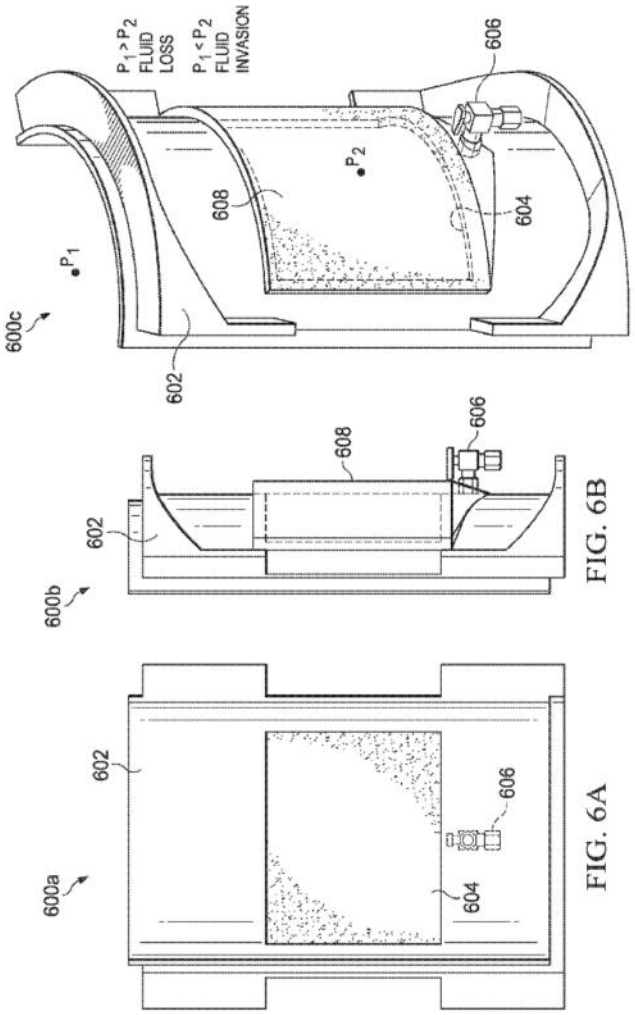

FIG. 6C

FIG. 6B

FIG. 6A

PUC-Rio - Certificação Digital Nº 1612794/CA

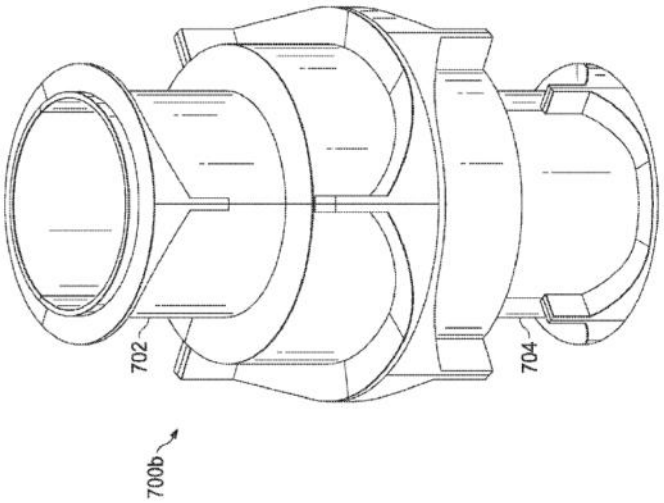

FIG. 7B

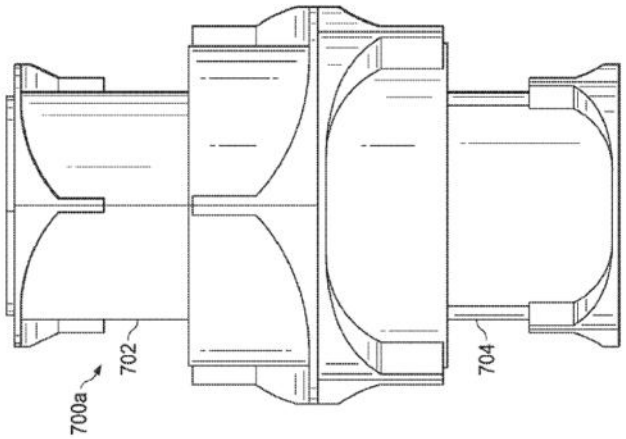

FIG. 7A

PUC-Rio - Certificação Digital Nº 1612794/CA

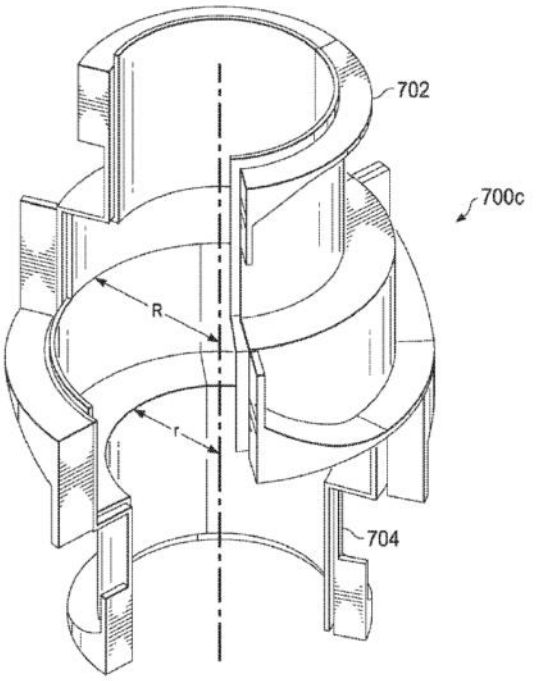

FIG. 7C

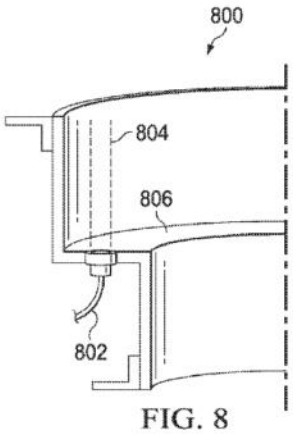

FIG. 8

PUC-Rio - Certificação Digital Nº 1612794/CA

Patent Application Publication Sep. 22, 2016 Sheet 12 of 14 US 2016/0274078 A1

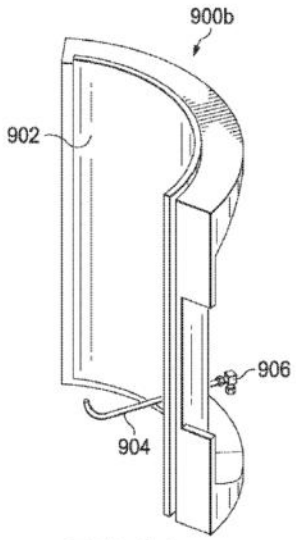

FIG. 9A

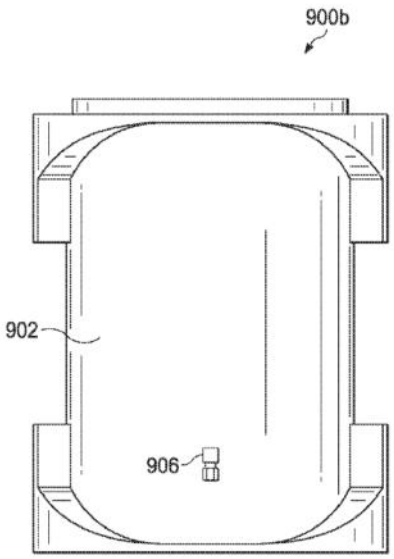

FIG. 9B

PUC-Rio - Certificação Digital Nº 1612794/CA

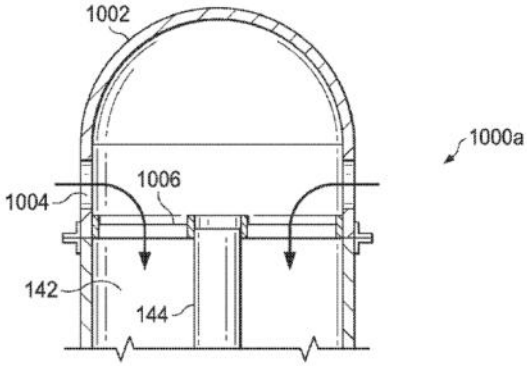

FIG. 10A

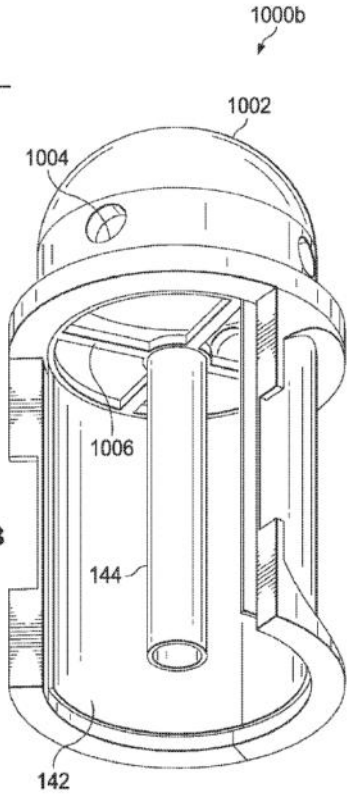

FIG. 10B

PUC-Rio - Certificação Digital Nº 1612794/CA

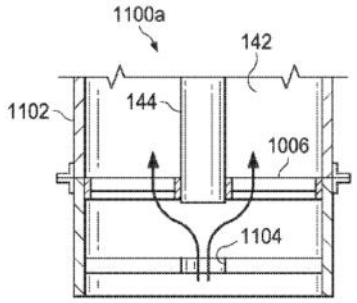

FIG. 11A

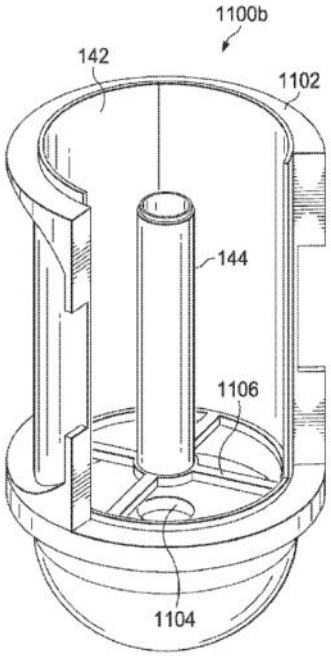

FIG. 11B

PUC-Rio - Certificação Digital Nº 1612794/CA

US 2016/0274078 A1 Sep. 22, 2016

MODULAR SENSED ANNULAR WELL APPARATUS FOR CEMENT TESTING

BACKGROUND

[0001] The specification relates to a cement testing system for predicting fluid invasion and migration phenomena in a cement column of a well after primary cementing. Fluid invasion and migration in cement are two well-known problems in the oil industry. While various contributing factors to the phenomena are associated with different cement and different well-zone characteristics, attempting to measure any of the various factors, particularly in combination, using an actual well is difficult and generally cost-prohibitive or not possible. Therefore, the predictive capability of the occurrence of fluid invasion and migration in zones of actual wells is very limited.

DESCRIPTION OF DRAWINGS

[0002] FIG. **1**A is side view of an example modular are designed sensed annular well (MADSAW) system according to an implementation.

[0003] FIG. **1**B is an illustration of an actual well in relation to an emulated well according to an implementation.

[0004] FIG. **2**A is a perspective view illustrating the interior of a regular arc module (RAM) according to an implementation.

[0005] FIG. **2**B is a view illustrating the exterior of a RAM according to an implementation.

[0006] FIG. **2**C is an intermediate axial cross-section of a plurality of RAMs used to form an intermediate well-wall emulating module (WEM) and an annulus around an emulated wellbore casing according to an implementation.

[0007] FIG. **3**A is a perspective view of RAM positional relationships with respect to coupled partial WEMs according to an implementation.

[0008] FIG. **3**B is a rear view of FIG. **3**A according to an implementation.

[0009] FIG. **4**A illustrates a sensored intermediate axial cross-section of FIG. **2**C according to an implementation.

[0010] FIG. **4**B is an illustration of a single piece casing emulating tubing according to an implementation

[0011] FIG. **4**C is an illustration of a modular casing emulating tubing according to an implementation.

[0012] FIG. **5** is an interior view of a roughened module (RM) special arc module (SAM) according to an implementation.

[0013] FIG. **6**A is a front view of a fluid exchange module (FEM) SAM according to an implementation.

[0014] FIG. **6**B is a side view of a FEM SAM according to an implementation.

[0015] FIG. **6**C is a perspective view of a FEM SAM according to an implementation.

[0016] FIG. **7**A is a side view of a coupled widening module (WM) SAM and a narrowing module (NM) SAM according to an implementation.

[0017] FIG. **7**B is a perspective view of a coupled WM SAM and a NM SAM according to an implementation.

[0018] FIG. **7**C is a cut-away view of a coupled WM SAM and a NM SAM according to an implementation.

[0020] FIG. **9**A is a perspective view of a fluid injection module (FIM) SAM according to an implementation.

[0021] FIG. **9**B is a front view of the FIM of FIG. **9**A according to an implementation.

[0022] FIG. **10**A is an illustration of a top module (TM) according to an implementation.

[0023] FIG. **10**B is a perspective cut-away view of the illustrated TM of FIG. **10**A.

[0024] FIG. **11**A is an illustration of a bottom module (BM) according to an implementation.

[0025] FIG. **11**B is a perspective cut-away view of the illustrated BM of FIG. **11**A.

[0026] Like reference numbers and designations in the various drawings indicate like elements.

DETAILED DESCRIPTION

[0027] The specification relates to a cement testing system for predicting fluid invasion and migration phenomena in a cement column of a well after primary cementing. The details of one or more implementations of the subject matter of this specification are set forth in the accompanying drawings and the description below. Other features, aspects, and advantages of the subject matter will become apparent from the description, the drawings, and the claims.

[0028] Fluid invasion and migration into a cement column after primary cementing are two well-known problems in the oil industry. Much effort has been devoted to understand various factors contributing to the occurrence of these phenomena and to different ways to prevent their occurrence. For example, cement-related factors contributing to fluid invasion and migration can include fluid loss to the formation, shrinkage, compressibility, yield stress, transient rheology, elasticity, and density. Formation-related factors contributing to fluid invasion and migration can include formation behavior, permeability, and long term mechanical properties. Other cement-related and/or formation-related factors contributing to fluid invasion and migration are also considered to be within the scope of this disclosure.

[0029] The following description relates to an implementation of a Modular Arc Designed Sensed Annular Well (MADSAW) system and method measuring fluid invasion and migration phenomena in a cement column of a well after primary cementing. The MADSAW creates an annular space to simulate in the laboratory a region of an actual well and can, among other things, simultaneously take into account all of the above-mentioned cement- and/or formation-related factors to reproduce an actual well condition in a controlled environment and to provide a predictive capability of the occurrence of fluid invasion in zones of actual wells. Additionally, the MADSAW has an external tube that is reusable after cement curing, reducing waste of resources and total cost of ownership. The MADSAW can also be used to measure and study pre- and post-cement set scenarios as well as a set cement sheath once the cement cures. As an example of pre-cement set scenario, the MADSAW can be used to study the effects of fluid properties and flow behavior on the displacement efficiency of one fluid by another inside an annular space, simulating a cement placement operation. The MADSAW permits testing of new technologies in a controlled laboratory environment before transitioning the technologies to the field.

PUC-Rio - Certificação Digital Nº 1612794/CA

intermediate well-wall emulating modules (WEMs) **102**, a top module (TM) **104**, and a bottom module (BM) **106**. Each WEM **102** is formed from a combination of regular arc modules (RAMs) **108** and/or special arc modules (SAMs) **110**. The TM **104** and BM **106** couple to an upper-end WEM **102** and to a lower-end WEM **102**, respectively, and to a casing emulating tubing (not illustrated—refer to FIG. **1**B) situated within the coupled WEMs **102**. The coupled WEMs **102** form an emulated annular space (not illustrated—refer to FIG. **1**B) around the casing emulated tubing. The TM **104** and BM **106** seal the emulated annular space.

[0031] FIG. **1**B is an illustration **100***b* of an actual well in relation to an emulated well according to an implementation. FIG. **1**B illustrates both an actual well **120** and an emulated well **140** (e.g., using the MADSAW illustrated in FIG. **1**A). An exemplary actual well **120** includes a wellbore **122**, a wellbore casing **124**, cement **126**, and a subterranean formation **128** through which the actual well **120** is drilled comprising one or more zones. The edge of the subterranean formation **128** adjacent to the cement forms a well wall **130**. The space between the well wall **130** and the outer surface of the wellbore casing **124** form an annular space **132** (here filled with cement **126**). Although illustrated with a single wellbore casing **124**, in some actual wells **120**, multiple diameter wellbore casings **124** can be nested partially within each other forming a plurality of differently sized annular spaces **132**. Each zone of the subterranean formation **128** can have different properties. For example, the illustrated permeable zone **134** can be permeable to a fluid or gas, such as water or natural gas, respectively, and the high-pressure zone **136** can subject the cement **126** at the well wall **130** of the high-pressure zone **136** to high pressures.

[0032] The emulated well **140** is illustrated using a simplified MADSAW as shown in FIG. **1**A. The MADSAW creates an emulated annular space (annulus) **142** around a casing emulated tubing **144** surrounding an emulated wellbore **146** using a plurality of WEMs **102** that are assembled in such a way to reproduce the different subterranean formation **128** zones of an actual well **120**, as illustrated in FIG. **1**. For example, WEM **102** can be used to emulate a permeable zone corresponding to the permeable zone **134** of the illustrated actual well **120**. Similarly, a WEM **102** can be used to emulate a high-pressure subterranean zone corresponding to the high-pressure zone **136** of the illustrated actual well **120**. The WEMs **102** can be arranged in such a manner as to emulate different actual well zone configurations. In some implementations, similar WEMs **102** can be combined, as needed, to provide additional length to cover different subterranean formation **110** zone lengths.

[0033] As illustrated, WEMs **102** can be coupled using a combination of one or more end flanges **148** and one or more interlocking end edges **150**. Any appropriate fastener (not illustrated) can be used in combination with the end flanges **148** to secure together the one or more end flanges **148** and to couple two WEMs **102**. Fasteners can include screws, bolts/nuts, rivets, welds, adhesives, and/or other fasteners. The interlocking end edge **150** (at the top and bottom of each illustrated WEM **102**) forms a "groove" for an interlocking end edge **150** of a second WEM **102** to fit into.

[0034] The casing emulating tubing **144** surrounding the surface of the WEMs **102** and the outer surface of the casing emulating tubing **144** can hold cement **126** and/or other substances.

[0035] The MADSAW also provides an upper end module **132** and a lower end module **134** (neither illustrated in detail). The top module **132** and bottom module **134** couple to an upper-end WEM **102** and a lower-end WEM **102**, respectively, and to the casing emulating tubing **144** to seal the emulated annular space **142**

[0036] FIGS. **2**A-**2**C illustrate views **200***a*-**200***c* of regular arc modules (RAMs) used to form a WEM **102** as illustrated in FIG. **1**. FIG. **2**A is a perspective view **200***a* of the interior of a RAM **108** according to an implementation. RAM **108** is configured with one or more side flanges **206**, one or more end flanges **148** (the "bottom" end flange **148** is not shown), interlocking side edges **210**, and interlocking end edges **212**. In some implementations, the side flanges **206** extend axially the length of the RAM **108**. In other implementations, the side flanges can be configured to form one or more separated side flanges **206** axially along the length of the RAM **108**. The interlocking side edges **210** form a lip/groove along the sides of the RAM **108** which interlock with a corresponding groove/lip of another RAM **108**. In some implementations, the interlocking side edges **210** can be coupled with a sealing material (not illustrated) to form a hermetic seal with an interlocking side edge **210** of another RAM **108**. For example, the sealing material can be rubber, plastic, silicone, and/or other sealing material.

[0037] Once interlocking side edges **210** of two RAMs **108** are interlocked, the corresponding side flanges **206** can be joined together with a fastener to secure the RAMs **108**. For example, the illustrated side flanges **206** are shown configured with plurality of fastener holes **214** passing through the side flanges **206** that can be used with bolt and nut type fasteners.

[0038] FIG. **2**B is a view **200***b* illustrating the exterior of a RAM according to an implementation. As illustrated, the RAM **108** has an exterior surface **216**. A particular implementation of the side flange **206**, end flange **208**, and interlocking end edge **212** as well as fastener holes **214** are also illustrated. Various implementations may have differently shaped side flanges **206**, end flanges **148**, and/or interlocking end edges **212**. In some implementations, there can be more or less fastener holes and/or different structures may be used for fasteners along the side edges **206** and/or end edges **208**.

[0039] FIG. **2**C is an intermediate axial cross-section **200***c* of a plurality of RAMs **108** used to form WEM **102** and an annulus **142** around casing emulating tubing **144** according to an implementation. Each RAM **108** that couples to form the WEM **102** forms a portion of the complete perimeter of the outer edge of the annulus **142** formed around the casing emulating tubing **144**. Each illustrated RAM **108** would span one-hundred and twenty degrees of the circumference of the illustrated WEM **102** forming the circular annulus **142** around the casing emulated tubing **144**. In other implementations, more or less RAMs **108** can be needed to form an annulus **142** around the casing emulated tubing **144**. For example, in some implementations, two RAMs **108** can be used, while in other implementations, three RAMs **108** can be used (as illustrated in the FIG. **3**A). While RAM **108** has been illustrated to be circular in shape, in other implementations, RAM **108** can be

PUC-Rio - Certificação Digital Nº 1612794/CA

the casing emulated tubing **144**. Other RAM **108** shapes are considered to also be within the scope of this disclosure.

[0040] In some implementations, RAMs **108** forming a WEM **102** can each span different portions of the perimeter of the outer edge of an annulus. For example, two RAMs **108** could each span sixty degrees of the perimeter of a circular annulus **142**, while two other RAMs **108** could each span one-hundred and twenty degrees to complete the perimeter.

[0041] FIG. **3**A is a perspective view **300***a* of RAM **108** positional relationships with respect to coupled partial WEMs **102** according to an implementation. To avoid stress concentration points in the MADSAW, in some implementations, RAMs **108** associated with a first WEM **102** can be rotated with respect to adjacent RAMs **108** associated with a second WEM **102**. For example, RAM **302***a* is rotated approximately sixty degrees in relation to RAMs **304***a*/**304***b* so that the edges of the RAMs do not line up with edges of adjacent RAMs. Note that the side flanges **206** are illustrated with an alternate configuration as compared to that shown in FIGS. **2**A-**2**C. Fastener holes **214** are also not illustrated.

[0042] Referring back to FIG. **2**A, the end flanges **148** and an end edges **212** are used in a similar manner to that of the side flanges **206** and side edges **210**, respectively, to couple a first WEM **102** to a second WEM **102**. For example, the WEM **102** formed by RAMs **304***a/b* (and another not illustrated RAM) is coupled to the WEM **102** formed by RAM **302***a* (and two other not illustrated RAMs).

[0043] Turning now to FIG. **3**B, FIG. **3**B is a rear view **300***b* of FIG. **3**A according to an implementation. Coupled alternate configurations of side flanges **206** and end flanges **148** are illustrated as discussed above with respect to FIG. **3**A.

[0044] FIGS. **4**A-**4**C illustrate views **400***a*-**400***c* of a casing emulated tubing **144** and sensor placement according to an implementation. FIG. **4**A illustrates a sensored intermediate axial cross-section of FIG. **2**C according to an implementation. As illustrated, one or more associated RAMs **108** can be individually sensored (e.g., with sensor **402**). Sensors **402** can be for temperature, pressure, strain, and/or other sensors and create a mesh of sensors through the MADSAW system. Sensors **402** monitor important physical quantities during a simulated scenario, providing insight into what is happening inside the MADSAW during testing. In some implementations, the casing emulating tubing **144** can be adapted with a sensor **402** to measure one or more characteristics of cement at the exterior of the casing emulating tubing **144**.

[0045] FIG. **4**B is an illustration **400***b* of a single piece casing emulating tubing **144***a* according to an implementation. Placement and/or reconfiguration of the sensor **404** within the single piece casing emulating tubing **144***a* can be difficult, time consuming, and/or cost prohibitive.

[0046] FIG. **4**C is an illustration **400***c* of a modular casing emulating tubing **144** according to an implementation. In some implementations, the modular casing emulating tubing **144***b* is formed from a plurality of single-piece intermediate tubing modules **404***a* . . . **404***n* that couple end-to-end to define an entire length of a casing emulating tubing **144**. In some implementations, fasteners can be used to couple the plurality of single-piece intermediate tubing modules **404***a* . . . **404***n*. In some implementations, each intermediate tubing module **404** has at least one threaded end to permit two intermediate tubing modules **404** to couple end-to-end. In casing emulating tubing. In this configuration, sensors **402** associated with an intermediate tubing module **404** in the interior/middle of a casing emulating tubing **144***b* can be unscrewed and swapped out for different sensors **402** much easier than in the implementation of the single piece casing emulating tubing **144***a* of FIG. **4**B. This modular design provides the advantage of allowing the MADSAW to have more sensors **402** placed along its length, because of relative ease of sensor **402** placement.

[0047] Special Arc Modules (SAMs) **110** (as illustrated in FIG. **1**A) are RAMs **108** modified for special purpose use. The SAMs **110** share groove/edge and flange connection patterns as described above, and can be assembled in different ways with RAMs **108** to form a variety of WEM **102** configurations. In some implementations, each WEM **102** can include different combinations of RAMs **108** and/or SAMs combined to form the perimeter of a WEM **102**. Several well conditions and scenarios can be reproduced individually or at the same time, depending on the assembled configuration.

[0048] FIG. **5** is an interior view **500** of a roughened module (RM) SAM **110** according to an implementation. In some implementations, the only difference between a roughened module (RM) **502** and a RAM **204** is the roughness of the internal surface **504**, as illustrated in FIG. **5**. For example, the roughness of the internal surface **504** of a roughened module (RM) **502** can range between 1 and 100 micrometers. In other implementations, macroscopic roughness ranging from 0.5 to 2 millimeters can be created on the internal surface **504** of a roughened module (RM) **502**. The roughness of the internal surface **504** is different than a roughness produced merely as a product of manufacturing the internal surface **504** of RM **502**. The roughness for the internal surface **504** is specially applied to the interior surface **504**. For example, the interior surface **504** can be machined, cast, adhered to, and/or manufactured in some other manner to yield a specified roughness. The roughness modification is designed for two primary purposes: 1) investigating well-wall roughness effects on simulated physical processes in the MADSAW, and 2) to prevent the occurrence in the MADSAW of phenomena such as apparent wall slip that can be observed in well field operations.

[0049] In typical implementations, roughness of a RM **502** can be easily configured using computer-aided drafting tools to produce a mold used to produce the RM **502** consistent with a specified roughness. Additionally, sets of RMs **502** with different roughness values can be assembled to emulate a well with multiple formation structures of various roughness values. To allow for a good comparison with the use of smoothly surfaced RAMs **204**, RMs **502** can be configured with the same sensors (not illustrated) that the RAMs **204** are configured with (as illustrated in FIG. **4** with sensor **402**).

[0050] FIGS. **6**A-**6**C illustrate views **600***a*-**600***c* of a fluid exchange module (FEM) according to an implementation. In some implementations, a RAM **108** is adapted as a fluid exchange module (FEM) to include a hermetic enclosure separated from the annulus **142** by an interface material with a specified permeability to fluid or gas to emulate different permeabilities of a well-wall in, for example, a highly-permeable zone or a high-pressure gas zone. In some implementations, a two-way valve is connected to the hermetic enclosure to establish a positive, equal, or negative pressure within

PUC-Rio - Certificação Digital Nº 1612794/CA

PUC-Rio - Certificação Digital Nº 1612794/CA

one set of FEMs **602** can be assembled in different MADSAW sections on an emulated well **140** to analyze the effect of changing the permeability between adjacent subterranean formation **128** layers. In some implementation, the permeable material **604** can be a metal mesh. In some implementations, the hermetic enclosure **608** can be made of polycarbonate or acrylic to permit visualization or from steel if the pressure P_2 is to exceed a tolerance threshold for the use of other materials. In some implementation, the two-way valve **606** can be automated by testing equipment to increase or decrease pressure within the hermetic enclosure **608** by allowing either the inlet or outlet of a fluid or gas.

[0051] FIG. **6**B is a side-view **600***b* of a FEM SAM according to an implementation. FIG. **6**B also illustrates the hermetic enclosure **608** surrounding the permeable material **604**.

[0052] FIG. **6**C is a perspective view **600***c* of the FEM SAM according to an implementation. As illustrated, a pressure P_2 can be applied inside the hermetic enclosure **608** to simulate either fluid loss or invasion depending on the magnitude of P_2 compared to P_1, the pressure inside the annulus. If $P_1>P_2$, than fluid loss can be simulated, otherwise fluid invasion can occur.

[0053] In some implementations, FEMs **602** can be configured with sensors **402** similar to those used with RAMs **108** and the casing emulated tubing **144**, in addition to a flow metering device (not illustrated) connected to the two-way valve **606** to measure a fluid loss/invasion flow rate. To enhance precision with a determination of P_2, the two-way valve **606** can, in some implementations, be replaced by an electrical valve with pressure control.

[0054] FIGS. **7**A-**7**C illustrate views **700***a*-**700***c* of views of a widening module (WM) and a narrowing module (NM) according to an implementation. Abrupt radius (r→R→r) variations of the annulus can drastically change flow behavior. WMs and NMs allow observation of the influence of radius changes in experiments such as fluid loss and cement placement. Modifying RAMs **204** with a radius R instead of r allows simulation of telescopic well sections and the evaluation of behavior of different slurries flowing through an expansion and/or contraction of a well. In some implementations, WMs and NMs are configured with the same sensors (e.g., sensor **402** of FIG. **4**) as RAMs **204** for gathering data.

[0055] FIG. **7**A is a side view **700***a* of a coupled WM **702** SAM and a NM **704** SAM according to an implementation. FIG. **7**B is a perspective view **700***b* of a coupled WM **702** SAM and a NM **704** SAM according to an implementation.

[0056] FIG. **7**C is a cut-away view **700***c* of a coupled WM **702** SAM and a NM **704** SAM according to an implementation. An abrupt radius (r→R→r) variation as described above is illustrated.

[0057] FIG. **8** is an illustration **800** of the use of a capacitive load cell on a horizontal surface of a WM **702** or a NM **704** according to an implementation. A WM **702** or a NM **704** can be configured with a capacitive load cell **802** or other sensor to measure a weight of a fluid column **804** above (or below in the case of a NM **704**) a horizontal surface **806**. In some implementations, other types of sensors can be substituted for, or used in conjunction with, the capacitive load cell **802** to collect data. For example, other sensors could be for temperature, pressure, and/or other data.

[0058] FIG. **9**A is a perspective view **900***a* of a fluid injection module (FIM) **902** and a RAM **108** according to an implementation. The FIM **902** is configured to inject a fluid or gas into the annulus **142** through a small pipe **904** that is inserted into the annulus **142** through a one-way valve **906**, which prevents contents within the annulus **142** from leaking through the small pipe **904**. The FIM **902** is designed for investigating the injection of a gas through the small pipe **904** into a cement slurry column, allowing for a better understanding of bubble growth and bubble migration phenomena.

[0059] In some implementations, the FIM **902** is configured with a sensor **402** in addition to a flow sensor incorporated into the one-way valve **906**. In some implementations, transparent FIMs **902** and RAMs **108** can be used together with a transparent modeling fluid if visualization is required; otherwise analysis of a cement **126** after curing can be made as a way to evaluate the bubble growth and bubble migration phenomena in each test. In some implementations, the FIM **902** can be used for the injection of other fluids besides gases. FIG. **9**B is a front view **900***b* of FIG. **9**A according to an implementation.

[0060] The bottom module (BM) and top module (TM) are SAMs designed not only to close the bottom and the top of the annulus **142**, respectively, but also, when desired, to allow the addition of an eccentricity on casing emulating tubing **144** of the MADSAW. In some implementations, each of the BM and TM has an internal wireframe, in which the casing emulating tubing **144** is connected. The internal wireframe can be changed in the TM and/or BM according to a desired eccentricity of the casing emulating tubing **144** in relation to the outer diameter of the annulus **142** formed by a plurality of WEMs **102**.

[0061] Typically, both the top and the bottom of the casing emulating tubing **144** are sealed to prevent entry of fluid into the casing emulating tubing **144**. In some instances, however, this configuration can be changed depending on a particular application under consideration. For example, fluid can be pumped from the top of the casing emulating tubing **144** and a study performed of the fluid displacement inside the annulus **142**. As will be appreciated by those of skill in the art, various modifications can be made to components of the MADSAW to accomplish desired types of testing.

[0062] FIGS. **10**A and **10**B illustrate views **1000***a* and **1000***b* of a TM **1002** according to an implementation. FIG. **10**A is an illustration **1000***a* of a TM according to an implementation. The illustrated TM **1002** is round in shape with four holes **1004** where different hoses can be connected for: 1) cement **126** or fluid exit from the annulus **142**, or 2) to pump cement **126** or other fluid into the annulus **142** from the top. In some implementations, a sensor **402** (not illustrated) that can measure the level of fluid inside the annulus **142** is placed on the top of the TM **1002**. Wireframe **1006** can be used to provide the above-described eccentricity to the casing emulating tubing **144** if desired. In other implementations, the illustrated TM **1002** can have more or less holes **1004** in different locations on the TM **1002**.

[0063] FIG. **10**B is a perspective cut-away view of the illustrated TM **1002** of FIG. **10**A. As can be seen in the perspective view **1000***b*, wireframe **1006** can be used to provide various eccentricities to the casing emulating tubing **144**. Although not illustrated in FIG. **10**A or **10**B, in some implementations, the casing emulating tubing **144** can be sealed to prevent introduction of cement **126** or other fluid when introduced into the annulus **142**.

[0064] FIGS. **11**A and **11**B illustrate views **1100***a* and **1100***b* of a bottom module according to an implementation.

connected to allow the injection of cement **126** or other fluids from the BM **1102**. The hole **104** can also be used as a cement **126**/fluid drain to remove cement **126**/fluid injected from the TM **1002**. In some implementations, the BM **1102** is sensed for pressure and temperature using one or more sensors **402**. In addition, in some implementations, a capacitive load cell as described in FIG. **8** can be installed to measure a fluid-column weight as a function of time. In some implementations, other types of sensors can be substituted for, or used in conjunction with, the capacitive load cell to collect data. For example, other sensors could be for temperature, pressure, strain, and/or other data. In other implementations, the illustrated BM **1102** can have more or less holes **1104** in different locations on the BM **1102**.

[0065] FIG. **11**B is a perspective cut-away view of the illustrated BM **1102** of FIG. **11**A. As can be seen in the perspective view **1100***b*, wireframe **1006** can be used to provide various eccentricities to the casing emulating tubing **144**. Although not illustrated in FIG. **11**A or **11**B, in some implementations, the casing emulating tubing **144** can be sealed to prevent introduction of cement **126** or other fluid when introduced into the annulus **142**.

[0066] In some implementations, an exemplary method for measuring fluid invasion and migration into a cement column is as follows. At a high-level, the MADSAW system is assembled to represent a well scenario of interest by, for example, assembling appropriate well-wall emulating modules in a particular order. A cement slurry is then placed into the annular space of the MADSAW system and relevant variables measured during cement gelation and hydration to evaluate the likelihood of fluid invasion and migration.

[0067] At a low-level, following the assembly of the MADSAW system, the first step is to prepare a cement slurry and continuously pump it from the bottom of the annulus. When a sensor placed on the top of the annulus indicates that the slurry has achieved a desired position in the annulus, the pumping is stopped and a test time is set to zero to identify the end of cement placement and the start of the test. Recording of some or all available measurements is then started. In some implementations, measurements can include temperature and pressure as a function of depth, cement slurry weight, position of the top of cement, fluid-loss rate, and or other measurement.

[0068] During the test, as the time increases and the gelation and hydration of the cement evolves, a cement volume reduction may be observed. The volume reduction is more relevant when both an early shrinkage of the cement and fluid loss are more significant. The volume reduction coupled with changes in rheology of the cement leads to a decrease in pressure inside the cement slurry column. As a consequence, two possible behaviors will likely be observed: 1) the pressure decrease is not so high that the pressure inside the cement slurry column is maintained above the outside annular pressure until the cement sets or 2) the pressure decrease is high enough to cause the pressure inside the cement slurry column to become lower than the pressure of the hermetic enclosures of FEMs.

[0069] Behavior 1) indicates little-to-no risk of fluid invasion during cement setting. Behavior 2), however, indicates a tendency of the pressurized fluid inside hermetic enclosures the top of the annulus. The gas invasion and the gas migration can be detected and evaluated by the sensors along the entire length of the MADSAW.

[0070] In some implementations, five primary cement-related factors are taken into account by this method. Fluid loss is directly measured by the MADSAW system. In addition, due to the fact that there would then be a total volume reduction of the cement column, the fluid loss, weight of the cement, and cement shrinkage can be measured as a function of time. Moreover, due to fluid loss and shrinkage, the yield stress and transient rheology of the cement can affect the measured pressure inside the cement column. Finally, as actual cement is being used in the test, if the pressure decrease inside the cement column is significant, compressibility of the cement can also play a role in fluid invasion and migration measurements.

[0071] In some implementations, the MADSAW can also be used to simulate fluid displacement and/or flow inside an actual well if modifications are made or new special modules are designed. As will be appreciated by those of skill in the art, operations involving fluid displacements, circulation, or cementing can also be simulated by the MADSAW and are considered to be within the scope of this disclosure.

[0072] The foregoing description is provided in the context of one or more particular implementations. Various modifications, alterations, and permutations of the disclosed implementations can be made. Thus, the present disclosure is not intended to be limited only to the described and/or illustrated implementations, but is to be accorded the widest scope consistent with the principles and features disclosed herein.

What is claimed is:

1. A cement testing system, comprising:

an upper end module;

a lower end module;

a casing emulating tubing that couples to the upper end module and to the lower end module and emulates a wellbore casing; and

a plurality of intermediate well-wall emulating modules that couple end-to-end and to the upper end module and the lower end module to form an annulus around the casing emulating tubing, each of the plurality of intermediate well-wall emulating modules configured to emulate one or more characteristics of a well wall.

2. The system of claim **1**, wherein the upper end module and the lower end module each comprise an internal wireframe to which the casing emulating tubing can connect, the internal wireframe configurable to put a specified eccentricity on the casing emulating tubing in relation to the outer diameter of the annulus formed by the plurality of intermediate well-wall emulating modules.

3. The system of claim **1**, wherein the casing emulating tubing comprises a plurality of intermediate tubing modules that couple end-to-end and one or more of the intermediate tubing modules comprise a sensor adapted to measure one or more characteristics of cement from the exterior of the casing emulating tubing.

4. The system of claim **3**, wherein each intermediate tubing module has at least one threaded end to permit two intermediate tubing modules to couple end-to-end by screwing

PUC-Rio - Certificação Digital Nº 1612794/CA

6. The system of claim **5**, wherein each arc module forms a portion of the complete perimeter of the outer edge of the annulus around the casing emulating tubing formed by the plurality of arc modules.

7. The system of claim **5**, wherein one or more of the arc module comprises a sensor.

8. The system of claim **5**, wherein each are module comprises an axial flange and an axial edge used to couple a first are module to a second are module in forming an intermediate well-wall emulating module.

9. The system of claim **5**, wherein each are module comprises a radial flange and a radial edge used to secure the arc module to an are module forming another intermediate well-wall emulating module.

10. The system of claim **5**, wherein an are module comprises a well-wall emulating inner surface comprising a specified roughness.

11. The system of claim **5**, wherein an are module comprises a hermetic enclosure separated from the annulus by a material with a specified permeability to fluid or gas to emulate the permeability of a wall of a wellbore and a valve connected to the hermetic enclosure to establish a pressure within the hermetic enclosure.

12. The system of claim **5**, wherein an arc module radius varies with respect to the radius of an intermediate well-wall emulating module.

13. The system of claim **5**, wherein an arc module comprises a one-way valve to inject a fluid or gas into the annulus.

14. A cement testing system having a plurality of intermediate well-wall emulating modules surrounding a casing emulating tubing and forming an annulus, each of the plurality of intermediate well-wall emulating modules configured to emulate one or more different characteristics of a well wall.

15. The cement testing system of claim **14**, having an upper end module and a lower end module that couples to the plurality of intermediate well-wall emulating modules and casing emulating tubing to seal the annulus.

16. The cement testing system of claim **14**, having a plurality of intermediate tubing modules that couple end-to-end to form the casing emulating tubing.

17. The cement testing system of claim **14**, wherein the plurality of intermediate well-wall emulating modules are configured to couple end-to-end.

18. A method for testing cement, comprising:

defining a casing emulating tubing by a plurality of intermediate tubing modules coupled end-to-end;

forming an annulus with a plurality of coupled intermediate well-wall emulating modules surrounding the casing emulated tubing with, each of the plurality of intermediate well-wall emulating modules configured to emulate one or more different characteristics of a well-wall;

sealing the annulus with an upper end module and a lower end module coupled to the casing emulating tubing and to the plurality of coupled intermediate well-wall emulating modules; and

measuring data associated with cement introduced into the annulus.

19. The method of claim **18**, wherein data is measured using a sensor associated with an intermediate well-wall emulating module or an intermediate tubing module.

20. The method of claim **18**, wherein cement is introduced into the annulus using the upper end module or the lower end module.

21. The method of claim **20**, wherein the measured data is used to predict fluid invasion into or fluid migration through a cement column placed into the annulus of an actual well.

* * * * *

PUC-Rio - Certificação Digital Nº 1612794/CA